

**INVESTIGATION OF THE MECHANOCHEMICAL CYCLE
OF THE MITOTIC KINESIN EG5**

by

Jared Clinton Cochran

B.S., University of Pittsburgh, 2000

Submitted to the Graduate Faculty of
Arts and Sciences in partial fulfillment
of the requirements for the degree of
Doctor of Philosophy

University of Pittsburgh

2005

UNIVERSITY OF PITTSBURGH
FACULTY OF ARTS AND SCIENCES

This dissertation was presented

by

Jared Clinton Cochran

It was defended on

November 18, 2005

and approved by

Dr. Roger W. Hendrix

Professor, Biological Sciences, University of Pittsburgh

Dr. John M. Rosenberg

Professor, Biological Sciences, University of Pittsburgh

Dr. Gordon S. Rule

Professor, Biological Sciences, Carnegie Mellon University

Dr. William S. Saunders

Associate Professor, Biological Sciences, University of Pittsburgh

Dr. Susan P. Gilbert

Associate Professor, Biological Sciences, University of Pittsburgh
Dissertation Director

Copyright © by Jared Clinton Cochran

2005

**INVESTIGATION OF THE MECHANOCHEMICAL CYCLE
OF THE MITOTIC KINESIN EG5**

Jared Clinton Cochran, Ph.D.

University of Pittsburgh, 2005

Cytoskeletal motor proteins utilize the energy from ATP turnover to perform work along their filament tracks. Eg5 is a microtubule-based motor of the Kinesin-5/BimC family that is essential for bipolar spindle formation during eukaryotic cell division. I have performed a detailed kinetic analysis to define the minimal Eg5 ATPase mechanism. Eg5 association with the microtubule, ADP product release, and ATP binding are rapid steps in the mechanism, while ATP hydrolysis, phosphate product release, and detachment from the microtubule occur relatively slowly. Phosphate release coupled to Mt•Eg5 dissociation represents the rate-limiting step. Therefore, Eg5 remains tightly associated with the microtubule during most of the ATPase cycle, thus adapting the motor for its function within the mitotic spindle.

Monastrol is a small molecule that specifically inhibits Eg5. I performed experiments to define the mechanistic basis for Eg5 inhibition by monastrol. The ATPase activity of Eg5 is reduced with weakened binding to microtubules. Monastrol also stabilizes a subpopulation of “non-productive” complexes that slowly hydrolyze ATP. After ATP hydrolysis, phosphate product is rapidly released coupled to detachment from the microtubule. Therefore, monastrol inhibits Eg5 force generation to yield a motor that cannot function properly in the mitotic spindle.

I have purified Eg5 in the nucleotide-free state to perform a detailed kinetic analysis in the absence of microtubules. ATP hydrolysis and phosphate product release are rapid steps in the mechanism, and the observed rate of these steps is limited by the relatively slow isomerization of the Eg5•ATP collision complex. A conformational change coupled to ADP release is the rate-limiting step in the pathway. These studies provide insight into how the microtubule guides the structural transitions needed to form the ATP hydrolysis-competent state and for rapid ADP release. In addition, monastrol appears to bind weakly to the Eg5•ATP collision complex, but after tight ATP binding, the affinity for monastrol increases, thus inhibiting the conformational change required for ADP product release. Taken together, we

hypothesize that loop L5 of Eg5 undergoes an “open” to “closed” structural transition that correlates with the rearrangements of the switch-1 and switch-2 regions at the active site during the ATPase cycle.

TABLE OF CONTENTS

PREFACE.....	XVI
1.0 CHAPTER ONE: INTRODUCTION.....	1
1.1 EUKARYOTIC CELL DIVISION	1
1.2 MOLECULAR MOTOR PROTEINS	2
1.3 MICROTUBULES.....	3
1.4 KINESIN SUPERFAMILY OF MICROTUBULE-BASED MOTORS.....	5
1.4.1 Kinesin Family Organization and Nomenclature	5
1.4.2 Kinesin-5 / BimC Family	7
1.5 THE STRUCTURE OF KINESIN MOTOR PROTEINS.....	10
1.5.1 The Nucleotide-Binding Site	11
1.5.2 The Microtubule-Binding Region.....	12
1.5.3 The Neck-Linker	14
1.6 EG5 STRUCTURE	14
1.6.1 Eg5•ADP Crystal Structure	14
1.6.2 Inhibitor•Eg5•ADP Crystal Structures.....	16
1.7 SELECTIVE INHIBITORS OF EG5 ATPASE	22
1.7.1 Monastrol – the Prototype Eg5 Inhibitor	22
1.7.2 Other Eg5-Specific Inhibitors.....	24
1.8 THESIS AIMS.....	25
2.0 CHAPTER TWO: MECHANISTIC ANALYSIS OF THE MT•EG5 ATPASE.....	28
2.1 BACKGROUND AND SIGNIFICANCE	29
2.2 MATERIALS AND METHODS	30
2.2.1 Experimental Conditions.....	30
2.2.2 Expression and Purification of Monomeric Eg5.....	30
2.2.3 Expression and Purification of MDCC-PBP	33

2.2.4	Characterization of the MDCC-PBP Preparations	37
2.2.5	Microtubules for Kinetic Experiments	38
2.2.6	Analytical Ultracentrifugation.....	41
2.2.7	Gel Filtration and Stokes Radii Calculations.....	42
2.2.8	Phosphocreatine Kinase Coupled Assay.....	42
2.2.9	Steady-State ATPase Kinetics.....	43
2.2.10	Mt•Eg5 Cosedimentation Assays.....	44
2.2.11	Mt•Eg5•[α - ³² P]ADP Cosedimentation Assays.....	45
2.2.12	Pulse-Chase Experiments.....	46
2.2.13	Acid-Quench Experiments.....	47
2.2.14	Stopped-Flow Experiments.....	48
2.3	RESULTS	51
2.3.1	Oligomeric State of Purified Eg5 Motors	51
2.3.2	Eg5 Active Site Determination.....	53
2.3.3	Eg5 Steady-State ATPase Kinetics	54
2.3.4	Eg5 Binding to Microtubules	55
2.3.5	ADP Equilibrium Binding to Mt•Eg5 Complex.....	56
2.3.6	MantATP Binding to Mt•Eg5 Complex.....	58
2.3.7	MgATP Binding Kinetics by Pulse-Chase	59
2.3.8	ATP Hydrolysis Kinetics by Acid-Quench	61
2.3.9	P _i Product Release from Mt•Eg5 Complexes	64
2.3.10	ATP-Promoted Dissociation of Mt•Eg5 Complexes	66
2.3.11	Eg5 Association with Microtubules.....	67
2.3.12	MantADP Release from the Mt•Eg5•mantADP Complex	68
2.4	DISCUSSION.....	72
2.4.1	Similarities and Differences Between Two Eg5 Monomers	72
2.4.2	Eg5 Compared to Kinesin, Ncd, and Kar3.....	73
2.4.3	Mt•Eg5 ATPase Mechanism	73
3.0	CHAPTER THREE: MONASTROL INHIBITION OF THE MT•EG5 ATPASE MECHANISM.....	75
3.1	BACKGROUND AND SIGNIFICANCE	76

3.2	MATERIALS AND METHODS	77
3.2.1	Experimental Conditions, <i>S</i> -Monastrol, and DMSO Control	77
3.2.2	Protein Preparation	78
3.2.3	Steady-State ATPase Kinetics.....	79
3.2.4	Mt•Eg5 _s Cosedimentation Assays	80
3.2.5	Pulse-Chase Experiments.....	81
3.2.6	Acid-Quench Experiments	82
3.2.7	Modeling of Burst Kinetics	83
3.2.8	Stopped-Flow Experiments.....	85
3.2.9	Phosphocreatine Kinase-Coupled Assays.....	87
3.3	RESULTS	88
3.3.1	Monastrol Inhibits Steady-State ATPase ± Microtubules	88
3.3.2	Monastrol Weakens Eg5 Affinity for Microtubules under Equilibrium Conditions.....	91
3.3.3	Monastrol Does Not Alter the Kinetics of ATP Binding to Mt•Eg5 Complex	94
3.3.4	Monastrol Promotes Reduction in Burst Amplitude during Acid- Quench Experiments	97
3.3.5	P _i Product Release Was Faster in the Presence of Monastrol	102
3.3.6	ATP Hydrolysis Reversals Do Not Explain the Reduction in Burst Amplitude	105
3.3.7	Monastrol Increases the Observed Rate of ATP-Promoted Dissociation of the Mt•Eg5 Complex.....	108
3.3.8	Monastrol Binding Occurs Prior to ATP Hydrolysis for Eg5-367, but not Eg5-437	110
3.3.9	Monastrol Dissociates Neither the Mt•Eg5 Complex nor the Mt•Eg5*•AMPPNP Complex Prior to ATP Hydrolysis	111
3.3.10	Monastrol Dramatically Slows Eg5 _s Association with Microtubules.....	113
3.3.11	Monastrol Slows MantADP Release.....	114
3.3.12	Monastrol Does Not Trap the Mt•Eg5 _s •ADP Complex	116

3.4	DISCUSSION	121
3.4.1	“Non-Productive” Mt•Eg5 ^x •ATP Intermediate	121
3.4.2	Monastrol Promotes Rapid P _i Release Coupled to Mt•Eg5 Dissociation	122
3.4.3	Weakening of the Microtubule Interactions by Monastrol.....	123
3.4.4	Model of Mt•Eg5•Monastrol ATPase Mechanism.....	124
4.0	CHAPTER FOUR: ATPASE MECHANISM OF EG5 IN THE ABSENCE OF MICROTUBULES: INSIGHT INTO MICROTUBULE ACTIVATION AND ALLOSTERIC INHIBITION BY MONASTROL	125
4.1	BACKGROUND AND SIGNIFICANCE	126
4.2	MATERIALS AND METHODS	127
4.2.1	Experimental Conditions.....	127
4.2.2	Purification of ApoEg5	128
4.2.3	Nucleotide-Free Determination of ApoEg5 Preparation.....	128
4.2.4	Steady-State ATPase Kinetics.....	129
4.2.5	Fluorescence Measurements	130
4.2.6	Acrylamide Quenching Experiment.....	130
4.2.7	Stopped-Flow Experiments	131
4.2.8	Quench-Flow Experiments.....	132
4.2.9	Modeling Acid-Quench and P _i Product Release Kinetics	134
4.3	RESULTS	135
4.3.1	ApoEg5 Was Active and Nucleotide-Free.....	135
4.3.2	Steady-State ATPase Reveals Tight ATP Binding, Yet Inefficient Catalysis.....	137
4.3.3	Intrinsic ApoEg5 Fluorescence Enhancement on Nucleotide Binding.....	139
4.3.4	ATP Binding Occurs Via a Two-Step Mechanism.....	140
4.3.5	Pulse-Chase Experiments Reveal Transient Pre-Hydrolysis Intermediate	144
4.3.6	ATP Hydrolysis and P _i Product Release are Rapid Steps in Mechanism.....	146

4.3.7	Reduction of Product Burst Amplitude Rescued by Microtubules.....	150
4.3.8	ATP Hydrolysis Reversals and Weak ATP Binding Do Not Explain the Reduction in Burst Amplitude	152
4.3.9	MantADP Binding Occurs Via a Two-Step Process.....	153
4.3.10	Monastrol Slows ADP Product Release	155
4.3.11	Monastrol Binds Weakly to the Eg5•ATP and Eg5•ADP Collision Complexes.....	156
4.4	DISCUSSION.....	159
4.4.1	ApoEg5 Was Active, Stable, and Nucleotide-Free.....	159
4.4.2	“Non-Productive” versus “Productive” ApoEg5 States	159
4.4.3	Substrate Binding Was Dramatically Slower.....	160
4.4.4	Structural Transition in Loop L5 Correlates with Movement of the Switch Regions	161
4.4.5	Monastrol Binding Occurs Via a Two-Step Mechanism.....	162
5.0	CHAPTER FIVE: CONCLUSIONS.....	164
5.1	STRUCTURAL MODEL OF NORMAL EG5 FUNCTION.....	166
5.1.1	Monomeric Eg5.....	167
5.1.2	Microtubule Binding.....	168
5.1.3	ATP Binding.....	169
5.1.4	ATP Hydrolysis.....	170
5.1.5	Phosphate Product Release and Eg5 Detachment from the Microtubule	171
5.2	STRUCTURAL MODEL OF EG5 INHIBITION BY MONASTROL	171
5.2.1	Inhibition of Microtubule Binding	172
5.2.2	“Non-Productive” Mt•Eg5*•ATP Complexes Promoted by Monastrol.....	173
5.2.3	Monastrol Accelerates the Rate of P _i Product Release and Mt•Eg5 Dissociation	174
5.3	FUTURE STUDIES.....	174
	BIBLIOGRAPHY.....	184

LIST OF TABLES

Table 2.1 Physical Properties of Eg5 Motors	69
Table 2.2 Eg5 Comparison to Conventional Kinesin, Kar3, and Ncd Monomers.....	70
Table 3.1 Monastrol Inhibition of the Eg5 ATPase Mechanism	120
Table 4.1 Comparison of Kinetic Constants for ApoEg5 and Mt•Eg5 ATPase ± Monastrol ...	158

LIST OF FIGURES

Figure 1.1 Tubulin structure and microtubule assembly	4
Figure 1.2 A kinesin phylogenetic tree	6
Figure 1.3 Localization of Eg5 in the mitotic spindle	8
Figure 1.4 Eg5 homotetrameric structure and function in the mitotic spindle	9
Figure 1.5 Conventional kinesin crystal structure	11
Figure 1.6 Conformational changes in the “switch” regions during ATP turnover.....	12
Figure 1.7 The microtubule-binding region of a kinesin motor.....	13
Figure 1.8 Eg5•ADP crystal structure.....	15
Figure 1.9 Monastrol•Eg5•ADP crystal structure.....	18
Figure 1.10 Comparison of Eg5•ADP and monastrol•Eg5•ADP crystal structures	20
Figure 1.11 Detailed structural features of the monastrol•Eg5•ADP complex.....	21
Figure 1.12 Localization of Eg5 in monastrol-treated spindles.....	23
Figure 1.13 Multiple sequence alignment of Eg5, Kinesin, Kar3, and Ncd	26
Figure 2.1 Summary gels for Eg5-367 and Eg5-437 preparations	32
Figure 2.2 MDCC-PBP purification summary	36
Figure 2.3 Characterization of MDCC-PBP preparations	38
Figure 2.4 Tubulin for biochemical experiments.....	40
Figure 2.5 Analytical ultracentrifugation and gel filtration	52
Figure 2.6 Active site determination.....	54
Figure 2.7 Steady-state ATPase kinetics	55
Figure 2.8 Microtubule equilibrium binding experiments.....	56
Figure 2.9 [α - ³² P]MgADP equilibrium binding experiments.....	58
Figure 2.10 Kinetics of mantATP binding to the Mt•Eg5 complex	59

Figure 2.11	Pulse-chase kinetics of ATP binding.....	61
Figure 2.12	Acid-quench kinetics of ATP hydrolysis	63
Figure 2.13	Presteady-state kinetics of P _i product release from the Mt•Eg5 complex	65
Figure 2.14	ATP-promoted dissociation of Mt•Eg5 complex	66
Figure 2.15	Kinetics of Eg5•ADP association with microtubules.....	67
Figure 2.16	Microtubule-activated mantADP release	69
Figure 2.17	Model of Mt•Eg5 ATPase mechanism.....	71
Figure 3.1	Monastrol inhibition of Eg5 steady-state ATPase.....	90
Figure 3.2	Mt•Eg5 _S cosedimentation experiments	92
Figure 3.3	Mt•Eg5 interactions ± monastrol under different nucleotide conditions.....	93
Figure 3.4	MantATP binding to the Mt•Eg5 _S complex	95
Figure 3.5	Pulse-chase and acid-quench kinetics for Mt•Eg5-367 ± monastrol.....	96
Figure 3.6	ATP hydrolysis kinetics for the Mt•Eg5-437 complex ± monastrol	100
Figure 3.7	Acid-quench experiments for P _i product re-binding to Eg5 active site.....	102
Figure 3.8	Presteady-state kinetics of P _i product release from Mt•Eg5 complex ± monastrol..	104
Figure 3.9	DynaFit simulations of Mt•Eg5 mechanism ± monastrol	107
Figure 3.10	ATP-promoted dissociation of the Mt•Eg5 complex ± monastrol	109
Figure 3.11	Experiments to evaluate sequential addition of monastrol.....	111
Figure 3.12	Monastrol-promoted dissociation of the Mt•Eg5 complex	112
Figure 3.13	Eg5 _S association with microtubules.....	114
Figure 3.14	MantADP release from Mt•Eg5 _S complex	116
Figure 3.15	Equilibrium state of Eg5 _S complexes	118
Figure 3.16	Model of Eg5 ATPase inhibition by monastrol.....	119
Figure 4.1	Determination of nucleotide-free state of apoEg5.....	137
Figure 4.2	ApoEg5 steady-state ATPase	138
Figure 4.3	MgATP binding to apoEg5 by tryptophan fluorescence enhancement.....	141
Figure 4.4	MantATP binding to apoEg5 ± monastrol	143
Figure 4.5	MgATP binding to apoEg5 by pulse-chase ± monastrol.....	145
Figure 4.6	Presteady-state kinetics of ATP hydrolysis ± monastrol.....	148
Figure 4.7	Presteady-state kinetics of P _i product release ± monastrol.....	149

Figure 4.8 Microtubules rescue lowered burst amplitudes	151
Figure 4.9 DynaFit simulations to understand burst amplitude reduction.....	154
Figure 4.10 MantADP binding to apoEg5 \pm monastrol.....	155
Figure 4.11 Model of apoEg5 ATPase mechanism	157
Figure 5.1 Models of Eg5 ATPase in the absence and presence of monastrol.....	167

LIST OF SCHEMES

Scheme 2.1	55
Scheme 3.1	89
Scheme 3.2	106
Scheme 3.3	106
Scheme 4.1	138
Scheme 4.2	138

PREFACE

“I praise You because I am fearfully and wonderfully made;
Your works are wonderful, I know that full well.” Psalm 139:14

The truth of this verse has been made clearer over the past five years. I am very thankful for the opportunity to research and study one small piece of an immense biological puzzle. During graduate school, I have met and interacted with a multitude of people to accomplish the goal of analyzing, synthesizing, and evaluating a complex biological problem. There is no possible way that I could have reached this goal without these people.

I want to thank my research advisor, Dr. Susan P. Gilbert, for her guidance, patience, and friendship during my studies in her laboratory. I can remember back to my undergraduate career at the University of Pittsburgh, and going to Susan’s office hours for my biochemistry class. I remember telling her, “I am not sure why I want to go to medical school.” Her advice was to acquire research experience, and she later offered me a position in her lab. It is truly amazing how life’s journey takes many detours! Needless to say, this experience extended into my graduate training, and I owe her many thanks along the way. I am very grateful for all that she has done for me. Thank you very much, Susan.

Lisa R. Sproul and Troy C. Krzysiak are two amazing graduate students, and are two of my closest friends. Lisa and I started our graduate studies at the same time, sat beside each other every day during Core Course, rotated in totally different labs, but we both decided to stay in Susan’s lab for our thesis work. Lisa is a very intelligent, caring, and strong woman, who has impacted my life in more ways than she is probably aware. Her wonderful personality truly makes the environment in the lab much better, and her scientific determination is addicting. I am very blessed to have worked with Lisa, and I look forward to seeing her career prosper. Lisa will

always have a special place in my heart, and I will miss her being in the lab. Troy came into the Gilbert lab a year after Lisa and I, and I had the privilege of training Troy during his rotation project. At the onset, I was honestly skeptical as to how Troy was going to “mold” into the lab, but as it turned out, his presence in the lab “broke the mold”, and raised the intellectual standard an order of magnitude! His passion and desire to understand every little detail about every little thing we do in the lab (especially the mathematical equations!) has truly made me a better scientist. I thoroughly enjoyed our daily half-hour “Eg5 sessions” and I will miss these “crazy idea-generating” discussions. I admire Troy’s work-ethic and I have learned a great deal from working with him. It will be interesting to see where his research project takes him, and I also look forward to keeping close contacts with Troy in the future.

Dr. Andrew Mackey and Dr. Lisa Klumpp were graduate students when I joined the lab, and played a large role in guiding me during the early days of my research. I am very grateful for their time and friendship when we were all in the lab. Many research technicians played a vital role in training me in protein purification and experimental procedures. Joseph Gatial III spent a fair amount of time during the beginning of my days in the Gilbert lab, and “got me on my feet” with many of the techniques that I would later use to complete my thesis work. Joe performed many experiments with Eg5-367 to understand the mechanism of monastrol inhibition. Brian Robertson was also a technician when I entered the lab, and I am grateful for his time in training me and his friendship during his stay in the lab. Recently, Dave Close joined the Gilbert lab as a research technician, and even though our interaction has been brief, I have enjoyed our conversations and discussions about his research project and other aspects of life. I can honestly say that Dave is probably the nicest guy I’ve ever met, and I look forward to communicating with him in the future because he is such a “talker”.

Several undergraduates have passed through the lab during my graduate work. Christopher Farrell was a very bright undergrad in the lab when I joined. His time was incredibly valuable in getting me familiar with several computer software programs. Merrian Brooks, Thanh Ha, and Daniel Anderson joined the lab around the same time, and I had the delight of working with these folks. Merrian is the sweetest woman a person could ever meet, and our spiritual discussions were always inspirational. Thanh (a.k.a. “Miss Tina”) is a very strong and intelligent individual, who I know will make a wonderful doctor some day. I was honored to interact with and guide Thanh during the later stages of her research project. Daniel

worked incredibly hard to get equilibrium binding experiments to work with Eg5 in the presence with monastrol, though things did not quite go as planned. Ben Williams is currently an undergraduate from Carnegie Mellon University who has been working part-time in the lab. I also want to thank Alycia Bittner and Fengfeng Xu for their rotations in the Gilbert lab. I had a great time mentoring these talented graduate students.

Many folks outside the Gilbert lab have been instrumental in making this experience complete. I would have not been able to complete this dissertation without the contributions from my collaborators. I would like to acknowledge and thank Merck Research Laboratories (West Point, PA), especially Dr. Wasyl Halczenko and Dr. George Hartman, for supplying the gifts of *S*-monastrol. I want to thank Zoltan Maliga, from Dr. Timothy Mitchison's lab at Harvard Medical School, who engineered the Eg5 constructs that I used in my research. I also would like to thank Dr. Tarun Kapoor at Rockefeller University for his insight into the mechanistic analysis of the mitotic kinesin Eg5. I want to acknowledge Dr. John J. Correia and his graduate student Christopher Sontag (University of Mississippi Medical Center) for their collaboration to perform the analytical ultracentrifugation experiments using Eg5-437. During my graduate work, I had the opportunity and delight to collaborate with Dr. Yiorgos Skiniotis (Dr. Andreas Hoenger's lab at EMBL, Germany) and Dr. Ian Robertson (Dr. Christopher Berger's lab at University of Vermont). Yiorgo came to the lab for a week to do biochemical experiments to study the modulation of kinesin binding by the C-terminal tails of tubulin. We spent approximately 100 hours in the lab that week, and had a great time. Yiorgos and I have kept close contact, and I thank him for his continued friendship and advice about my postdoctoral studies. Ian also came to the lab for a week to investigate the ATP hydrolysis mechanism of a myosin-II mutant using quench-flow techniques. Ian inspired me to use modeling as a means to design experiments as well as to assist in the interpretation of results.

I want to thank my thesis committee, Dr. Roger Hendrix, Dr. John Rosenberg, Dr. Gordon Rule, and Dr. William Saunders, for their time, suggestions, and guidance during my studies. I particularly want to thank John Rosenberg for the great deal of time he spent mentoring me during my comprehensive exam, and for his inspiration to continue my scientific endeavors as a postdoctoral fellow to learn X-ray crystallography. I can still remember after John's first Core Course lecture on crystallography, I asked him, "What does a person need to do to become a crystallographer?" He exclaimed, "Why don't you rotate in my lab for ten weeks

and find out!” Inevitably, I did rotate in his lab, and I am grateful for all the time John has invested in my scientific training. I would also like to thank Dr. Jeffrey Brodsky and Dr. Gerard Campbell who invested time and resources during my rotations. The experience that I gained in their labs is priceless.

My teaching experience at the University of Pittsburgh has been superb, and I want to thank those who made this experience successful. Dr. Susan Godfrey and Dr. Paula Grabowski were my teaching mentors, and I especially want to thank Paula for all she has taught me about being a teacher. The education process involves a tremendous sacrifice of time and resources from both the teacher and the student. I am very grateful for the sacrifice that my teaching mentors (and others) have made, and I look forward to applying my acquired teaching skills in a variety of different arenas.

Several research laboratories have been generous in their assistance during my studies. Dr. Anthony Schwacha’s lab provided reagents and instruments to borrow so that I would be able to complete several protein purifications. Dr. Jeffrey Lawrence’s lab has trained me to use the fluorimeter. I especially would like to acknowledge and thank Hans Wildschutte for his time and friendship throughout this process.

I would like the entire Department of Biological Sciences at the University of Pittsburgh for making graduate school such a wonderful experience. I especially want to thank Cathy Barr for being the wonderful, sincere, caring, patient, and friendly person that she is. The work that she does behind the scenes to make a graduate student’s life much easier is priceless. Other members of the main office that have also been great are Natalie Marintel, Kathy Hoffman, and Crystal Petrone. The women in the fiscal office who made sure I was paid each month and who have been wonderful people are Lynn Weber, Pat Dean, and Patty Henry.

My family has been incredibly supportive throughout this long haul. I love my mom and dad very much, and I am thankful for all they have done to get me where I am today. Even though they did not quite comprehend what I was doing over the last five years, they were eager to hear about another paper that I published, or about how things were going in the lab. The influence of my parents has truly shaped and molded me into the person that I am, and I am forever grateful for their love, patience, and support throughout life. Who would have ever known that their “little terror” would become a doctor! Thank you, mom and dad, for not giving up on me. I love you very much!

I also want to thank my parents-in-law for their love and support. They have been great support over the years, and I am thankful that my wife has such wonderful parents! Living with them over the last few months has brought us much closer. I am especially thankful for the help that my mother-in-law has provided with watching the kids.

Finally, I dedicate this work to my beautiful wife Lisa, and the two cutest boys on the planet, Noah and Nathan. My wife is my best friend. There is nobody in the world that I would rather be with than my wife. She has been beside me every step of the way during this entire process. From my long days at work, to my frustrated complaining, to my joy and excitement of successfully defending my thesis, she has been there for me. My love for her is immense, and I thank her for showing me unconditional love every day. Not only is she a fabulous wife, but she is certainly the best mother a child could ever have. Noah and Nathan are my pride and joy, and I love them so much. Being a father to these boys has been the greatest blessing one could ever imagine. I look forward to watching these boys grow up to become men. One of my goals as a husband and a father is pursue a career where I will be able to provide for my family. The completion of this dissertation is a giant landmark on the path to attain this goal.

1.0 CHAPTER ONE: INTRODUCTION

One of the essential mechanisms for the sustenance of life is the capability of a cell to accurately segregate its genetic material during cell division. The intricacy and complexity of cell division rests in the necessary and proper interactions between molecular motor proteins and the cell's architectural framework. Molecular motor proteins utilize the energy from ATP binding, ATP hydrolysis, and product release to perform mechanical work along its filament track. The nucleotide state at the motor active site is thought to dictate the affinity of the motor for its filament partner. However, it is not clear how different motor proteins confer specific properties based on the modulation of the rate and equilibrium constants that define the ATPase mechanism. A detailed kinetic analysis of a mitotic kinesin motor protein called Eg5 will provide insight into how this motor functions to establish and maintain the bipolar spindle during cell division. In addition, studying the inhibition of Eg5 by a selective small molecule can offer mechanistic insight into the ATPase cycle of Eg5, as well as providing knowledge for the design of more effective chemotherapeutic agents for the treatment of cancer.

1.1 EUKARYOTIC CELL DIVISION

Mitosis is a biological phenomenon that has been studied since the late nineteenth century, yet a detailed molecular description remains incomplete. Mitosis (from Greek *mitos* meaning “thread”) is the phase of the cell cycle where the nucleus of a eukaryotic cell containing duplicated chromosomes is divided into two daughter nuclei, each containing a copy of the genetic information. A complex machine called the mitotic spindle is responsible for segregating replicated chromosomes and dividing the cell with high fidelity. Although there are >800 different proteins that function during mitosis (1), the mitotic spindle is composed primarily of

microtubules and microtubule-based motor proteins. The current model for spindle organization and morphogenesis during the different stages of mitosis centers on the balance of forces that are generated by dynamic microtubules and motor proteins (2). However, the mechanism of force generation by motor proteins remains largely uncharacterized.

1.2 MOLECULAR MOTOR PROTEINS

Molecular motor proteins are a diverse set of mechanochemical machines that convert the energy stored in different nucleotide triphosphates into molecular motion. This motion produces unidirectional force upon the associated track, which is utilized differently depending on the function of the motor. There are many mechanochemical systems that have been identified in nature. Remarkably, three distinct families of motor proteins – myosin, dynein, and kinesin – are responsible for powering most eukaryotic cellular movements. These motor proteins share similarities in their capability to catalyze the conversion of the substrate ATP to ADP+P_i products. Yet, each superfamily is diverse in sequence and structure, which leads to differences in their function *in vivo*.

The myosin superfamily comprises 18 different classes of proteins that cyclically interact with actin filaments. Myosins display a variety of functions including muscle contraction, vesicle transport, membrane trafficking, cell locomotion, and signal transduction [reviewed in (3-6)]. The dynein superfamily of microtubule-based motors includes 15 “axonemal” forms (motors associated with ciliary and flagellar movements) and 2 “cytoplasmic” forms that participate during retrograde axonal transport, vesicle transport, mitotic spindle organization, and nuclear and cell migration [reviewed in (7, 8)]. The kinesins, which also interact with microtubules, consist of 14 groups plus 1 orphan group. The different kinesin families are organized based on similar sequences within the conserved motor domain as well as similar *in vivo* functions. These proteins perform various functions in eukaryotic cells including anterograde axonal transport, intracellular transport of organelles, mRNAs and multisubunit protein complexes, mitotic spindle establishment and maintenance, chromosome and spindle movements, signal transduction, as well as regulation of microtubule dynamics [reviewed in (9-14)]. Several kinesins and cytoplasmic dynein participate in the organization, maintenance, and

morphology of the mitotic spindle between the stages of prophase and telophase. However, all three families of motor proteins drive movements during cytokinesis – the final stage of mitosis – to fully separate the two daughter cells (15).

1.3 MICROTUBULES

In eukaryotic cells, the cytoskeleton or cell architecture is primarily composed of three structures: filamentous actin, intermediate filaments, and microtubules. Microtubules are very large, non-covalent polymers built from the protein tubulin. Tubulin exists as a stable heterodimer containing a non-exchangeable (α -subunit) and exchangeable (β -subunit) guanine nucleotide-binding site. Each subunit consists of three domains: a N-terminal nucleotide-binding domain, an intermediate domain that is the site of Taxol binding in the β -subunit, and a C-terminal domain, composed of helices $\alpha 11/\alpha 12$ and the acidic C-terminal “tails”, which together comprise the binding region for microtubule-based motor proteins (16) ([Figure 1.1](#)). The $\alpha\beta$ tubulin heterodimers interact with each other longitudinally (head-to-tail) to form long, rod-like polymers called protofilaments. Approximately 10–15 parallel protofilaments interact laterally (side-by-side) to form a hollow cylindrical structure analogous to a drinking straw. The structural polarity of the microtubule gives rise to different rates of polymerization (growing) at either end (17). The rapidly polymerizing end of the microtubule is designated as the plus-end, while the slow growing end is called the minus-end. Different microtubule-based motor proteins have been shown to move along the microtubule track in either direction, as well as regulating the polymerization/depolymerization dynamics at either end. During mitosis, different members of the kinesin superfamily function to establish and maintain the dynamic structural arrangement of microtubules within the bipolar spindle (18).

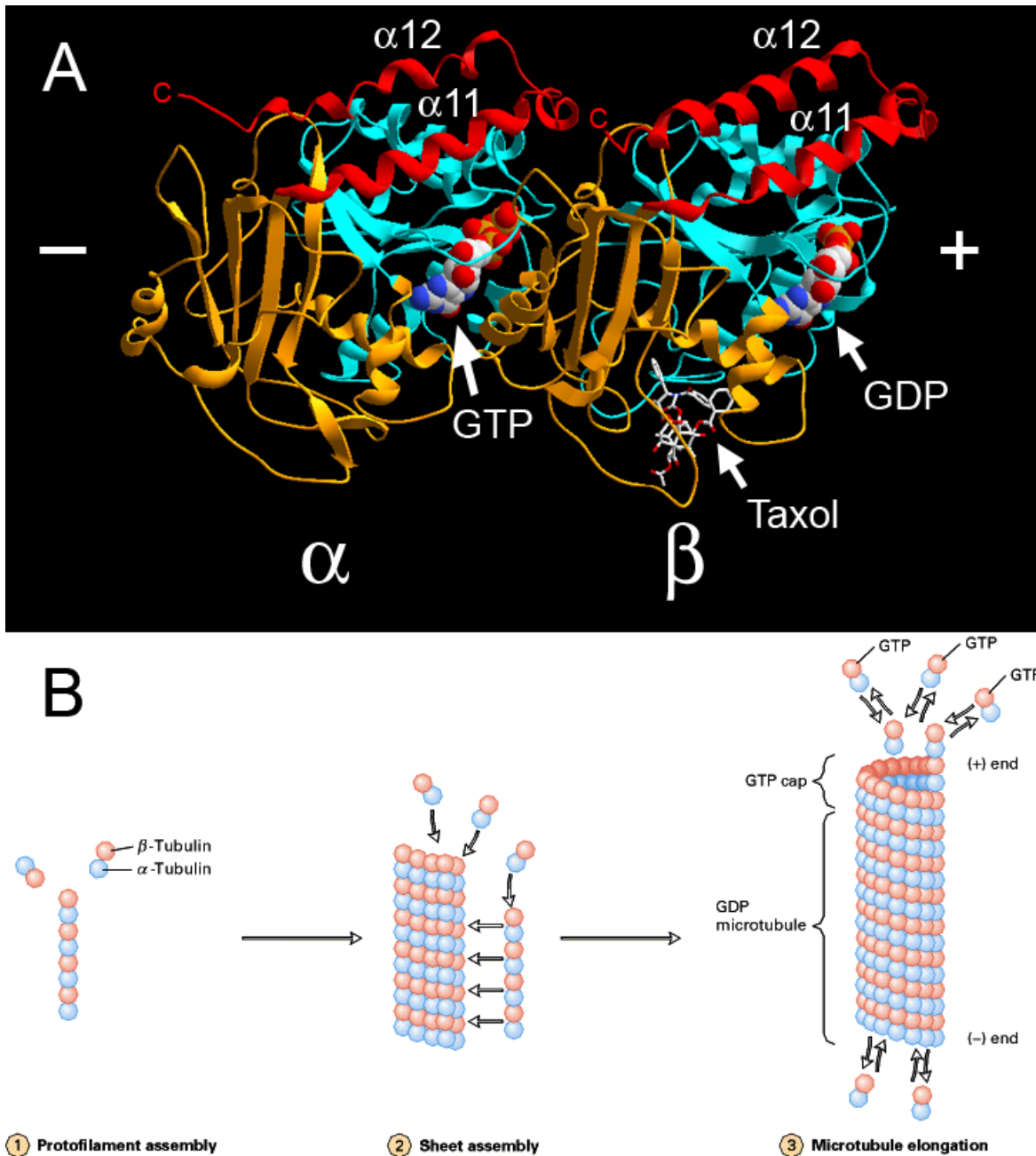


Figure 1.1 Tubulin structure and microtubule assembly

(A) Ribbon diagram of the tubulin heterodimer illustrating the α -subunit (left) with bound GTP, and the β -subunit (right) with bound GDP and Taxol (16). The structure is oriented such that the plus-end of the microtubule points right, the minus-end points left, the outside surface of the microtubule is positioned at the top, and the inside is at the bottom. The N-terminal domain (cyan), the intermediate domain (orange), and the C-terminal domain (red) are highlighted. The flexible, acidic C-terminal tails of tubulin are not visible in the crystal structure. (B) Model for microtubule assembly (19). Heterodimers of tubulin are thought to first interact longitudinally to form long protofilaments. These protofilaments interact laterally to form curved sheets. Eventually a sheet wraps around into a microtubule with 10-15 protofilaments. The plus-end of the microtubule shows faster polymerization kinetics compared to the minus-end.

1.4 KINESIN SUPERFAMILY OF MICROTUBULE-BASED MOTORS

The kinesin superfamily of microtubule-based motors has received much attention over the past 20 years since the discovery of the first kinesin (termed conventional kinesin or Kinesin-1) in 1985 (20, 21). All kinesins share a ~350 amino acid motor domain that contains the ATP binding site and the microtubule-binding region [reviewed in (22, 23)]. A third region that is somewhat conserved within kinesin families is the ~14–20 amino acid sequence adjacent to the motor domain called the neck-linker. Together, the motor domain and the neck-linker make up the core domain, which represents the minimal structure that is necessary and sufficient to hydrolyze ATP and produce force *in vitro* (24, 25). However, outside the core domain, the sequence similarity between kinesins diverges. Most kinesins contain a long α -helical coiled-coil stalk domain, which is often utilized for the stabilization of higher order oligomers. Finally, at the end of the stalk domain resides a small, non-catalytic globular domain (often called the tail domain), which has not yet been well studied in comparison to the kinesin core domain. The differences between the tail domains in the kinesin superfamily are correlated to different functions (e.g. cargo binding and core domain regulation) (26-28). In addition, several kinesins interact with non-motor polypeptides, which also affect the regulation of motor activity and function (29-35).

1.4.1 Kinesin Family Organization and Nomenclature

The kinesin superfamily can be divided into three broad classes depending on the location of the core domain at the N-terminus (KinN), at the C-terminus (KinC), or at an Internal position (KinI) of the primary structure (Figure 1.2). Within these three major classes, a standardized kinesin nomenclature based on 14 family designations has been set forth (36). Family members from Kinesin-1 through Kinesin-12 reside in the KinN class. The Kinesin-13 family represents the KinI class, and Kinesin-14 denotes the KinC class. KinN kinesins share similar plus-end-directed motility properties such that the motor moves to the plus-end (fast-growing end) of the microtubule, whereas KinC kinesins display minus-end-directed motility, thus moving toward the minus-end (slow-growing end) of the microtubule. The directional preference of kinesins seems to be dictated by the neck-linker region and not solely the motor domain (37-42). KinI

kinesins appear to lack the ability to move unidirectionally along the microtubule, but instead utilize their generated force to destabilize the microtubule ends (43, 44).

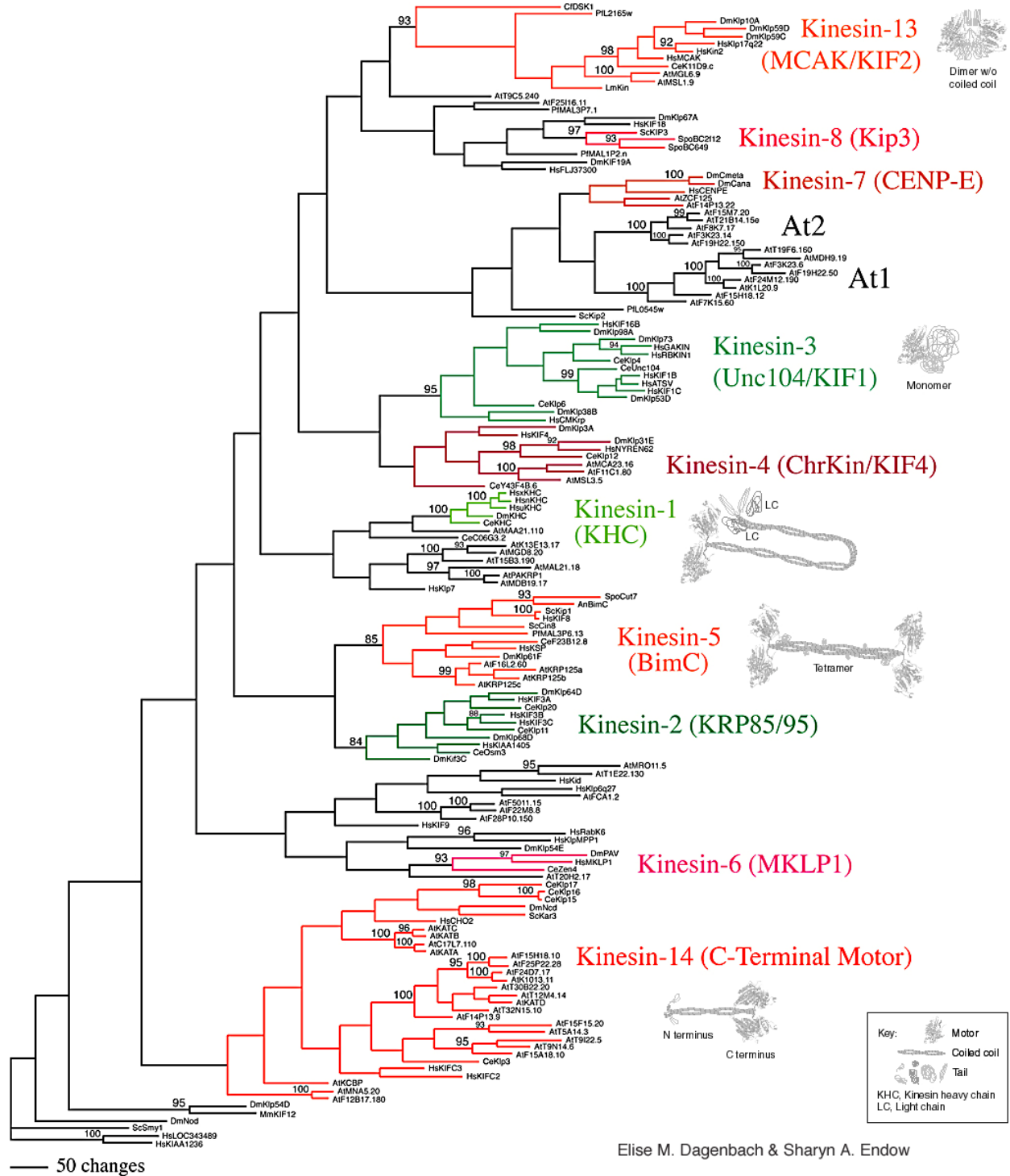


Figure 1.2 A kinesin phylogenetic tree

A representation of the 14 families plus 1 orphan family that comprise the kinesin superfamily of microtubule-based motor proteins (45). The tree was built from a kinesin motor domain sequence alignment using the heuristic search method of PAUP v4.0b10 (Swofford, 2002), a maximum parsimony program. This classification is based on the new standardized nomenclature, yet the previous naming of the various families is also included. In addition, the proposed quaternary structure of each family is included.

1.4.2 Kinesin-5 / BimC Family

The Kinesin-5 or BimC family of kinesins are relatively slow, plus-end-directed motors that are required for proper establishment and maintenance of the mitotic spindle – the cytoskeletal machine used to segregate the genetic material during eukaryotic cell division (46). The first identified member of the Kinesin-5 family (called BimC) was discovered in a genetic screen in *Aspergillus nidulans* as a mutation in a mitotic gene that resulted in a phenotype described as “blocked in mitosis” (47). This mutated gene product lead to failure of the duplicated spindle pole bodies to separate, thus the mitotic spindle could not be established and the nucleus could not be divided properly. Other members of the Kinesin-5 family that are required for proper spindle assembly and maintenance in different organisms include *Schizosaccharomyces pombe* Cut7 (48, 49), *Saccharomyces cerevisiae* Kip1p and Cin8p (50-52), *Drosophila melanogaster* Klp61F (53, 54), *Xenopus laevis* Eg5 and Eg52 (55-57), *Mus musculus* Kif11 (58), and *Homo sapiens* Eg5/KSP (59). These nine genes share considerable sequence identity (~50–60%) within their N-terminal motor domain and neck-linker, but virtually no similarity in the stalk and tail regions except in a ~40 amino acid sequence near the C-terminal end of the protein called the “BimC box” (46). This “BimC box” contains the consensus sequence for the mitotic cyclin-dependent kinase p34^{cdc2}, and both *Xenopus* and human Eg5 have been shown to require phosphorylation of a single threonine within the sequence to regulate Eg5’s interaction with the microtubule lattice (59, 60).

Eg5 has been shown to localize along the entire length of the mitotic spindle, from each spindle pole toward the metaphase plate where the chromosomes are positioned ([Figure 1.3](#)). The microtubules that make up the bipolar spindle are oriented such that the minus-ends are located at the centrosomes or spindle poles, while the plus-ends emanate toward the cell periphery and toward the chromosomes at the metaphase plate. Eg5’s function at the different regions of the mitotic spindle remains unclear; however, there appears to be a more pronounced staining of Eg5 at the spindle poles compared to the interpolar region. Nevertheless, the rate of

spindle assembly *in vivo* correlates well with the rate at which Eg5 can glide microtubules *in vitro* (61). In addition, when Eg5 is inhibited by specific antibodies, the mitotic spindle is monopolar containing two or more non-separated spindle poles, thus implicating this motor protein in centrosome separation as well as spindle maintenance.

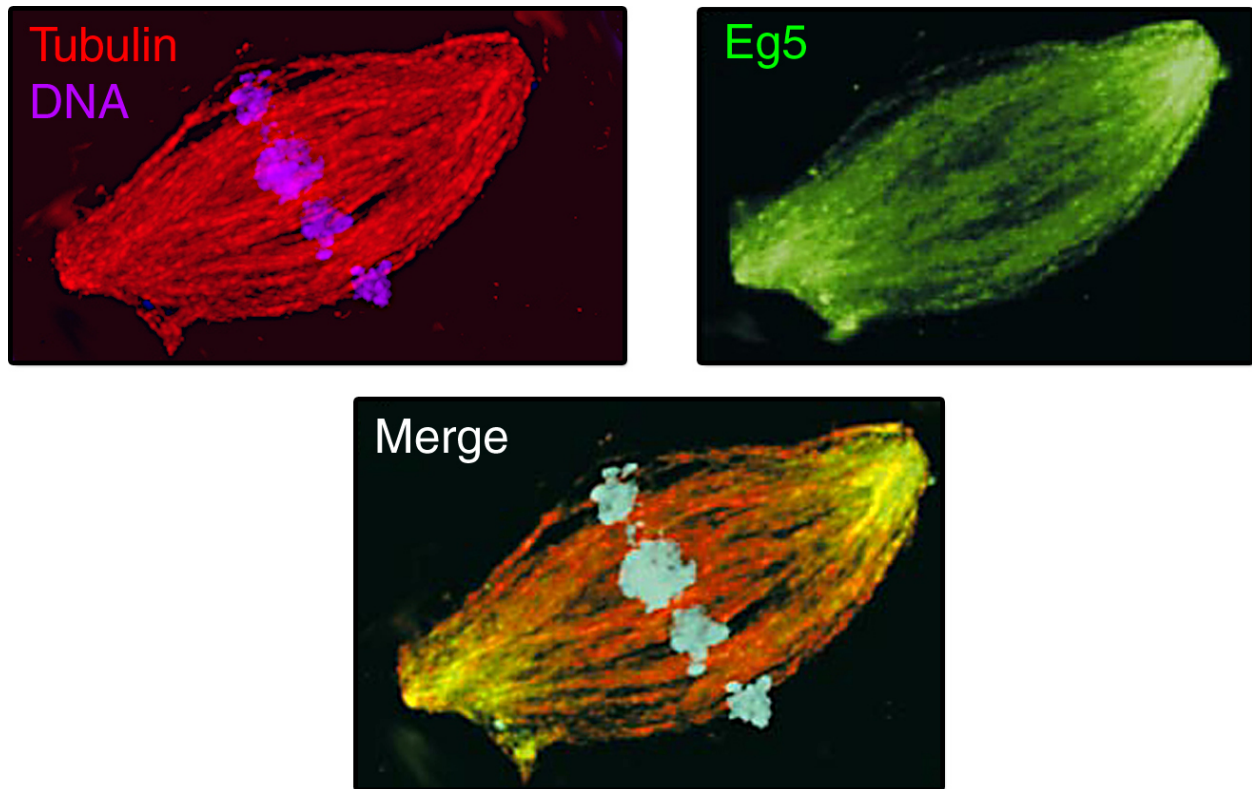


Figure 1.3 Localization of Eg5 in the mitotic spindle

Immunolocalization of Eg5 within bipolar mitotic spindles *in vitro* (62). The merge shows the chromatin (blue), tubulin (red), and Eg5 (green) in a *Xenopus* spindle. Eg5 stained along microtubules throughout the entire spindle and showed enrichment at the spindle poles.

Kinesin-5 family members are thought to share a similar quaternary structure ([Figure 1.4A](#)). Electron microscopy studies of Klp61F suggest that these kinesins exhibit a homotetrameric structure with two N-terminal motor domains positioned at each end of a coiled-coil stalk (63, 64). It is hypothesized that this structure assembles by two parallel heavy chains interacting through their stalk domains to form a coiled-coil, then two anti-parallel dimers interacting through their coiled-coil regions to form the bipolar tetramer. It is intriguing to speculate that the C-terminal tails, each containing a “BimC box” and located in close proximity

to the opposite motor domains, physically interact and somehow regulate the motor's ability to associate with microtubules. Nevertheless, this bipolar homotetrameric structure facilitates the ability of Kinesin-5 members to interact with and slide adjacent microtubules during mitosis (61, 65-67) ([Figure 1.4B](#)).

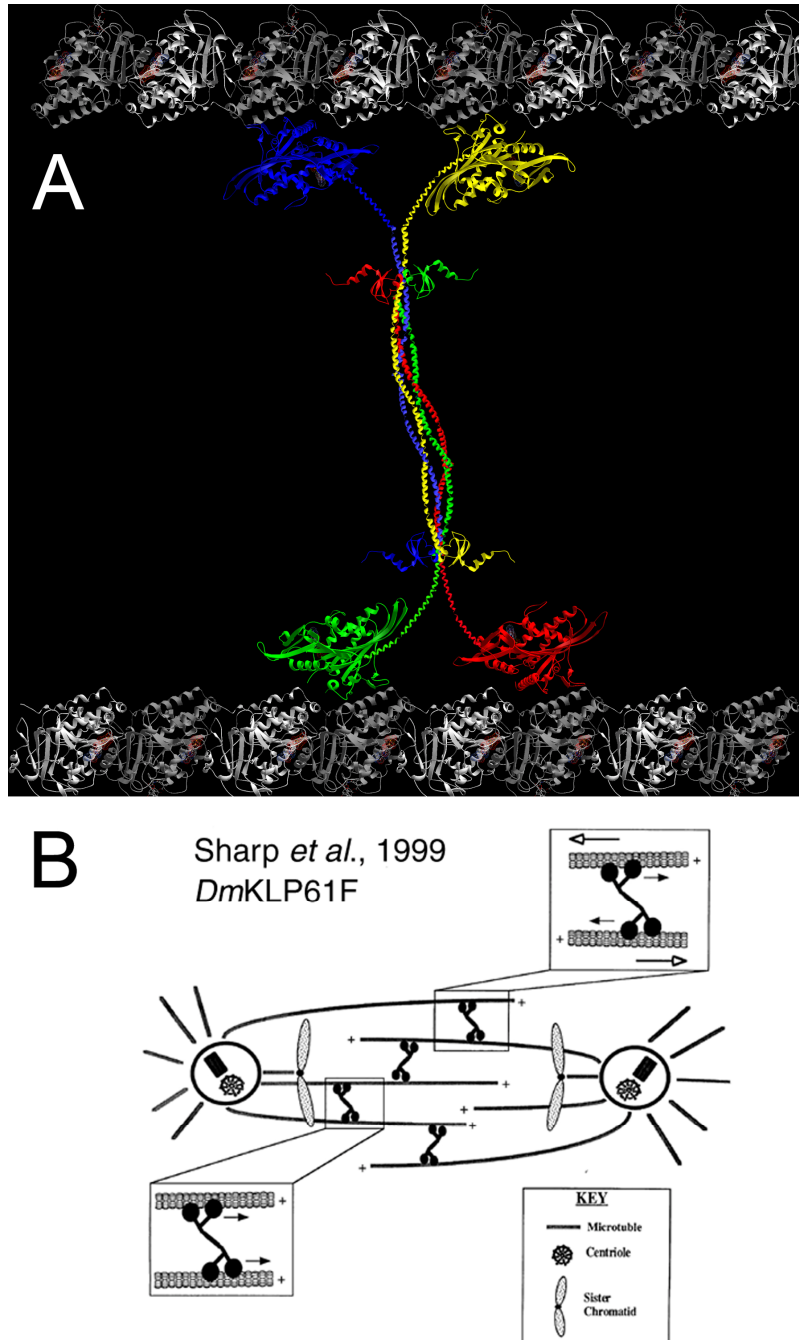


Figure 1.4 Eg5 homotetrameric structure and function in the mitotic spindle

(A) Model for the homotetrameric quaternary structure of Eg5. This model was generated using the x-ray crystal structure coordinates for tubulin (Nogales *et al.* (16) PDB 1JFF) and Eg5•ADP (Turner *et al.* (68) PDB 1II6; red and blue) and monastrol•Eg5•ADP (Yan *et al.* (69) PDB 1Q0B; green and yellow) for the motor domains, tropomyosin (Whitby *et al.* (70) PDB 1C1G) for the coiled-coil stalk region, and the N-terminal domain of ribosomal protein L9 (Luisi *et al.* (71) PDB 1CQU) for the C-terminal globular domains of each Eg5 heavy chain. This model is not meant to convey the exact structure of the stalk and C-terminal domains of Eg5. In addition, this model is also not to scale with respect to the length of the stalk region. (B) Proposed model of Eg5's function within the bipolar mitotic spindle based on the structural studies with the Kinesin-5 member from *Drosophila*, Klp61F (65). Depending on the localization of Eg5 within the spindle, the probability to interact with and slide parallel microtubules increases at the spindle poles, whereas the probability to bind and slide anti-parallel microtubules increases toward the spindle midzone.

1.5 THE STRUCTURE OF KINESIN MOTOR PROTEINS

In order to better understand the different working parts of a motor protein, a high resolution structure of the core domain is needed to define the three dimensional arrangement of secondary structure elements. The first high-resolution crystal structure of a Kinesin-1 motor domain was solved by Kull *et al.* in 1996 (72) ([Figure 1.5](#)). To date, there are more than 28 kinesin crystal structures from several different families deposited in the Protein Data Bank (<http://www.rcsb.org/pdb/>). The six kinesin families represented include Kinesin-1 (conventional kinesin) (72-76), Kinesin-3 (Kif1a/Unc104) (77, 78), Kinesin-5 (BimC) (68, 69, 79), Kinesin-7 (CENP-E) (80), Kinesin-13 (MCAK) (81, 82), and Kinesin-14 (Ncd/Kar3/KCBP) (40, 83-88). Kinesin motor domains display a three-layer ($\alpha\beta\alpha$) sandwich architecture, where the central eight-stranded parallel β -sheet is surrounded by three α -helices flanking either side (89, 90). The core domain of each structure consists of a relatively open nucleotide-binding cleft containing MgADP bound. Exceptions include the KinI motor core from *Plasmodium falciparum*, which lacks nucleotide at the active site (81), and Kif1a with either AMPPCP, AMPPNP, ADP•Vi, or ADP•AlF₄ bound at the active site (77, 78). The nucleotide is positioned among four motifs, N1 to N4, also found in other nucleotide triphosphate-binding proteins, such as myosins and G-proteins (73). The nucleotide state at the active site is thought to trigger a switch in conformation that is then transmitted to the adjacent regions of the core that interacts with the microtubule, which results in changes in binding affinity (77, 91, 92). In addition, the change in nucleotide state at the active site is thought to elicit conformational changes in the motor domain that ultimately generates the force that the motor utilizes for its specific purpose *in vivo*.

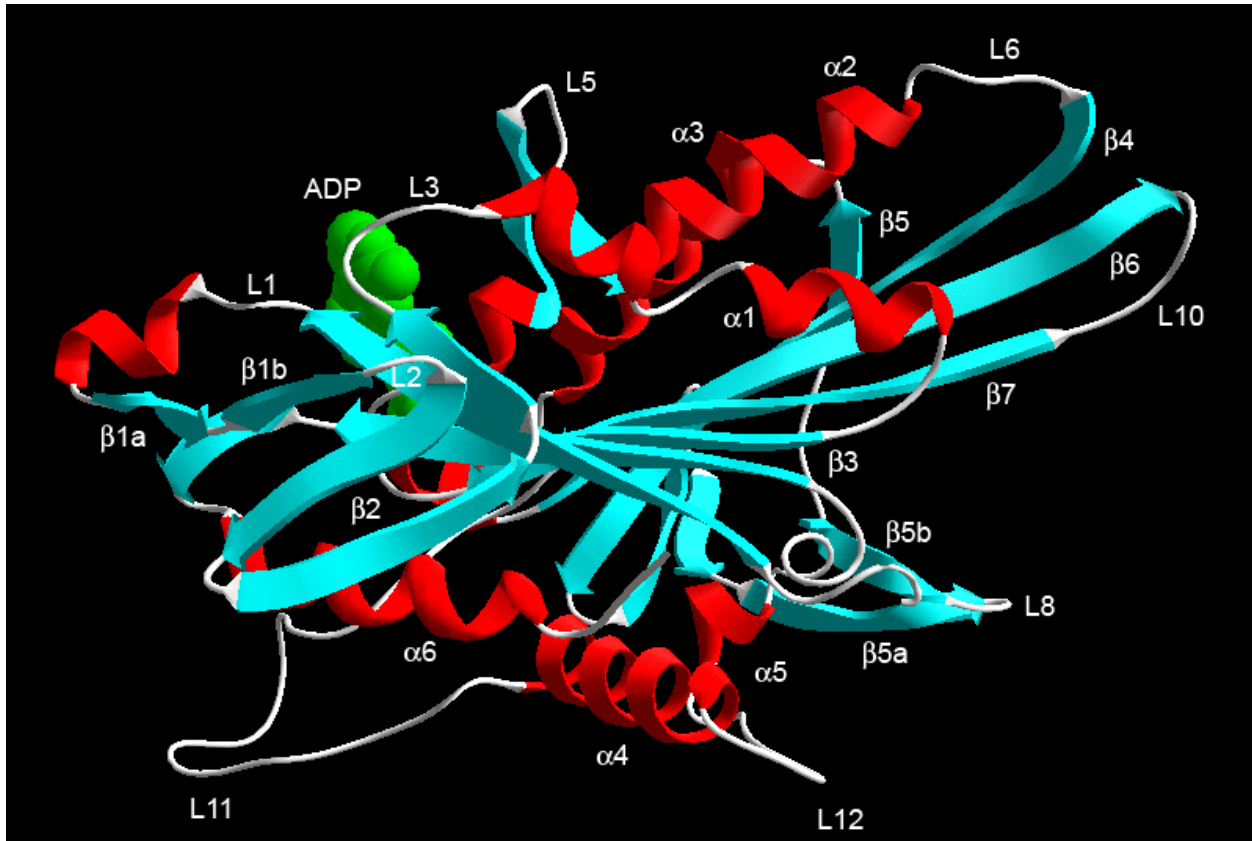


Figure 1.5 Conventional kinesin crystal structure

Ribbon diagram of the human conventional kinesin motor domain [PDB 1BG2; (72)]. The α -helices (red), β -sheets (cyan), and the loops (white) are highlighted to convey the $\alpha\beta\alpha$ architecture. The microtubule binding region of the molecule is positioned at the bottom of the diagram. The active site containing bound ADP (green) is positioned at the top. The visible secondary structure elements are labeled.

1.5.1 The Nucleotide-Binding Site

The active site of motor proteins and G-proteins contain four common motifs called N1, N2, N3 and N4 in kinesins. N1 is also called the Walker A motif (GQTxxGKT, consensus motif underlined, “x” = any amino acid) that forms the “P-loop”, which binds oxygen atoms of the α - and β -phosphates. N4 (RxRP) is involved in interactions with the adenine base. N2 (NxxSSR) and N3 (DxxGxE) are known as switch-1 and switch-2, respectively, in analogy to G-proteins and myosins (93). The switches are thought to function as γ -phosphate sensors to change position and conformation depending on the nucleotide at the active site – either ATP, ADP•P_i, ADP, or nucleotide-free (77) (Figure 1.6). The small conformational changes in the switches are

thought to trigger the motion of adjacent elements to cause a transduction and amplification of information from the active site to the working regions of the motor including the microtubule-binding interface and neck-linker (92).

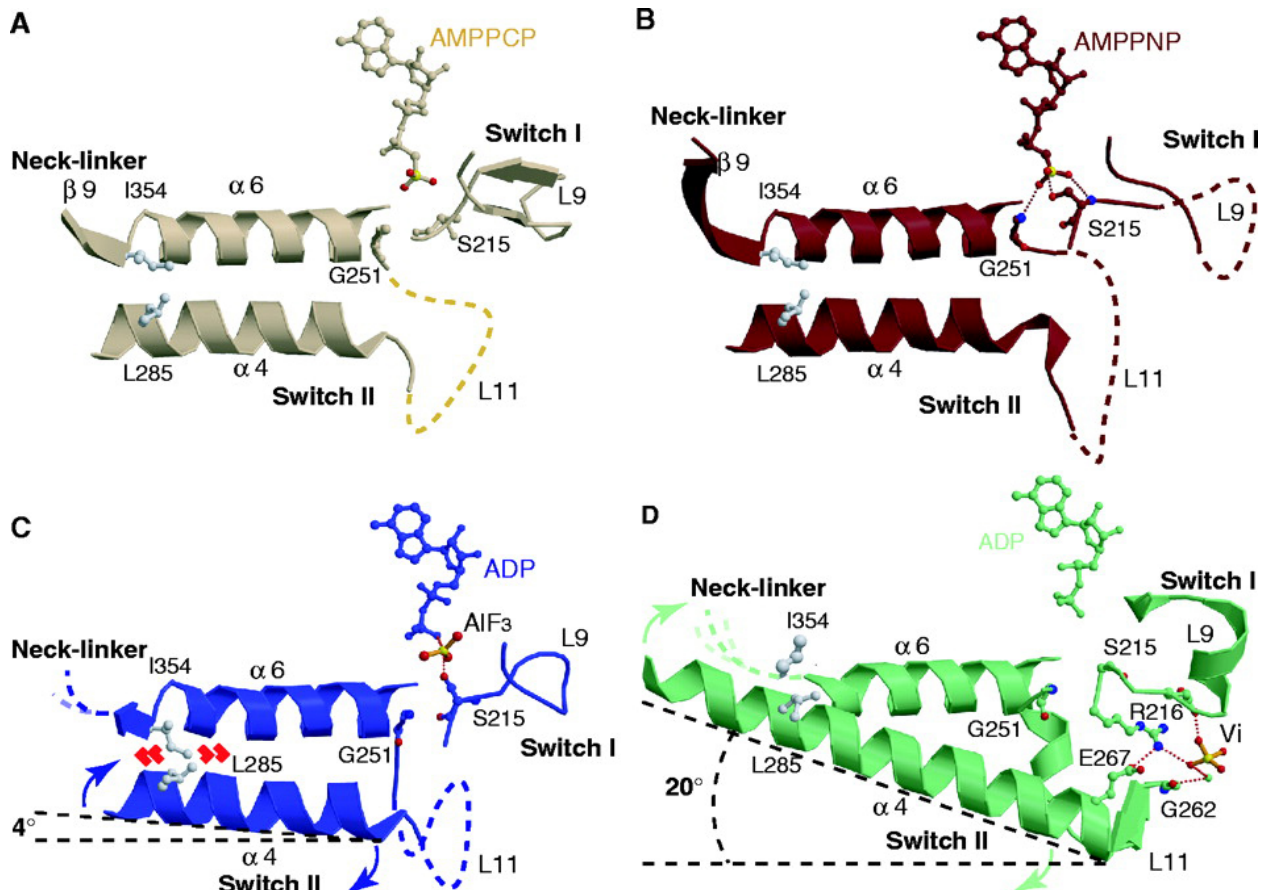


Figure 1.6 Conformational changes in the “switch” regions during ATP turnover

The “switch” regions of Kif1a•AMPPCP (A), Kif1a•AMPPNP (B), Kif1a•ADP•AlF₃ (C), Kif1a•ADP•Vi (D) are shown in brown, red, blue, and green, respectively (78). Nucleotides and their coordinating residues are shown as ball-and-stick models. Sequences not visible in the crystal structure are shown by dashed lines.

1.5.2 The Microtubule-Binding Region

The region of the kinesin core domain that comprises the microtubule-binding interface has been mapped based on results obtained through alanine-scanning mutagenesis (94) as well as models generated by superposing crystal structures of kinesin motor domains with low-resolution

electron density maps obtained through cryo-electron microscopy of motor-microtubule complexes (74, 95-98). From these studies, the microtubule-binding region consists of 1) the β 5-L8 motif, 2) the “switch-2 cluster” containing helix α 4, loop L12, and α 5, and 3) loop L11, which links switch-2 with the “switch-2 cluster” via 15 amino acids (Figure 1.7A). The “switch-2 cluster” and loop L11 show dramatically different conformations in the different kinesins that have been crystallized to date (Figure 1.7B). Loop L11 is disordered and not visible in most kinesins, except for *Homo sapiens* Kinesin-1 (72), *Neurospora crassa* Kinesin-1 (74), *Mus musculus* Kif1a•ADP•Vi complex (78), the R598A mutant of *Saccharomyces cerevisiae* Kar3p (86), and the *Plasmodium falciparum* MCAK (81). It is thought that loop L11 adopts a rigid conformation when kinesins bind to microtubules, thus re-connecting the pathway of communication from the active site to the “switch-2 cluster”. The “switch-2 cluster” shows dramatic differences in the relative positioning of its components, even between the same Kinesin-1 protein crystallized under different conditions (72, 73, 75, 76). These differences are thought to represent conformational states of the motor domain that are mechanistically relevant during the ATPase cycle of the motor.

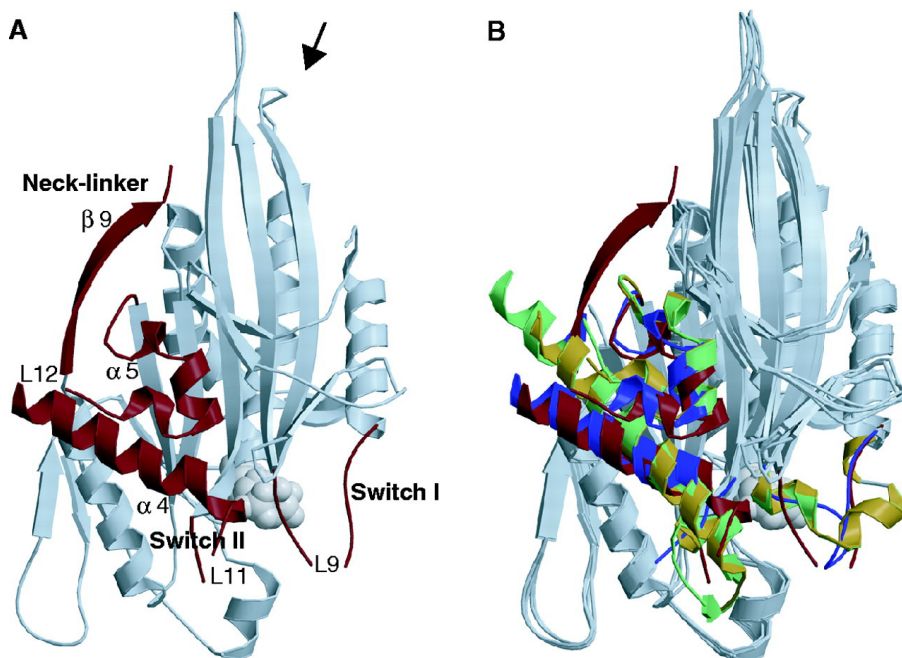


Figure 1.7 The microtubule-binding region of a kinesin motor

(A) The microtubule-binding, switch-1, switch-2, and neck-linker regions of Kif1a•AMPPNP are highlighted in red (78). (B) Superposition of Kif1a bound to AMPPNP (red), ADP•AlF₃ (blue), ADP•Vi (green), and ADP (yellow).

1.5.3 The Neck-Linker

The “neck-linker” – a ~15 amino acid sequence extending C-terminal to the motor domain of KinN and KinI kinesins and N-terminal to the motor domain of KinC kinesins – has been implicated in the force generation mechanism of kinesin motor proteins (39, 89). It has been demonstrated that when Kinesin-1 binds microtubules and AMPPNP (a non-hydrolyzable ATP analog), the neck-linker region becomes immobilized and extended towards the microtubule plus-end (99) [[Figure 1.6 \(A and B\)](#)]. In addition, Kinesin-1, Kinesin-3, and Kinesin-5 structures show different orientations of the neck-linker (68, 69, 72, 75, 77-79), which appear to correlate well with the conformation of the “switch-2 cluster”. Recent studies demonstrate that the Kinesin-5 neck-linker conformation is tightly linked to the mechanochemical cycle (100). However, it is still debated whether kinesins utilize a “power stroke” mechanism (non-processive motors) to generate force, or a “stepping” mechanism (processive motors) to account for the unidirectional movement.

1.6 EG5 STRUCTURE

1.6.1 Eg5•ADP Crystal Structure

The x-ray crystal structure of the Eg5 core domain was published early in 2001 by Turner *et al.* (68). The construct expressing human Eg5 (residues 1 to 368) contained the motor domain and the entire neck-linker region. The Eg5 active site contained MgADP, similar to other kinesin crystal structures, as well as displaying the $\alpha\beta\alpha$ sandwich architecture ([Figure 1.8](#)). After superimposing Kinesin-1 with Eg5 using the atoms from the P-loop region, the core β -sheets were nearly identical; however, subtle differences were found throughout the regions that flanked this core.

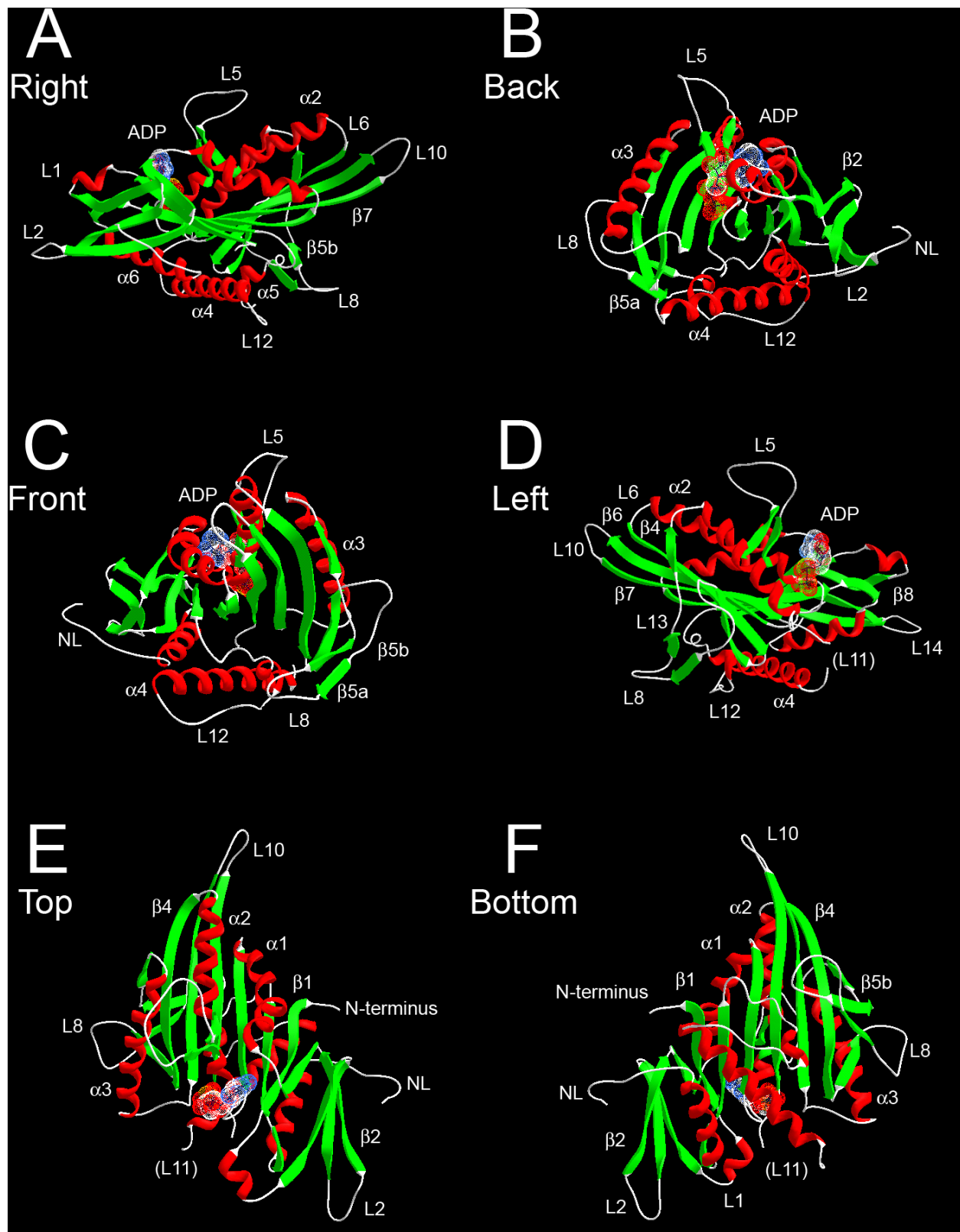


Figure 1.8 Eg5•ADP crystal structure

The crystal structure of Eg5•ADP is shown from different view points (68). **(A)** The microtubule binding interface is positioned at the bottom of the molecule and loop L10 is oriented to the right which points towards the plus-end of the microtubule. The α -helices (red), β -sheets (green), and loops (white) are highlighted. Several secondary structure elements are labeled based on the naming scheme for Kinesin-1 (72). “NL” corresponds to the neck-linker. MgADP nucleotide is shown in space-fill. **(B)** Rotate Panel A approximately 90° around vertical axis. **(C)** Rotate Panel A approximately 180° around vertical axis. **(D)** Rotate Panel A approximately 270° around vertical axis. **(E)** View down the vertical axis of Panel A. **(F)** View up the vertical axis of Panel A, showing the microtubule-binding region of the motor.

The switch-1 region in Kinesin-1 was found to be a short α -helix, whereas in Eg5, switch-1 was a loop ([Figure 1.11A](#)). These two conformations of the switch-1 region are thought to be relevant states that exist during force generation. For Kinesin-3, the motor domain was crystallized with several different nucleotides bound at the active site, and the conformation of switch-1 appeared to change depending on the progression of states through the ATPase cycle (78). However, the Kinesin-3 crystal structure was a chimera with the catalytic motor domain of Kif1a fused to the neck-linker of Kinesin-1 (77, 78). The Eg5 relay helix $\alpha 4$, which is part of the “switch-2 cluster” and microtubule-binding region, shows an increased length and slight rotation compared to Kinesin-1. These differences are thought to reflect structural intermediates that have been trapped in the crystal state.

The most distinctive difference between the structure of Eg5 motor and other kinesins was a unique conformation of the neck-linker ([Figure 1.8](#)). Unlike Kinesin-1, where the neck-linker is disordered in the MgADP state ([Figure 1.5](#)), the Eg5 neck-linker is ordered in a position perpendicular to the long axis of the motor domain. This neck-linker position was not stabilized by crystal lattice contacts, but a clustering of hydrogen bonds between the neck-linker and $\beta 1/\beta 2$ lobe it docks against. In addition, a number of Kinesin-5-conserved residues lined the perpendicular docking site for the neck-linker, thus supporting the notion that this orientation of the neck-linker is relevant for the mechanochemical cycle. However, it is not clear whether this neck-linker conformation is relevant to the Mt•Eg5 ATPase mechanochemical cycle.

1.6.2 Inhibitor•Eg5•ADP Crystal Structures

Recently, two crystal structures of Eg5 have been solved with MgADP bound at the active site and a specific inhibitor bound at an allosteric site distant from both the active site and the microtubule-binding region (69, 79). The Yan *et al.* structure was determined with monastrol

bound, the first identified selective inhibitor of Eg5 ([Figure 1.9](#)). The Cox *et al.* structure was solved with a more potent inhibitor, Dihydropyrazole 15. Both inhibitors occupied a similar allosteric pocket and stabilized a similar conformation of the entire motor core. Given the similarity of these two crystal structures, I will refer primarily to the Yan *et al.* structure when discussing the differences between the Eg5•ADP and the Inhibitor•Eg5•ADP structures. The nucleotide-binding site and the core β -structure remained relatively unchanged when the inhibitor was bound to the motor domain; however, significant rearrangements in the functional regions of the motor (switch-1, switch-2, and the neck-linker) were observed ([Figure 1.10](#)).

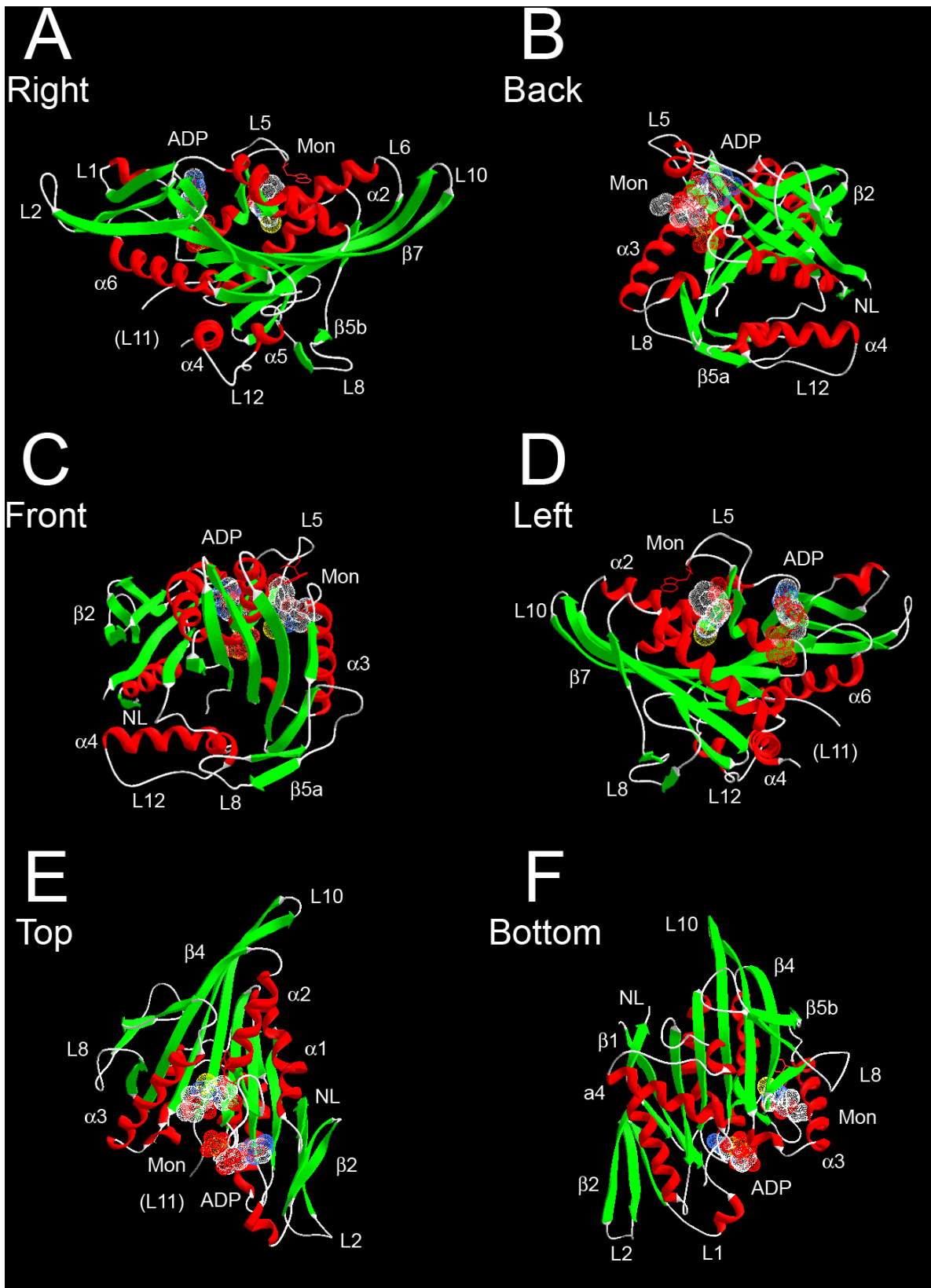


Figure 1.9 Monastrol•Eg5•ADP crystal structure

The crystal structure of monastrol•Eg5•ADP is shown from different view points (69). **(A)** The microtubule binding interface is positioned at the bottom of the molecule and loop L10 is oriented to the right which points towards the plus-end of the microtubule. The α -helices (red), β -sheets (green), and loops (white) are highlighted. Several secondary structure elements are labeled based on the naming scheme for Kinesin-1 (72). “NL” corresponds to the neck-linker. MgADP nucleotide and monastrol are shown in space-fill. **(B)** Rotate Panel A approximately 90° around vertical axis. **(C)** Rotate Panel A approximately 180° around vertical axis. **(D)** Rotate Panel A approximately 270° around vertical axis. **(E)** View down the vertical axis of Panel A. **(F)** View up the vertical axis of Panel A, showing the microtubule-binding region of the motor.

When comparing the Eg5•ADP structure (Turner *et al.*) with the inhibitor•Eg5•ADP structures (Yan *et al.* and Cox *et al.*), the conserved switch-1 region, which is responsible for nucleotide binding and recognition, shows a structural transformation from a loop to a short α -helix, similar to the conformation in the Kinesin-1 crystal structure (72). The γ -phosphate sensor, Serine233 (S233), remains in the same “open” position, which is not unexpected given that MgADP is at the active site for all Eg5 structures solved to date. S233 resides in loop L9, which is connected to helix α 3. Helix α 3 shows a shift by approximately 6 Å toward the N-terminal end of this helix, which is located in close proximity of the inhibitor binding cleft. The mechanistic understanding of these structural rearrangements in the switch-1 region remains unknown, though this subtle difference in the switch-1 region seems likely to be a significant alteration in the motor domain.

In addition to the rearrangements of the switch-1 region, there are also major conformational changes that occur in the “switch-2 cluster” (α 4, L12, α 5), which composes a majority of the microtubule-binding region. Helix α 4 rotates relative to helix α 5, such that the gap between these helices expands by ~6 Å. This rearrangement in the “switch-2 cluster” permits the neck-linker to “dock” onto the motor core in a similar fashion to the Kif1a•AMPPCP and Kif1a•AMPPNP (“ATP-like”) structures (77, 78). It is unclear whether the inhibitor stabilizes this conformation of the motor domain, or that the observed structures represent two possible conformations of the motor domain that are selectively stabilized by different conditions used for crystallization, as observed for human and rat Kinesin-1/conventional kinesin (72, 73, 75). Nevertheless, these rearrangements are thought to represent mechanistically relevant conformations of the Eg5 motor domain that relate to species along the ATPase pathway.

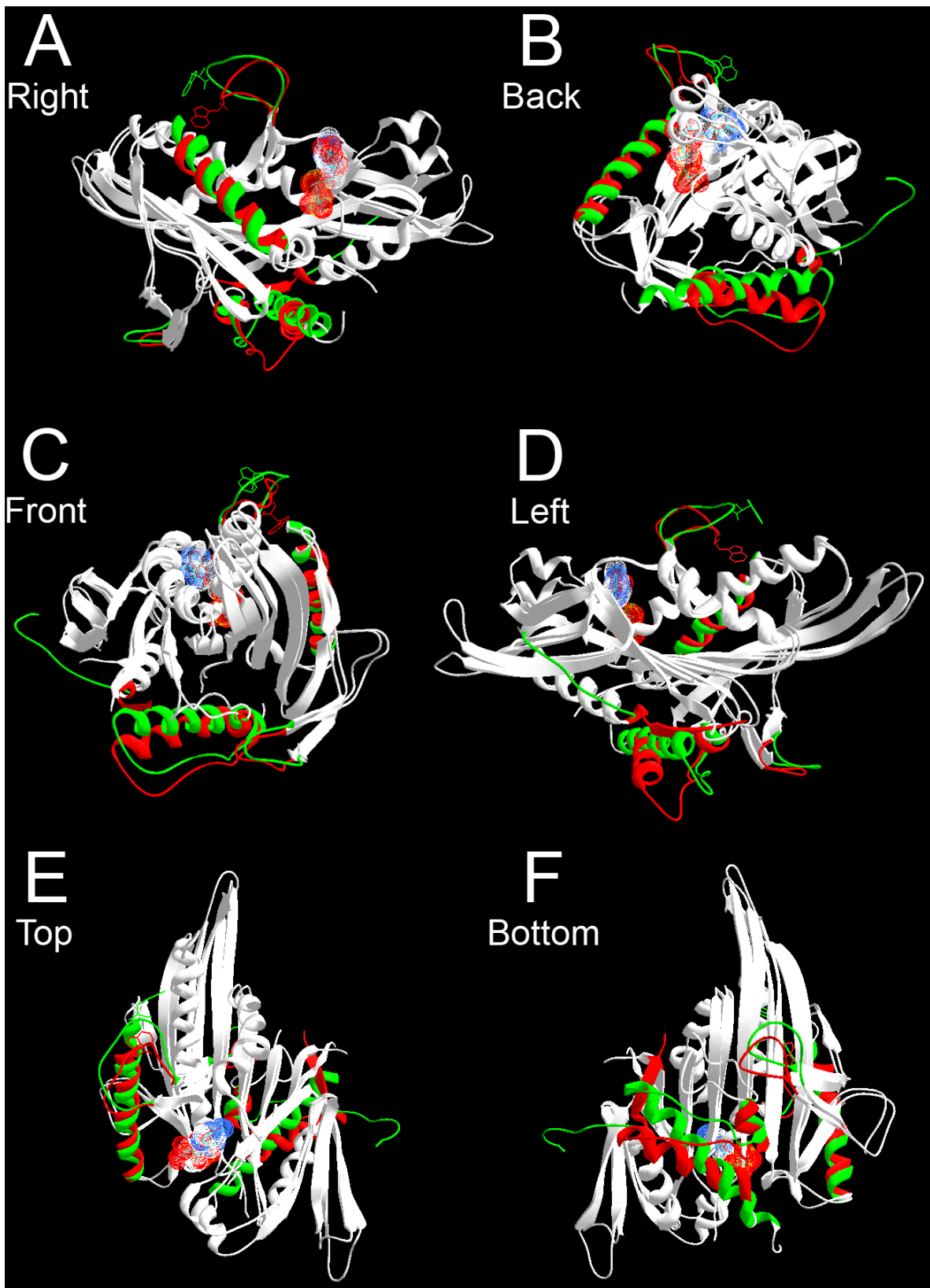


Figure 1.10 Comparison of Eg5•ADP and monastrol•Eg5•ADP crystal structures

(A) This model was generated using DeepView Swiss Pdb Viewer (version 3.7) to superposition the Eg5•ADP structure [PDB code: 1H6 (68); labeled green] with the monastrol•Eg5•ADP structure [PDB code: 1Q0B (69); labeled red] based on the position of C_α atoms of the P-loop region (F102–T112). The differences in the the switch-1 and switch-2 regions are highlighted. (B) Rotate Panel A approximately 90° around vertical axis. (C) Rotate Panel A approximately 180° around vertical axis. (D) Rotate Panel A approximately 270° around vertical axis. (E) View down the vertical axis of Panel A. (F) View up the vertical axis of Panel A, showing the microtubule-binding region of the motor.

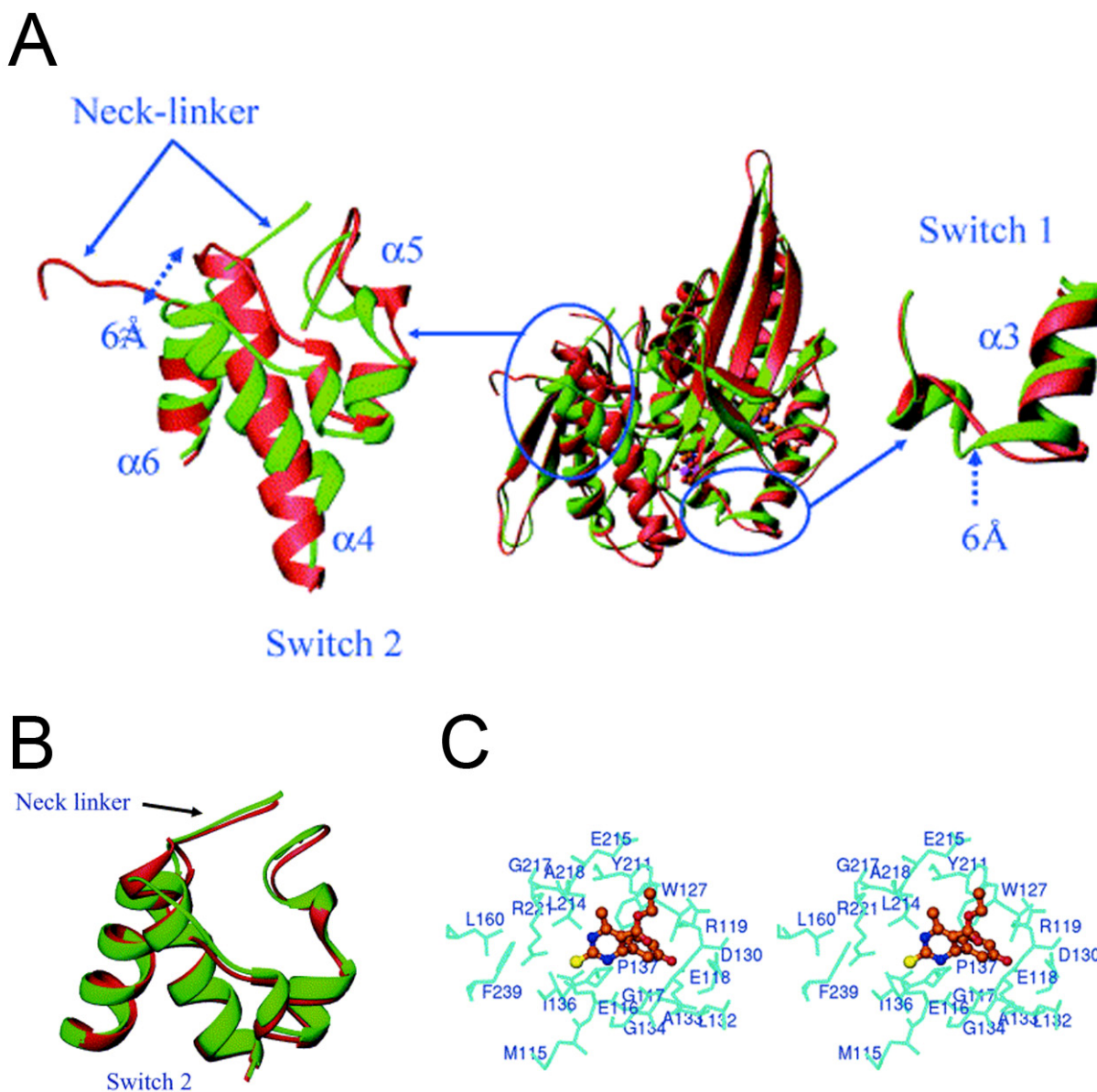


Figure 1.11 Detailed structural features of the monastrol•Eg5•ADP complex

(A) Comparison of the switch-1, switch-2, and neck-linker regions between the Eg5•ADP complex (red) (68) and the monastrol•Eg5•ADP complex (green) (69). The circled areas are enlarged and shown as insets. (B) Comparison of the switch-2 “cluster” and neck-linker regions between monastrol•Eg5•ADP (green) and Kif1a•AMPPCP (red) (77). (C) Stereo view of the 20 side-chains that comprise the monastrol-binding site.

1.7 SELECTIVE INHIBITORS OF EG5 ATPASE

1.7.1 Monastrol – the Prototype Eg5 Inhibitor

In late 1999, Mayer *et al.* (101) published the results of a “phenotype-based” screen for small molecule inhibitors of mitotic spindle bipolarity. This screen selected for inhibitors that caused mitotic arrest, but did not affect the microtubule cytoskeleton. One of the five potential compounds that met the criteria of the screen (named monastrol) promoted BS-C-1 (monkey epithelial kidney) cells to form a monoastral spindle (hence, the drug was named “monastrol”) during mitosis, with a “rosette-like” microtubule array surrounded by a ring of chromosomes ([Figure 1.12C](#)). Monastrol does not perturb microtubules in interphase cells or microtubule polymerization *in vitro*. It also does not disrupt microtubule-dependent lysosome and Golgi apparatus distribution or chromosome dynamics in cells (101).

Inhibition of Kinesin-5 with specific antibodies induced a similar spindle phenotype to those observed after monastrol treatment (56, 59). Mayer *et al.* hypothesized that Eg5 was the target of monastrol and obtained *in vitro* motility results that supported their hypothesis (101). The interesting discovery in this study and subsequent studies was the selectivity of monastrol for Eg5. Monastrol could not bind or inhibit other Kinesin family members tested including Kinesin-1/conventional kinesin from *H. sapiens*, *N. crassa*, and *D. melanogaster*, as well as Kinesin-14 members from *D. melanogaster* (Ncd) and *C. elegans* (Klp15) (101, 102). Surprisingly, even different members of the Kinesin-5 family, including *A. nidulans* BimC and *D. melanogaster* Klp61F, were not significantly inhibited by monastrol treatment (102). This extreme specificity and selectivity by monastrol has piloted the initiative for developing more potent compounds for anticancer drugs.

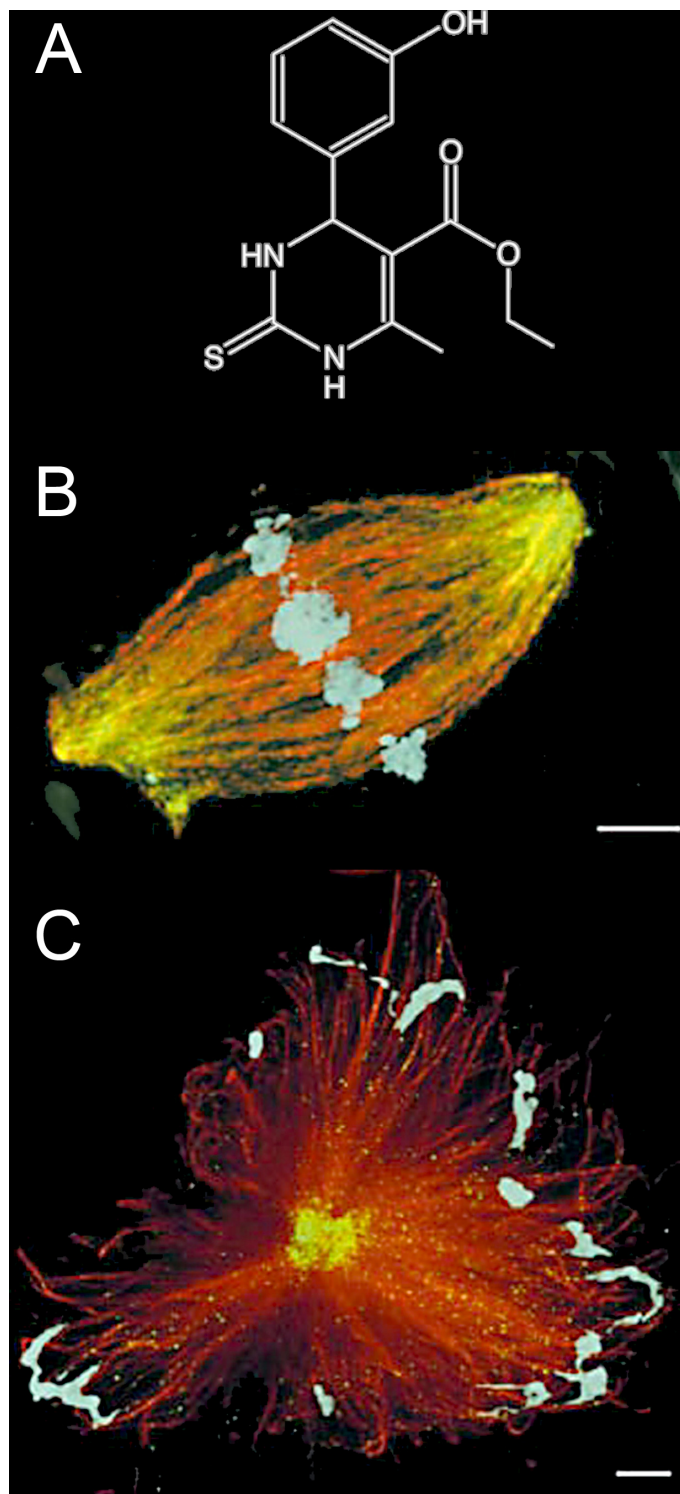


Figure 1.12 Localization of Eg5 in monastrol-treated spindles

(A) The chemical structure of the 1,4-dihydropyrimidine-based compound called monastrol (101). **(B)** Immunolocalization of Eg5 within the bipolar spindle (control reaction) (62). **(C)** Immunolocalization of Eg5 in monastrol-treated spindles (62). Chromatin (blue), tubulin (red), and Eg5 (green) in both Panel B and C.

1.7.2 Other Eg5-Specific Inhibitors

A tremendous effort has been exerted to synthesize and evaluate new Eg5-specific inhibitors. Four other classes of Eg5 inhibitors have been published: terpendole E (103), *S*-trityl-L-cysteine (104, 105), HR22C16 (106), and CK0106023 (107). As of June 2005, several derivatives of these Eg5 inhibitor classes are at various stages of clinical trials, including Ispinesib (Cytokinetics), SB-743921 (Cytokinetics), and other Eg5 inhibitors from Merck, CombinatoRx, and Kyowa Hakko Kogyo Co. (108). These Eg5 inhibitors are expected to have fewer side effects compared to other drugs that perturb mitosis like vinca alkaloids, Taxol, and epothilone. A recent study with monastrol demonstrated a lack of neurotoxicity in cultured sympathetic neurons (109). In addition, the HR22C16 class of inhibitors do not appear to be substrates for the “drug efflux pump” P-glycoprotein (PgP), which is suggested as one of the primary causes for taxane resistance in tumors (110, 111). These studies provide an optimistic view for the use of Eg5 inhibitors in the treatment of cancer

Several recent investigations showed that monastrol, *S*-trityl-L-cysteine, and Dihydropyrazole 15 all bind the same region of the Eg5 motor domain (69, 79, 105). Together, these studies provided evidence that these structurally different drugs may utilize a similar mechanism to inhibit the Eg5 ATPase. Clearly, this inhibitor binding cleft was not engineered for the binding of small molecules, but this region likely undergoes key structural transitions during the Eg5 ATPase cycle. By investigating the mechanistic basis for Eg5 inhibition by monastrol, we will hopefully be able to design more effective chemotherapeutic agents for the treatment of cancer.

1.8 THESIS AIMS

The structural and functional aspects of the Eg5 mechanochemical cycle will be explored by using several biochemical and biophysical techniques. In order to better understand how this kinesin family member converts the energy of ATP binding, ATP hydrolysis, and the release of ADP and inorganic phosphate (P_i) products into molecular motion that drives force production, I will utilize several steady-state and presteady-state kinetic as well as equilibrium binding approaches to dissect the Eg5 ATPase mechanism. I will use two truncated, bacterially-expressed Eg5 proteins that include the primary structure for the core motor domain only (Eg5-367) and for the core domain plus sequence within the stalk domain (Eg5-437). These two constructs were designed to yield monomeric and dimeric Eg5 proteins, respectively, and a comparison of the kinetic and thermodynamic profiles of each protein should provide insight into the communication between the motor domains in the Eg5 dimer. Moreover, this investigation plans to define the minimal ATPase mechanism of Eg5 in the presence and absence of its microtubule filament partner, as well as in the absence and presence of the inhibitor monastrol.

Previous studies have demonstrated that Eg5 is a slow, plus-end-directed molecular motor from the Kinesin-5/BimC kinesin family (112). There are remarkable structural similarities in the catalytic core domain of Eg5, Kar3, Ncd, and conventional kinesin ([Figure 1.13](#)) (68, 69, 72, 73, 83, 85, 86), yet these different kinesin family members exhibit different characteristics *in vitro* and different cellular functions *in vivo* (10, 12, 113-116). Each of these kinesins has been shown to function through a characteristic cyclic interaction with the microtubule whereby the nucleotide state at the active site modulates the affinity of the motor for the microtubule. The kinetic mechanisms of conventional kinesin, Ncd, and Kar3 have been extensively studied (99, 112, 117-146). The aim of this study was to establish the kinetic basis of Eg5 force generation in direct comparison to conventional kinesin (Kinesin-1) and other well-characterized spindle motors, Kar3 and Ncd (Kinesin-14).

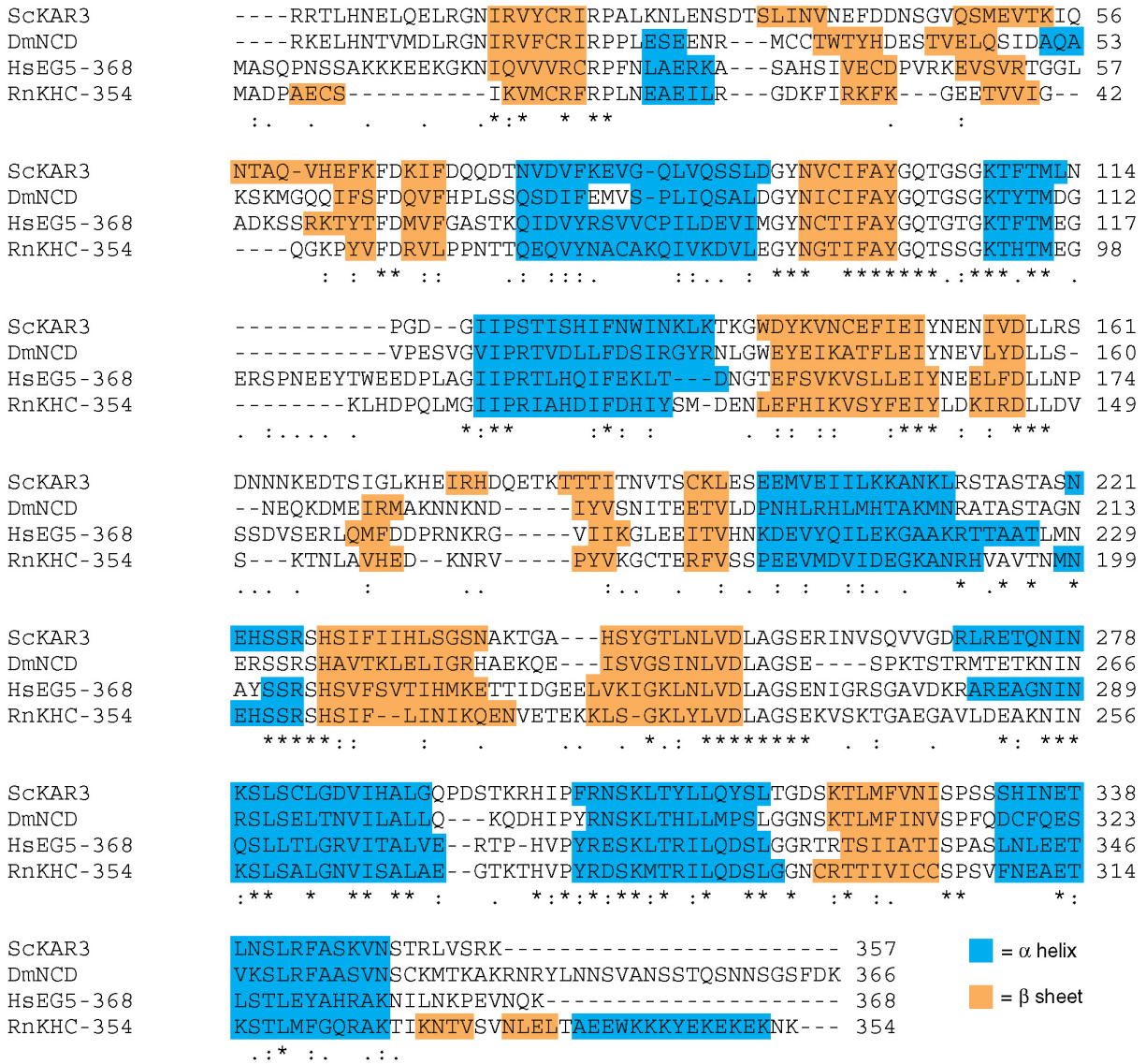


Figure 1.13 Multiple sequence alignment of Eg5, Kinesin, Kar3, and Ncd

The core motor domain sequences of conventional kinesin (RnKHC-354), Eg5 (HsEG5-368), Ncd (DmNCD), and Kar3 (ScKAR3) were aligned using CLUSTAL W (v. 1.82). The secondary structure elements are highlighted: α -helix (blue) and β -sheet (orange). These proteins share 49% similarity to the Eg5 sequence.

After defining the minimal ATPase mechanism for monomeric Eg5, I can use this knowledge as a platform to investigate the mechanistic basis of Eg5 inhibition by monastrol. Monastrol is a reversible, cell-permeable, small molecule that selectively inhibits the plus-end-directed Kinesin-5 family member, Eg5 (62, 69, 101, 102, 147). Previous studies with monastrol have revealed an induced-fit, allosteric binding site outside the nucleotide-binding pocket of the protein (69, 102, 105, 147). How the conformational changes throughout the catalytic core domain alter the ATPase mechanism of Eg5 and disturb force generation by the Mt•Eg5 complex is not well understood. In this study, I will utilize kinetic and equilibrium binding methodologies to define the mechanistic basis of Mt•Eg5 inhibition by *S*-monastrol, the more active enantiomer for inhibition (69, 102, 147).

The ATPase mechanism of kinesin family members in the absence of microtubules remains largely uncharacterized. I adopted a strategy to purify a monomeric Eg5 motor in the nucleotide-free state (apoEg5) in order to perform a detailed transient state kinetic analysis. I have used steady-state and presteady-state kinetics to define the minimal ATPase mechanism for apoEg5 in the absence and presence of the Eg5-specific inhibitor, monastrol. This study will provide insight into the microtubule-based activation of steady-state ATP turnover, as well as the allosteric mechanism of Eg5 inhibition by monastrol.

2.0 CHAPTER TWO: MECHANISTIC ANALYSIS OF THE MT•EG5 ATPASE¹

We have analyzed two human Eg5 motors, Eg5-367 and Eg5-437. These truncations were engineered based on sequence similarity to monomeric and dimeric *Drosophila* Kinesin-1 proteins, respectively. However, both Eg5 proteins are monomeric based on results from sedimentation velocity and sedimentation equilibrium centrifugation as well as analytical gel filtration. The steady-state parameters were Eg5-367: $k_{cat} = 5.5 \text{ s}^{-1}$, $K_{1/2,Mt} = 0.7 \text{ }\mu\text{M}$, and $K_{m,ATP} = 10 \text{ }\mu\text{M}$ and Eg5-437: $k_{cat} = 2.9 \text{ s}^{-1}$, $K_{1/2,Mt} = 4.5 \text{ }\mu\text{M}$, and $K_{m,ATP} = 4 \text{ }\mu\text{M}$. ATP binding is rapid at $2\text{-}3 \text{ }\mu\text{M}^{-1}\text{s}^{-1}$ and follows a two-step mechanism with the maximum observed rate being limited by an isomerization of the Mt•Eg5•ATP collision complex to tighten ATP binding. ATP hydrolysis follows the isomerization event at $11\text{-}15 \text{ s}^{-1}$, which occurs at all Eg5 active sites during the first ATP turnover. Phosphate product release and ATP-dependent Mt•Eg5 dissociation are coupled in the mechanism and are relatively slow and rate-limiting at $6\text{-}8 \text{ s}^{-1}$. Eg5•ADP binding to the microtubule lattice proceeds rapidly for both motors and occurs via a two-step mechanism as well, where an isomerization of the Mt•Eg5•ADP collision complex tightens Eg5's binding to the microtubule. Eg5-367 binds microtubules more effectively ($11 \text{ }\mu\text{M}^{-1}\text{s}^{-1}$) than Eg5-437 ($0.7 \text{ }\mu\text{M}^{-1}\text{s}^{-1}$), consistent with the lower steady-state $K_{1/2,Mt}$ and the lower mantADP release $K_{1/2,Mt}$ for Eg5-367. We propose that ADP release from the Mt•Eg5•mantADP intermediate occurs rapidly at $35\text{-}45 \text{ s}^{-1}$ and is the result of the isomerization of the Mt•Eg5•ADP collision complex to increase Eg5's affinity for the microtubule. These results indicate that the ATPase pathway for monomeric Eg5 is more similar to Kinesin-1/conventional kinesin than the spindle motors Kinesin-14/Ncd/Kar3 where ADP product release is rate-limiting for steady-state turnover.

¹ Reproduced in part with permission from 148. Cochran, J. C., Sontag, C. A., Maliga, Z., Kapoor, T. M., Correia, J. J., and Gilbert, S. P. (2004) Mechanistic analysis of the mitotic kinesin Eg5, *J Biol Chem* 279, 38861-70. Copyright 2004 American Society for Biochemistry and Molecular Biology.

2.1 BACKGROUND AND SIGNIFICANCE

Eukaryotic cell division requires proper assembly and maintenance of the bipolar spindle, an intricate protein complex composed of a dynamic array of microtubules and microtubule-based motor proteins [reviewed in (2, 149-154)]. Bipolar spindle formation requires a specific balance between counteracting forces generated by cytoplasmic dynein and several families of kinesins to organize and position opposite spindle poles (12, 66, 155-160). Kinesin-5/BimC family members contribute to the plus-end-directed force necessary to separate microtubule asters, thus aiding in the establishment and maintenance of the bipolar spindle (47, 49-52, 55, 56, 59, 60, 64).

Electron microscopy studies of *Drosophila melanogaster* Kinesin-5 (Klp61F) suggest that these proteins exhibit a unique homotetrameric structure with two N-terminal motor domains positioned at each end of a coiled-coil stalk, thus facilitating the ability to interact with and slide adjacent microtubules (63-65, 67). HsEg5/KSP², the human homologue of *Xenopus* Eg5, is a slow, plus-end-directed Kinesin-5 that has been shown to localize along interpolar spindle microtubules and at the spindle poles (60, 112, 161). This spindle association is regulated by the cell cycle-dependent phosphorylation of a single threonine within a highly conserved region of the Eg5 tail domain by p34^{cdc2} protein kinase (59, 60, 161). A small, cell permeable molecule, monastrol, can reversibly inhibit the function of Eg5 to arrest cells in mitosis, providing a useful model for anti-mitotic drug design (62, 69, 101, 102, 147, 162).

There are remarkable structural similarities in the catalytic core domain of Eg5, Kar3, Ncd, and conventional kinesin (68, 69, 72, 73, 83, 85, 86), yet these proteins exhibit different characteristics *in vitro* and different cellular functions *in vivo* (10, 12, 113-116). Each of these kinesins has been shown to function through a characteristic cyclic interaction with the microtubule (Scheme 2.1) whereby the nucleotide state at the active site modulates the affinity of the motor for the microtubule. The kinetic mechanisms of conventional kinesin, Ncd, and Kar3 have been extensively studied (99, 112, 120-127, 129-146). The aim of this study was to establish the kinetic basis of force generation of Eg5 in direct comparison to conventional

² The abbreviations used are: HsEg5/KSP, *Homo sapiens* Eg5/KSP; KSP, Kinesin spindle protein; Mt, microtubule; AMPPNP, adenosine 5'-(β,γ -imino)triphosphate; mant, 2'(3')-O-(*N*-methylantraniloyl).

kinesin (Kinesin-1) and other well-characterized minus-end-directed spindle motors, Kar3 and Ncd (Kinesin-14).

We have utilized kinetic and thermodynamic approaches to define the mechanochemistry of two truncated human Eg5 motors, Eg5-367 and Eg5-437. Eg5-367, containing the N-terminal 367 amino acids, represents a single Eg5 catalytic domain (68, 69, 147). Surprisingly, we found that Eg5-437, designed to yield a dimeric motor, was monomeric based on results from sedimentation velocity and sedimentation equilibrium analytical ultracentrifugation as well as analytical gel filtration. The kinetics and equilibrium binding characteristics for Eg5 presented here reveal a unique ATPase mechanism more similar to KinN kinesins, such as conventional kinesin, compared to the KinC spindle motors, Kar3 and Ncd.

2.2 MATERIALS AND METHODS

2.2.1 Experimental Conditions

Experiments were performed at 25 °C in ATPase buffer (20 mM HEPES, pH 7.2 with KOH, 5 mM magnesium acetate, 0.1 mM EDTA, 0.1 mM EGTA, 50 mM potassium acetate, 1 mM dithiothreitol, 5% sucrose). MgATP and MgADP concentrations were determined by absorbance at 259 nm using the extinction coefficient (ϵ) of 15,400 M⁻¹cm⁻¹. All concentrations reported for experiments are final after mixing.

2.2.2 Expression and Purification of Monomeric Eg5

We have expressed two human Eg5 constructs as described previously (147). Eg5-367 contains the N-terminal 367 amino acids, Met¹-Gln³⁶⁷ followed by a 6xHis tag (M_r = 41,700 Da without MgADP and 42,100 Da with MgADP) and Eg5-437 contains the N-terminal 437 amino acids, Met¹-Thr⁴³⁷ followed by a 6xHis tag, (M_r = 49,800 Da without MgADP and 50,200 Da with MgADP). Both recombinant Eg5 motors were initially expressed in the *Escherichia coli* cell line BL21-(DE3)-pLysS (Stratagene, La Jolla, CA) and purified using column chromatography.

However, the protein yield was minimal (1–5 mg of Eg5 protein per 30 g cells). We surveyed the human Eg5 gene and found several codons that were under represented in *E. coli* due to codon usage bias. Therefore, we were able to find the *E. coli* cell line BL21-CodonPlus(DE3)-RIL (Stratagene), which supplemented the tRNAs and enhanced expression by greater than 10-fold.

The column chromatography protocol that was followed for 10 preparations of each motor is summarized. The harvested cells (30–40 g wet pellet) were diluted after induction to 1 g/10 ml in lysis buffer [10 mM NaPO₄ buffer (pH 7.2), 20 mM NaCl, 2 mM MgCl₂, 1 mM EGTA, 1 mM DTT, 2 mM PMSF] and lysozyme (0.2 mg/ml) and incubated on ice for 30 min with gentle stirring. The cells were lysed with 3 cycles of freezing (liquid nitrogen) and thawing (34 °C). The cell extract was clarified by ultracentrifugation and the soluble cell lysate was loaded onto a 25-ml S-Sepharose (Sigma-Aldrich Co., St. Louis, MO) column to select for the Eg5 motor domain. Eg5 was eluted from the S-Sepharose column using a linear NaCl gradient (20–600 mM NaCl), and the protein eluted between 290–420 mM NaCl. Fractions enriched in Eg5 were pooled and dialyzed against Ni-NTA buffer [10 mM NaPO₄ buffer (pH 7.2), 20 mM NaCl, 2 mM MgCl₂, 0.1 mM EGTA, 1 mM DTT, 0.02 mM ATP]. The dialysate was loaded onto a 5-ml Ni-NTA agarose column (Qiagen, Valencia, CA), and Eg5 was eluted using a linear imidazole gradient (0–200 mM imidazole). Fractions enriched in Eg5 were pooled and dialyzed against ATPase buffer plus 200 mM NaCl to remove the imidazole. The dialysate was concentrated by ultrafiltration (Millipore Centriprep 30, Bedford, MA) and further dialyzed against ATPase buffer with 5% sucrose. Finally, the dialyzed protein was clarified by ultracentrifugation at 50,000 rpm, and the protein was aliquoted and frozen in liquid nitrogen, then stored at -80 °C. We determined the Eg5 protein concentration by the Bio-Rad Protein Assay (Bio-Rad Laboratories, Inc., Hercules, CA) with IgG as the protein standard. This purification method yielded 40–150 mg of Eg5 protein per 30 g of *E. coli* BL21-CodonPlus(DE3)-RIL cells at >99% purity ([Figure 2.1](#)).

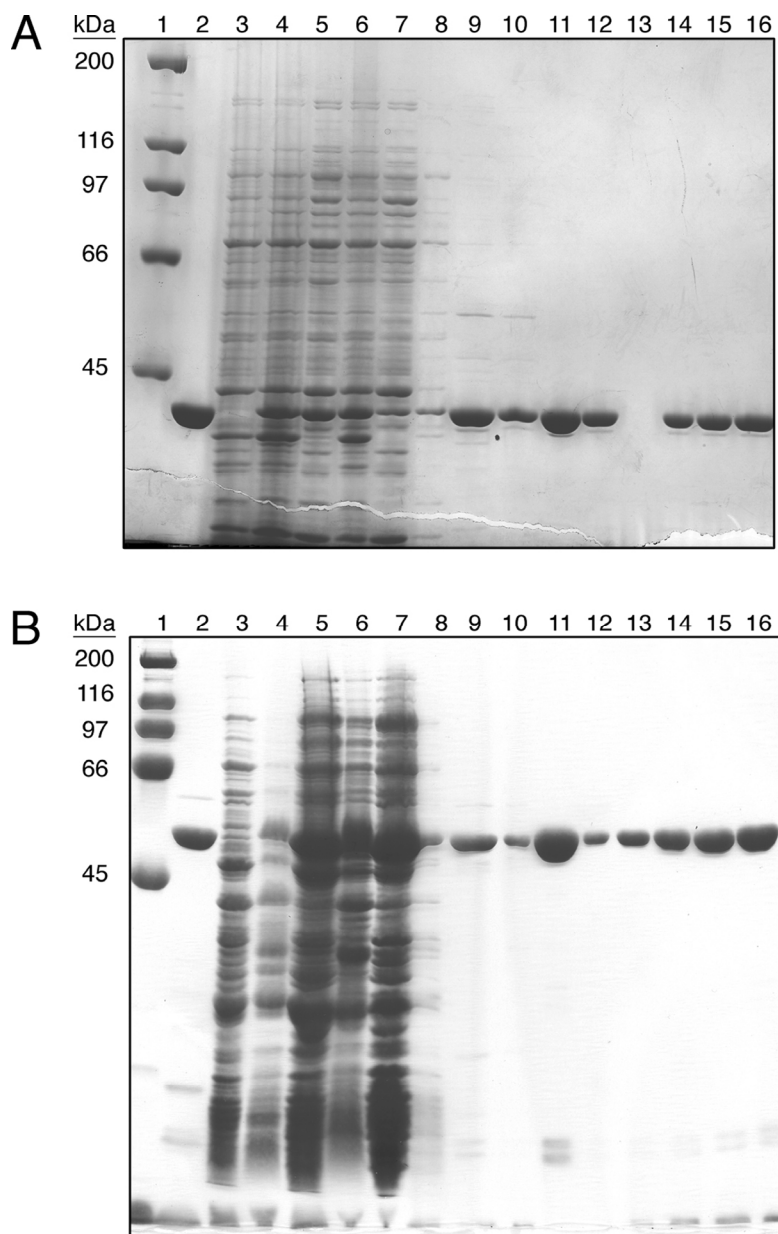


Figure 2.1 Summary gels for Eg5-367 and Eg5-437 preparations

(A) Eg5-367 final preparation gel (8% SDS-polyacrylamide) stained with Coomassie brilliant blue. Lane 1: SDS-PAGE molecular weight standards; Bio-Rad Laboratories, Inc. Lane 2: HsEg5-367 standard. Lane 3: Pre-induced cell sample. Lane 4: Post-induced cell sample. Lane 5: 18,000 rpm supernatant. Lane 6: 18,000 rpm pellet. Lane 7: 40,000 rpm supernatant. Lane 8: 40,000 rpm pellet. Lane 9: Pooled S-Sepharose fractions. Lane 10: Ni-NTA load. Lane 11: Pooled Ni-NTA fractions. Lane 12: Centriprep 30 retentate. Lane 13: Centriprep 30 filtrate. Lanes 14 through 16: final protein preparation at increasing protein quantities. **(B)** Eg5-437 final preparation gel (10% SDS-polyacrylamide) stained with Coomassie brilliant blue. Lane 1: SDS-PAGE molecular weight standards; Bio-Rad Laboratories, Inc. Lane 2: HsEg5-437 standard. Lane 3: Pre-induced cell sample. Lane 4: Post-induced cell sample. Lane 5: 18,000 rpm supernatant. Lane 6: 18,000 rpm pellet. Lane 7: 40,000 rpm supernatant. Lane 8: 40,000 rpm pellet. Lane 9: Pooled S-Sepharose fractions. Lane 10: Ni-NTA load. Lane 11: Pooled Ni-NTA fractions. Lanes 12 through 16: final protein preparation at increasing protein quantities.

2.2.3 Expression and Purification of MDCC-PBP

A fluorescent protein has been engineered to directly measure rapid inorganic phosphate (P_i) release in real time from enzymes such as molecular motor proteins (163). This protein utilizes the A197C mutant of the *Escherichia coli* phosphate binding protein (PBP) coupled to attachment of the 7-diethylamino-3-(((2-maleimidyl)ethyl)amino)carbonyl coumarin (MDCC) fluorophore to the single cysteine. E.W. Taylor (University of Chicago) and W. Epstein (University of Chicago) developed an expression methodology where PBP was under the control of a rhamnose promoter (plasmid pSN5182) in *E. coli* strain BW 24777 (164). The protocol from Brune *et al.* (163) was primarily followed to express, purify, and label PBP with the coumarin fluorophore; however, H. White invested a significant amount of time into modifying the purification protocol in order to minimize the duration of the preparation and maximize the protein yield and purity (unpublished). The detailed protocol that I followed for the MDCC-PBP preparation is described below.

Day 1: *E. coli* BW 2477 cells containing plasmid pSN5182 (conferring tetracycline resistance) were grown in 2x10 ml Luria Broth (LB) supplemented with 12.5 $\mu\text{g/ml}$ tetracycline for 6 hrs at 37 °C (120 rpm) and then transferred to 2x90 ml LB + tetracycline for 16 hrs at 37 °C (120 rpm). During the growth, media and reagents were prepared for the remainder of the preparation, including the supplemented minimal media, the *L*-rhamnose stock, and the buffers for osmotic lysis. For all Tris buffers, we used Tris from EM Laboratories (Catalog # 9210), and we determined the pH of the solutions at their respective temperatures (either 4 °C or room temperature) as the pH of Tris-HCl buffers changes with temperature.

Day 2: After the 16 hr growth, eight 500 ml minimal media + tetracycline [100 mM Hepes, pH 7.5 with KOH, 20 mM KCl, 15 mM $(\text{NH}_4)_2\text{SO}_4$, 1 mM MgCl_2 , 10 μM FeSO_4 , 1 $\mu\text{g/ml}$ thiamine, 0.25 % glycerol (v/v), 2 mM KH_2PO_4 , and 12.5 $\mu\text{g/ml}$ tetracycline] were inoculated with 10 ml from one of the 100 ml LB overnight cultures. The supplemented minimal media cultures were shaken at 120 rpm at 37 °C until the optical density at 600 nm (OD_{600}) was 0.2. When the OD_{600} reached 0.2, the cells were induced with 2 mM *L*-rhamnose (filter sterilized) and incubated overnight at 37 °C (120 rpm). During the growth, the Q-sepharose column reagents were prepared.

Day 3: After the overnight induction (18–22 hrs), the cells were harvested by centrifugation (Sorvall GSA rotor, 4,000 rpm, 20 min, 25 °C) and were washed twice using Lysis Buffer 1 [10 mM Tris-HCl (pH 7.6), 30 mM NaCl] at 25 °C. The wet cell pellets were weighed for record (10–15 g) and were resuspended in 100 ml (total) of Lysis Buffer 2 [33 mM Tris-HCl (pH 7.6)] at 25 °C. The resuspended cells were incubated with Lysis Buffer 3 [40% sucrose, 0.1 mM EDTA, 33 mM Tris-HCl (pH 7.6)] at 25 °C while stirring for 10 min. The cells were pelleted by centrifugation (Sorvall GSA rotor, 10,000 rpm, 20 min, 4 °C) and rapidly resuspended in 200 ml ice cold 0.5 mM MgCl₂ while rapidly stirring for 15 min at 4 °C. At this point, the cells were disrupted by osmotic lysis and the PBP was in the soluble fraction. The cell extract was clarified by ultracentrifugation (45 Ti rotor, 10,000 rpm, 20 min, 4 °C), the concentration of PBP was determined by subtracting A₃₂₀ from A₂₈₀ ($\epsilon = 60,880 \text{ M}^{-1}\text{cm}^{-1}$; $M_r = 34,440 \text{ Da}$; yield = 200–250 mg PBP), and the supernatant and pellet samples were resolved on a 12% SDS-polyacrylamide gel ([Figure 2.2A](#)). The PBP lysate was either dialyzed against 4 L of 5 mM Tris-HCl (pH 8.0) for 1 hr at 4 °C, frozen in liquid nitrogen, and stored at -80 °C, or dialyzed against 4 L of 5 mM Tris-HCl (pH 8.0) overnight at 4 °C if the Q-sepharose column chromatography was performed on the following day.

Day 4: The PBP lysate was clarified by ultracentrifugation (45Ti rotor, 10,000 rpm, 20 min, 4 °C), and the supernatant was loaded onto a 25-ml Q-sepharose column (binding capacity = ~10 mg PBP/ml resin). The PBP was eluted from the column with a linear NaCl gradient (0–100 mM NaCl; 100 ml each), and the fractions were analyzed by SDS-PAGE ([Figure 2.2B](#)). Fractions enriched for PBP were pooled, and the concentration of PBP was determined by subtracting A₃₂₀ from A₂₈₀ ($\epsilon = 60,880 \text{ M}^{-1}\text{cm}^{-1}$; $M_r = 34,440 \text{ Da}$; yield \cong 100 mg PBP). The pooled PBP fractions were concentrated to 3.5 mg/ml (~100 μM) using Millipore Centriprep 10 (Sorvall GSA rotor, 3,500 rpm, 15 min, 4 °C). The concentrated PBP was dialyzed against 2 x 4 L of 20 mM Tris-HCl (pH 8.0) at 4 °C for 30 min and overnight, respectively. The Q-sepharose beads were regenerated by washing the resin with 100 ml of 2 M NaCl/5 mM Tris-HCl (pH 8.0) at 5 ml/min flow rate. The resin was re-equilibrated with 5 mM Tris-HCl (pH 8.0).

Day 5: The concentrated PBP (~100 μM) was dialyzed against 4 L of 20 mM Tris-HCl (pH 8.0) at 25 °C for 30 min. Samples of unlabeled PBP (3 x 100 μl aliquots) were saved for mass spectrometry analysis (see below). The PBP solution was adjusted to 0.2 mM 7-

methylguanosine (MEG) and 0.2 U/ml purine nucleoside phosphorylase (PNPase) to remove contaminating P_i from PBP and was incubated at 25 °C for 30 min using a temperature-controlled incubator. The PBP solution was adjusted to 150 μ M MDCC dissolved in *N,N*-dimethylformamide and was mixed end-over-end for 30 min at 25 °C in the incubator. Note: The MDCC probe (light-sensitive) should be purchased from Molecular Probes (Eugene, OR) the week of the preparation, and the sample should be stored at -20 °C in anhydrous calcium sulfate desiccant (Drierite, Xenia, OH). Immediately following the 30 min labeling incubation, the MDCC-PBP solution was brought to 5 mM Tris-HCl (pH 8.0) by quadrupling the volume with cold ddH₂O. The diluted MDCC-PBP was loaded onto a 25-ml Q-sepharose column, eluted with 50 ml of 200 mM NaCl in 5 mM Tris-HCl (pH 8.0) [no gradient], and the fractions were analyzed by spotting 1.5 μ l of each fraction onto a Whatmann filter paper, followed by staining with Coomassie brilliant blue ([Figure 2.2C](#)). The A_{280} and A_{430} values were determined for all fractions containing protein based on the spot assay (described above), and the fractions displaying the A_{280} / A_{430} ratio between 1.5–1.7 were pooled (a ratio of 1.6 indicates stoichiometric labeling) ([Figure 2.2D](#)). The pooled MDCC-PBP fractions were dialyzed against 2 x 4 L of 10 mM Hepes (pH 7.2 with KOH) for 1 hr each at 4 °C. The final MDCC-protein was diluted with 10 mM Hepes (pH 7.2 with KOH) to reach a concentration approximately 100 μ M, was clarified by ultracentrifugation (70Ti rotor, 40,000 rpm, 30 min, 4 °C), was aliquoted, and frozen with liquid nitrogen for storage at -80 °C. The final yield from the preparation was approximately 15 ml at 3.3 mg/ml MDCC-PBP at >99% purity.

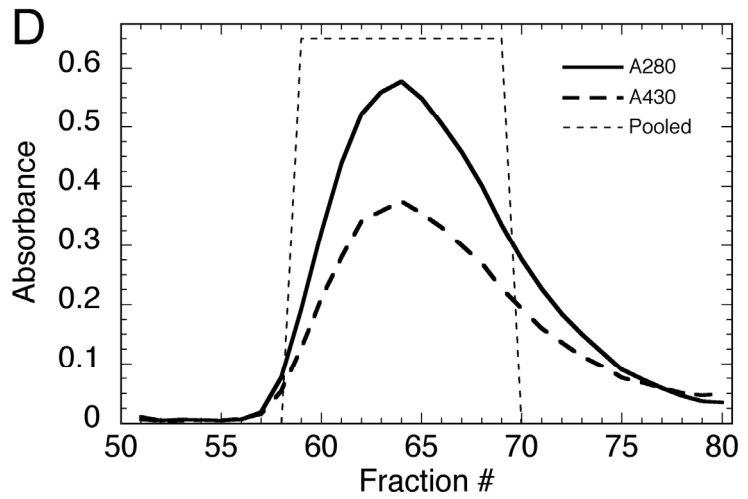
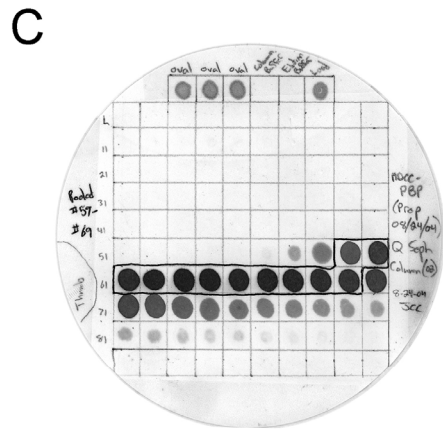
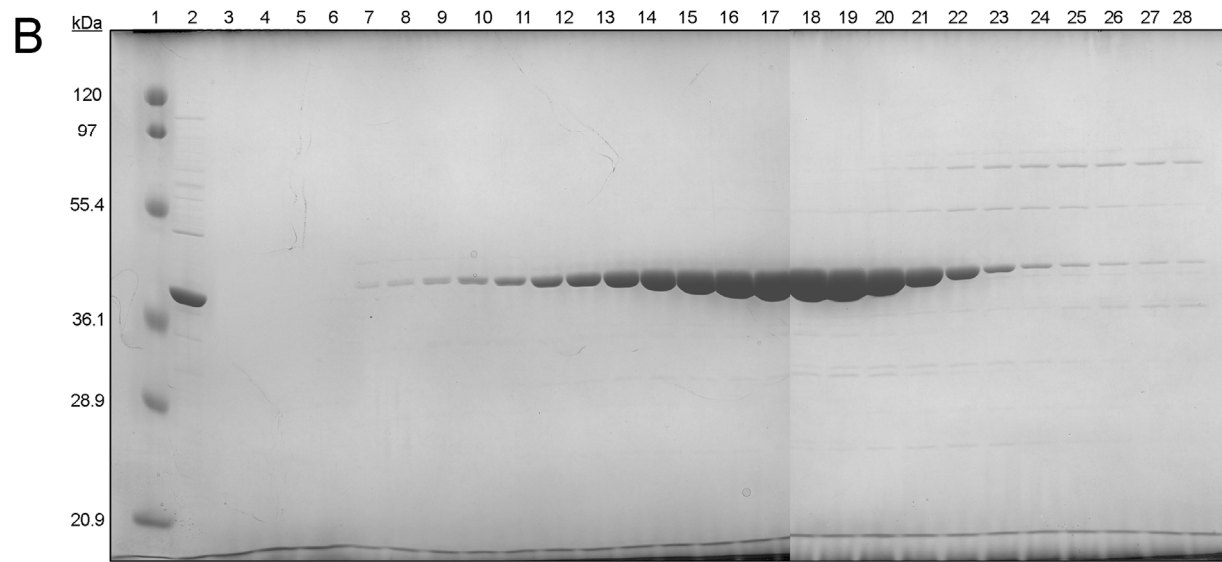
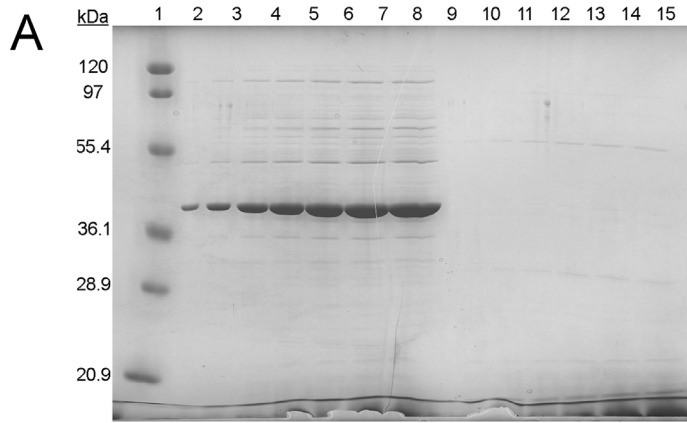


Figure 2.2 MDCC-PBP purification summary

(A) Coomassie-stained 12% SDS-polyacrylamide gel showing samples of the supernatant (lanes 2-8) and pellet (lanes 9-15) fractions of the clarifying spin after osmotic lysis. Lane 1: Low range SDS-PAGE standards; Bio-Rad Laboratories, Inc. (B) Coomassie-stained 12% SDS-polyacrylamide gels resolving the protein isolated in flow-through (lanes 3-6) and elution (lanes 7-28) fractions from the Q-sepharose column. Fractions enriched in PBP (lanes 11-21) were pooled. (C) Coomassie-stained filter paper from the spot assay to determine the MDCC-PBP protein content in flow-through and elution fractions. Fractions enriched for MDCC-PBP (highlighted) were further analyzed for A_{280} and A_{430} . (D) The relative absorbance values (A_{280} and A_{430}) for the MDCC-PBP enriched fractions are plotted. The small dashed lines show the fractions that were pooled in the preparation. The average A_{280}/A_{430} ratio for the pooled fractions was 1.58.

2.2.4 Characterization of the MDCC-PBP Preparations

In order to characterize the MDCC-PBP preparations, several experiments were performed to determine to verify proper labeling of PBP, and to assay the response of MDCC-PBP to binding P_i in solution. We sent samples of the unlabeled and labeled PBP to the PAN Facility (Stanford University Medical Center, Palo Alto, CA) for MALDI-TOF and MS/MS mass spectrometry analysis. A virtual trypsin digest predicts that the engineered C197 residue should occur in a peptide fragment of 1,500 Da that ends in a Lysine, and the mass of the fragment should increase approximately 383 Da due to the attachment of the coumarin fluorophore. All the samples yielded excellent matches to the PBP sequence, and a peptide fragment with unlabeled C197 was reported in all preparations, thus indicating that the labeling procedure was not 100 % efficient, though with MALDI-TOF quantitative comparisons cannot be made. A search for peaks in the MDCC-PBP preparations that were not in the unlabeled PBP controls provided a peak at 1948.01 Da (a difference of 401 Da from the unlabeled peptide). MS/MS analysis on these peaks demonstrated that they were the modified peptide containing C197. Also, there was good evidence that the modification occurred on the cysteine residue.

The MDCC-PBP preparations were also tested for the ability to bind P_i based on the expected fluorescence increase of the MDCC-PBP• P_i complex (163). The fluorescence emission spectra for MDCC-PBP in the absence and presence of excess P_i were analyzed using an Aminco-Bowman Series 2 luminescence spectrometer (Thermo Spectronic, Madison, WI) equipped with a 150-Watt continuous wave xenon arc lamp source. The samples were excited at 425 nm (2-nm halfwidth), and the emission spectrum was scanned from 430–600 nm (2-nm halfwidth) (Figure 2.3A). We observed a 4.6-fold increase in fluorescence intensity of MDCC-PBP in the presence of P_i , and we also observed a blue-shift in maximum intensity wavelength

from 474 nm to 466 nm. Thus, these results suggest our MDCC-PBP preparations bind P_i in solution.

We measured the P_i concentration-dependence on the observed rate constant for P_i association with MDCC-PBP using a SF-2003 KinTek stopped-flow instrument (KinTek Corp., Austin TX). The observed rates at P_i concentrations less than 2 μM increased linearly with $[P_i]$, and the data were fit to a simple one-step binding model with a slope of the plot of the observed rate constants *versus* P_i concentration being the apparent association rate constant at $182 \pm 24 \mu\text{M}^{-1}\text{s}^{-1}$ (Figure 2.3B). These data provide evidence for very rapid P_i binding to MDCC-PBP, and it has been shown that P_i binds very tightly to MDCC-PBP as well (163, 165), thus providing an excellent coupled assay for direct measurement of rapid P_i release from Eg5 in real-time.

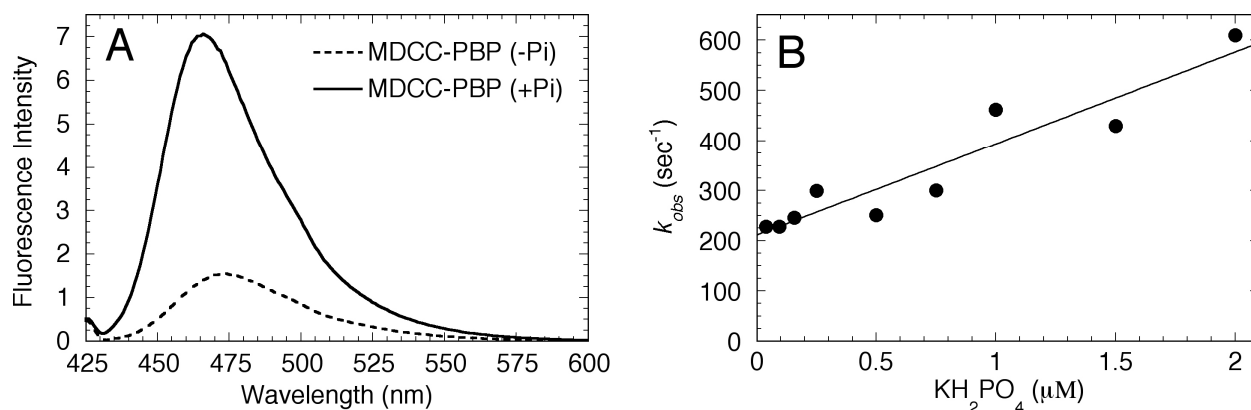


Figure 2.3 Characterization of MDCC-PBP preparations

(A) Fluorescence emission spectra of MDCC-PBP in the absence and presence of excess P_i . Final concentrations: 5 μM MDCC-PBP, 0.1 U/ml PNPase, 150 μM MEG, $\pm 100 \mu\text{M}$ KH_2PO_4 . There was a 4.58-fold change in fluorescence intensity ($\lambda_{\text{max}} / \lambda_{\text{max}}$) in the presence of P_i . (B) P_i concentration dependence of the observed rate constant of P_i binding to MDCC-PBP. Final concentrations: 5 μM MDCC-PBP, 0.1 U/ml PNPase, 150 μM MEG, 0.05–2 μM KH_2PO_4 . The data were fit the following linear relationship: $k_{\text{obs}} = k_{\text{on}} * [P_i] + k_{\text{off}}$, where k_{on} corresponds to the second-order rate constant for P_i binding to MDCC-PBP at $182 \pm 24 \mu\text{M}^{-1}\text{s}^{-1}$, and k_{off} equals the apparent off-rate for P_i at $212 \pm 23 \text{s}^{-1}$.

2.2.5 Microtubules for Kinetic Experiments

Purified bovine brain tubulin was isolated by two temperature-dependent cycles of polymerization and depolymerization (166, 167), followed by a modified DEAE column chromatography method to separate tubulin from microtubule-associated proteins (168, 169).

We received two fresh bovine brains from a local slaughterhouse, and after removing the outer meninges of the brain, we homogenized ~1 g tissue/ml of PM buffer [100 mM PIPES (pH 6.7), 5 mM MgCl₂, 1 mM EGTA, 1 mM PMSF]. The homogenate was clarified by ultracentrifugation, and the supernatant was adjusted to 1 mM GTP and 25% glycerol to lower the critical concentration for effective microtubule polymerization. The mixture was incubated at 34 °C for 30 min, and the assembled microtubules were pelleted by ultracentrifugation. The supernatant was discarded, and the microtubule pellets were resuspended in cold PM buffer containing 1 mM GTP and incubated on ice for 30 min to depolymerize the microtubule polymers. The soluble tubulin was further clarified by ultracentrifugation, and the supernatant was adjusted to 1 mM GTP and 25% glycerol, followed by incubation at 34 °C for 30 min. The microtubules were pelleted by ultracentrifugation in the presence of 1 mM MgATP and 200 mM KCl to partially remove some of the microtubule-associated proteins, especially cytoplasmic dynein. The microtubules were resuspended in PM buffer plus 1 mM GTP and frozen with liquid nitrogen for storage at -80 °C. This cycling procedure was repeated.

In order to remove the remaining microtubule-associated proteins from the tubulin, we employ a column chromatography method to select for the highly acidic tubulin protein (168, 169). On the day of the “tubulin column”, two microtubule pellets (as described above) were thawed, and adjusted the solution to 1 mM GTP. We incubated the tubulin solution on ice for 30 min, followed by ultracentrifugation to clarify the supernatant. The supernatant was adjusted to 200 mM KCl and loaded onto a 25-ml DEAE anion-exchange column (BioRad Laboratories, Inc.). Tubulin was eluted from the column with PM buffer + 500 mM KCl, and fractions enriched in tubulin were pooled. The pooled fractions were adjusted to 1 mM GTP and were dialyzed against 2 L of PM buffer + 0.5 mM GTP + 0.5 mM ATP to remove the excess salt. The solution was adjusted to 7% DMSO and incubated at 34 °C for 30 min to assemble the microtubules. The microtubules were pelleted in the presence of 1 mM MgATP + 200 mM KCl to remove trace amounts of cytoplasmic dynein and remaining associated proteins. The microtubule pellet was resuspended and thoroughly homogenized in PM buffer + 1 mM GTP, and the purified tubulin was aliquoted, frozen in liquid nitrogen, and stored at -80 °C. This method yielded >98% pure bovine tubulin based on a Coomassie brilliant blue stained SDS-

polyacrylamide gel (Figure 2.4). Each tubulin column typically yielded approximately 10 ml of 15 mg/ml tubulin.

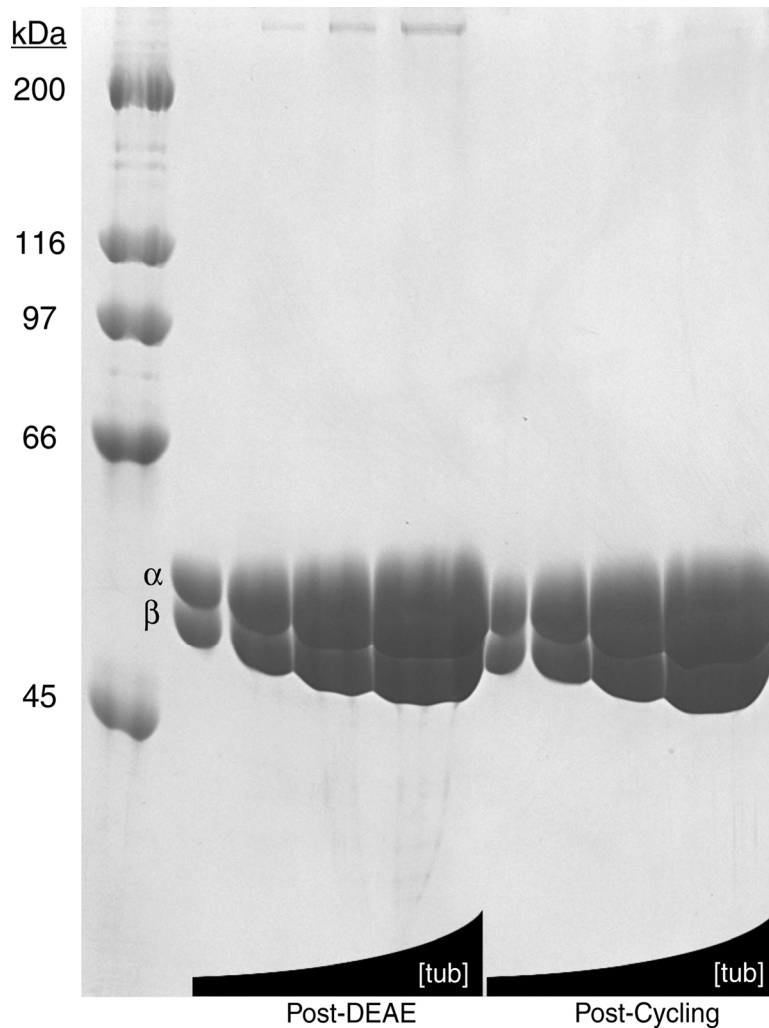


Figure 2.4 Tubulin for biochemical experiments

SDS-polyacrylamide gel (10%) stained with Coomassie blue showing the tubulin preparation post-DEAE column as well as post-cycling that was performed the day of each experiment (see below). SDS-PAGE High Range standards are shown in left lane.

On the day of each experiment, we cycled an aliquot of tubulin by thawing, diluting 1:2 with PM buffer, and adjusting to 1 mM GTP. The mixture was incubated on ice for 30 min, followed by centrifugation at 14,000 rpm for 30 min at 4 °C to remove aggregated tubulin. The supernatant was transferred to a 1.5 ml Eppendorf tube and incubated at 34 °C for 10 min to

polymerize the microtubules. The polymers were stabilized with 20 μ M Taxol (paclitaxel, Sigma-Aldrich Co.) and incubated at 34 °C for another 10 min. The reaction mixture was diluted with 1 ml PM buffer + Taxol to dilute the excess GTP, incubated at 34 °C for 10 min, and then centrifuged at 14,000 rpm for 30 min at room temperature. The microtubule pellet was resuspended in ATPase buffer plus 20–40 μ M Taxol. The concentration of this tubulin stock was determined by the hot Lowry assay (170, 171) using BSA as the protein standard.

2.2.6 Analytical Ultracentrifugation

It is possible to use sedimentation to analyze purified proteins and determine their oligomeric state in solution based on a comparison of the expected and observed molecular weights. Analytical ultracentrifugation experiments were performed to determine the sedimentation coefficient ($S_{20,w}$) and the average molecular weight of Eg5-437 in order to characterize its oligomeric state in the absence of microtubules. In collaboration with Dr. John J. Correia and colleagues at the University of Mississippi Medical Center (Department of Biochemistry, Jackson, MS 39216), sedimentation velocity experiments were conducted at 42,000 rpm, and sedimentation equilibrium experiments at 17,000 rpm in a Beckman Optima XLA analytical ultracentrifuge (Beckman Coulter Inc., Fullerton CA) equipped with absorbance optics and an An60Ti rotor. Velocity and equilibrium data were collected at a wavelength of 235 nm. The conditions for sedimentation velocity experiments included ATPase buffer with and without 50 μ M AMPPNP (a non-hydrolyzable ATP analog) at 25 °C (Figure 2.5A). Velocity data were analyzed by DCDT+ (v. 1.15) (172) as described previously (173) and, where appropriate, SVEDBERG (v. 6.39) (174) to verify the results. The reported weight average sedimentation coefficient values ($S_{20,w}$) obtained from DCDT+ are corrected for the solution density and viscosity (173) and are calculated by a weighted integration over the entire range of sedimentation coefficients covered by the $g(s)$ distribution. Equilibrium data were analyzed by NONLIN (v. 1.035) as described (173) (Figure 2.5B).

2.2.7 Gel Filtration and Stokes Radii Calculations

Analytical gel filtration is a form of chromatography in which proteins are separated based on their molecular size and shape. Therefore, this method can be used to characterize our purified Eg5 proteins, in comparison to other well-studied kinesin oligomers, to determine the oligomeric state of the proteins. Proteins were resolved by a Superose-6 HR 10/30 gel filtration column (Amersham Biosciences, Piscataway NJ) equilibrated in ATPase buffer at 25 °C using the System Gold high performance liquid chromatography system (Beckman Coulter Inc., Fullerton CA) ([Figure 2.5C](#)). The elution volumes (V_e) of proteins were determined by intrinsic protein fluorescence detection (Jasco FP-2020, Victoria British Columbia). The Stokes radii (R_s) of Eg5-367, Eg5-437, and dimeric *Drosophila* Kinesin-1 (K401) were calculated as described (*175*). Briefly, the partition coefficients (K_{av}) were calculated for four standard proteins of known Stokes radii (R_s): ovalbumin, 3.05 nm; aldolase, 4.81 nm; catalase, 5.22 nm; and ferritin, 6.10 nm. The apparent Stokes radius of each motor was determined from interpolation of a semilog plot of the markers K_{av} versus the known R_s of the markers ([Table 2.1](#)).

2.2.8 Phosphocreatine Kinase Coupled Assay

An estimation of the concentration of active Eg5 sites was determined by performing a modified Hackney coupled assay (*176*) that utilized a phosphocreatine kinase ATP regeneration system as described (*177*). Briefly, Eg5 (5 μ M final concentration) was incubated with a trace amount of [α - 32 P]ATP for 90 min to convert all radiolabeled ATP to ADP ([Figure 2.6A, inset](#)). In some experiments, additional non-radiolabeled ADP was then added to yield a final concentration of 5-15 μ M [α - 32 P]ADP. The Eg5•[α - 32 P]ADP complex was combined with a creatine kinase/phosphocreatine-based ATP regeneration system to convert unbound [α - 32 P]ADP to [α - 32 P]ATP. However, ADP tightly bound at the Eg5 active site was inaccessible to the creatine kinase, and therefore protected from enzymatic conversion to ATP. This assay measures the Eg5 concentration based on ADP tightly bound at the Eg5 active site. The protected [α - 32 P]ADP was quantified as a function of time by incubating the Eg5•[α - 32 P]ADP complex with the

regeneration system ± 2.5 mM unlabeled MgATP ([Figure 2.6B](#)). Each data set was fit to the following single exponential function,

Equation 2.1

$$[\text{ADP}] = A_0 * \exp(-k_{\text{off,ADP}} t) + C$$

where the active site concentration is the sum of the amplitude (A_0) and the constant term (C) to extrapolate to zero time (t). In the experiment with excess non-radioactive MgATP, $k_{\text{off,ADP}}$ is the first-order rate constant for ADP release in the absence of microtubules.

This assay was only effective for “estimating” the active site concentration of Eg5-437, but not Eg5-367 due to the inability of Eg5-367 to bind ADP tightly. If the ATP regeneration system of this assay is significantly faster at converting $[\alpha\text{-}^{32}\text{P}]\text{ADP}$ to $[\alpha\text{-}^{32}\text{P}]\text{ATP}$ compared to the rate of $[\alpha\text{-}^{32}\text{P}]\text{ADP}$ release from the Eg5 active site, then this coupled-assay provides a means to attain the first-order rate constant of $[\alpha\text{-}^{32}\text{P}]\text{ADP}$ product release from Eg5 in the absence of microtubules (e.g. Eg5-437). However, as the rate of $[\alpha\text{-}^{32}\text{P}]\text{ADP}$ product release increases, a significant error is introduced into the assay (e.g. Eg5-367).

2.2.9 Steady-State ATPase Kinetics

Eg5 steady-state ATPase activity was determined by following $[\alpha\text{-}^{32}\text{P}]\text{ATP}$ hydrolysis to form $[\alpha\text{-}^{32}\text{P}]\text{ADP}\cdot\text{P}_i$ as previously described (*178*). Briefly, each Eg5 protein preparation was tested for activity by measuring the steady-state ATPase kinetics as a function of microtubule concentration at saturating MgATP, and as a function of MgATP concentration at saturating microtubule concentration. Reactions were carried out at different time domains in order for 20–30% of the initial substrate to be converted to product. The plot of product formed *versus* reaction time provides a linear relationship with the slope of the line correlating to the rate of ATP turnover at the given substrate concentration. Multiple substrate concentrations were used to define the $K_{m,\text{ATP}}$ and the $K_{1/2,\text{Mt}}$, as well as the k_{cat} . In [Figure 2.7A](#), the rate of ATP turnover was plotted as a function of microtubule concentration, and the data were fit to the following quadratic equation,

Equation 2.2

$$Rate = 0.5 * k_{cat} * \{(E_0 + K_{1/2,Mt} + [Mt]) - [(E_0 + K_{1/2,Mt} + [Mt])^2 - (4E_0[Mt])]^{1/2}\}$$

where E_0 is the Eg5 site concentration, $K_{1/2,Mt}$ is the tubulin concentration as microtubules needed to provide one-half the maximal velocity, and $[Mt]$ is the tubulin concentration. For the MgATP-concentration dependence steady-state experiments ([Figure 2.7B](#)), the rate was plotted as a function of MgATP concentration, and the data were fit to the Michaelis Menten equation,

Equation 2.3

$$Rate = k_{cat} * [ATP] / (K_{m,ATP} + [ATP])$$

where *Rate* is the amount of hydrolysis product formed per second per active site, k_{cat} is the maximum rate constant of product formation at saturating substrate, and $K_{m,ATP}$ is the MgATP concentration required to provide half the maximal velocity.

2.2.10 Mt•Eg5 Cosedimentation Assays

In order to characterize Eg5 binding to microtubules at equilibrium, we performed cosedimentation assays based on the pelleting of microtubules, and analyzing the Eg5 protein in both the supernatant fraction (unbound Eg5) and the pellet fraction (bound Eg5). Holding the Eg5 concentration constant, and varying the concentration of microtubules, we are able to attain the upper limit of the dissociation constant for the microtubule ($K_{d,Mt}$) for each Eg5 motor. Eg5 at 2 μ M was incubated with varying microtubule concentrations (0–6 μ M tubulin) in the absence of added nucleotide for 30 min, followed by centrifugation in a Beckman Airfuge (Beckman Coulter Inc., Fullerton CA) at 30 psi (100,000 x g) for 30 min as described previously (*140*). The microtubule pellet was resuspended in ATPase buffer to equal the volume of the supernatant. Gel samples for the pellet and supernatant were prepared in 5x Laemmli sample buffer, the proteins resolved by SDS-PAGE, followed by staining with Coomassie brilliant blue. The gels were analyzed with a Scan Maker X6EL scanner (Microtek, Carson CA), and the proteins were quantified using NIH Image (v. 1.62) to determine the fraction of Eg5 in the supernatant and pellet at each microtubule concentration. The fraction of Eg5 that partitioned to

the pellet was plotted as a function of microtubule concentration ([Figure 2.8](#)), and the data were fit to the following quadratic equation,

Equation 2.4

$$\text{Mt}\cdot\text{E}/\text{E}_0 = 0.5 * \{(\text{E}_0 + K_{d,\text{Mt}} + [\text{Mt}]) - [(\text{E}_0 + K_{d,\text{Mt}} + [\text{Mt}])^2 - (4\text{E}_0[\text{Mt}])]^{1/2}\} / \text{E}_0$$

where $\text{Mt}\cdot\text{E}/\text{E}_0$ is the fraction of Eg5 partitioning with the microtubule pellet, E_0 is total Eg5 concentration, $K_{d,\text{Mt}}$ is the dissociation constant, and $[\text{Mt}]$ is the tubulin concentration.

2.2.11 Mt•Eg5•[α -³²P]ADP Cosedimentation Assays

We wanted to directly measure the re-binding of MgADP product to the Mt•Eg5 complex under equilibrium conditions. To address this question, we performed cosedimentation assays at constant microtubule and Eg5 concentrations that were sufficient to allow all Eg5 protein to partition to the pellet, and increasing the concentration of radiolabeled MgADP. In this assay, we were able to directly quantify the concentration MgADP that partitions with the Mt•Eg5 complex; thus, we were able to attain the lower limit of the dissociation constant of ADP ($K_{d,\text{ADP}}$) for both Eg5 motors. Eg5 at 5 μM was incubated with microtubules (6 μM and 8 μM tubulin for Eg5-367 and Eg5-437, respectively) and with varying concentrations of [α -³²P]MgADP (2.5–100 μM) for 30 min as described previously (*145*). The reaction mixture was centrifuged, the supernatant was removed, the unwashed pellet was resuspended in 4 N NaOH, and the volume of the pellet was adjusted with buffer to equal the volume of the supernatant. Control reactions were performed at each microtubule concentration in the absence of Eg5 to determine the amount of radiolabeled nucleotide that was non-specifically trapped in the microtubule pellet. The concentration of [α -³²P]ADP for each Mt•Eg5 reaction was corrected for [α -³²P]ADP that partitioned with microtubules in the absence of motor. [Figure 2.9A](#) shows the data fit to the following quadratic equation,

Equation 2.5

$$\text{Mt}\cdot\text{E}\cdot\text{ADP} = 0.5 * \{(\text{E}_0 + K_{d,\text{ADP}} + [\text{ADP}]) - [(\text{E}_0 + K_{d,\text{ADP}} + [\text{ADP}])^2 - (4\text{E}_0[\text{ADP}])]^{1/2}\}$$

where $Mt \cdot E \cdot ADP$ is the concentration of ADP bound to the $Mt \cdot Eg5$ complex, E_0 is total Eg5, $[ADP]$ is the total nucleotide present, and $K_{d,ADP}$ is the dissociation constant for ADP. For [Figure 2.9B](#), the fraction of Eg5 that partitioned to the pellet was plotted as a function of MgADP concentration.

2.2.12 Pulse-Chase Experiments

The presteady-state kinetics of MgATP binding was determined by pulse-chase methodologies using a KinTek RQF-3 chemical quench-flow instrument (KinTek Corp.) ([Figure 2.11](#)). The quench-flow instrument consists of three syringes controlled by a computerized motor to force the mixing of the $Mt \cdot Eg5$ complex with increasing $[\alpha\text{-}^{32}\text{P}]\text{MgATP}$ concentrations plus KCl, followed a chase solution (excess unlabeled MgATP) to allow time for any tightly bound radiolabeled MgATP to continue forward in the pathway. Whereas, any weakly bound or unbound MgATP substrate will be diluted by the unlabeled chase. The reaction was quenched with formic acid after a chase time sufficient for 8-10 turnovers. Radiolabeled product was separated from substrate by thin layer chromatography, and the concentration of product formed was plotted as a function of reaction time. We observed two phases in the kinetics of product formation: 1) a rapid exponential phase that corresponds to the product formed during the first turnover event, and 2) a slow linear phase that corresponds to subsequent ATP turnovers. From the exponential phase, we gain information about the observed presteady-state rate of MgATP binding, and the amplitude of the exponential, which is correlated to the concentration of Eg5 sites that report during the first ATP turnover. From the linear phase, we obtain an estimate of the rate of the slow step (downstream in the pathway from MgATP binding) that limits steady-state ATP turnover.

In the pulse-chase experiments, a preformed $Mt \cdot Eg5$ complex was rapidly mixed with increasing $[\alpha\text{-}^{32}\text{P}]\text{MgATP}$ concentrations plus KCl, and the reaction continued for various times (0.005–0.5 sec) followed by the non-radioactive MgATP chase (10 mM) for 3 sec (~10 turnovers). The additional KCl was added to the MgATP syringe to lower Eg5 steady-state ATPase activity, without affecting the kinetics of the first ATP turnover [[Figure 2.12 \(A and B\)](#)]. The concentration of $[\alpha\text{-}^{32}\text{P}]\text{ADP}$ product was plotted as function of time, and each pulse-chase transient was fit to the following burst equation [[Figure 2.11 \(A and B\)](#)],

Equation 2.6

$$[\text{Product}]_{\text{obs}} = A_0 * [1 - \exp(-k_b t)] + k_{ss} t$$

where A_0 corresponds to the concentration of tightly-bound Mt•Eg5*•ATP complexes that proceed in the forward direction toward ATP hydrolysis, k_b is the rate constant of the exponential phase, and k_{ss} is the rate constant of the linear phase ($\mu\text{M ADP}\cdot\text{s}^{-1}$) defining subsequent ATP turnovers.

The exponential rate of the presteady-state burst (k_b) and burst amplitude (A_0) [Figure 2.11 (C and D)] were plotted as a function of MgATP concentration. The rate of ATP binding was expected to increase linearly with increasing ATP concentration; however, we observed curvature in the concentration dependence of the rate of the reaction, suggesting (at least) a two-step binding mechanism (179). The first step involves the collision of ATP with the Eg5 active site to form a weakly ATP-bound complex. The second step consists of an isomerization of the Mt•Eg5•ATP collision complex to form a tightly ATP-bound complex. Both data sets in Figure 2.11 (C and D) were fit to a hyperbola.

2.2.13 Acid-Quench Experiments

The presteady-state kinetics of ATP hydrolysis for the Mt•Eg5 complex were defined in this assay. When the Mt•Eg5 complex was rapidly mixed with MgATP plus KCl, we observed a burst of product formation at a rate faster than the rate of a subsequent step in the pathway that limits steady-state ATP turnover. In acid-quench experiments, the presteady-state burst is correlated to product formation at the Eg5 active site during the first ATP turnover event. After the reaction is quenched with formic acid, Eg5 denatures and the products can be quantified. The observed quantity of products includes the sum of the Eg5-bound products and the products free in solution at the time of the quench. Radiolabeled product was separated from unreacted substrate by thin layer chromatography, and the concentration of product formed was plotted as a function of reaction time. We observed two phases in the kinetics of product formation: 1) a rapid exponential phase that corresponds to the product formed during the first turnover event, and 2) a slow linear phase that corresponds to subsequent ATP turnovers. From the exponential phase, we gain information about the observed presteady-state rate of ATP hydrolysis, and the

amplitude of the exponential, which is correlated to the concentration of Eg5 sites that report during the first ATP turnover. From the linear phase, we obtain an estimate of the rate of the slow step (downstream in the pathway from ATP hydrolysis) that limits steady-state ATP turnover.

A preformed Mt•Eg5 complex was rapidly mixed with varying concentrations of radiolabeled MgATP plus 100 mM KCl in a quench-flow instrument (KinTek Corp.). We added the additional salt in the ATP syringe to lower steady-state turnover without affecting the presteady-state burst of product formation [Figure 2.12 (A and B)]. The reaction was incubated (0.01–1 sec), quenched with formic acid, and radiolabeled product formation was quantified after separating [α - 32 P]ADP+P_i from unreacted [α - 32 P]ATP by thin layer chromatography (178). The concentration of [α - 32 P]ADP was plotted as a function of time [Figure 2.12 (C and D)], and the data were fit to Equation 2.6, where A_0 is the amplitude of the initial rapid exponential phase which corresponds to the formation of [α - 32 P]ADP•P_i at the Eg5 active site during the first ATP turnover, k_b is the rate constant of the exponential burst phase, and k_{ss} is the rate constant of the linear phase ($\mu\text{M ADP}\cdot\text{s}^{-1}$) corresponding to subsequent ATP turnovers. The exponential rate of the presteady-state burst (k_b) and burst amplitude (A_0) were plotted as a function of MgATP concentration, and each data set was fit to a hyperbola [Figure 2.12 (E and F)].

2.2.14 Stopped-Flow Experiments

Several experiments were performed using a SF-2003 KinTek stopped-flow instrument (KinTek Corp.) to investigate the kinetics of mantATP binding, P_i product release, ATP-dependent dissociation of the Mt•Eg5 complex, Eg5 association with microtubules, and mantADP release from the Mt•Eg5 complex. The kinetics of P_i product release from the Mt•Eg5 complex were measured using the MDCC-PBP coupled-assay, as described previously (122, 138). A preformed Mt•Eg5 complex plus MDCC-PBP and “P_i mop” were rapidly mixed with increasing MgATP concentrations plus KCl and “P_i mop”. The concentrations of the “P_i mop” reagents were experimentally determined to eliminate competition with the MDCC-PBP for P_i in solution (138). The experimental design assumes that after ATP hydrolysis, P_i product will be released from the Eg5 active site, followed immediately by P_i binding rapidly and tightly to MDCC-PBP, thus triggering the fluorescence enhancement of the MDCC-PBP•P_i complex (163). In order to

convert the observed change in fluorescence intensity into units of P_i concentration, a phosphate calibration curve was used ([Figure 2.13A](#)).

The data in [Figure 2.13B](#) show a burst of P_i product release at a rate faster than the rate of a subsequent slow step, thus the data were fit to [Equation 2.6](#), where A_0 equals the amplitude of the exponential burst phase, and k_b is the observed exponential rate of P_i product release from Eg5. The burst amplitude and burst rate were plotted as a function of MgATP concentration, and each data set was fit to a hyperbola ([Figure 2.13C](#)). In [Figure 2.13D](#), the P_i release kinetics were modeled in terms of a two-step irreversible mechanism, because once the P_i is released from the Eg5 active site, it rapidly and tightly binds to the MDCC-PBP, which effectively prevents P_i re-binding to Eg5. The amplitude and rate constants from [Equation 2.6](#) were defined by,

Equation 2.7

$$A_0 = E_0 * \{ [k_{+3} / (k_{+3} + k_{slow})]^2 \}$$

Equation 2.8

$$k_b = k_{+3} + k_{slow}$$

Equation 2.9

$$k_{ss} = E_0 * [k_{+3} k_{slow} / (k_{+3} + k_{slow})]$$

where E_0 is the Eg5 site concentration, k_{+3} denotes the rate constant for P_i product release ([Scheme 2.1](#)), and k_{slow} is the rate constant of the slow step that occurs after P_i product release that limits steady-state ATP turnover.

Fluorescent nucleotides are valuable probes for the structure and kinetics of nucleotide-binding enzymes. Mant-adenosine nucleotides show an enhancement of fluorescence when bound to the active site of kinesin motor proteins (*112, 122, 126, 127, 141-143, 180-182*) as well as myosin motors (*183-187*), and this fluorescence is quenched in solution. When we rapidly mix the Mt•Eg5 complex with increasing mantATP concentrations in a stopped-flow instrument, then we can monitor the exponential increase in fluorescence that is a result of mantATP binding the Eg5 active site. The mantATP and mantADP experiments were performed with a racemic mixture of mantAXP isomers (2'mant-3'dAXP and 3'mant-2'dAXP), and excitation wavelength

was set at 360 nm (Hg arc lamp) with emitted light measured through a 400-nm cutoff filter (mant $\lambda_{em} = 450$ nm). The mantATP binding data ([Figure 2.10](#)) were fit to the following equation,

Equation 2.10

$$k_{obs} = k_{+1}' * [mATP] / (K_{d,mATP} + [mATP]) + k_{-1}'$$

where k_{obs} is the rate constant obtained from the exponential phase of the fluorescence change, k_{+1}' is the rate constant for the ATP-dependent isomerization ([Scheme 2.1](#)), $K_{d,mATP}$ is the dissociation constant for weak mantATP binding, and k_{-1}' is mantATP off-rate. The mantATP binding data at low mantATP concentrations ([Figure 2.10, insets](#)) were fit to a linear function,

Equation 2.11

$$k_{obs} = K_{+1}k_{+1}' * [mantATP] + k_{off,ATP}$$

where k_{obs} is the rate constant of the fluorescence enhancement, $K_{+1}k_{+1}'$ is the apparent second-order rate constant for mantATP binding, and $k_{off,ATP}$ obtained from the y -intercept is the apparent mantATP off-rate from the Mt•Eg5•mantATP ternary complex.

We can use the optical signal of turbidity (the optical property that causes light to be scattered rather than being transmitted in straight lines through the sample) to measure the kinetics of Mt•Eg5 dissociation or Eg5 association with the microtubule. The size of a macromolecule (or macromolecular complex) affects the reading of turbidity; therefore, when Eg5 is bound to the microtubule, there is an increase in turbidity compared to the microtubule or Eg5 by themselves. These assays were designed based on the stopped-flow experiment that was performed to monitor the change in light scattering upon dissociation of the actomyosin complex (188). The Mt•Eg5 dissociation kinetics ([Figure 2.14](#)) and microtubule association kinetics ([Figure 2.15](#)) were determined by monitoring the change in solution turbidity at 340 nm. The rate constants of Eg5 dissociation from the microtubule were plotted as a function of MgATP concentration, and the data were fit to a hyperbola. The exponential rate constants of Eg5 association with microtubules were plotted as a function of microtubule concentration and fit to the following equation,

Equation 2.12

$$k_{obs} = K_{+5}k_{+6} * [\text{tubulin}] + k_{off,Mt}$$

where k_{obs} is the rate constant of the exponential phase, $K_{+5}k_{+6}$ is the apparent second-order rate constant for microtubule association, and $k_{off,Mt}$ corresponds to the observed rate constant for motor dissociation from Mt•Eg5 complex as determined from the y -intercept.

To measure the kinetics of ADP product release from the Mt•Eg5 complex, we can preform the Eg5•mantADP complex, and rapidly mix this complex with microtubules plus an unlabeled MgATP chase. Thus, in this assay we are able to monitor the exponential decrease in fluorescence as mantADP is released from the Mt•Eg5•mantADP intermediate. Release of mantADP from the Eg5 active site in the presence of microtubules was measured by incubating Eg5 with mantADP at a ratio of 1:2 (Eg5:mantADP) and rapidly mixing the complex with varying concentrations of microtubules plus 1 mM MgATP ([Figure 2.16](#)). The experimental design assumes that once mantADP is released from the Mt•Eg5•mantADP intermediate, the Mt•Eg5 complex will bind MgATP, thus effectively preventing mantADP re-binding. The rate constants for the initial fast exponential phase were plotted as a function of microtubule concentration, and the data were fit to a hyperbola.

2.3 RESULTS

2.3.1 Oligomeric State of Purified Eg5 Motors

We utilized analytical ultracentrifugation and gel filtration techniques to establish the oligomeric state of our purified Eg5 motors at the conditions used for the kinetic and equilibrium experiments presented here. We performed sedimentation velocity experiments with Eg5-437 in ATPase buffer without added nucleotide (Eg5•ADP) and with the non-hydrolyzable ATP analog, AMPPNP, to mimic ATP conditions. The $g(s)$ curves for both conditions superimpose, indicating that there is no difference in oligomeric state for Eg5-437 in these adenine nucleotide states ([Figure 2.5A](#)). DCDT+ analysis of both sedimentation velocity experiments provided an

average sedimentation coefficient ($S_{20,w}$) at 3.5 S. SVEDBERG analysis of these data also gave an average S value of 3.5 S and an average molecular weight of 44.6 kDa. These results are consistent with the predicted molecular weight of a monomeric Eg5-437•ADP complex (50.2 kDa) ([Table 2.1](#)).

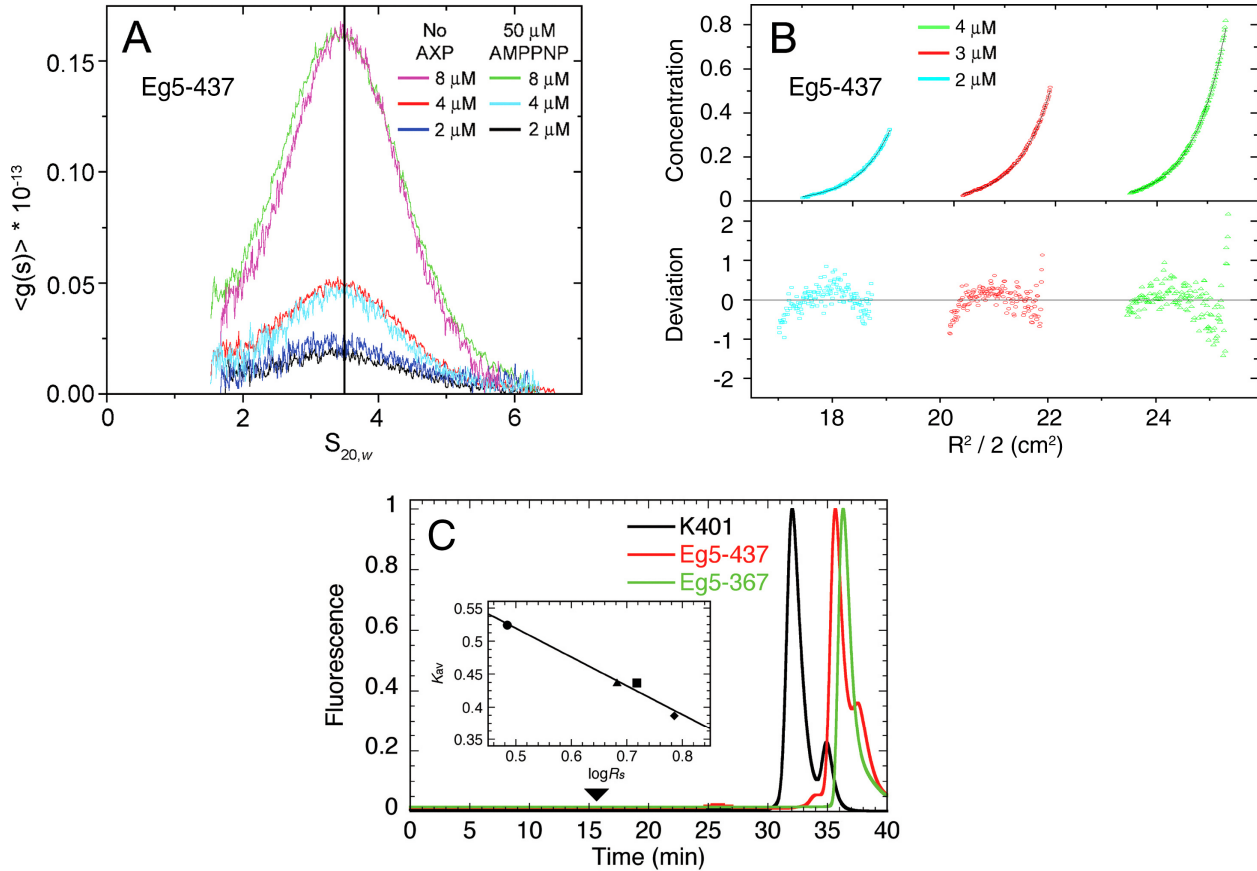


Figure 2.5 Analytical ultracentrifugation and gel filtration

(A) The sedimentation velocity data at 2, 4, and 8 μ M Eg5-437 were analyzed for sedimentation coefficient distribution $g(s)$ in the absence of adenine nucleotide and in the presence of 50 μ M AMPPNP (as indicated). The vertical line represents the average Eg5-437 $S_{20,w}$, corresponding to the three different protein concentrations in both conditions. For Eg5-437, $S_{20,w}$ is 3.49 ± 0.08 S. **(B)** The sedimentation equilibrium data at 2, 3, and 4 μ M Eg5-437 are shown in the presence of 50 μ M AMPPNP. For Eg5-437, a global single species fit of these data by NONLIN gave a Z average molecular weight (M_z) value of 49.3 ± 1.8 kDa. **(C)** Analytical gel filtration was performed at 10 μ M motor sites with detection by continuous monitoring of intrinsic protein fluorescence. The gel filtration profiles for *Drosophila* Kinesin-1 (K401), Eg5-437, and Eg5-367 are shown. The scale at the bottom indicates the elution time. The void volume elutes at 15.6 min (arrowhead) and the included volume at 52.1 min. **Inset**, semilog plot of the K_{av} values for four marker proteins (●, ovalbumin; ▲, aldolase; ■, catalase; ◆, ferritin) versus their known Stokes radii (R_s).

Further confirmation that Eg5-437 is monomeric under our experimental conditions was obtained from the results of sedimentation equilibrium centrifugation and analytical gel filtration. The equilibrium experiment was performed using Eg5 at 2, 3, and 4 μM in the ATPase buffer with 50 μM AMPPNP ([Figure 2.5B](#)). A global single species fit of these data by NONLIN gave a Z average molecular weight (M_z) value of 49.3 ± 1.8 kDa, consistent with the expected molecular weight of the Eg5 monomer with MgADP bound (50.2 kDa). In addition, we used analytical gel filtration ([Figure 2.5C](#)) to compare Eg5-437 with the well-established dimeric kinesin, *Drosophila* kinesin heavy chain, K401 (173), and the Eg5 monomer, Eg5-367 (68, 69, 147). From this experiment, the Stokes radii were calculated: K401 at 4.79 nm; Eg5-437, 3.37 nm; and Eg5-367, 2.86 nm ([Table 2.1](#)). Taken together, these results indicate that Eg5-437 is monomeric in solution at the buffer conditions reported here. Previous studies with *Xenopus* Eg5-437GST and untagged Eg5-437 suggested both were dimeric (112); however, studies with 6xHis-tagged human Eg5-401 indicated that there was an equilibrium of association states between monomers and dimers (102). This evidence suggests that our 6xHis tag may be disrupting the formation of a stable coiled-coil in the Eg5-437 motor in solution.

2.3.2 Eg5 Active Site Determination

Most kinesin superfamily members exhibit the ability to bind ADP tightly to the active site in the absence of microtubules (143, 176, 189). We exploited this tight affinity for ADP to determine the Eg5-437 active site concentration for each protein preparation ([Figure 2.6B](#)). Each data set in [Figure 2.6](#) was fit to a single exponential function ([Equation 2.1](#)). The amplitude data provided the active site concentration at 4.75 μM ADP of 5 μM Eg5 sites, and the early time points at 3 sec and 5 sec show 4.8-4.9 μM ADP. These results demonstrated that >96% of the motor population was active upon purification based on these criteria. In the MgATP chase experiment, the rate constant for ADP release ($k_{\text{off,ADP}}$) in the absence of microtubules (Eg5-367: 0.05 s^{-1} ; Eg5-437: 0.003 s^{-1}) was determined and was comparable to the steady-state k_{cat} in the absence of microtubules (Eg5-367: 0.018 s^{-1} ; Eg5-437: 0.002 s^{-1}). These results indicate that the rate-limiting step for Eg5 in the absence of microtubules is most likely ADP product release. The significant difference observed between the Eg5 motors suggests that the Eg5-367

nucleotide pocket exists in a more open conformation than Eg5-437 which has a more extended α -helical C-terminus.

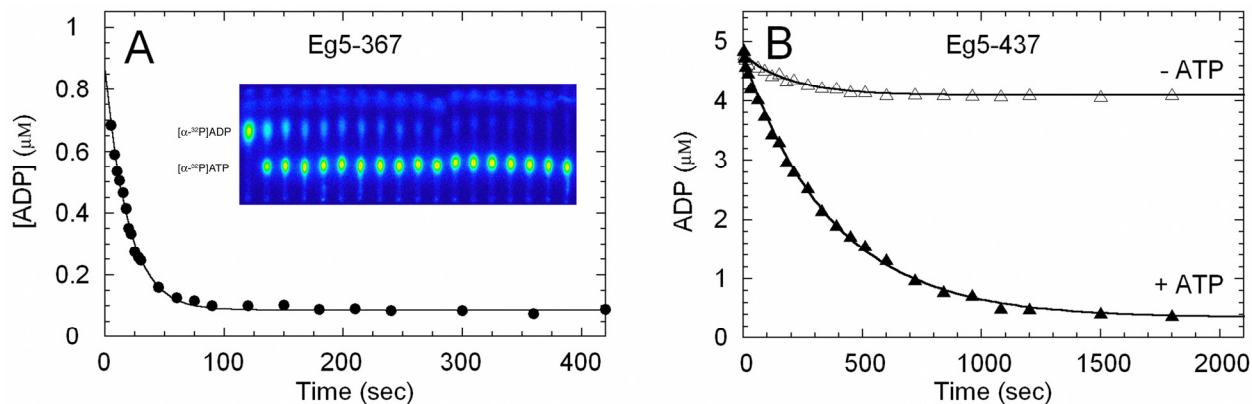


Figure 2.6 Active site determination

(A) The Eg5-367•[α - 32 P]ADP complex was incubated with an ATP regeneration system in the presence of a non-radioactive MgATP chase (●). Final concentrations: 5 μ M Eg5, 0.3 mg/ml creatine kinase, 4 mM phosphocreatine, 2.5 mM chase. The data set was fit to [Equation 2.1](#) to define $k_{off,ADP}$ at 0.05 s^{-1} for Eg5-367. The y -intercept does not reasonably estimate the active site concentration in this assay due to the relatively weak binding of ADP to Eg5-367. *Inset*, thin layer chromatography image showing the separation of [α - 32 P]ADP from [α - 32 P]ATP during the time course of the experiment shown in Panel A. Note: the first lane represented zero time where all the radiolabeled nucleotide was [α - 32 P]ADP. (B) The Eg5-437•[α - 32 P]ADP complex was incubated with an ATP regeneration system in the presence (▲) or absence (Δ) of a non-radioactive MgATP chase. Both data sets were fit to [Equation 2.1](#), providing an active site concentration at $4.72 \pm 0.09 \text{ } \mu\text{M}$ (+ATP) and $4.77 \pm 0.04 \text{ } \mu\text{M}$ (-ATP). In the presence of the non-radioactive ATP chase, the $k_{off,ADP}$ was determined to be $0.003 \pm 0.0001 \text{ s}^{-1}$ for Eg5-437.

2.3.3 Eg5 Steady-State ATPase Kinetics

In the presence of microtubules, the steady-state rate of ATP turnover was dramatically increased for both Eg5 motors, which is a characteristic of kinesin proteins (143, 176, 177, 189, 190). [Figure 2.7](#) shows steady-state kinetics as a function of microtubule concentration at 1 mM MgATP and as a function of MgATP concentration at 40 μ M tubulin. Eg5-367 appears to be able to turn over ATP approximately 2-fold faster than Eg5-437 (Eg5-367: $k_{cat} = 5.5 \text{ s}^{-1}$ versus Eg5-437: $k_{cat} = 2.9 \text{ s}^{-1}$) as well as to bind microtubules more tightly under cycling conditions (Eg5-367: $K_{1/2,Mt} = 0.7 \text{ } \mu\text{M}$ versus Eg5-437: $K_{1/2,Mt} = 4.5 \text{ } \mu\text{M}$). Both Eg5 proteins show similar values for $K_{m,ATP}$ (Eg5-367: $K_{m,ATP} = 10 \text{ } \mu\text{M}$ versus Eg5-437: $K_{m,ATP} = 4 \text{ } \mu\text{M}$). These steady-state

kinetics are comparable to those determined in previous studies when ionic strength and other experimental conditions are considered (69, 102, 112).

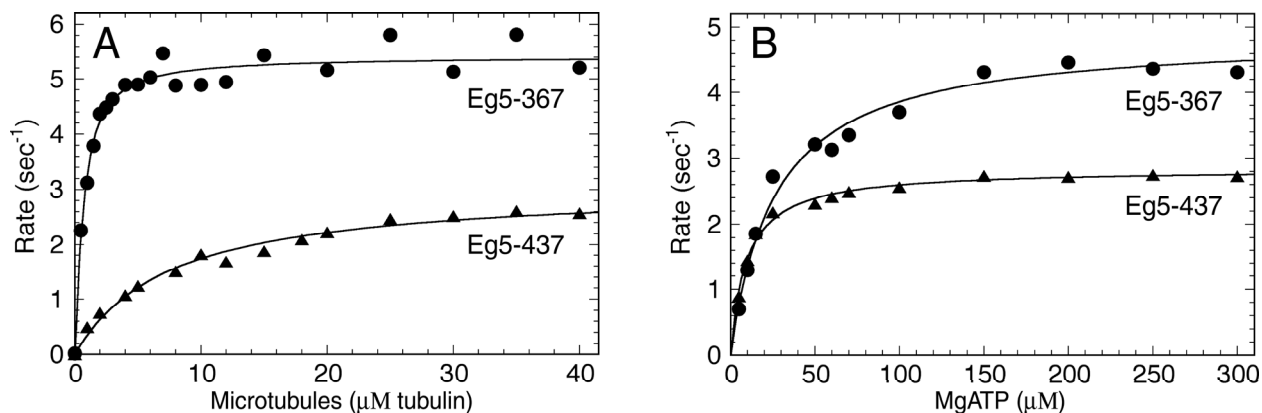
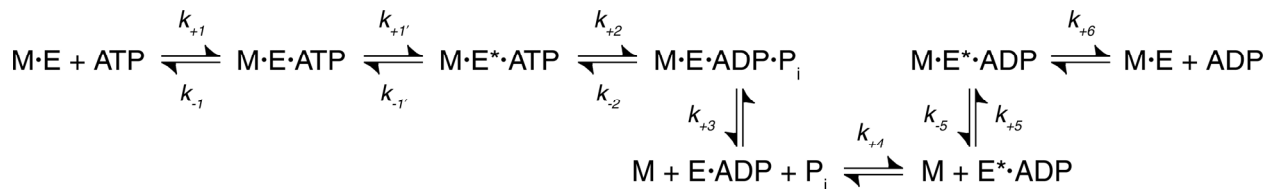


Figure 2.7 Steady-state ATPase kinetics

(A) The Mt•Eg5 complex was preformed with varying concentrations of Taxol-stabilized microtubules, and the reaction was initiated by mixing with MgATP. Final concentrations: 0.5 μM Eg5, 0–40 μM tubulin, 20 μM Taxol, 1 mM [α - 32 P]MgATP. The data were fit to Equation 2.2. For Eg5-367 (●), $k_{cat} = 5.42 \pm 0.08 \text{ s}^{-1}$ and $K_{1/2,Mt} = 0.46 \pm 0.06 \text{ μM}$. For Eg5-437 (▲), $k_{cat} = 3.05 \pm 0.08 \text{ sec}^{-1}$ and $K_{1/2,Mt} = 7.31 \pm 0.68 \text{ μM}$. (B) ATP concentration dependence. Final concentrations: 1 μM Eg5, 40 μM tubulin, 20 μM Taxol, 0–300 μM [α - 32 P]MgATP. The data were fit to Equation 2.3. For Eg5-367, $k_{cat} = 4.88 \pm 0.08 \text{ s}^{-1}$ and $K_{m,ATP} = 26.5 \pm 2.0 \text{ μM}$. For Eg5-437, $k_{cat} = 2.84 \pm 0.02 \text{ s}^{-1}$ and $K_{m,ATP} = 9.3 \pm 0.5 \text{ μM}$.



Scheme 2.1

2.3.4 Eg5 Binding to Microtubules

To determine the affinity of Eg5 for microtubules in the absence of added nucleotide, microtubule-cosedimentation assays were performed (Figure 2.8). Eg5 was incubated with increasing concentrations of microtubules, followed by centrifugation and analysis by SDS-PAGE. Eg5 partitioned with the microtubules as a function of microtubule concentration with 100% maximal binding at 2 μM tubulin. The stoichiometry for both Eg5 proteins indicates that

one motor domain binds per $\alpha\beta$ -tubulin heterodimer. The fit of the data to [Equation 2.3](#) provides $K_{d,Mt}$ values at 0.03–0.05 μM tubulin for each Eg5 motor, which represents the upper limit for the $K_{d,Mt}$ at the motor concentration used in this assay. Our determined $K_{d,Mt}$ in the absence of added nucleotide (30–50 nM tubulin) was approximately 50-fold lower than the $K_{d,Mt}$ determined previously by Lockhart and Cross (2.2 μM tubulin) (112). This difference may be the result of differing buffer conditions as well as the oligomeric state of the motors.

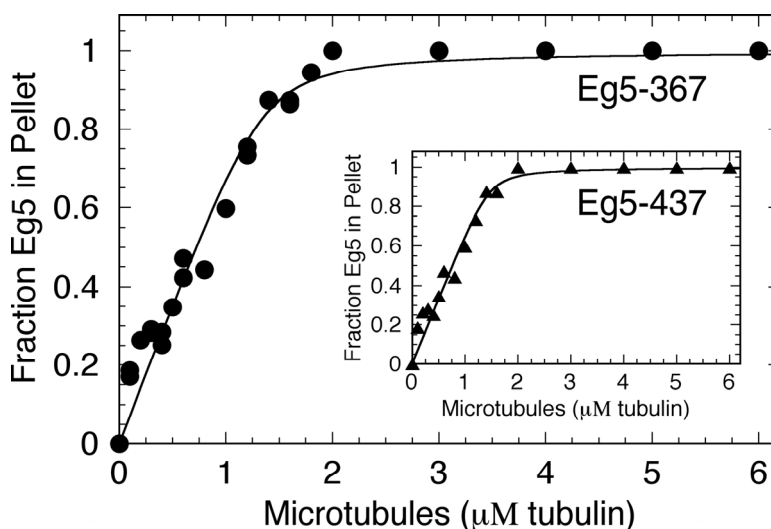


Figure 2.8 Microtubule equilibrium binding experiments

Eg5 at 2 μM was incubated with varying concentrations of microtubules (0–6 μM tubulin, 20 μM Taxol) in the absence of added nucleotide. The fraction of Eg5 in the microtubule pellet was plotted as a function of the total microtubule concentration, and the data were fit to [Equation 2.3](#). For Eg5-367 (\bullet), the $K_{d,Mt} = 0.046 \pm 0.019 \mu\text{M}$. The *inset* shows the data for Eg5-437 (\blacktriangle): $K_{d,Mt} = 0.030 \pm 0.027 \mu\text{M}$.

2.3.5 ADP Equilibrium Binding to Mt•Eg5 Complex

To determine the affinity of the Mt•Eg5 complex for MgADP, cosedimentation assays were performed ([Figure 2.9A](#)). A preformed Mt•Eg5 complex was incubated with increasing concentrations of $[\alpha\text{-}^{32}\text{P}]\text{MgADP}$, followed by centrifugation. Any radiolabeled MgADP still bound at the active site should partition to the pellet with the Mt•Eg5 complexes. The reaction mixtures at each MgADP concentration were analyzed by SDS-PAGE to verify that 100% of Eg5 partitioned with the microtubule pellet ([Figure 2.9B, inset](#)). Note that we did not saturate the 5 μM Eg5 sites at 90 μM $[\alpha\text{-}^{32}\text{P}]\text{MgADP}$, and the fit of the data provided the apparent ADP

dissociation constant for Eg5-367, $K_{d,ADP} = 117 \pm 86 \mu\text{M}$ with maximal ADP binding at $3.9 \pm 1.9 \mu\text{M}$. For Eg5-437, $K_{d,ADP} = 202 \pm 64 \mu\text{M}$, and the maximal ADP binding was $5.4 \pm 1.4 \mu\text{M}$. Because of the weak affinity for ADP and the loss of sensitivity at higher ADP concentrations, the upper region of the curve is not well defined; therefore, the error estimate on these constants is high. However, the results indicate that microtubules rapidly stimulate ADP release from the active site of Eg5 and that most ADP remains in solution as seen previously for conventional kinesin and in contrast to Kar3 [Table 2.2; (121, 145, 191)]. Figure 2.9B also provides insight into the behavior of the Mt•Eg5 complex at increasing MgADP concentrations. Note that at 2 mM MgADP, conditions where one would expect to see motor release from the microtubule, the monomeric Eg5 continues to partition with the microtubule pellet. One interpretation of these data is that the monomer in the absence of the partner motor domain(s) has lost cooperative interactions that facilitate motor domain release as observed previously for kinesin, Ncd, and Kar3 (127, 143, 145). However, the experiments to test this hypothesis have not yet been completed (125, 127, 192). Another interpretation of these data is that the weak binding state of Eg5 for the microtubule cannot be attained by driving the equilibrium reactions in the reverse direction. The weak binding state of Eg5 seems to be attained in the forward direction, with ATP hydrolysis being a critical step in the mechanism for reaching the weak binding state.

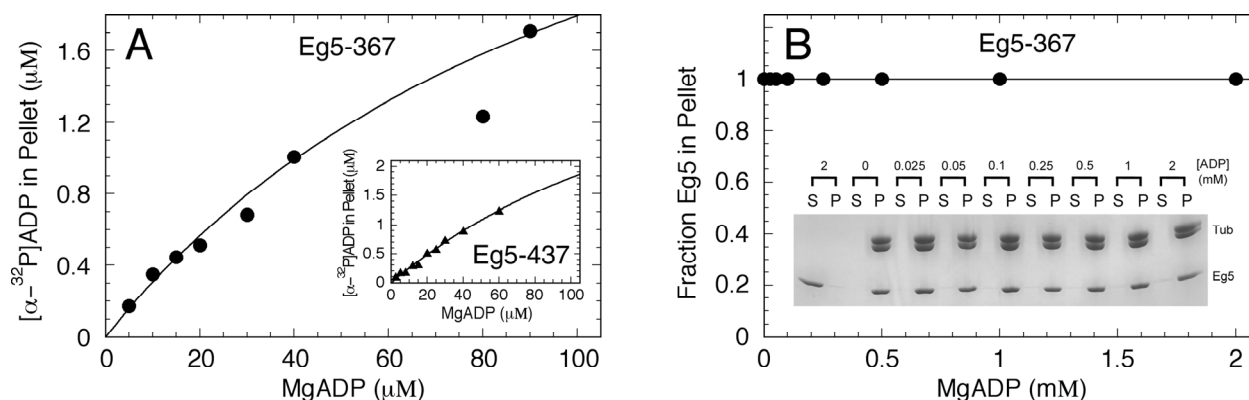


Figure 2.9 [α - ^{32}P]MgADP equilibrium binding experiments

(A) A preformed Mt•Eg5 complex was incubated with varying concentrations of [α - ^{32}P]MgADP. Final concentrations: 5 μM Eg5, 6 μM tubulin, 30 μM Taxol, 5-90 μM [α - ^{32}P]MgADP. The concentration of [α - ^{32}P]ADP that partitioned with the Mt•Eg5 complex was plotted as a function of total MgADP concentration (\bullet , Eg5-367; \blacktriangle , Eg5-437). The data were fit to [Equation 2.4](#), which yielded for Eg5-367 the $K_{d,ADP} = 117 \pm 86 \mu\text{M}$ with maximal ADP binding at $3.9 \pm 1.9 \mu\text{M}$. For Eg5-437 (*inset*), the $K_{d,ADP} = 202 \pm 64 \mu\text{M}$ with maximal ADP binding at $5.4 \pm 1.4 \mu\text{M}$. (B) Eg5-367 at 2 μM was incubated with 4 μM microtubules plus varying MgADP concentrations (0-2 mM). The fraction of Eg5 bound was plotted as a function of MgADP concentration yielding 100% bound at all MgADP concentrations. *Inset*, Coomassie blue-stained SDS gel following sedimentation of Mt•Eg5 complexes in the presence of increasing MgADP concentrations. The supernatant (S) and pellet (P) for each reaction were loaded consecutively with the concentration of MgADP indicated above each supernatant/pellet pair. Lanes 1 & 2 represent a control reaction with 2 μM Eg5-367 plus 2 mM MgADP (no microtubules).

2.3.6 MantATP Binding to Mt•Eg5 Complex

MantATP binding experiments were performed to determine the kinetics of nucleotide binding to the Mt•Eg5 complex. Using a stopped-flow instrument to rapidly mix a preformed Mt•Eg5 complex with increasing mantATP concentrations, we measured the exponential increase in fluorescence, which was interpreted as mantATP binding to the more hydrophobic environment of the Eg5 active site ([Figure 2.10, insets](#)). The observed rate of mantATP binding increased hyperbolically as a function of the mantATP concentration for each Eg5 motor, suggesting that ATP binding occurs via (at least) a two-step mechanism. The maximum rate of mantATP binding (k_{max}) was 37 s^{-1} , thus indicating a rate-limiting conformational change prior to ATP hydrolysis for both motors. The fit of the initial linear phase yields the apparent second-order rate constant for mantATP binding ($K_{+1}k_{+1}$) at $3.4 \mu\text{M}^{-1}\text{s}^{-1}$ for Eg5-367 and $1.9 \mu\text{M}^{-1}\text{s}^{-1}$ for Eg5-437 ([Figure 2.10, insets](#)). The first step in the mechanism likely corresponds to a rapid

equilibrium step where Mt•Eg5•ATP collision complex is formed with ATP weakly bound. The second step corresponds to a conformational change in the motor domain (Mt•Eg5*•ATP) that tightens Eg5's affinity for ATP. The mantATP binding kinetics do indicate that these nucleotide binding steps are fast in the Mt•Eg5 ATPase cycle.

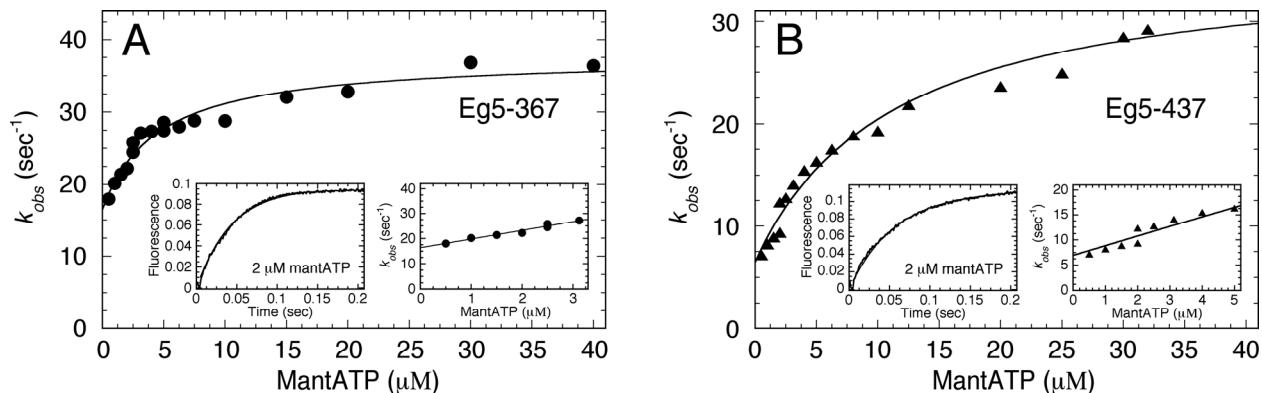


Figure 2.10 Kinetics of mantATP binding to the Mt•Eg5 complex

The preformed Mt•Eg5 complex was rapidly mixed in the stopped-flow instrument with varying concentrations of mantATP. Final concentrations: 0.5 μM Eg5 for 0.5-2 μM mantATP and 2 μM Eg5 for 2-40 μM mantATP, 10 μM tubulin, 20 μM Taxol. **(A)** Kinetics of mantATP binding to the Mt•Eg5-367 complex (\bullet). A representative transient at 2 μM mantATP was fit to a single exponential function and is shown in the left inset. The observed rate of the exponential fluorescence enhancement increased as a function of mantATP concentration. The fit of the data to [Equation 2.11](#) defined the maximum rate of mantATP binding, $k_{+1} = 21.2 \pm 1.3 \text{ s}^{-1}$, $K_{d,mATP} = 4.4 \pm 1.1 \text{ }\mu\text{M}$, and $k_{-1} = 16.5 \pm 1.4 \text{ s}^{-1}$. The right inset shows that at low concentrations of mantATP (0-3 μM), the rate data were linear. The fit to [Equation 2.10](#) yielded the apparent second-order rate constant for mantATP binding $K_{+1}k_{+1} = 3.4 \pm 0.3 \text{ }\mu\text{M}^{-1}\text{s}^{-1}$; $k_{off} = 16.3 \pm 0.6 \text{ s}^{-1}$. **(B)** Kinetics of mantATP binding to the Mt•Eg5-437 complex (\blacktriangle). The left inset shows a representative transient at 2 μM mantATP fit to a single exponential, and the right inset shows the data at low mantATP concentrations. Conditions and treatment of the data as described in Panel A: $k_{+1} = 29.8 \pm 1.7 \text{ s}^{-1}$, $K_{d,mATP} = 11.3 \pm 2.6 \text{ }\mu\text{M}$, $k_{-1} = 6.5 \pm 1.0 \text{ s}^{-1}$, $K_{+1}k_{+1} = 1.9 \pm 0.2 \text{ }\mu\text{M}^{-1}\text{s}^{-1}$, and $k_{off} = 6.9 \pm 0.7 \text{ s}^{-1}$.

2.3.7 MgATP Binding Kinetics by Pulse-Chase

Pulse-chase experiments for the Mt•Eg5 complex were performed as a function of [α - ^{32}P]MgATP concentration to gain insight into the equilibrium constant for ATP binding to the Mt•Eg5 complex and the lifetime of the Mt•Eg5*•ATP intermediate ([Scheme 2.1](#)). The experimental design assumes any tightly-bound [α - ^{32}P]MgATP substrate will proceed in the forward reaction, while any loosely-bound or unbound substrate will be diluted by the excess non-radioactive MgATP in the chase ([179, 193](#)). [Figure 2.11 \(C and D\)](#) shows that the rate and

amplitude of the exponential burst phase increases with increasing $[\alpha\text{-}^{32}\text{P}]\text{MgATP}$ concentration, and the maximum observed rate of MgATP binding was 22.0 s^{-1} for Eg5-367 and 21 s^{-1} for Eg5-437. In addition, the burst amplitude was similar between Eg5 monomers [Eg5-367 = 0.75 ADP/site; Eg5-437 = 0.78 ADP/site; [Figure 2.11 \(C and D\) insets](#)], indicating that the entire Mt•Eg5 population bound MgATP tightly during the first ATP turnover. The observation that the burst rate in the pulse-chase experiments saturates at increasing concentrations of substrate indicates a rate-limiting conformational change that occurs prior to ATP hydrolysis, consistent with our results from mantATP binding experiments. These results support the two-step model for ATP binding, yet the Mt•Eg5*•ATP state is not long lived but proceeds directly to ATP hydrolysis.

The ATP-concentration dependence of the presteady-state kinetics of MgATP binding by pulse-chase shows that a burst stoichiometry of approximately 1 per active site was observed at high MgATP concentrations. This observation indicates that the reverse rate constant of the ATP-dependent isomerization step ([Scheme 2.1](#)) was very low. Experiments to directly measure k_{-1} or k_{-1}' were not possible. However, the apparent $K_{d,ATP}$ determined for Eg5-367 and Eg5-437 [[Figure 2.11 \(C and D\)](#)] were $26 \pm 15\text{ }\mu\text{M}$ and $45 \pm 8\text{ }\mu\text{M}$, respectively, which provides the apparent dissociation constant for weak ATP binding. Fitting the initial data points at low MgATP to [Equation 2.11](#), $k_{off}/K_{+1}k_{+1}'$ was $24 \pm 1\text{ }\mu\text{M}$ for Eg5-367 and $29 \pm 1\text{ }\mu\text{M}$ for Eg5-437. In [Figure 2.10](#), the apparent $K_{d,mATP}$ was lower for both Eg5 proteins (Eg5-367: $K_{d,mATP} = 4.4 \pm 1.1\text{ }\mu\text{M}$ and Eg5-437: $K_{d,mATP} = 11.3 \pm 2.6\text{ }\mu\text{M}$). Fitting the initial data points at low MgATP to [Equation 2.11](#), $k_{off}/K_{+1}k_{+1}'$ was $4.8 \pm 0.6\text{ }\mu\text{M}$ for Eg5-367 and $3.6 \pm 0.7\text{ }\mu\text{M}$ for Eg5-437. These results suggest that mantATP binding to form the Mt•Eg5•mATP collision complex is tighter than MgATP (lower $K_{d,mATP}$ compared to $K_{d,ATP}$); however, the off-rate for the isomerization step (k_{-1} ; [Scheme 2.1](#)) is much higher for mantATP compared to MgATP (higher $k_{off,mATP}$ compared to $k_{off,ATP}$). The structural explanation for this observation remains unknown.

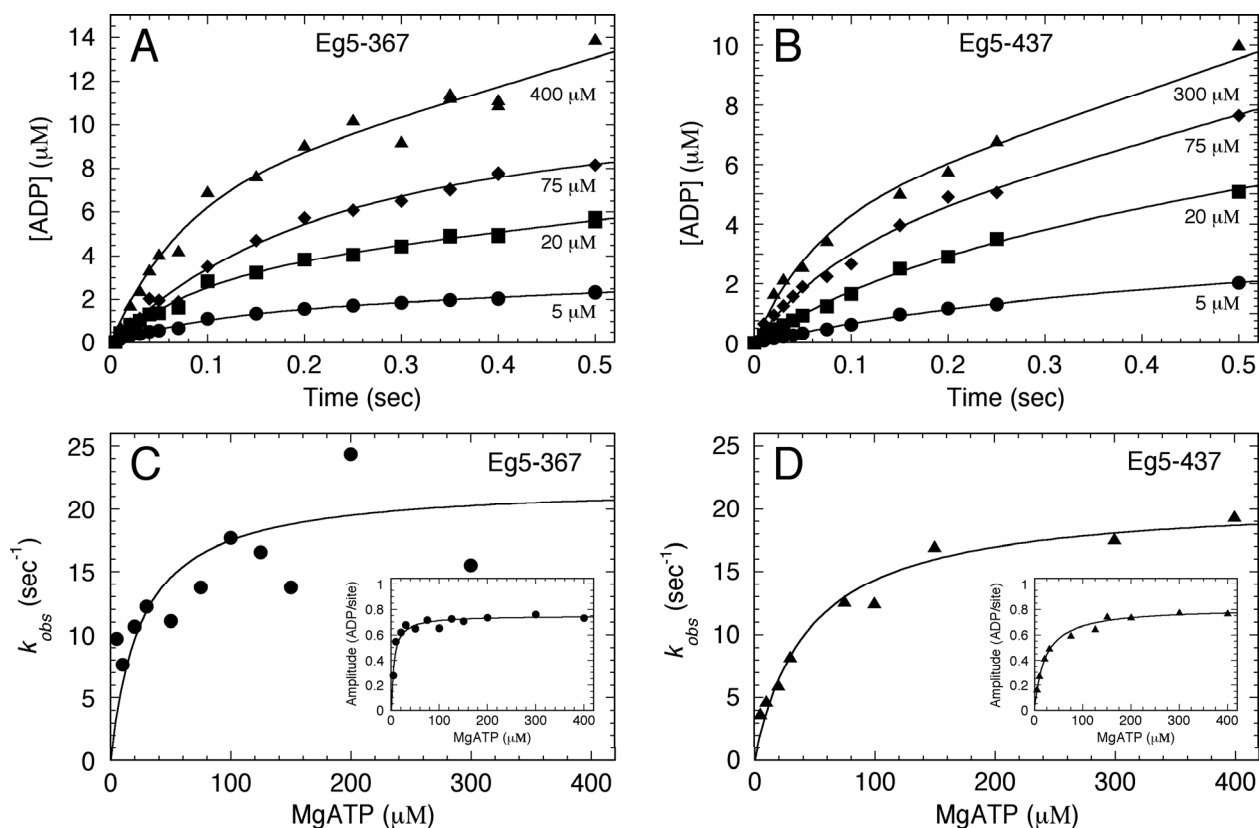


Figure 2.11 Pulse-chase kinetics of ATP binding

The preformed Mt•Eg5 complex was reacted with $[\alpha\text{-}^{32}\text{P}]\text{MgATP}$ plus KCl for 0-500 msec, followed by the MgATP chase as described in [Materials and Methods 2.2.10](#). Final concentrations: 5 μM Eg5, 6 μM tubulin, 20 μM Taxol, 0-400 μM $[\alpha\text{-}^{32}\text{P}]\text{MgATP}$, 100 mM KCl, followed by 10 mM non-radioactive MgATP chase. **(A and B)** Representative transients for Eg5-367 and Eg5-437, respectively, fit to [Equation 2.6](#). **(C and D)**, The rate of the exponential burst phase was plotted as a function of MgATP concentration for Eg5-367 and Eg5-437, respectively. The data were fit to a hyperbola to determine the rate of the conformational change after formation of the Mt•Eg5•ATP collision complex. The ATP-dependent isomerization, $k_{+1'} = 22.0 \pm 3.0 \text{ s}^{-1}$ with $K_{d,ATP} = 26 \pm 15 \text{ }\mu\text{M}$ for Eg5-367, and $k_{+1'} = 20.8 \pm 1.1 \text{ s}^{-1}$ with $K_{d,ATP} = 45 \pm 8 \text{ }\mu\text{M}$ for Eg5-437. **Insets**, the amplitude of each burst phase was plotted as a function of MgATP concentration. Each data set was fit to a hyperbola yielding the maximum burst amplitude at $0.75 \pm 0.02 \text{ ADP/site}$ and the $K_{d,ATP} = 6 \pm 1 \text{ }\mu\text{M}$ for Eg5-367, and $0.78 \pm 0.05 \text{ ADP/site}$ and the $K_{d,ATP} = 22 \pm 5 \text{ }\mu\text{M}$ for Eg5-437.

2.3.8 ATP Hydrolysis Kinetics by Acid-Quench

In order to determine the time dependence of ATP hydrolysis by Eg5, a Mt•Eg5 complex was rapidly mixed in a chemical quench-flow instrument with increasing concentrations of $[\alpha\text{-}^{32}\text{P}]\text{MgATP}$. There was a rapid initial burst of product formation related to the formation of $[\alpha\text{-}^{32}\text{P}]\text{ADP}\cdot\text{P}_i$ at the active site during the first ATP turnover, followed by a slower linear phase of product formation which corresponded to subsequent ATP turnovers. To better define the burst

phase, additional salt was added with the MgATP syringe to reduce the linear phase. The results in [Figure 2.12 \(A and B\)](#) show that the initial exponential phase was not affected by the additional salt (100 mM KCl final concentration after mixing), yet the linear phase was markedly slower. [Figure 2.12 \(E and F\)](#) show that the observed exponential rate of ATP hydrolysis increased as a function of MgATP concentration, with a maximum observed rate of 11.3 s^{-1} for Eg5-367. This observed rate of ATP hydrolysis was slower than the maximum rate determined for Eg5-437 at 14.9 s^{-1} . The magnitude of the burst amplitude increased as a function of MgATP concentration as well [[Figure 2.12 \(E and F\), insets](#)], with the maximum amplitude at 0.75 ADP/site for Eg5-367 and 0.78 ADP/site for Eg5-437. These results suggest the entire Mt•Eg5 population hydrolyzes ATP during the first turnover event, consistent with pulse-chase results that show the entire Mt•Eg5 population binds ATP tightly during the first ATP turnover ([Figure 2.11](#)).

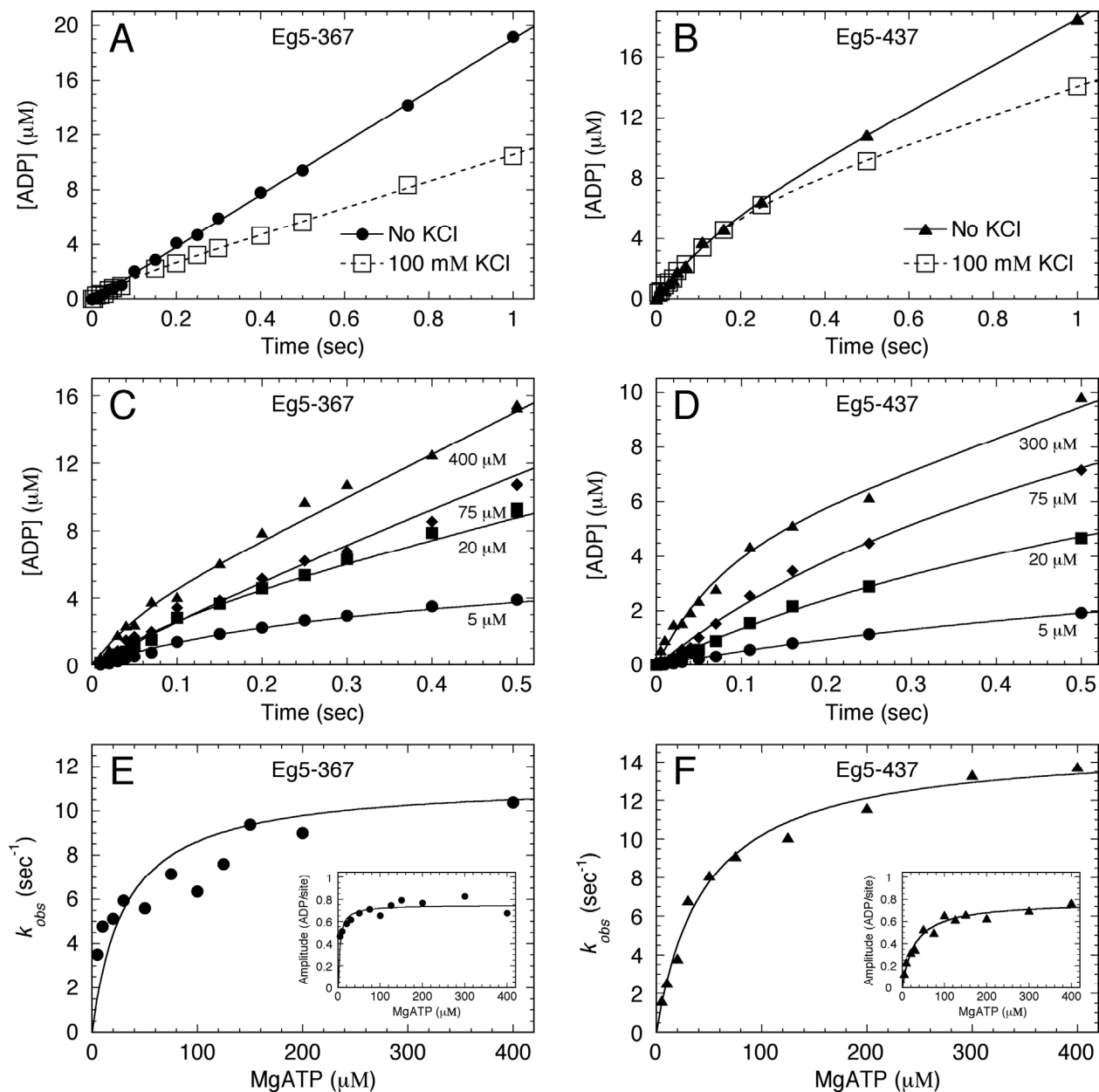


Figure 2.12 Acid-quench kinetics of ATP hydrolysis

Time course of radiolabeled product formation after rapidly mixing a preformed Mt•Eg5-367 complex (A) or Mt•Eg5-437 complex (B) with [α -³²P]MgATP. Additional salt was added to the MgATP syringe to lower steady-state ATP turnover (●, absence KCl; □, presence KCl). Final concentrations: 5 μM Eg5, 6 μM tubulin, 20 μM Taxol, 5–200 μM [α -³²P]MgATP, ± 100 mM KCl, and the data were fit to Equation 2.6. (C and D) Time course of ADP•P_i formation by Mt•Eg5-367 and Mt•Eg5-437 complexes (respectively) at increasing MgATP concentrations. (E and F) The observed rate of the exponential burst phase was plotted as a function of MgATP concentration. The fit of the data to a hyperbola defined the maximum rate constant of ATP hydrolysis for Eg5-367, $k_{b,max} = 11.3 \pm 1.4$ s⁻¹ and the $K_{d,ATP} = 31 \pm 15$ μM, and for Eg5-437, $k_{b,max} = 14.9 \pm 0.5$ s⁻¹ and the $K_{d,ATP} = 46 \pm 6$ μM. **Insets**, the amplitude of the burst phase was plotted as a function of MgATP concentration. The data were fit to a hyperbola yielding a maximum burst amplitude at 0.75 ± 0.02 ADP/site, and the $K_{d,ATP} = 4 \pm 1$ μM for Eg5-367, and 0.78 ± 0.03 ADP/site, and the $K_{d,ATP} = 30 \pm 5$ μM for Eg5-437.

2.3.9 P_i Product Release from Mt•Eg5 Complexes

To directly measure the kinetics of P_i product release from the Mt•Eg5 complex, we performed stopped-flow experiments that detect the change in MDCC-PBP fluorescence upon binding P_i released into solution ([Figure 2.13](#)). The maximum observed rate of P_i product release was the slowest step measured in the pathway ($k_{obs,max} = 6.0 \text{ s}^{-1}$). The maximum amplitude of the exponential burst of P_i product release during the first ATP turnover was 0.75 P_i/site (100% of expected amplitude based on Eg5-367 site concentration), consistent with the ATP hydrolysis kinetics reported in [Figure 2.12E, inset](#). Again, these kinetics are suggestive of the entire Mt•Eg5 population binding and hydrolyzing ATP during the first ATP turnover.

The experimental design to measure P_i product release from the Mt•Eg5 complex assumes that P_i released from Eg5 rapidly and tightly binds to MDCC-PBP, thus rendering the P_i release step irreversible. In [Figure 2.13 \(E and F\)](#), the presteady-state burst kinetics of P_i release were modeled to a two-step irreversible mechanism ([Equations 2.6–2.9](#)). The modeled rate of P_i product release (k_{+3} ; [Scheme 2.1](#)) was similar to the k_{cat} measured by steady-state ATPase assays: $k_{+3} = 5.2 \pm 0.1 \text{ s}^{-1}$ versus $k_{cat} = 5.5 \pm 0.3 \text{ s}^{-1}$ ([Figure 2.7](#)), thus supporting the hypothesis that the entire Mt•Eg5 population binds and hydrolyzes ATP during subsequent ATP turnovers as well.

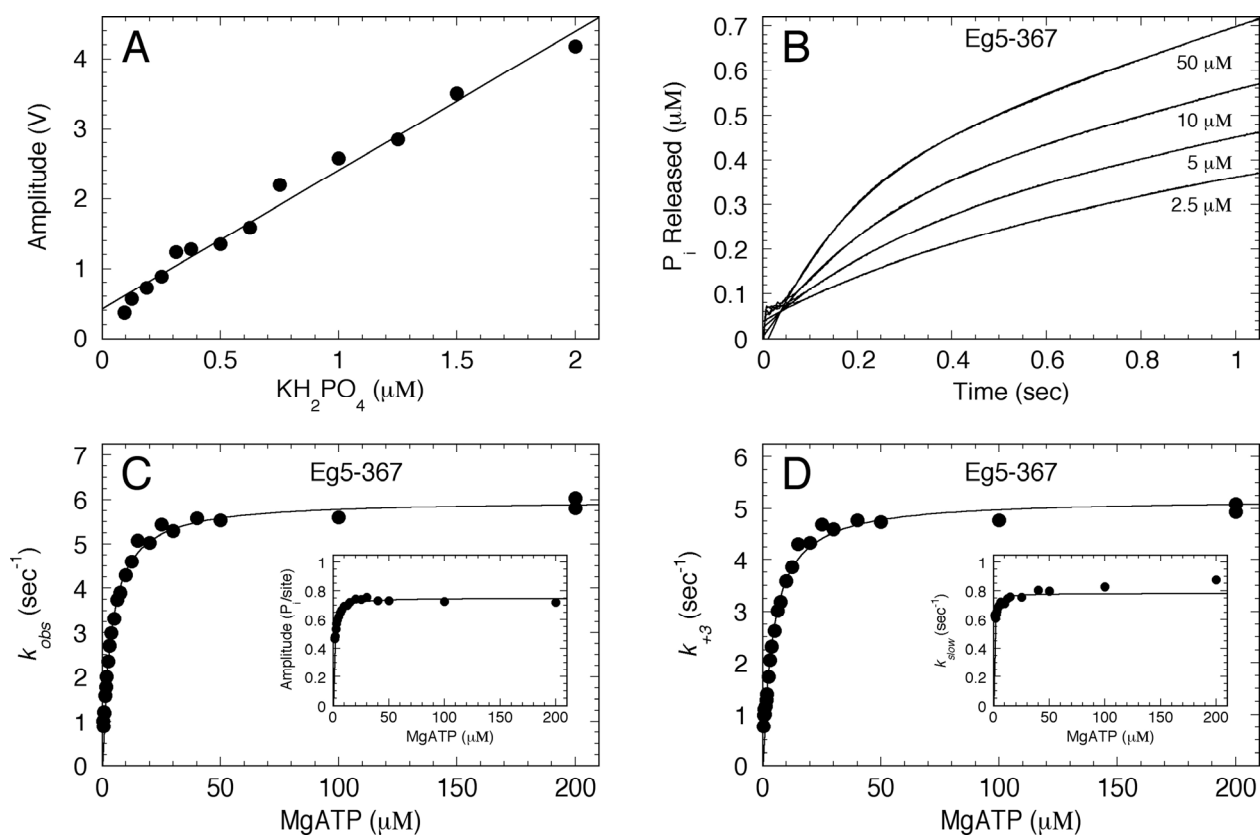


Figure 2.13 Presteady-state kinetics of P_i product release from the Mt•Eg5 complex

A preformed Mt•Eg5 complex and MDCC-PBP was rapidly mixed with increasing MgATP concentrations plus KCl, and the fluorescence enhancement of MDCC-PBP binding inorganic phosphate (P_i) was monitored in a stopped-flow instrument. Final concentrations: 0.5 μM Eg5, 1 μM tubulin, 20 μM Taxol, 5 μM MDCC-PBP, 0.05 U/ml PNPase, 75 μM MEG, 0.3125–200 μM MgATP, 100 mM KCl. **(A)** The calibration curve used to convert monitored fluorescence voltage to known phosphate concentration. **(B)** Representative stopped-flow transients of P_i product released from Mt•Eg5 are shown (MgATP concentrations are indicated). Each transient displayed burst kinetics, and was fit to [Equation 2.6](#). **(C)** The exponential rate of P_i product release was plotted *versus* MgATP concentration, and each data set was fit to a hyperbola: $k_{b,max} = 6.0 \pm 0.1 \text{ s}^{-1}$ and $K_{1/2,ATP} = 3.7 \pm 0.2 \mu\text{M}$. *Inset*, the amplitude of the rapid exponential phase was plotted as a function of MgATP concentration, and each data set was fit to a hyperbola: $A_{0,max} = 0.75 \pm 0.006 \text{ P}_i/\text{site}$ (100% of expected amplitude based on Eg5 site concentration) and $K_{1/2,ATP} = 0.94 \pm 0.05 \mu\text{M}$. **(D)** The rate of P_i product release (k_{+3}) determined by fitting the P_i release transients to [Equations 2.6–2.9](#) was plotted as a function of MgATP concentration: $k_{+3} = 5.2 \pm 0.1 \text{ s}^{-1}$ and $K_{1/2,ATP} = 4.4 \pm 0.3 \mu\text{M}$. *Inset*, the rate of the slow step after P_i release (k_{slow}) was plotted as a function of MgATP concentration: $k_{slow} = 0.78 \pm 0.01 \text{ s}^{-1}$ and $K_{1/2,ATP} = 0.39 \pm 0.07 \mu\text{M}$.

2.3.10 ATP-Promoted Dissociation of Mt•Eg5 Complexes

The preformed Mt•Eg5 complex was rapidly mixed in a stopped-flow instrument with increasing concentrations of MgATP plus 100 mM KCl (Figure 2.14). In this experimental design, the motor binds and hydrolyzes ATP followed by motor detachment, but the additional salt weakens the interaction of the motor with the microtubule upon re-binding; therefore, the kinetics of ATP-promoted dissociation can be measured. The insets of Figure 2.14 show representative stopped-flow transients corresponding to different MgATP concentrations. The transients show an initial lag due to the time required for ATP binding and ATP hydrolysis prior to dissociation. The dissociation kinetics show an ATP-concentration dependence with the maximum rate of Mt•Eg5 dissociation (k_{+3}) at approximately 8 s^{-1} for both motors. However, the $K_{1/2,ATP}$ was $1.9 \text{ }\mu\text{M}$ for Eg5-367 and $15 \text{ }\mu\text{M}$ for Eg5-437. These results suggest that dissociation is a relatively slow step in the pathway and coupled to phosphate release as observed for Kinesin-1 (122).

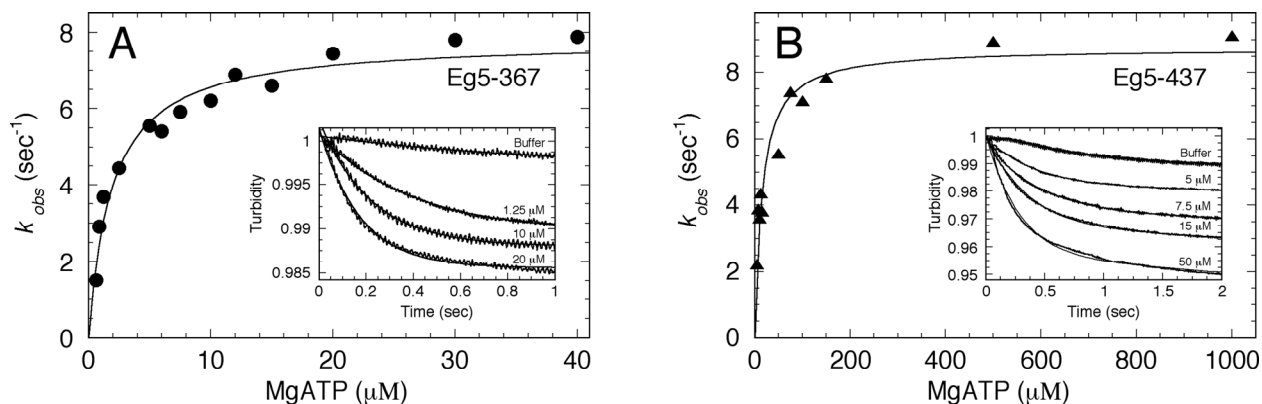


Figure 2.14 ATP-promoted dissociation of Mt•Eg5 complex

A preformed Mt•Eg5 complex was rapidly mixed in the stopped-flow instrument with varying concentrations of MgATP plus KCl. Final concentrations: $5 \text{ }\mu\text{M}$ Eg5, $4.9 \text{ }\mu\text{M}$ tubulin, $20 \text{ }\mu\text{M}$ Taxol, $0\text{-}1 \text{ mM}$ MgATP, 100 mM KCl. **(A)** The rate of the exponential phase of Mt•Eg5-367 dissociation was plotted as a function of MgATP concentration (\bullet). The data were fit to a hyperbola with the maximum rate of dissociation at $7.8 \pm 0.2 \text{ s}^{-1}$ and $K_{1/2,ATP} = 1.9 \pm 0.2 \text{ }\mu\text{M}$. **(B)** The rate of the exponential phase of Mt•Eg5-437 dissociation was plotted against MgATP concentration (\blacktriangle). The hyperbolic fit yielded a maximum rate of dissociation at $8.7 \pm 0.3 \text{ s}^{-1}$ with $K_{1/2,ATP} = 15.1 \pm 2.5 \text{ }\mu\text{M}$. **Insets**, representative stopped-flow transients are shown.

2.3.11 Eg5 Association with Microtubules

We measured the rate of formation of the Mt•Eg5 complex using a stopped-flow instrument to monitor changes in turbidity as the motor binds to the microtubule (Figure 2.15). The observed rate increased linearly with microtubule concentration, and the data revealed a significant difference in the apparent second-order rate constant for microtubule association ($K_{+5}k_{+6}$) for the two motors: Eg5-367, $K_{+5}k_{+6} = 11 \mu\text{M}^{-1}\text{s}^{-1}$ versus Eg5-437, $K_{+5}k_{+6} = 0.7 \mu\text{M}^{-1}\text{s}^{-1}$. The apparent association constant based on steady-state ATPase ($k_{cat}/K_{1/2,Mt}$) predicted the lower limit at $8 \mu\text{M}^{-1}\text{s}^{-1}$ and $0.6 \mu\text{M}^{-1}\text{s}^{-1}$ for Eg5-367 and Eg5-437, respectively. The apparent second-order rate constant for microtubule association is much lower than a diffusion-limited reaction, which suggests (at least) a two-step mechanism for microtubule binding by monomeric Eg5. The first step likely corresponds to the Mt•Eg5•ADP collision complex with the motor weakly bound, and the second step corresponds to an isomerization of the collision complex to tighten Eg5's affinity for the microtubule. The difference in the apparent second-order rate constant for microtubule association demonstrates that Eg5-367 binds much more effectively than Eg5-437, although at this time we do not know the structural and/or mechanistic reasons for this difference.

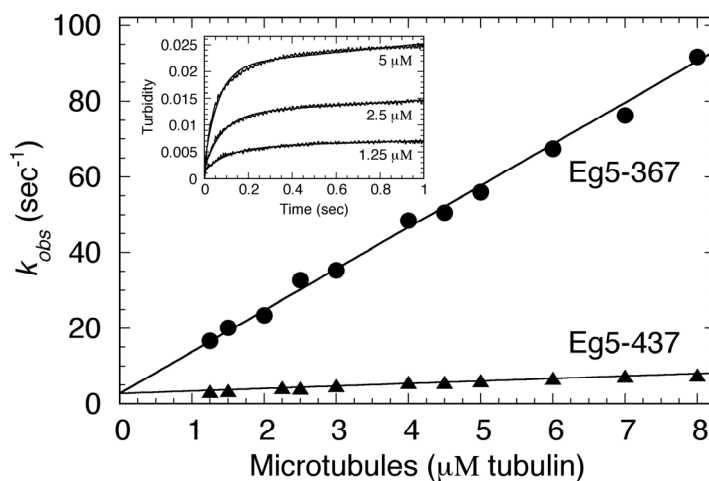


Figure 2.15 Kinetics of Eg5•ADP association with microtubules

The Eg5 motor was rapidly mixed in the stopped-flow instrument with increasing concentrations of Taxol-stabilized microtubules. Final concentrations: $1.25 \mu\text{M}$ Eg5 for $1.25\text{--}2.25 \mu\text{M}$ tubulin and $2.5 \mu\text{M}$ Eg5 for $2.5\text{--}8 \mu\text{M}$ tubulin, $20 \mu\text{M}$ Taxol. The rate constant obtained from the exponential phase of each transient (*inset*) was plotted as a function of microtubule concentration, and the data were fit to Equation 2.12. For Eg5-367 (●), the apparent second-order rate constant for microtubule association, $K_{+5}k_{+6} = 11.0 \pm 0.2 \mu\text{M}^{-1}\text{s}^{-1}$ with $k_{off,Mt} = 2.76 \pm 1.12 \text{ s}^{-1}$. For Eg5-437 (▲), $K_{+5}k_{+6} = 0.66 \pm 0.03 \mu\text{M}^{-1}\text{s}^{-1}$ and $k_{off,Mt} = 2.73 \pm 0.11 \text{ s}^{-1}$.

2.3.12 MantADP Release from the Mt•Eg5•mantADP Complex

Eg5 was incubated with mantADP to exchange ADP at the active site with mantADP. MantADP release from the Eg5 motor domain was activated by rapidly mixing in the stopped-flow instrument with microtubules plus 1 mM MgATP. The MgATP competes with and effectively prevents re-binding of mantADP to the active site once it is released. [Figure 2.16](#) shows the time dependence of the exponential decrease in fluorescence as a function of microtubule concentration, and the maximum rate of mantADP release for Eg5-367 was 43 s^{-1} and 34 s^{-1} for Eg5-437 ([Table 2.2](#)). The microtubule concentration required to produce half the maximal rate of mantADP release ($K_{1/2,Mt}$) was $2.5 \text{ }\mu\text{M}$ for Eg5-367 and $15 \text{ }\mu\text{M}$ for Eg5-437. This difference in half-maximal stimulation was consistent with the $K_{1/2,Mt}$ observed in the steady-state ATPase assays, indicating that Eg5-367 exhibits a tighter affinity for microtubules during ATP turnover. We propose that the isomerization of the Mt•Eg5•mantADP collision complex to tighten Eg5's affinity for the microtubule promotes the rapid release of ADP from the active site. Therefore, the kinetics of mantADP release are limited by the rate of the isomerization event. Movements of switch-1 residues are thought to disrupt the water-mediated coordination of the bound Mg^{2+} , which could result in loss of Mg^{2+} and ADP from the active site (92). A recent study suggests that a conformational change in the nucleotide-binding site via the switch-1 region occurs when kinesin-family motors bind to microtubules (194).

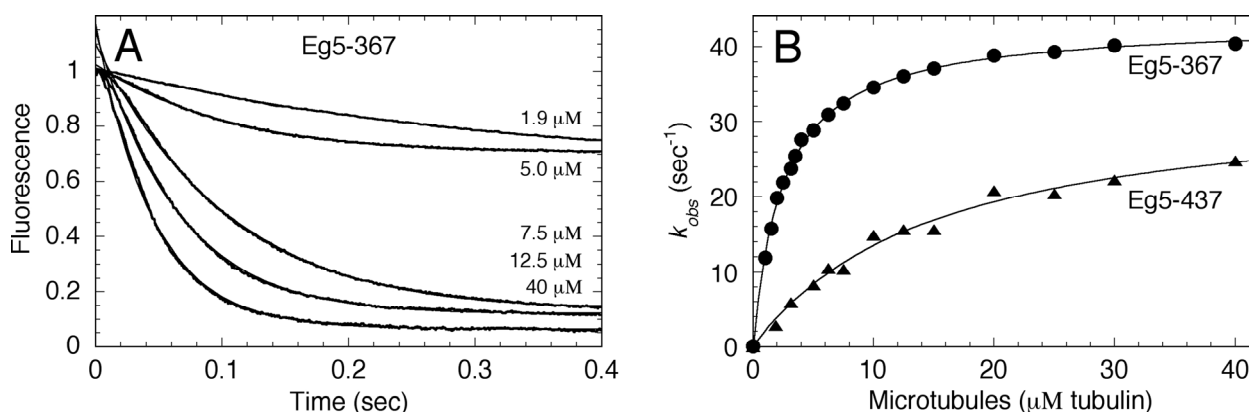


Figure 2.16 Microtubule-activated mantADP release

The Eg5•mantADP complex was rapidly mixed in the stopped-flow instrument with varying concentrations of microtubules plus MgATP. Final concentrations: 1 μM Eg5-2 μM mantADP for 1.9-4 μM tubulin and 2 μM Eg5-4 μM mantADP for 2-40 μM tubulin, 20 μM Taxol, and 1 mM MgATP. **(A)** Representative transients are shown for different microtubule concentrations, and each was fit to a single exponential function. **(B)** The rate of the exponential phase of each transient was plotted as a function of microtubule concentration, and the data were fit to a hyperbola. For Eg5-367 (\bullet), the maximum rate of mantADP release, $k_{+6} = 43.3 \pm 0.2 \text{ s}^{-1}$ with $K_{1/2, Mt} = 2.48 \pm 0.05 \mu\text{M}$ tubulin. For Eg5-437 (\blacktriangle), $k_{+6} = 34.2 \pm 1.6 \text{ s}^{-1}$ and $K_{1/2, Mt} = 15.2 \pm 1.6 \mu\text{M}$ tubulin.

Table 2.1 Physical Properties of Eg5 Motors

Protein	Polypeptide M_r^a	R_s^b	$s_{20,w}^c$	Calculated M_r^d	Association State
Eg5-367	42,119	2.86	ND	ND	Monomer
Eg5-437	50,217	3.37	3.49	48,229	Monomer
K401	45,531	4.79	5.06	91,902	Dimer

^a The monomer polypeptide with MgADP bound was determined from amino acid sequence and nucleotide molecular weight (Da). ^b R_s is the Stokes radius (nm) determined by analytical gel filtration. ^c $s_{20,w}$ is the sedimentation coefficient determined from sedimentation velocity experiments. ^d The molecular weight (Da) was calculated as described (195).

Table 2.2 Eg5 Comparison to Conventional Kinesin, Kar3, and Ncd Monomers

Constants		Eg5-367	Eg5-437	Kinesin (K341) ^a	Kar3 (MD) ^b	Ncd (MC6) ^c
MantATP Binding	$K_{+1}k_{+1}'$	$3.4 \pm 0.3 \mu\text{M}^{-1}\text{s}^{-1}$	$1.9 \pm 0.2 \mu\text{M}^{-1}\text{s}^{-1}$	$20 \pm 5 \mu\text{M}^{-1}\text{s}^{-1}$	$1.2 \pm 0.02 \mu\text{M}^{-1}\text{s}^{-1}$	$1.1 \pm 0.1 \mu\text{M}^{-1}\text{s}^{-1}$
	k_{+1}'	$21.2 \pm 1.3 \text{s}^{-1}$	$29.8 \pm 1.7 \text{s}^{-1}$	$565 \pm 50 \text{s}^{-1}$		
	$K_{d,\text{MantATP}}$	$4.4 \pm 1.1 \mu\text{M}$	$11.3 \pm 2.6 \mu\text{M}$	$23 \pm 10 \mu\text{M}$		
	$K_{\text{off},\text{MantATP}}$	$16.3 \pm 0.6 \text{s}^{-1}$	$6.9 \pm 0.7 \text{s}^{-1}$	$113 \pm 60 \text{s}^{-1}$	50s^{-1}	$6.9 \pm 7.3 \text{s}^{-1}$
ATP Binding	$k_{b,\text{max}}$	$22 \pm 3 \text{s}^{-1}$	$21 \pm 1 \text{s}^{-1}$		$498 \pm 76 \text{s}^{-1}$	
(Pulse-chase)	$K_{d,\text{ATP}}$	$26 \pm 15 \mu\text{M}$	$45 \pm 8 \mu\text{M}$	ND ^d	$83 \pm 33 \mu\text{M}$	ND
	$A_{0,\text{max}}$	0.75 ± 0.02 ADP/site	0.78 ± 0.05 ADP/site			
	$k_{b,\text{max}}$	$11.3 \pm 1.4 \text{s}^{-1}$	$14.9 \pm 0.5 \text{s}^{-1}$	$>300 \text{s}^{-1}$	$16.2 \pm 1.9 \text{s}^{-1}$	$11.0 \pm 2.3 \text{s}^{-1}$
ATP Hydrolysis (Acid-quench)	$K_{d,\text{ATP}}$	$31 \pm 15 \mu\text{M}$	$46 \pm 6 \mu\text{M}$			
	$A_{0,\text{max}}$	0.75 ± 0.02 ADP/site	0.78 ± 0.03 ADP/site			
	$k_{b,\text{max}}$	$6.0 \pm 0.1 \text{s}^{-1}$				
P _i Release (MDCC-PBP)	$K_{1/2,\text{ATP}}$	$3.7 \pm 0.2 \mu\text{M}$				
	$A_{0,\text{max}}$	0.75 ± 0.01 P _i /site				
	k_{+3}	$5.2 \pm 0.1 \text{s}^{-1}$	ND	ND	ND	ND
P _i Release (Modeling)	k_{slow}	$0.78 \pm 0.01 \text{s}^{-1}$				
	E_o	0.499 of 0.5 μM (100%)				
	$k_{b,\text{max}}$	$7.8 \pm 0.2 \text{s}^{-1}$	$8.7 \pm 0.3 \text{s}^{-1}$	$22.5 \pm 1.4 \text{s}^{-1}$	$6.7 \pm 0.1 \text{s}^{-1}$	$14.0 \pm 0.9 \text{s}^{-1}$
ATP-Promoted Dissociation ^e	$K_{1/2,\text{ATP}}$	$1.9 \pm 0.2 \mu\text{M}$	$15.1 \pm 2.5 \mu\text{M}$	$72 \pm 20 \mu\text{M}$	$5.7 \pm 0.3 \mu\text{M}$	$19.6 \pm 4.5 \mu\text{M}$
	$K_{+5}k_{+6}$	$11.0 \pm 0.2 \mu\text{M}^{-1}\text{s}^{-1}$	$0.66 \pm 0.3 \mu\text{M}^{-1}\text{s}^{-1}$	$10.8 \pm 1.4 \mu\text{M}^{-1}\text{s}^{-1}$	$0.5 \mu\text{M}^{-1}\text{s}^{-1}$	$0.8 \pm 0.1 \mu\text{M}^{-1}\text{s}^{-1}$
Microtubule Association ^e	k_{-5}	$2.8 \pm 1.1 \text{s}^{-1}$	$2.7 \pm 0.1 \text{s}^{-1}$		3s^{-1}	$3.6 \pm 0.6 \text{s}^{-1}$
	$k_{\text{off},\text{ADP}}$	$0.05 \pm 0.001 \text{s}^{-1}$	$0.003 \pm 0.001 \text{s}^{-1}$	$0.03 \pm 0.001 \text{s}^{-1}$	$0.03 \pm 0.001 \text{s}^{-1}$	$0.03 \pm 0.001 \text{s}^{-1}$
[α - ³² P]ADP Release (-Mts)	$k_{b,\text{max}}$	$43.3 \pm 0.2 \text{s}^{-1}$	$34.2 \pm 1.6 \text{s}^{-1}$	$303 \pm 22 \text{s}^{-1}$	$0.4 \pm 0.01 \text{s}^{-1}$	$3.9 \pm 0.4 \text{s}^{-1}$
	$K_{1/2,\text{ATP}}$	$2.5 \pm 0.1 \mu\text{M}$	$15.2 \pm 1.6 \mu\text{M}$	$15 \pm 3 \mu\text{M}$	$3.9 \pm 0.3 \mu\text{M}$	$28.0 \pm 5.7 \mu\text{M}$
	k_{cat}	$5.5 \pm 0.3 \text{s}^{-1}$	$2.9 \pm 0.1 \text{s}^{-1}$	$81 \pm 2 \text{s}^{-1}$	$0.49 \pm 0.02 \text{s}^{-1}$	$1.9 \pm 0.1 \text{s}^{-1}$
Mt-Activated ATPase	$K_{m,\text{ATP}}$	$9.5 \pm 0.4 \mu\text{M}$	$20.7 \pm 3.2 \mu\text{M}$	$91 \pm 10 \mu\text{M}$	$12.2 \pm 2.8 \mu\text{M}$	$27.8 \pm 10.9 \mu\text{M}$
	$K_{1/2,\text{Mt}}$	$0.71 \pm 0.15 \mu\text{M}$	$4.5 \pm 0.6 \mu\text{M}$	$3.2 \pm 0.1 \mu\text{M}$	$6.0 \pm 0.7 \mu\text{M}$	$9.6 \pm 3.9 \mu\text{M}$
	$K_{d,\text{Mt}}$	$0.046 \pm 0.019 \mu\text{M}$	$0.030 \pm 0.027 \mu\text{M}$	$0.22 \pm 0.06 \mu\text{M}$	$0.68 \pm 0.13 \mu\text{M}$	$0.20 \pm 0.06 \mu\text{M}$
Mt Equilibrium Binding	$K_{d,\text{ADP}}$	$117 \pm 86 \mu\text{M}$	$202 \pm 64 \mu\text{M}$	$99 \pm 20 \mu\text{M}$	$1.7 \pm 0.6 \mu\text{M}$	ND
ADP Equilibrium Binding						

^a Monomeric *Drosophila melanogaster* Kinesin-1/conventional kinesin, K341: (127, 177, 191, 196). ^b Monomeric *Saccharomyces cerevisiae* Kinesin-14/Kar3 motor domain (145). ^c Monomeric *Drosophila melanogaster* Kinesin-14/Ncd, MC6 (143). ^d ND, not determined. ^e Turbidity (122, 127). ^f MantADP competed with excess unlabeled MgATP.

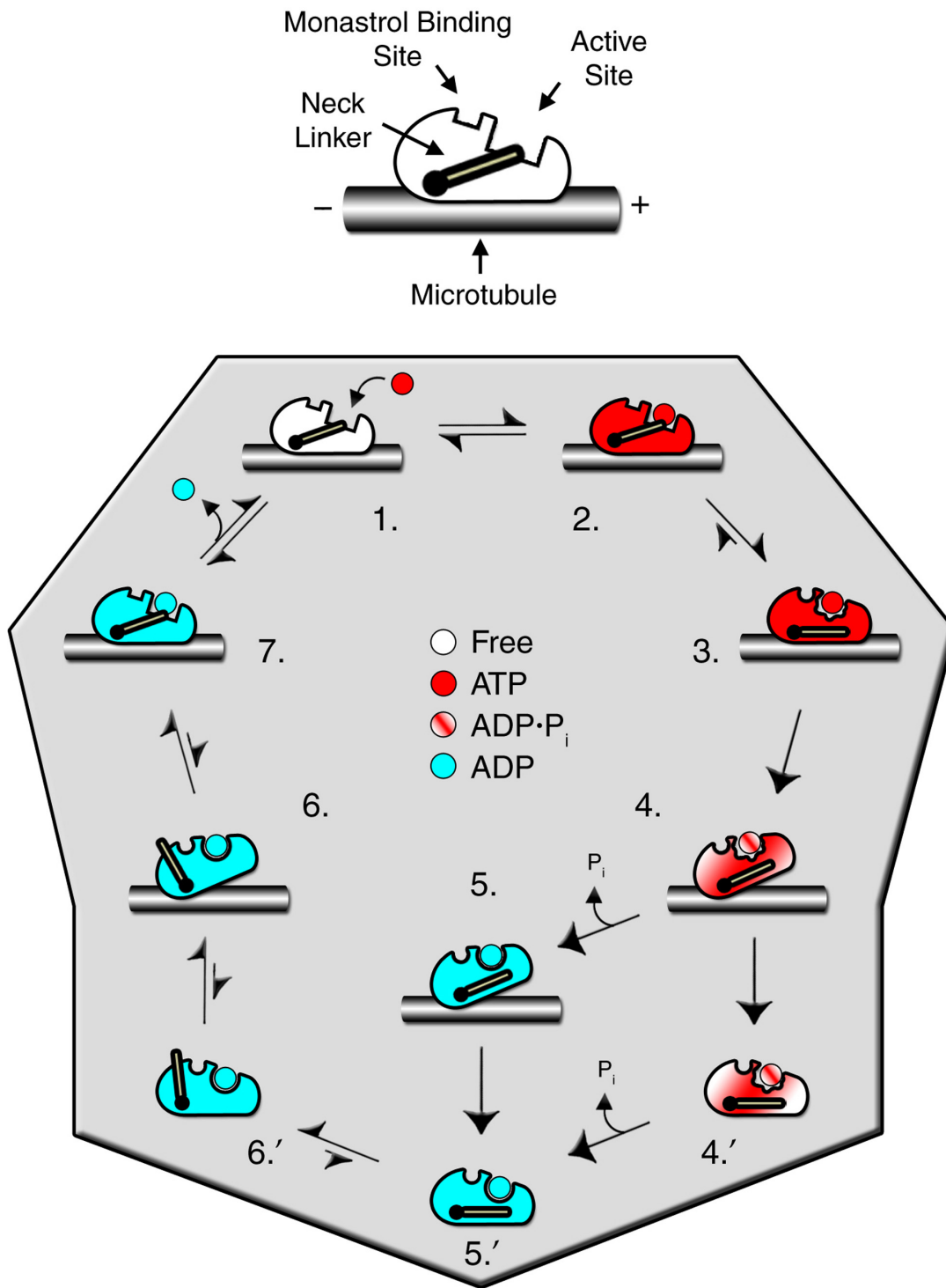


Figure 2.17 Model of Mt•Eg5 ATPase mechanism

This presentation of Mt•Eg5 ATPase cycle incorporates the specific kinetic steps in [Scheme 2.1](#) with proposed states on the microtubule. Red, Eg5•ATP; Blue, Eg5•ADP, Red-White-Striped, Mt•Eg5 intermediate after ATP hydrolysis. The neck-linker conformations along the ATPase pathway are inferred from previous studies (68, 69, 79, 100).

2.4 DISCUSSION

This study has provided a minimal ATPase mechanism of the human mitotic kinesin, Eg5 ([Figure 2.17](#)). Overall, the ATPase mechanism is unique among kinesin superfamily members, but is more similar to KinN kinesins, such as Kinesin-1/conventional kinesin, compared to the KinC spindle motors, Kinesin-14/Kar3/Ncd. Using various kinetic and thermodynamic approaches, we have defined the mechanochemical cycle of two truncated Eg5 motors, Eg5-367 and Eg5-437. Each motor shares many similarities in its mechanochemical cycle; however, there are several significant differences observed.

2.4.1 Similarities and Differences Between Two Eg5 Monomers

Both Eg5 motors have similar kinetics for ATP binding, ATP hydrolysis, ATP-promoted microtubule detachment, and ADP product release, though differences have been identified in steady-state kinetics and microtubule association kinetics. In the absence of microtubules, a difference in the rate of ATP turnover ($k_{off,ADP}$) was observed, suggesting a more open nucleotide pocket of Eg5-367 compared to Eg5-437. Also, in the presence of microtubules, a dramatic difference was discovered between the steady-state k_{cat} of Eg5-367 compared to Eg5-437. Even though ATP hydrolysis, P_i release, and ATP-promoted dissociation are relatively slow steps measured in this study, the k_{cat} of Eg5-367 (6 s^{-1}) is ~ 2 -fold faster than Eg5-437 (3 s^{-1}). This decreased k_{cat} could be a result of Eg5-437 dimerizing on the microtubule. Currently, we do not have additional evidence to support Eg5-437 being dimeric on the microtubule. The difference in microtubule association kinetics could not account for the difference in the measured k_{cat} , because under the steady-state conditions used in our ATPase assays ($40\text{ }\mu\text{M}$ tubulin), the observed rate of microtubule association would be approximately 28 s^{-1} for Eg5-437.

Another major kinetic difference between our two Eg5 motors was observed in microtubule association ($K_{+5}k_{+6} = 11\text{ }\mu\text{M}^{-1}\text{s}^{-1}$ for Eg5-367 *versus* $0.7\text{ }\mu\text{M}^{-1}\text{s}^{-1}$ for Eg5-437). The steady-state $K_{1/2,Mt}$ ([Figure 2.7](#)) as well as the mantADP release $K_{1/2,Mt}$ ([Figure 2.16](#)) support this kinetic difference. One possible interpretation is that the extended C-terminal α -helical sequence of Eg5-437 may result in interference at the microtubule-binding region either through

interaction with the catalytic core or the microtubule lattice. The crystal structure of Eg5 identified a unique neck-linker docking conformation perpendicular to the long edge of the motor domain when MgADP is bound (68). This perpendicular docking may position the α -helical segment that extends beyond the neck-linker in Eg5-437 near the microtubule-binding interface, thus weakening the binding of the Mt•Eg5•ADP collision complex.

2.4.2 Eg5 Compared to Kinesin, Ncd, and Kar3

Eg5 shares structural similarities in the motor domain with Kar3, Ncd, and conventional kinesin (68, 69, 72, 73, 83, 85), yet these proteins display differences in the coupling of the ATPase cycle to force generation (Table 2.2). Eg5 exhibits an ATPase mechanism that is more similar to conventional kinesin than the spindle motors, Kar3 and Ncd. Eg5 is similar to conventional kinesin based on its fast ADP product release, slow detachment from the microtubule, and fast microtubule association (Eg5-367). However, Eg5 also displays distinct differences. For Eg5, ATP binding was a two-step process, but there was no evidence of a rapid ATP off-rate as observed with kinesin that would result in partitioning of the Mt•Eg5•ATP intermediate. The $K_{d,ATP}$ was much tighter for Eg5 compared to conventional kinesin, again suggestive of a low ATP off-rate in the mechanism. The Eg5 burst amplitude and $K_{d,ATP}$ were similar for both the acid-quench and the pulse-chase experiments supporting this interpretation.

2.4.3 Mt•Eg5 ATPase Mechanism

We propose the minimal model shown in Figure 2.17, where motor binding to the microtubule results in rapid ADP release. ATP binding initiates a series of structural transitions that result in movement of the switch-2 cluster for neck-linker docking (68, 69), resulting in the Mt•Eg5*•ATP intermediate (Species 3) that proceeds directly to ATP hydrolysis. ATP hydrolysis results in a weak binding state (Species 4); however, we do not yet know the identity of this intermediate. Phosphate release may occur on the microtubule, followed by detachment as the Eg5•ADP intermediate as determined for conventional kinesin (138), or detachment may occur as the Eg5•ADP•P_i intermediate (k_{+3} , Scheme 2.1) as observed for Ncd (140, 144). A recent study has

provided additional information about the neck-linker conformations during the Eg5 ATPase cycle to understand its similarities to kinesin and its role in the mechanochemical cycle (100). The rapid microtubule association kinetics suggest that the Eg5 motor domain would immediately rebind once detached, thereby assuring that one motor domain of the dimer (or homotetramer) was always bound to the microtubule at any one time. This model acts as the conceptual framework for our future experiments.

3.0 CHAPTER THREE: MONASTROL INHIBITION OF THE MT•EG5 ATPASE MECHANISM³

We have used steady-state and presteady-state kinetics as well as equilibrium binding approaches to define the mechanistic basis for monastrol inhibition of monomeric human Eg5/KSP. In the absence of microtubules, the ATPase activity is inhibited through slowed product release. In the presence of microtubules, the ATPase activity is also reduced with weakened binding of Eg5 to microtubules during steady-state ATP turnover. Monastrol-treated Eg5 also shows a decreased relative affinity for microtubules under equilibrium conditions, which is dependent on nucleotide bound at the active site. The Mt•Eg5 presteady-state kinetics of ATP binding and the subsequent ATP-dependent isomerization are unaffected during the first ATP turnover. In the absence and presence of monastrol, the entire population of Mt•Eg5 complexes binds ATP tightly, but in the presence of monastrol only a fraction of the complexes hydrolyzes ATP during the first turnover. The steps of phosphate product release and ATP-promoted dissociation of the Mt•Eg5 complex are coupled in the mechanism, and the observed rate for each reaction significantly increased in the presence of monastrol. Monastrol promotes a dramatic decrease in the observed rate of Eg5 association with microtubules, and ADP release is slowed without trapping the Mt•Eg5•ADP intermediate. I propose monastrol stabilizes a “non-productive” subpopulation of Mt•Eg5 complexes that is incapable of undergoing the proper ATP-promoted conformational changes to rapidly reach the ATP hydrolysis-competent state. The aberrant interactions with the microtubule and the stabilization of the “non-productive” intermediate alter the ability of Eg5 to generate force, thereby yielding a motor that cannot participate in the establishment or maintenance of the bipolar spindle.

³ Reproduced in part with permission from 197. Cochran, J. C., Gatial, J. E., 3rd, Kapoor, T. M., and Gilbert, S. P. (2005) Monastrol inhibition of the mitotic kinesin Eg5, *J Biol Chem* 280, 12658-67. Copyright 2005 American Society for Biochemistry and Molecular Biology.

3.1 BACKGROUND AND SIGNIFICANCE

Accurate segregation of replicated chromosomes during cell division depends on the correct assembly and proper maintenance of the bipolar spindle (2, 12, 66, 149-160). Several members of the kinesin superfamily localize to the mitotic spindle and inhibition of one or more of these motors leads to drastic spindle abnormalities and loss of normal chromosome segregation (151, 198-200). Monastrol is a reversible, cell-permeable, small molecule that selectively inhibits the plus-end-directed Kinesin-5 family member, Eg5 (62, 69, 101, 102, 147), a microtubule-based motor protein that is required for the formation and maintenance of the bipolar spindle (56, 59-61). On the other hand, monastrol does not bind to or inhibit the ATPase activity of other well-studied kinesin superfamily members (102, 201). Monastrol treatment of dividing cells results in spindle collapse and cell cycle arrest with a monoastrol spindle, which is similar to the phenotype observed when Eg5 is inhibited by anti-Eg5 antibodies (56, 59, 62, 202) (Figure 1.12). Recently, several classes of Eg5 inhibitors with nanomolar affinity have been identified (103-107).

Previous studies with monastrol have revealed an induced-fit, allosteric binding site outside the nucleotide-binding pocket of the protein (69, 102, 105, 147). By comparing the monastrol-treated Eg5 crystal structure (Eg5_S•ADP)⁴ (69) to the Eg5•ADP structure (68), monastrol appears to induce dramatic conformational changes throughout the catalytic core including transformation of the loop L5, conversion of the switch-1 loop to a short α -helix, and the neck-linker/“switch-2 cluster” without considerably altering the structure of the β -sheet core and nucleotide-binding site (69). How these conformational changes alter the ATPase mechanism of Eg5 and disturb force generation by the Mt•Eg5 complex is not well understood. Monastrol has been shown to inhibit ADP release in the absence and presence of microtubules (102, 147, 197). Also, a recent study using motility assays suggests that monastrol produces an Eg5 state that is weakly bound to the microtubule, and does not appear to generate force (203).

In this study, we utilized kinetic and equilibrium approaches to define the mechanistic basis of Eg5 inhibition by *S*-monastrol, the more active enantiomer for inhibition [Figure 3.1B, inset; (69, 102, 147)]. We have evaluated two monomeric human Eg5 motors, Eg5-367 and

⁴ The abbreviations used are: Eg5_S, *S*-monastrol-treated Eg5; Eg5-367, human Eg5 motor containing N-terminal 367 residues followed by a C-terminal His₆-tag; Eg5-437, human Eg5 motor containing N-terminal 437 residues followed by a C-terminal His₆-tag; Mt, microtubule; AMPPNP, adenosine 5'-(β,γ -imino)triphosphate; AMPPCP, adenylyl (\square,\square -methylene)diphosphonate; mant, 2'(3')-*O*-(*N*-methylanthraniloyl); AXP, ATP or ADP.

Eg5-437 (69, 102, 147). The ATPase mechanism of both monomeric Eg5 motors has been well-characterized ([Chapter 2.0](#)), which provides a foundation to better understand the monastrol-dependent effect(s) on microtubule-based motility. The kinetics and equilibrium binding characteristics of Eg5_S presented here reveal an aberrant ATPase cycle, whereby monastrol stabilizes a “non-productive” subpopulation of Mt•Eg5 complexes and weakens Eg5’s affinity for the microtubule, which leads to rapid detachment of Eg5_S after ATP hydrolysis and inefficient re-binding to the microtubule lattice. The “non-productive” subpopulation corresponds to a Mt•Eg5_S^x•ATP intermediate that cannot undergo the proper ATP-promoted conformational changes to proceed forward toward ATP hydrolysis. In addition, our data are consistent with the microtubule-binding ability of the motor being compromised by monastrol binding. Taken together, monastrol promotes an ineffective Mt•Eg5_S complex that cannot generate the force required to establish and maintain the bipolar mitotic spindle for chromosome segregation.

3.2 MATERIALS AND METHODS

3.2.1 Experimental Conditions, *S*-Monastrol, and DMSO Control

Experiments were performed at 25 °C in ATPase buffer (20 mM Hepes, pH 7.2 with KOH, 5 mM magnesium acetate, 0.1 mM EDTA, 0.1 mM EGTA, 50 mM potassium acetate, 1 mM dithiothreitol, 5% sucrose). MgATP and MgADP concentrations were determined by absorbance at 259 nm using the extinction coefficient (ϵ) of 15,400 M⁻¹cm⁻¹. Previous studies have indicated that the *S*-enantiomer of monastrol was more active than either its *R* counterpart or the racemic mixture (69, 102, 147). We have confirmed these results ([Figure 3.1B, inset](#)) and have used the *S*-enantiomer in all experiments presented here (a generous gift from Merck Research Laboratories, West Point, PA). Our monastrol stock (100 mM) was prepared in dimethyl sulfoxide (DMSO analytical grade; Sigma-Aldrich Co., St. Louis, MO). For each experiment, a 1 mM monastrol stock was prepared by diluting the 100 mM stock to 1 mM in ATPase buffer (~1% DMSO). A DMSO control stock was also prepared by dilution of the same

volume of DMSO in ATPase buffer. In all control experiments shown, the concentration of DMSO is equivalent to the DMSO concentration at the corresponding monastrol concentration. All concentrations reported for experiments are final after mixing.

3.2.2 Protein Preparation

We have expressed and purified two human Eg5 motors (Eg5-367 and Eg5-437) as described in [Section 2.2.2](#). In several experiments reported in this chapter, we used Eg5-367 purified in the absence of nucleotide at the active site (apoEg5) (117, 204). The figure legends contain the detail for when apoEg5-367 protein was used in the experiment, and when conventionally purified Eg5-367 and Eg5-437 protein was used. A detailed explanation of the apoEg5 protein characterization can be found in [Chapter 4.0](#).

The modifications to the Eg5-367 purification protocol in [Section 2.2.2](#) are summarized. I did not attempt to purify Eg5-437 in the absence of nucleotide at the active site. In all column chromatography buffers, magnesium chloride and ATP were excluded. After Eg5 was eluted from the nickel-nitrilotriacetic acid agarose column (Qiagen, Valencia, CA), the enriched fractions were pooled and incubated with 5 mM EGTA and 5 mM EDTA for 30 min at 4 °C. Following the incubation, the mixture was loaded onto a 100-ml Bio-Gel P-6 size exclusion column (Bio-Rad Laboratories Inc.; exclusion limit 6000 Daltons) to remove chelating reagents and any residual nucleotide. The elution volume containing the excluded apoEg5 was concentrated by ultrafiltration and dialyzed against ATPase buffer. We determined the apoEg5 protein concentration by the Bio-Rad Protein Assay with IgG as the standard. This purification strategy yielded >99% pure apoEg5 protein with >95% basal and microtubule-activated ATPase activity under the same experimental conditions when compared to prior Eg5 purifications [[Figure 4.1](#), [Table 2.2](#), [Table 4.1](#)]. In addition, we performed pulse-chase, acid-quench, and P_i product release experiments with apoEg5 in the presence of microtubules, and observed a burst stoichiometry near unity [[Figure 4.8 \(B–D\)](#)], suggesting the entire population of apoEg5 enzyme binds and hydrolyzes ATP during the first ATP turnover. On the day of each experiment, an aliquot of purified bovine brain tubulin was thawed, cycled, and the microtubules were stabilized with 20 μM Taxol (paclitaxel, Sigma-Aldrich Co.) as described in [Section 2.2.5](#).

3.2.3 Steady-State ATPase Kinetics

The inhibition of Eg5 steady-state ATP turnover by monastrol was determined by monitoring [α - 32 P]ADP•P_i product formation in the absence and presence of microtubules [as described (178)]. In the absence of microtubules, Eg5 was treated with varying concentrations of monastrol for 30 min and reacted with [α - 32 P]MgATP. In [Figure 3.1A](#), the inhibition of the rate of the ATPase activity in the absence of microtubules was plotted as a function of monastrol concentration, and each data set was fit to the following quadratic equation,

Equation 3.1

$$Rate = -0.5 * \{(A_{inh} + K_{d,S} + [Mon]) - [(A_{inh} + K_{d,S} + [Mon])^2 - (4A_{inh}[Mon])]^{1/2}\} + k_{max}$$

where *Rate* is the amount of product formed per second per active site, A_{inh} is the amplitude of monastrol inhibition defined by k_{max} (k_{cat} at no monastrol) minus k_{min} (k_{cat} at saturating monastrol), $K_{d,S}$ is the apparent dissociation constant for S-monastrol, and [Mon] is the monastrol concentration.

In the presence of microtubules, Eg5 was treated with increasing concentrations of monastrol for 15 min, incubated with microtubules for 30 min, and then reacted with [α - 32 P]MgATP. [Figure 3.1B](#) shows the steady-state rate of ATP turnover as a function of monastrol concentration, and each data set was fit to [Equation 3.1](#). In [Figure 3.1 \(C and D\)](#), the rate of ATP turnover at constant monastrol and [α - 32 P]MgATP concentrations was plotted as a function of microtubule concentration for each Eg5 motor, and the data were fit to the following quadratic equation,

Equation 3.2

$$Rate = 0.5 * k_{cat} * \{(E_0 + K_{1/2,Mt} + [Mt]) - [(E_0 + K_{1/2,Mt} + [Mt])^2 - (4E_0[Mt])]^{1/2}\}$$

where *Rate* is the concentration of product formed per second per active site, k_{cat} is the maximum rate constant of product formation at saturating substrate, E_0 is the total Eg5 site concentration, $K_{1/2,Mt}$ is the microtubule concentration needed to provide one-half the maximal velocity, and [Mt] is the microtubule concentration. In [Figure 3.1 \(E and F\)](#), the rate of ATP turnover at

constant monastrol and microtubule concentrations was plotted as a function of $[\alpha\text{-}^{32}\text{P}]\text{MgATP}$ concentration for each Eg5 motor, and each data set was fit to the Michaelis-Menten equation (see [Equation 2.3](#)).

3.2.4 Mt•Eg5_s Cosedimentation Assays

In order to characterize Eg5 binding to microtubules at equilibrium in the presence of monastrol, we performed cosedimentation assays based on the pelleting of microtubules, and analyzing the Eg5 protein in both the supernatant fraction (unbound Eg5) and the pellet fraction (bound Eg5). Holding the Eg5 and monastrol concentration constant, and varying the concentration of microtubules, we are able to attain the upper limit of the dissociation constant for the microtubule ($K_{d,Mt}$) for each Eg5 motor. Equilibrium binding experiments were performed where Eg5 was treated in the absence and presence of monastrol for 15 min, followed by incubation with increasing microtubule concentrations for 30 min either in the absence of additional nucleotide ([Figure 3.2](#)) or in the presence of different nucleotide conditions ([Figure 3.3](#)) [as described (*140*)]. The Mt•Eg5 complexes were pelleted by centrifugation in a Beckman Airfuge (Beckman Coulter Inc., Fullerton, CA) at 30 psi (100,000 x g) for 30 min. Gel samples were prepared for the supernatant and pellet fractions at equal volumes for each microtubule concentration, and the proteins were resolved by SDS-PAGE and stained with Coomassie brilliant blue. In [Figure 3.2A](#), each data set was fit to the following quadratic equation,

Equation 3.3

$$\text{Mt}\cdot\text{E}/\text{E}_0 = 0.5 * \{(\text{E}_0 + K_{d,Mt} + [\text{Mt}]) - [(\text{E}_0 + K_{d,Mt} + [\text{Mt}])^2 - (4\text{E}_0[\text{Mt}])]^{1/2}\} / \text{E}_0$$

where $\text{Mt}\cdot\text{E}/\text{E}_0$ is the fraction of Eg5 partitioning with the microtubule pellet, E_0 is total Eg5 protein concentration, $K_{d,Mt}$ defines the upper limit for the equilibrium dissociation constant, and $[\text{Mt}]$ is the microtubule concentration.

3.2.5 Pulse-Chase Experiments

The presteady-state kinetics of MgATP binding was determined by pulse-chase methodologies using a KinTek RQF-3 chemical quench-flow instrument (KinTek Corp.) ([Figure 3.5](#)). The quench-flow instrument consists of three syringes controlled by a computerized motor to force the mixing of the Mt•Eg5_s complex with increasing [α -³²P]MgATP concentrations plus KCl, followed a chase solution (excess unlabeled MgATP) to allow time for any tightly bound radiolabeled MgATP to continue forward in the pathway. Whereas, any weakly bound or unbound MgATP substrate will be diluted by the unlabeled chase. The reaction was quenched with formic acid after a chase time sufficient for 8-10 turnovers. Radiolabeled product was separated from substrate by thin layer chromatography, and the concentration of product formed was plotted as a function of reaction time. We observed two phases in the kinetics of product formation: 1) a rapid exponential phase that corresponds to the product formed during the first turnover event, and 2) a slow linear phase that corresponds to subsequent ATP turnovers. From the exponential phase, we gain information about the observed presteady-state rate of MgATP binding, and the amplitude of the exponential, which is correlated to the concentration of Eg5 sites that report during the first ATP turnover. From the linear phase, we obtain an estimate of the rate of the slow step (downstream in the pathway from MgATP binding) that limits steady-state ATP turnover.

In the pulse-chase experiments, a preformed Mt•Eg5 complex \pm monastrol was rapidly mixed with increasing [α -³²P]MgATP concentrations plus KCl, and the reaction continued for various times (0.005–0.5 sec) followed by the non-radioactive MgATP chase (10 mM) for 3 sec (~10 half-lives) for control reactions and 14 sec for monastrol reactions. The additional KCl was added to the MgATP syringe to lower Eg5 steady-state ATPase activity without affecting the first ATP turnover ([Figure 2.12](#)). The concentration of [α -³²P]ADP product was plotted as function of time, and each pulse-chase transient was fit to the following burst equation ([Figure 3.5A](#)),

Equation 3.4

$$[\text{Product}]_{\text{obs}} = A_0 * [1 - \exp(-k_b t)] + k_{ss} t$$

where A_0 corresponds to the concentration of tightly-bound $\text{Mt}\cdot\text{Eg5}^*\cdot\text{ATP}$ complexes that proceed in the forward direction toward ATP hydrolysis, k_b is the rate constant of the exponential phase, and k_{ss} is the rate constant of the linear phase ($\mu\text{M ADP}\cdot\text{s}^{-1}$) defining steady-state ATP turnover. The exponential rate of the presteady-state burst (k_b) ([Figure 3.5C](#)) and burst amplitude (A_0) ([Figure 3.5E](#)) were plotted as a function of MgATP concentration, and each data set was fit to a hyperbola.

3.2.6 Acid-Quench Experiments

The presteady-state kinetics of ATP hydrolysis for the $\text{Mt}\cdot\text{Eg5}_S$ complex were defined in this assay. When the $\text{Mt}\cdot\text{Eg5}_S$ complex was rapidly mixed with MgATP plus KCl, we observed a burst of product formation at a rate faster than the rate of a subsequent step in the pathway that limits steady-state ATP turnover. In acid-quench experiments, the presteady-state burst is correlated to product formation at the Eg5 active site during the first ATP turnover event. After the reaction is quenched with formic acid, Eg5 denatures and the products can be quantified. The observed quantity of products includes the sum of the Eg5-bound products and the products free in solution at the time of the quench. Radiolabeled product was separated from unreacted substrate by thin layer chromatography, and the concentration of product formed was plotted as a function of reaction time. We observed two phases in the kinetics of product formation: 1) a rapid exponential phase that corresponds to the product formed during the first turnover event, and 2) a slow linear phase that corresponds to subsequent ATP turnovers. From the exponential phase, we gain information about the observed presteady-state rate of ATP hydrolysis, and the amplitude of the exponential, which is correlated to the concentration of Eg5 sites that report during the first ATP turnover. From the linear phase, we obtain an estimate of the rate of the slow step (downstream in the pathway from ATP hydrolysis) that limits steady-state ATP turnover.

The kinetics of ATP hydrolysis for Eg5 in the presence of monastrol were defined through a series of acid-quench experiments using a chemical quench-flow instrument (KinTek Corp.) ([Figures 3.5](#) and [3.6](#)). In all experiments, a preformed $\text{Mt}\cdot\text{Eg5}$ complex \pm monastrol was rapidly mixed with $[\alpha\text{-}^{32}\text{P}]\text{MgATP} \pm$ monastrol plus 100 mM KCl. The additional salt was added to the MgATP syringe to lower Eg5 steady-state ATPase activity without affecting the

kinetics of the first ATP turnover ([Figure 3.6F](#)). The reaction continued for various times (0.005–1 sec), was quenched with formic acid, and radiolabeled product formation was quantified [as described (*178*)]. The concentration of [α - 32 P]ADP was plotted as a function of time, and the data were fit to [Equation 3.4](#) where A_0 is the amplitude of the presteady-state burst phase that corresponds to formation of product at the Eg5 active site during the first turnover, k_b is the rate constant of the exponential burst phase, and k_{ss} is the rate constant of the linear phase ($\mu\text{M ADP}\cdot\text{s}^{-1}$) defining subsequent ATP turnovers. In [Figure 3.5 \(D and F\)](#) and [Figure 3.6 \(B and D\)](#), the exponential burst rate (k_b) and burst amplitude (A_0) were plotted as a function of monastrol and MgATP concentration, respectively, and each data set was fit to a hyperbola.

In order to understand the lowered burst amplitude observed in our acid-quench experiments in the presence of monastrol [[Figures 3.5F](#) and [3.6 \(B and D\)](#)], we designed a modified acid-quench experiment in order to test whether P_i product was released from Eg5, and then rapidly re-bound the active site to favor ATP re-synthesis. A preformed Mt•Eg5 complex \pm monastrol was rapidly mixed with either [α - 32 P]ATP or [γ - 32 P]ATP plus excess non-radioactive KH_2PO_4 (10 mM) and KCl (90 mM), and the reaction continued for various times (0.01–1 sec) followed by quenching with formic acid. The concentration of [α - 32 P]ADP or [γ - 32 P] P_i product was plotted as function of time, and each transient was fit to [Equation 3.4](#) ([Figure 3.7](#)). The experimental design assumes that [γ - 32 P] P_i product released from the Eg5 active site after ATP hydrolysis will be diluted by the excess non-radioactive P_i in solution, thus effectively preventing [γ - 32 P] P_i re-binding. Therefore, if [γ - 32 P] P_i product were released from the Eg5 active site and then rapidly re-bound to favor ATP re-synthesis in the presence of monastrol, we would expect to see full burst amplitude for [γ - 32 P]ATP reactions. However, if [γ - 32 P] P_i product remains at the active site to favor ATP re-synthesis, then we would expect to observe a similar amplitude compared to the [α - 32 P]ATP control reactions.

3.2.7 Modeling of Burst Kinetics

We used DynaFit software (BioKin Ltd., Pullman, WA) to model the acid-quench and P_i product release kinetics at 20, 150, and 400 μM MgATP (acid-quench) and 50 μM MgATP (P_i release) to the mechanisms proposed in [Scheme 3.1–3.4](#) (*205*). For our acid-quench transients, we modeled

the formation of ADP product, which represents $Mt \cdot Eg5 \cdot ADP \cdot P_i + Mt \cdot Eg5 \cdot ADP + Eg5 \cdot ADP + ADP$. Our P_i release transients were modeled based on the P_i product that was released from the nucleotide-binding site of Eg5. In [Figure 3.9 \(A and B\)](#), acid-quench and P_i release transients were simulated based on our proposed kinetic mechanism in the absence of monastrol ([Scheme 3.1](#)). In [Figure 3.9 \(C and D\)](#), the Eg5 site concentration was held constant based on the total Eg5 protein used in the reaction, and the rate constants for all steps in the mechanism were held constant during the simulation, except for the rate of ATP re-synthesis (k_{-2}) as indicated. [Figure 3.9E](#) was the simulation based on Schemes [3.2](#) and [3.3](#), and [Figure 3.9F](#) was the simulation based on [Scheme 3.4](#). The “rapid” and “slow” rates were allowed to float in the analysis.

The experimental design to measure P_i product release from the $Mt \cdot Eg5$ complex assumes that P_i released from Eg5 rapidly and tightly binds to MDCC-PBP, thus rendering the P_i release step irreversible. For a kinetic pathway including an irreversible reaction followed by a slow reaction ([Scheme 3.1](#)), the time dependence of product formation follows [Equation 3.4](#) where the rates and amplitude are defined by the following equations (179),

Equation 3.5

$$A_0 = E_0 * \{ [k_{+3} / (k_{+3} + k_{slow})]^2 \}$$

Equation 3.6

$$k_b = k_{+3} + k_{slow}$$

Equation 3.7

$$k_{ss} = E_0 * [k_{+3} k_{slow} / (k_{+3} + k_{slow})]$$

where k_{+3} is the exponential rate constant for the P_i release step, k_{slow} is the rate of the slow step in the pathway that occurs after P_i release, which limits the rate of subsequent ATP turnovers, and E_0 is the Eg5 site concentration. The data from [Figure 3.8 \(A and B\)](#) were modeled to [Equations 3.4–3.7](#) to define the P_i release constants k_{+3} , k_{slow} , and E_0 ([Scheme 3.1](#)). All variables k_{+3} , k_{slow} , and E_0 were all allowed to float in the analysis.

3.2.8 Stopped-Flow Experiments

The stopped-flow experiments were performed using a SF-2003 KinTek stopped-flow instrument (KinTek Corp.) to investigate the effect of monastrol on mantATP binding, P_i product release, ATP-promoted dissociation of the Mt•Eg5_S complex, Eg5_S association with the microtubule lattice, and mantADP release. Fluorescent nucleotides are valuable probes for the structure and kinetics of nucleotide-binding enzymes. Mant-adenosine nucleotides show an enhancement of fluorescence when bound to the active site of kinesin motor proteins (112, 122, 126, 127, 141-143, 180-182) as well as myosin motors (183-187), and this fluorescence is quenched in solution. When we rapidly mix the Mt•Eg5 complex with increasing mantATP concentrations in a stopped-flow instrument, then we can monitor the exponential increase in fluorescence that is a result of mantATP binding the Eg5 active site. For racemic mantAXP experiments, fluorescence emission at 450 nm was measured using a 400-nm cutoff filter with excitation at 360 nm (mercury arc lamp). In [Figure 3.4](#), the mantATP binding data in the absence or presence of monastrol were fit to the following hyperbola,

Equation 3.8

$$k_{obs} = k_{+1}' * [mATP] / (K_{d,mATP} + [mATP]) + k_{-1}'$$

where k_{obs} is the exponential rate constant obtained from the fluorescence enhancement, k_{+1}' is the rate constant for the ATP-dependent isomerization ([Scheme 3.1](#)), $K_{d,mATP}$ is the dissociation constant for weak mantATP binding, and k_{-1}' is the mantATP off-rate. The mantATP binding data at low mantATP concentrations ([Figure 3.4, inset](#)) were fit to the following linear function,

Equation 3.9

$$k_{obs} = K_{+1}k_{+1}' * [mATP] + k_{off,mATP}$$

where $K_{+1}k_{+1}'$ is the apparent second-order rate constant for mantATP binding, and $k_{off,mATP}$ represents the apparent off-rate for mantATP.

The kinetics of P_i product release from the Mt•Eg5 complex were measured using the MDCC-PBP coupled-assay (163). A preformed Mt•Eg5 complex ± monastrol plus MDCC-PBP

and “P_i mop” were rapidly mixed with increasing MgATP concentrations plus KCl and “P_i mop”. The concentrations of the “P_i mop” reagents were experimentally determined to eliminate competition with the MDCC-PBP for P_i in solution (138). The experimental design assumes that after ATP hydrolysis, P_i product will be released from the Eg5 active site, followed immediately by P_i binding rapidly and tightly to MDCC-PBP, thus triggering the fluorescence enhancement of the MDCC-PBP•P_i complex (163). In order to convert the observed change in fluorescence intensity into units of P_i concentration, a phosphate calibration curve was used (Figure 2.13A). The data in Figure 3.8 (A and B) and Figure 3.11C show a burst of P_i product release at a rate faster than the rate of a subsequent slow step, thus the data were fit to Equation 3.4, where A₀ equals the amplitude of the exponential burst phase and k_b is the observed exponential rate of P_i product release from Eg5. In Figure 3.8 (E and F), the P_i release kinetics were modeled in terms of a two-step irreversible mechanism described by Equations 3.4–3.7.

We can use the optical signal of turbidity (the optical property that causes light to be scattered rather than being transmitted in straight lines through the sample) to measure the kinetics of Mt•Eg5 dissociation or Eg5 association with the microtubule in the presence of monastrol. The size of a macromolecule (or macromolecular complex) affects the reading of turbidity; therefore, when Eg5 is bound to the microtubule, there is an increase in turbidity compared to the microtubule or Eg5 by themselves. These assays were designed based on the stopped-flow experiment that was performed to monitor the change in light scattering upon dissociation of the actomyosin complex (188). The Mt•Eg5_S dissociation kinetics (Figures 3.10 and 3.12) and the kinetics of Eg5_S association with microtubules (Figure 3.13) were determined by monitoring the change in solution turbidity at 340 nm using a stopped-flow instrument. In Figure 3.10 (C and D), the exponential rate and amplitude of Mt•Eg5 dissociation ± monastrol were plotted as a function of MgATP concentration, and each data set was fit to a hyperbola. The observed rate constant of Eg5_S association with microtubules was plotted as a function of monastrol concentration [Figure 3.13 (C and D)], and the data were fit to the following quadratic equation,

Equation 3.10

$$k_{obs} = -0.5 * \{ (A_{inh} + K_{d,S} + [\text{Mon}]) - [(A_{inh} + K_{d,S} + [\text{Mon}])^2 - (4A_{inh}[\text{Mon}])]^{1/2} \} + k_{max}$$

where k_{obs} is the observed exponential rate obtained from the change in turbidity, A_{inh} defines the amplitude of monastrol inhibition equal to k_{max} (k_{obs} with no monastrol) minus k_{min} (k_{obs} at saturating monastrol), $K_{d,S}$ is the apparent dissociation constant for monastrol, and $[Mon]$ is the monastrol concentration.

To measure the kinetics of ADP product release from the Mt•Eg5_S complex, we can preform the Eg5•mantADP complex, and rapidly mix this complex with microtubules plus an unlabeled MgATP chase. Thus, in this assay we are able to monitor the exponential decrease in fluorescence as mantADP is released from the Mt•Eg5•mantADP intermediate. MantADP release from the Mt•Eg5_S•mantADP complex was determined by pre-incubating Eg5 with mantADP at a 1:2 ratio (Eg5:mantADP) to exchange ADP for mantADP at the nucleotide pocket, followed by treatment with increasing concentrations of monastrol for 15 min. This reaction mixture was then rapidly mixed with microtubules plus MgATP (to effectively prevent mantADP re-binding), and the fluorescence emission at 450 nm was monitored ([Figure 3.14](#)). The observed rate and amplitude of mantADP release obtained from the fluorescence reduction were plotted as a function of monastrol concentration, and each data set was fit to [Equation 3.10](#).

3.2.9 Phosphocreatine Kinase-Coupled Assays

The experiments presented in [Figure 3.15](#) were performed [as described (*178*)] to determine the rate of ADP release from the Eg5_S•ADP complex and to characterize the equilibrium state of the Mt•Eg5_S•ADP complex. Briefly, Eg5•ADP was incubated with trace amounts of [α -³²P]ATP for 90 min to convert all radioactive ATP to ADP (see [Figure 2.6A](#)). The Eg5•[α -³²P]ADP complex was treated with monastrol for 30 min, followed by mixing with 2.5 mM non-radioactive MgATP plus a creatine kinase/phosphocreatine ATP regeneration system (\pm microtubules) to transfer P₁ to the [α -³²P]ADP free in solution. The experimental design assumes that ADP at the Eg5 active site is inaccessible to the creatine kinase and therefore is protected from enzymatic conversion to ATP. The tightly bound [α -³²P]ADP concentration was quantified as a function of time, and each data set was fit to the following exponential equation,

Equation 3.11

$$[\text{ADP}] = A_0 * \exp(-k_{\text{off,ADP}} t) + C$$

where the total Eg5 sites with ADP tightly bound [Eg5•ADP] is the sum of the amplitude (A_0) and the constant term (C) to extrapolate to zero time (t). The term $k_{\text{off,ADP}}$ is the first-order rate constant for ADP release.

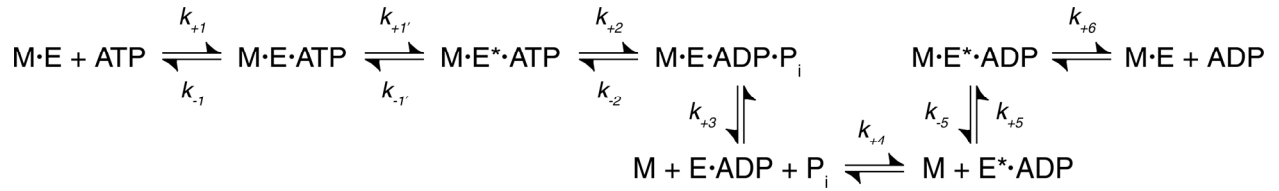
3.3 RESULTS

3.3.1 Monastrol Inhibits Steady-State ATPase \pm Microtubules

We began our mechanistic study of monastrol inhibition of two monomeric Eg5 motors (Eg5-367 and Eg5-437) by characterizing the ATPase activity of Eg5_s in the presence and absence of microtubules. In the absence of microtubules, the rate of ATP turnover decreased as a function of monastrol concentration (Eg5-367: 0.02 s⁻¹ to 0.001 s⁻¹; Eg5-437: 0.001 s⁻¹ to 0.0005 s⁻¹), and the apparent $K_{d,S}$ was approximately 2 μM for each motor ([Figure 3.1A](#), [Table 3.1](#)). These results confirm that monastrol inhibits the ATPase activity of Eg5-367 and Eg5-437 in the absence of microtubules as reported previously ([69](#), [102](#), [147](#)).

Microtubules stimulate the steady-state k_{cat} for both Eg5 monomers (see [Figure 2.7](#)). However, monastrol treatment results in a concentration-dependent decrease in the ATPase activity (Eg5-367: 5.3 s⁻¹ to 1.0 s⁻¹; Eg5-437: 3.7 s⁻¹ to 0.3 s⁻¹) ([Figure 3.1B](#)). The Eg5 motors also showed differences in the apparent $K_{d,S}$ in these experiments: Eg5-367 = 14 μM *versus* Eg5-437 = 4 μM . These steady-state kinetics are comparable to those reported from previous studies ([69](#), [102](#), [147](#), [201](#)) and suggest that microtubule binding weakens Eg5's affinity for monastrol. [Figure 3.1 \(C and D\)](#) shows steady-state kinetics as a function of microtubule concentration at saturating MgATP and monastrol for Eg5-367 and Eg5-437, respectively. Note that the $K_{1/2,Mt}$ was considerably increased (Eg5-367: Control = 0.7 μM , Monastrol = 6.7 μM ; Eg5-437: Control = 4.5 μM , Monastrol = 33.3 μM) indicating that monastrol causes monomeric Eg5 to bind microtubules more weakly during steady-state ATP turnover. Previous investigations reported

that monastrol was not competitive with microtubules (102, 147). Our data suggest a monastrol-dependent interference with Mt•Eg5 interaction based on the increased steady-state $K_{1/2, Mt}$ for both Eg5 monomers. [Figure 3.1 \(E and F\)](#) shows steady-state kinetics as a function of MgATP concentration at saturating microtubules and monastrol for Eg5-367 and Eg5-437, respectively. We observe similar $K_{m, ATP}$ values between control and monastrol experiments indicating that monastrol does not disrupt nucleotide binding during steady-state ATP turnover ([Table 3.1](#)).



Scheme 3.1

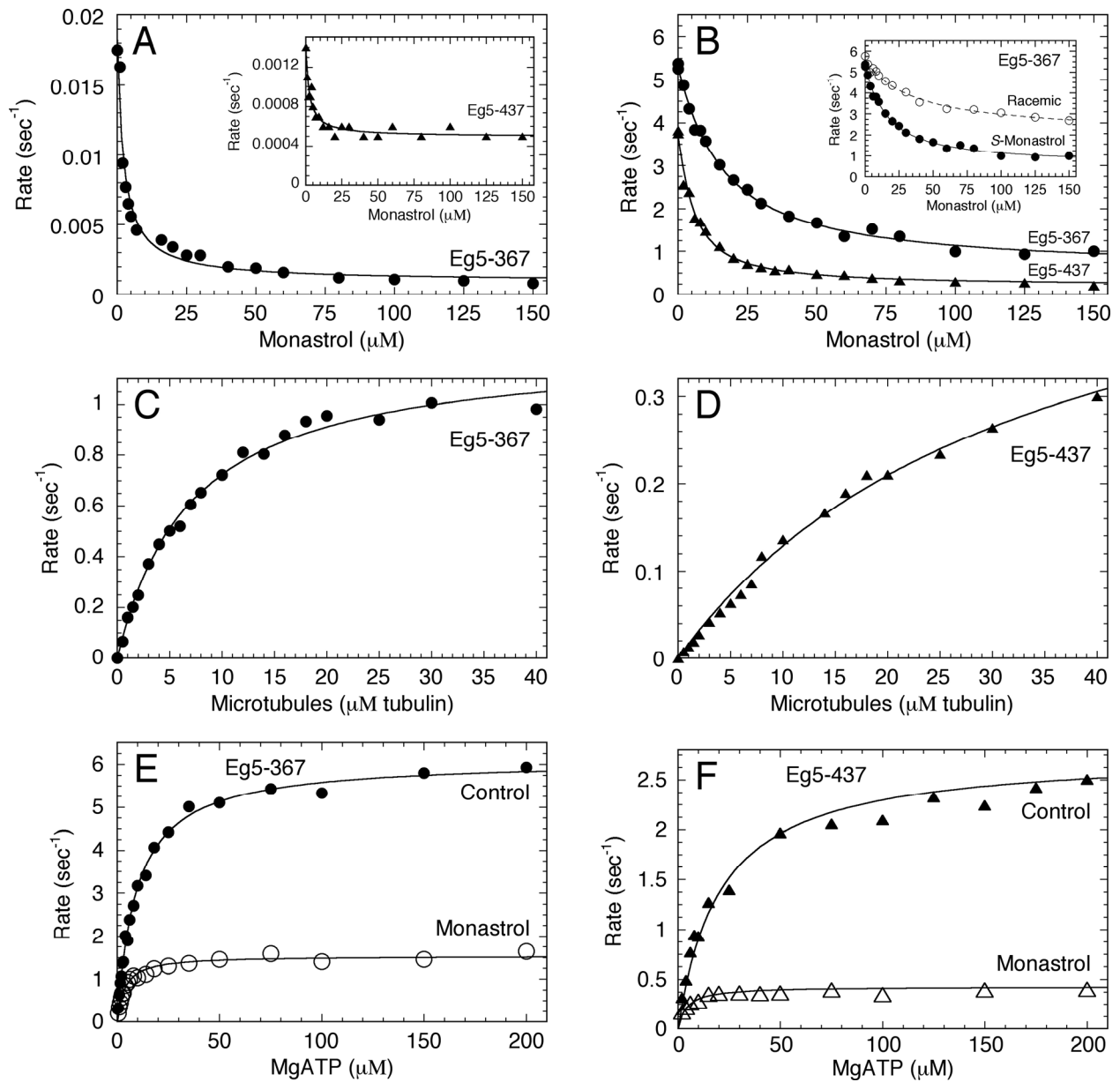


Figure 3.1 Monastrol inhibition of Eg5 steady-state ATPase

(A) In the absence of microtubules, Eg5•ADP was treated with varying concentrations of monastrol for 30 min and was reacted with MgATP. Final concentrations: 1 μ M Eg5, 0–150 μ M monastrol, 100 μ M [α - 32 P]MgATP. The rate of product formation was plotted as a function of monastrol concentration, and each data set was fit to [Equation 3.1](#). For Eg5-367 (●), $K_{d,S} = 2.3 \pm 0.4 \mu\text{M}$. *Inset*, Eg5-437 (▲), $K_{d,S} = 2.5 \pm 0.5 \mu\text{M}$. (B) Eg5•ADP was treated with varying concentrations of *S*-monastrol for 30 min, and then the Mt•Eg5_S complex was formed and reacted with MgATP. Final concentrations: 1 μ M Eg5, 30 μ M tubulin, 20 μ M Taxol, 0–150 μ M monastrol, 1 mM [α - 32 P]MgATP. For Eg5-367 (●), $K_{d,S} = 13.8 \pm 1.0 \mu\text{M}$, and for Eg5-437 (▲), $K_{d,S} = 4.0 \pm 0.4 \mu\text{M}$. *Inset*, Eg5•ADP was treated with varying concentrations of either *S*-monastrol or racemic monastrol for 30 min, and then the Mt•Eg5 complex was formed and reacted with MgATP. Final concentrations: 1 μ M Eg5-367, 30 μ M tubulin, 20 μ M Taxol, 0–150 μ M monastrol, 1 mM [α - 32 P]MgATP. For *S*-monastrol, (●), $K_{d,S} = 13.8 \pm 1.0 \mu\text{M}$, and for racemic monastrol (○), $K_{d,r} = 30.0 \pm 4.6 \mu\text{M}$. (C) Eg5-367 was treated with monastrol for 30 min, and then the Mt•Eg5_S complex was formed with increasing microtubule concentrations and reacted with MgATP. Final concentrations: 1 μ M Eg5, 0–40 μ M tubulin, 20 μ M Taxol, 150 μ M monastrol, 500 μ M [α - 32 P]MgATP. Data were fit to [Equation 3.2](#), and the steady-state parameters were $k_{cat} = 1.22 \pm 0.03 \text{ s}^{-1}$ and $K_{1/2,Mt} = 6.7 \pm 0.4 \mu\text{M}$. (D) Eg5-437 under similar conditions as Panel C: $k_{cat} = 0.56 \pm 0.03 \text{ s}^{-1}$ and $K_{1/2,Mt} = 33.3 \pm 3.3 \mu\text{M}$. (E) Eg5-367 (\pm monastrol) was incubated for 30 min, and then the Mt•Eg5_S complex was formed and reacted with increasing MgATP concentrations. Final concentrations: 0.1 μ M Eg5, 20 μ M tubulin, 20 μ M Taxol, \pm 150 μ M monastrol, 0.5–200 μ M [α - 32 P]MgATP. Data were fit to the Michaelis-Menten equation ([Equation 2.3](#)), and the steady-state parameters were determined. Control: $k_{cat} = 6.10 \pm 0.07 \text{ s}^{-1}$ and $K_{m,ATP} = 9.5 \pm 0.4 \mu\text{M}$; Monastrol: $k_{cat} = 1.54 \pm 0.03 \text{ s}^{-1}$ and $K_{m,ATP} = 3.6 \pm 0.3 \mu\text{M}$. (F) Eg5-437 under similar conditions as Panel C. Control: $k_{cat} = 2.77 \pm 0.08 \text{ s}^{-1}$ and $K_{m,ATP} = 20.7 \pm 3.2 \mu\text{M}$; Monastrol: $k_{cat} = 0.43 \pm 0.01 \text{ s}^{-1}$ and $K_{m,ATP} = 4.1 \pm 0.7 \mu\text{M}$.

3.3.2 Monastrol Weakens Eg5 Affinity for Microtubules under Equilibrium Conditions

Microtubule equilibrium binding assays were performed to determine the relative affinity of Eg5_S for microtubules in the absence of additional nucleotide or in the presence of different nucleotide/analog conditions. In [Figure 3.2A](#), Eg5 was treated in the absence or presence of monastrol and then incubated with increasing microtubule concentrations. Each Eg5 motor was found to partition with the microtubule pellet as a function of microtubule concentration, yet the $K_{d,Mt}$ was significantly different in the presence of monastrol (Control: $K_{d,Mt} = 0.07 \mu\text{M}$; Monastrol: $K_{d,Mt} = 2.3 \mu\text{M}$). These data reveal that under equilibrium conditions, the affinity of Eg5 for microtubules was weakened in the presence of monastrol. This effect was monastrol-concentration dependent as shown in [Figure 3.2B](#). Together, the increased steady-state $K_{1/2,Mt}$ and the increased $K_{d,Mt}$ provide evidence for an altered microtubule-binding ability of Eg5 by monastrol.

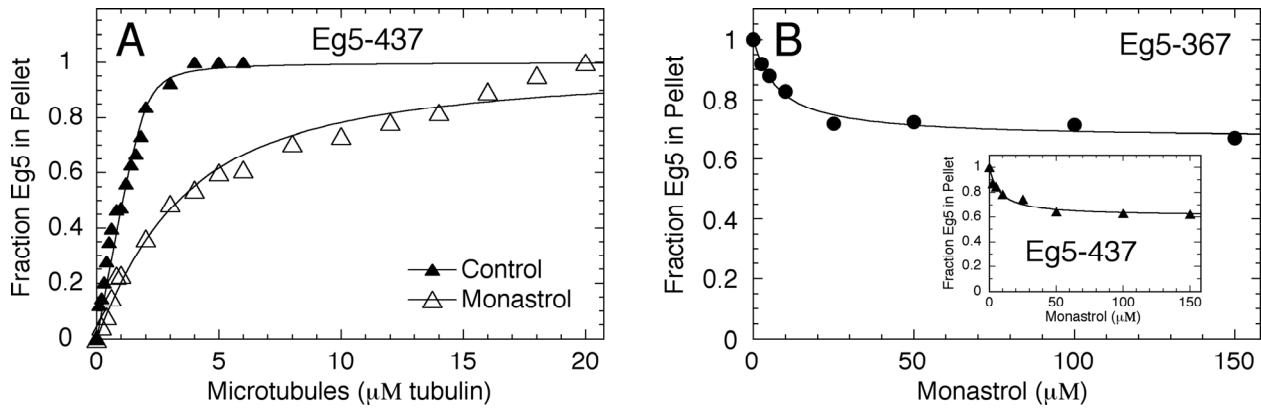


Figure 3.2 Mt•Eg5_S cosedimentation experiments

(A) In the absence of additional nucleotide, Eg5•ADP was treated with or without monastrol for 15 min, followed by incubation with increasing concentrations of microtubules for 30 min. Final concentrations: 2 μM Eg5-437, 0–6 μM tubulin for control reactions, 0–20 μM tubulin for monastrol reactions, 20 μM Taxol, ± 150 μM monastrol. The fraction of Eg5 in the microtubule pellet was plotted as a function of the total microtubule concentration, and the data were fit to [Equation 3.3](#). In the absence of monastrol (▲), the $K_{d,Mt} = 0.07 \pm 0.03$ μM, and in the presence of monastrol (△), $K_{d,Mt} = 2.3 \pm 0.2$ μM. (B) Eg5•ADP was treated with increasing monastrol concentrations for 15 min, followed by incubation with microtubules for 30 min. Final concentrations: 2 μM Eg5, 4 μM tubulin, 20 μM Taxol, 0–150 μM monastrol. The fraction of Eg5 in the microtubule pellet was plotted as a function of monastrol concentration, and each data set was fit to [Equation 3.1](#).

We also sought to investigate the microtubule-binding behavior of the Eg5_S complex under different nucleotide conditions ([Figure 3.3](#)). In the absence of monastrol, Eg5 partitions with the microtubules at each nucleotide condition as expected for a monomeric kinesin. However, with the addition of monastrol, some Eg5_S appears to partition with the supernatant in the absence of additional nucleotide, consistent with the data presented in [Figure 3.2](#). Interestingly, with 2 mM MgATP or MgADP, the Eg5_S motor exhibits enhanced partitioning with the supernatant, suggesting a weak-binding state for Eg5_S with MgADP at the active site in the presence of monastrol. In the reaction containing MgATP, we do not know the proportion unreacted MgATP *versus* MgADP+P_i products; therefore, it is difficult to conclude what nucleotide species contributes to the partitioning effect. On the other hand, with excess MgAMPPNP (a non-hydrolyzable ATP analog), all Eg5_S partitions with the microtubule pellet, indicating a strong-binding state regardless of monastrol treatment.

Mt•Eg5 cosedimentation assays were performed to determine the microtubule-binding behavior of the apoEg5_S complex under nucleotide-free conditions. In [Figure 3.3B](#), apoEg5 was found to partition with the microtubules in the absence and presence of monastrol. However,

Eg5•ADP (1:1) began to partition with the supernatant in the presence of monastrol, consistent with [Figure 3.3A](#). These cosedimentation experiments were repeated at lower concentrations of the Mt•Eg5 complex (0.5 μ M Eg5, 1 μ M tubulin), and similar results were obtained. Therefore, these cosedimentation results suggest that all apoEg5 protein in the absence of nucleotide was bound to the microtubule in the absence and presence of monastrol.

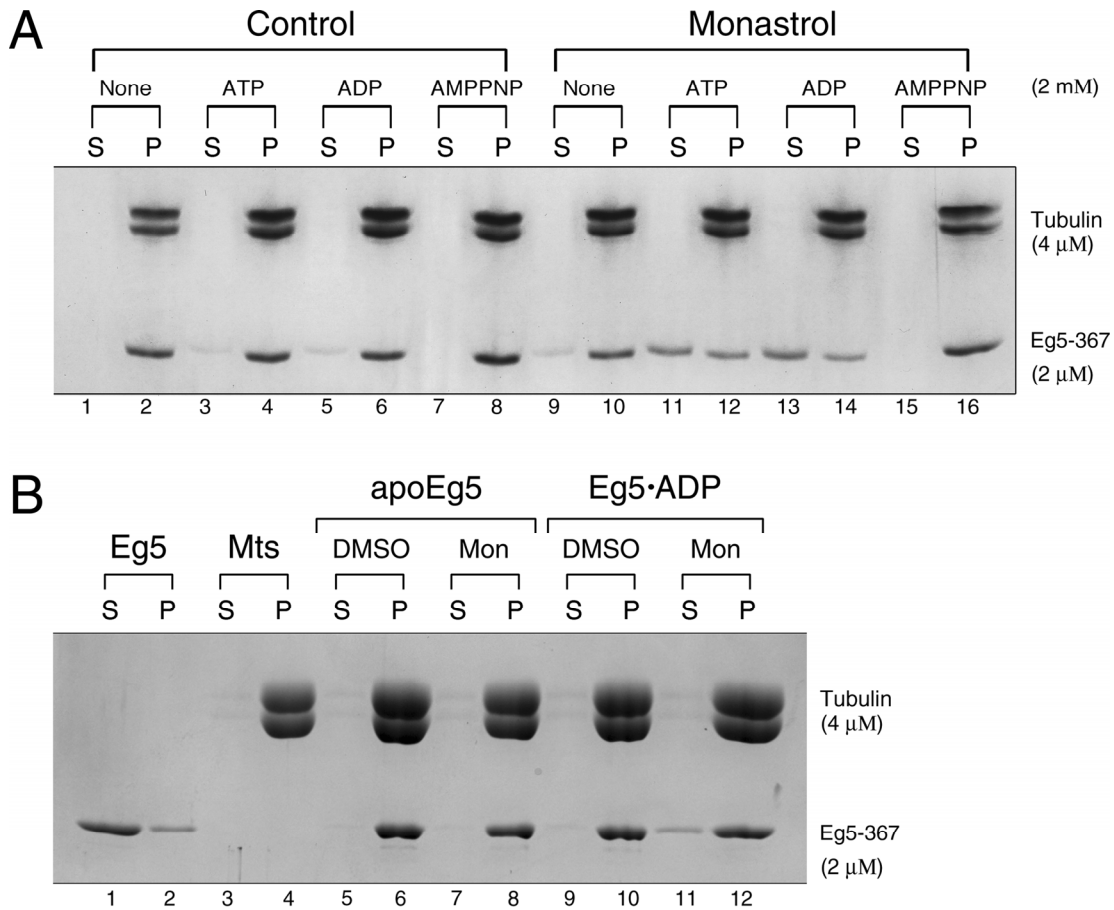


Figure 3.3 Mt•Eg5 interactions \pm monastrol under different nucleotide conditions

(A) Coomassie blue-stained SDS gel from Mt•Eg5₅ cosedimentation experiments at different nucleotide conditions. Eg5 was treated with or without monastrol for 15 min, followed by incubation with microtubules for 30 min. Each nucleotide was rapidly mixed with the solution at the end of the incubation, and the reaction mixture was immediately subjected to centrifugation. Final concentrations: 2 μ M Eg5-367, 4 μ M tubulin, 20 μ M Taxol; 150 μ M monastrol, 2 mM AXP. The supernatant (S) and pellet (P) for each reaction were loaded consecutively with an indication of the additional nucleotide above each supernatant/pellet pair. **(B)** Coomassie blue-stained SDS polyacrylamide gel from a Mt•Eg5 cosedimentation experiment in the absence of nucleotide. ApoEg5 and Eg5•ADP (1:1) were treated in the absence or presence of monastrol, then reacted with microtubules. Final concentrations: 2 μ M apoEg5, \pm 2 μ M MgADP, 4 μ M tubulin, 20 μ M Taxol; \pm 150 μ M monastrol. After each reaction mixture was centrifuged, samples of the supernatant (S) and pellet (P) were loaded consecutively with an indication of the reaction conditions above each supernatant/pellet pair.

3.3.3 Monastrol Does Not Alter the Kinetics of ATP Binding to Mt•Eg5 Complex

The model of the Eg5•ADP crystal structure indicates that monastrol binds approximately 12 Å from the active site (69, 79). Previous studies (102, 147) and data from [Figure 3.1 \(E and F\)](#) suggest that monastrol binding was not competitive with respect to MgATP during steady-state ATP turnover. To determine whether the presteady-state steps of ATP binding to the Mt•Eg5_S complex were altered, we performed mantATP binding and pulse-chase experiments. For the mantATP binding experiments, we used a stopped-flow instrument to rapidly mix a preformed Mt•Eg5_S complex with mantATP and monitor the exponential increase in fluorescence that corresponds to mantATP binding to the Eg5 active site ([Figure 3.4A](#)). In one experiment, we held the mantATP concentration at 10 μM and varied monastrol concentration ([Figure 3.4A, insets](#)). For both Eg5-367 and Eg5-437, the observed rate of mantATP binding did not change as we increased the monastrol concentration. The amplitude of the exponential phase at each monastrol concentration was slightly decreased, which can be interpreted as either a decrease in the population of Eg5_S bound to microtubules at increasing monastrol concentrations, or a reduction in the quantum yield from the mant-fluorophore due to monastrol altering the local environment of the Eg5 active site.

In another mantATP binding experiment, we held the monastrol concentration constant and varied mantATP concentration ([Figure 3.4B](#)). The data were superimposable, which indicates that the apparent second-order rate constant for mantATP binding ($K_{+1}k_{+1}$), the off-rate for mantATP from the collision complex (k_{off}), and the rate constant for the ATP-dependent isomerization step before ATP hydrolysis (k_{+1}) were unaffected by monastrol treatment ([Scheme 3.1, Table 3.1](#)).

In order to measure the presteady-state kinetics of the formation of a tightly-bound Mt•Eg5*•ATP intermediate in the absence and presence of monastrol, we performed pulse-chase experiments using a chemical quench-flow instrument. The experimental design assumes any tightly-bound [α -³²P]MgATP substrate will proceed in the forward reaction, while any loosely-bound or unbound substrate will be diluted by the excess non-radioactive MgATP in the chase

(179). [Figure 3.5 \(A, C, and E\)](#) shows that the rate of the exponential burst phase increases with increasing $[\alpha\text{-}^{32}\text{P}]\text{MgATP}$ concentration, and the maximum observed rate of MgATP binding was 22.0 s^{-1} for control experiments and 18.2 s^{-1} for monastrol. In addition, the burst amplitude was similar (Control = 0.75 ADP/site ; Monastrol = 0.78 ADP/site ; [Figure 3.5E](#)), indicating that the entire Mt•Eg5 population bound MgATP tightly in the absence or presence of monastrol. Taken together, these results suggest that monastrol binding to Eg5 does not inhibit the kinetics of ATP binding. Binding of monastrol to the Mt•Eg5 complex was confirmed by our acid-quench experiments presented next.

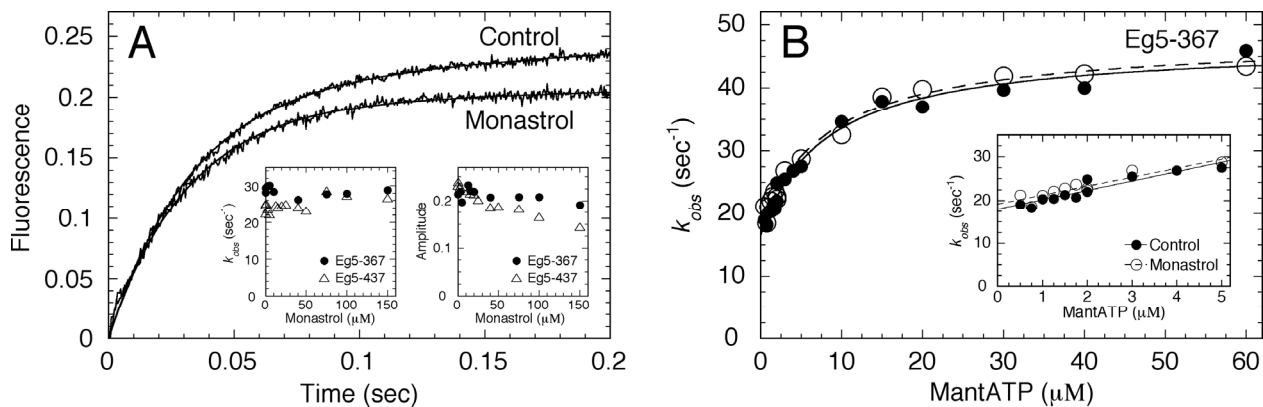


Figure 3.4 MantATP binding to the Mt•Eg5_s complex

(A) Eg5 was treated with increasing concentrations of monastrol, followed by incubation with microtubules for 30 min. Final concentrations: $3\text{ }\mu\text{M}$ Eg5, $10\text{ }\mu\text{M}$ tubulin, $20\text{ }\mu\text{M}$ Taxol, $0\text{--}150\text{ }\mu\text{M}$ monastrol, $10\text{ }\mu\text{M}$ mantATP. The preformed Mt•Eg5_s complex was rapidly mixed in a stopped-flow instrument with mantATP and two representative transients for Eg5-367 ($\pm 150\text{ }\mu\text{M}$ monastrol) are shown. *Insets*, the observed rate and amplitude of the exponential increase in fluorescence were plotted as a function of monastrol concentration. (B) Eg5-367 was incubated in the presence or absence of monastrol, and the preformed Mt•Eg5 complexes were reacted with increasing mantATP concentrations. Final concentrations: $0.5\text{ }\mu\text{M}$ Eg5 for $0.5\text{--}3\text{ }\mu\text{M}$ mantATP and $3\text{ }\mu\text{M}$ Eg5 for $3\text{--}60\text{ }\mu\text{M}$ mantATP, $10\text{ }\mu\text{M}$ tubulin, $20\text{ }\mu\text{M}$ Taxol, $150\text{ }\mu\text{M}$ monastrol. The observed rate of the fast exponential increase in fluorescence was plotted as a function of mantATP concentration, and the data were fit to [Equation 3.8](#). In the absence of monastrol (\bullet), $k_{+1'} = 30.5 \pm 1.3\text{ s}^{-1}$, $K_{d,\text{mantATP}} = 7.9 \pm 1.6\text{ }\mu\text{M}$, $k_{-1'} = 16.5 \pm 1.0\text{ s}^{-1}$. In the presence of monastrol (\circ), $k_{+1'} = 30.0 \pm 1.1\text{ s}^{-1}$, $K_{d,\text{mantATP}} = 8.3 \pm 1.6\text{ }\mu\text{M}$, $k_{-1'} = 17.8 \pm 0.8\text{ s}^{-1}$. *Inset*, the observed rate of mantATP binding at the lowest mantATP concentrations. The data were fit to [Equation 3.9](#) to yield the apparent second-order rate constant for mantATP binding in the absence ($K_{+1}k_{+1'} = 2.2 \pm 0.3\text{ }\mu\text{M}^{-1}\text{s}^{-1}$) and in the presence of monastrol ($K_{+1}k_{+1'} = 2.1 \pm 0.3\text{ }\mu\text{M}^{-1}\text{s}^{-1}$).

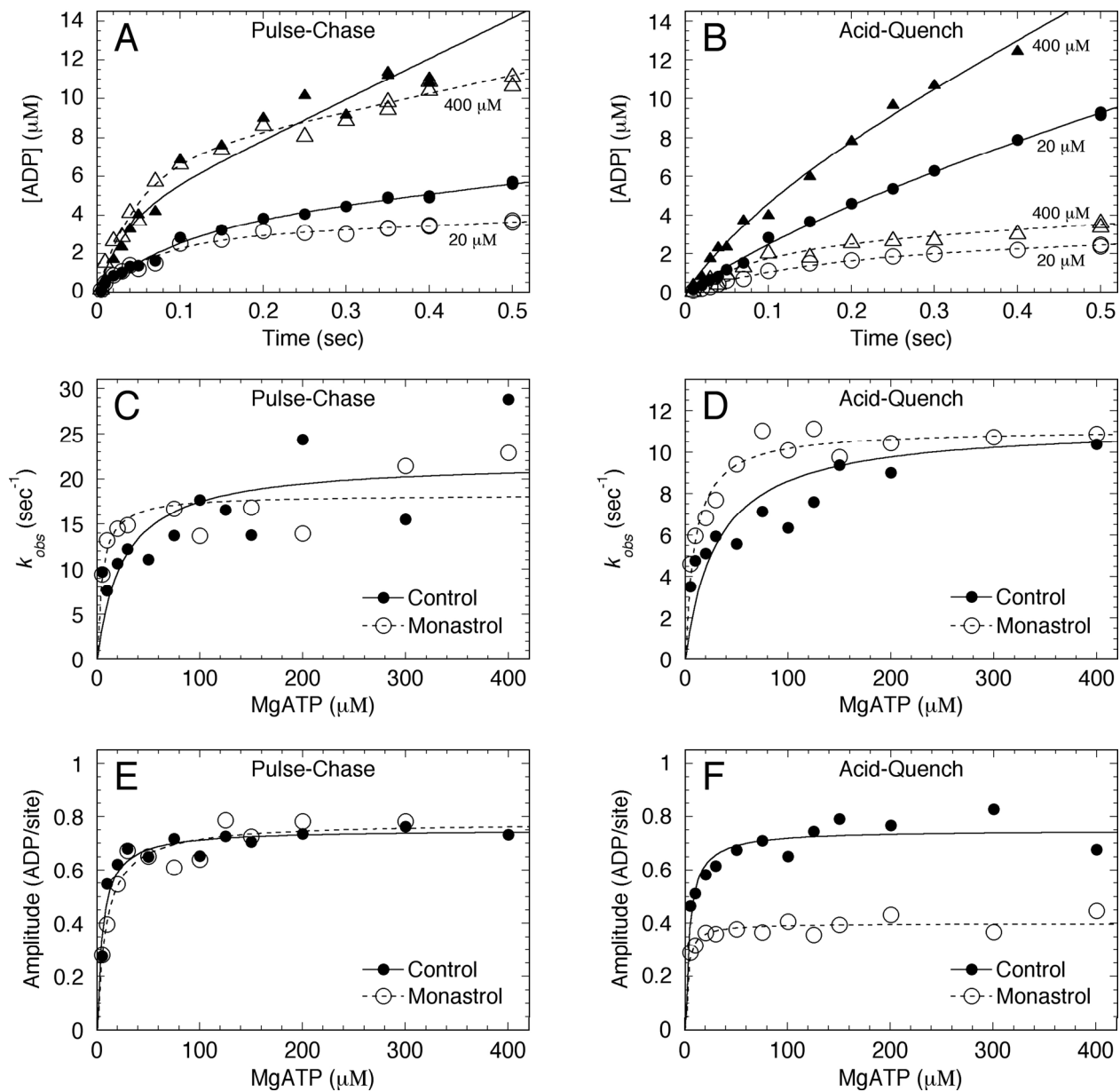


Figure 3.5 Pulse-chase and acid-quench kinetics for Mt•Eg5-367 \pm monastrol

For pulse-chase experiments, Mt•Eg5 ± monastrol was reacted with increasing concentrations of [α - 32 P]MgATP for 0.005–0.5 sec in a chemical quench-flow instrument, followed by the non-radioactive MgATP chase for 3 sec for control reactions or 14 sec for monastrol reactions (~10 half-lives). Final concentrations: 5 μ M apoEg5, 6 μ M tubulin, 20 μ M Taxol, \pm 150 μ M monastrol, 5–400 μ M [α - 32 P]MgATP, 100 mM KCl, 10 mM unlabeled MgATP chase. For acid-quench experiments, Mt•Eg5 ± monastrol was reacted with increasing [α - 32 P]MgATP concentrations for 0.005–1 sec, followed by quenching with formic acid. Final concentrations: 5 μ M apoEg5, 6 μ M tubulin, 20 μ M Taxol, \pm 150 μ M monastrol, 5–400 μ M [α - 32 P]MgATP, 100 mM KCl. Shown in Panels (A and B) are time courses of [α - 32 P]MgADP product formation for pulse-chase and acid-quench experiments, respectively, in the absence (● and ▲) and presence (○ and Δ) of monastrol (MgATP concentrations are indicated). Each transient displayed burst kinetics and was fit to Equation 3.4 to provide the amplitude (A_o) and observed exponential rate (k_b) of the formation of a tight Mt•Eg5*•ATP complex (pulse-chase) or the formation of the Mt•Eg5•ADP•P_i complex (acid-quench), followed by the linear steady-state ATP turnover (k_{ss}). Shown in Panels (C and D) are the maximum observed rates from the pulse-chase and acid-quench experiments, respectively, plotted against MgATP concentration in the absence (●) and presence (○) of monastrol. Each data set was fit to a hyperbola. For pulse-chase, Control: $k_{b,max} = 22.0 \pm 3.0 \text{ s}^{-1}$ with $K_{d,ATP} = 25.8 \pm 14.9 \text{ }\mu\text{M}$; Monastrol: $k_{b,max} = 18.2 \pm 1.3 \text{ s}^{-1}$ with $K_{d,ATP} = 5.0 \pm 2.5 \text{ }\mu\text{M}$. For acid-quench, Control: $k_{b,max} = 11.3 \pm 1.4 \text{ s}^{-1}$ with $K_{d,ATP} = 31.3 \pm 15.4 \text{ }\mu\text{M}$; Monastrol: $k_{b,max} = 11.1 \pm 0.3 \text{ s}^{-1}$ with $K_{d,ATP} = 9.2 \pm 1.5 \text{ }\mu\text{M}$. Panels (E and F) show the amplitude of the exponential phase *versus* MgATP concentration for pulse-chase and acid-quench experiments, respectively. Each data set was fit to a hyperbola. For pulse-chase, Control: $A_{o,max} = 0.75 \pm 0.02 \text{ ADP/site}$ (100% of expected amplitude based on Eg5 site concentration) with $K_{d,ATP} = 5.5 \pm 1.0 \text{ }\mu\text{M}$; Monastrol: $A_{o,max} = 0.78 \pm 0.03 \text{ ADP/site}$ (100% of expected amplitude) with $K_{d,ATP} = 8.9 \pm 1.8 \text{ }\mu\text{M}$. For acid-quench, Control: $A_{o,max} = 0.75 \pm 0.02 \text{ ADP/site}$ (99% of expected amplitude) with $K_{d,ATP} = 4.2 \pm 1.0 \text{ }\mu\text{M}$; Monastrol: $A_{o,max} = 0.40 \pm 0.01 \text{ ADP/site}$ (41% of expected amplitude) with $K_{d,ATP} = 2.2 \pm 0.6 \text{ }\mu\text{M}$.

3.3.4 Monastrol Promotes Reduction in Burst Amplitude during Acid-Quench

Experiments

We measured the kinetics of ATP hydrolysis in the presence of monastrol by performing a series of acid-quench experiments [Figure 3.5 (B, D, and F) and Figure 3.6]. We have demonstrated that ATP binding is at least a two-step process for Eg5-367 and Eg5-437, with an isomerization event yielding a short-lived Mt•Eg5*•ATP intermediate that proceeds directly to ATP hydrolysis (Scheme 3.1). Again, the mantATP binding kinetics (Figure 3.4) and pulse-chase kinetics (Figure 3.5) showed that monastrol does not affect the two ATP binding steps which occur prior to ATP hydrolysis. To determine if monastrol affects the ATP hydrolysis step, we used a chemical quench-flow instrument to rapidly mix a preformed Mt•Eg5_s complex with MgATP, and radiolabeled product formation was quantified as a function of time.

We carried out acid-quench experiments as a function of [α - 32 P]MgATP concentration in the absence and presence of monastrol. The initial burst of product formation correlates to the formation of [α - 32 P]ADP•P_i at the active site of Eg5 during the first ATP turnover, followed by a slower linear phase, which corresponds to subsequent ATP turnovers. The additional KCl with

the MgATP syringe was included to lower the rate of the linear phase to allow better definition of the exponential burst phase. We have demonstrated that the additional salt does not alter the kinetics of ATP hydrolysis by Eg5 in the absence [Figure 2.12 (A and B)] or presence of monastrol (Figure 3.6F). Figure 3.5D shows that the observed exponential rate of ATP hydrolysis increased as a function of MgATP concentration, with a maximum observed rate of 11.3 s^{-1} in the absence of monastrol and 11.1 s^{-1} in the presence of monastrol. This observed rate of ATP hydrolysis was slower than the maximum rate determined for Eg5-437 = 14.9 s^{-1} (Figure 2.12F). The magnitude of the burst amplitude increased as a function of MgATP concentration as well (Figure 3.5F), yet the maximum amplitude was dramatically different in the presence of monastrol (Control: $A_{0,max} = 0.75 \text{ ADP/site}$; Monastrol: $A_{0,max} = 0.40 \text{ ADP/site}$). For control reactions, these results suggest the entire Mt•Eg5 population hydrolyzes ATP during the first turnover event. In the presence of monastrol, the lowered burst amplitude may possibly be due to reversals at the ATP hydrolysis step during the first turnover, or it may be due to a “non-productive” subpopulation of Mt•Eg5 complexes that cannot properly bind and hydrolyze ATP during the first ATP turnover.

In Figure 3.6 (A and B), we held the Mt•Eg5 complex and MgATP concentration constant and varied monastrol concentration. The exponential burst rate increased as a function of monastrol concentration (10 s^{-1} to 50 s^{-1}), however, the burst amplitude decreased (0.77 ADP/site to 0.23 ADP/site). In Figure 3.6 (C and D), we held the Mt•Eg5 complex and monastrol concentration constant and varied MgATP concentration. This experiment was designed to yield the maximum observed burst rate of ATP hydrolysis in the presence of saturating monastrol ($k_{b,max} = 36.3 \text{ s}^{-1}$). This increased rate suggests that monastrol lowers the activation energy barrier for chemistry to occur, thus leading to a significantly faster rate of the ATP hydrolysis step. This increase in the rate of ATP hydrolysis was not observed for Eg5-367, which seems to indicate that the kinetics of ATP hydrolysis were slightly different between the two constructs. When this result is taken together with the difference in the efficiency to bind microtubules (Figure 2.15), and the observation of monastrol disrupting the microtubule binding behavior of Eg5, perhaps we can hypothesize that the microtubule typically slows down ATP hydrolysis when Eg5 is more tightly bound the microtubule (in the absence of monastrol), but when Eg5 is weakly bound (in the presence of monastrol), the hydrolysis reaction occurs at a faster rate. Therefore, in the presence of monastrol, the difference in the rate of ATP hydrolysis

between Eg5-367 and Eg5-437 arises from a difference in the microtubule-binding behavior of the motors.

Again, we observed a decrease in the maximum burst amplitude (0.29 ADP/site) for Eg5-437. Several hypotheses could explain the decrease in burst amplitude: 1) inactive Eg5 enzyme (disfavored due to full burst amplitude for control experiments), 2) weakened ATP binding (disfavored based on steady-state $K_{m,ATP}$ and the mantATP binding kinetics), 3) monastrol-promoted partitioning of Eg5_S off the microtubule prior to ATP binding, 4) monastrol-promoted dissociation of either the Mt•Eg5•ATP collision complex, or the Mt•Eg5*•ATP complex prior to ATP hydrolysis, 5) reversals at the ATP hydrolysis step, and/or 6) a “non-productive” subpopulation of Mt•Eg5_S complexes that cannot undergo the ATP-promoted structural transitions to generate the ATP hydrolysis-competent intermediate.

At the same Mt•Eg5_S conditions used in the acid-quench experiments presented in [Figure 3.6 \(A–D\)](#), our cosedimentation data from [Figure 3.2](#) indicate that 66 % of the Eg5-437 motor population remains tightly bound to the microtubule. Assuming the lower burst amplitude corresponds to a decreased population of Eg5_S motors bound to the microtubules (Hypothesis #3 above), we reasoned that increasing the microtubule concentration would “rescue” the burst amplitude to near full amplitude (~0.78 ADP/site) by driving the equilibrium to have all Eg5_S bound to the microtubule. We performed acid-quench experiments as a function of microtubule concentration at constant MgATP and monastrol concentrations. [Figure 3.6E](#) shows the ATP hydrolysis kinetics at increasing microtubule concentrations for Eg5-437. Even though these data show a modest increase in burst amplitude (from 0.29 to 0.40 ADP/site), the amplitude does not reach 0.78 ADP/site as seen in the absence of monastrol. In addition, the experiment in [Figure 3.6F](#) provides evidence that the additional salt in the ATP syringe used to lower the steady-state phase does not affect the first ATP turnover. Therefore, the lower burst amplitude cannot be totally explained by Eg5_S•ADP partitioning off the microtubule (disfavoring Hypothesis #3). Alternatively, the results obtained from our acid-quench experiments are consistent with either monastrol-promoted dissociation of the Mt•Eg5*•ATP complex before ATP hydrolysis (Hypothesis #4), reversals in the chemical reaction, whereby the Mt•Eg5_S•ADP•P_i intermediate reforms ATP at the active site at a rate defined by k_{-2} (Hypothesis #5), or a “non-productive” subpopulation of Mt•Eg5 complexes that do not properly bind and

hydrolyze ATP during the first ATP turnover (Hypothesis #6). Experiments to directly test the Hypothesis #5 (intermediate O^{18} exchange) have not yet been performed in our laboratory.

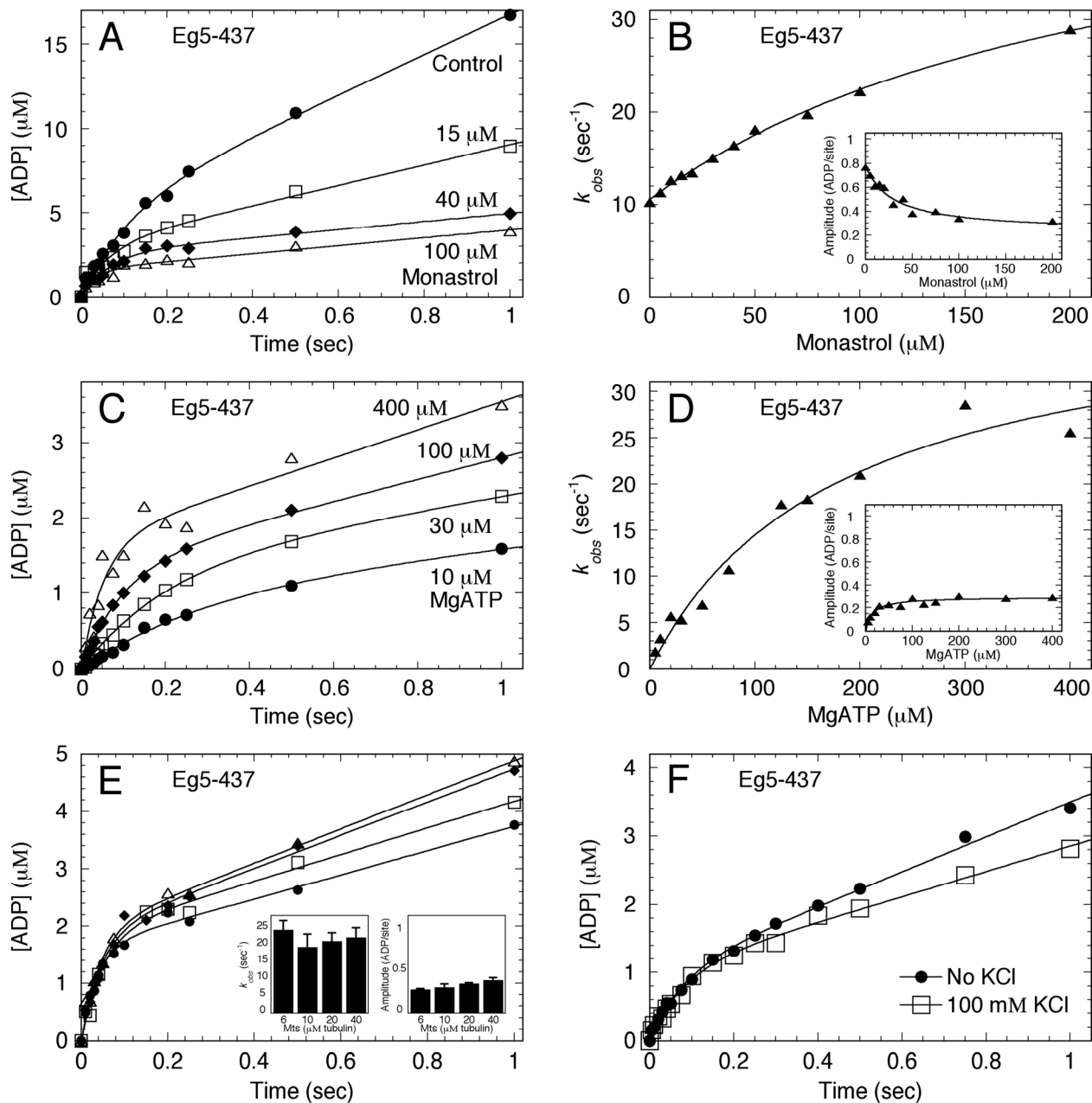


Figure 3.6 ATP hydrolysis kinetics for the Mt•Eg5-437 complex \pm monastrol

(A) Time course of $[\alpha\text{-}^{32}\text{P}]\text{ADP}\cdot\text{P}_i$ formation after rapidly mixing a preformed Mt•Eg5_S complex with MgATP plus additional KCl to lower steady-state turnover (see [Materials and Methods 3.2.5](#)). Final concentrations: 5 μM Eg5-437, 6 μM tubulin, 20 μM Taxol, 0–200 μM monastrol, 300 μM MgATP, 100 mM KCl. (B) The observed exponential rate of the burst phase was plotted as a function of monastrol concentration. The fit of the data to a hyperbola provided the observed rate constant for ATP hydrolysis at $49.9 \pm 3.4 \text{ s}^{-1}$. *Inset*, the amplitude of the burst phase decreased as a function of monastrol concentration. The data were fit to [Equation 3.1](#), yielding an apparent $K_{d,S} = 29 \pm 9 \mu\text{M}$. (C) Time course of radiolabeled product formation by Mt•Eg5_S complex at increasing MgATP concentrations. Final concentrations: 5 μM Eg5-437, 6 μM tubulin, 20 μM Taxol, 100 μM monastrol, 10–400 μM MgATP, 100 mM KCl. (D) The exponential burst rate was plotted as a function of MgATP concentration. The fit of the data to a hyperbola defined the maximum burst rate of ATP hydrolysis for Eg5-437 in the presence of monastrol, $k_{b,max} = 36.3 \pm 3.2 \text{ s}^{-1}$ and the $K_{d,ATP} = 154 \pm 28 \mu\text{M}$. *Inset*, the amplitude of the burst phase was plotted as a function of MgATP concentration. The data were fit to a hyperbola yielding a maximum burst amplitude at $1.3 \pm 0.1 \mu\text{M}$, and the $K_{d,ATP} = 15 \pm 3 \mu\text{M}$. (E) Time course of ADP•P_i formation by the Mt•Eg5-437_S complex at increasing microtubule concentrations. Final concentrations: 5 μM Eg5-437, 6–40 μM tubulin, 20 μM Taxol, 100 μM monastrol, 300 μM MgATP, 100 mM KCl. *Insets*, the burst rate and burst amplitude of each transient are shown, respectively. Error bars represent the standard error in the fit of the data. (F) Time course of ADP•P_i formation by the Mt•Eg5_S-437 complex \pm 100 mM KCl with the MgATP. Final concentrations: 5 μM Eg5-437, 20 μM tubulin, 20 μM Taxol, 100 μM monastrol, 100 μM MgATP, \pm 100 mM KCl. Each data set was fit to [Equation 3.4](#). No KCl (\bullet): $k_b = 12.7 \pm 1.6 \text{ s}^{-1}$, $A_o = 0.95 \pm 0.06 \mu\text{M}$, and $k_{ss} = 2.5 \pm 0.1 \mu\text{M ADP}\cdot\text{s}^{-1}$. Reaction with 100 mM KCl (\square): $k_b = 12.4 \pm 1.7 \text{ s}^{-1}$, $A_o = 1.01 \pm 0.07 \mu\text{M}$, and $k_{ss} = 1.8 \pm 0.1 \mu\text{M ADP}\cdot\text{s}^{-1}$.

If the lowered burst amplitude in the presence of monastrol can be attributed to ATP hydrolysis reversals (Hypothesis #5), then at least two hypotheses adequately explain this observed phenomenon: 1) monastrol binding to Eg5 allows for P_i product release, but the P_i product rapidly re-binds the active site to allow for ATP re-synthesis, and/or 2) monastrol binding to Eg5 dramatically slows P_i product release such that sufficient time is allotted for ATP re-synthesis to occur. A modified acid-quench experiment was designed to directly test the first hypothesis (see [Materials & Methods 3.2.6](#) for details). By following the time course of product formation using $[\gamma\text{-}^{32}\text{P}]\text{MgATP}$ in the presence of excess non-radioactive KH_2PO_4 , any $[\gamma\text{-}^{32}\text{P}]\text{P}_i$ product released from the Eg5 active site would be diluted by the unlabeled P_i in solution. Control reactions were performed using the same Mt•Eg5 complex and $[\alpha\text{-}^{32}\text{P}]\text{MgATP}$ to provide a direct comparison to $[\gamma\text{-}^{32}\text{P}]\text{MgATP}$ reactions. Data in [Figure 3.7](#) show that the kinetics of product formation for $[\gamma\text{-}^{32}\text{P}]\text{MgATP}$ reactions in the absence and presence of monastrol were not significantly different compared to the $[\alpha\text{-}^{32}\text{P}]\text{MgATP}$ control reactions.

Another acid-quench experiment was designed to test this hypothesis. The conditions of the reaction were similar to those reported in [Figure 3.6](#) with the exception of a “P_i Mop” to remove contaminating P_i in the buffer, as well as adding the P_i binding protein (MDCC-PBP) in excess to bind any γ P_i released into solution (data not shown). The experimental design assumes that any P_i product released from Eg5 would have rapidly and tightly bound MDCC-PBP, thus

effectively preventing P_i re-binding to Eg5. The kinetics of product formation in the presence of monastrol under these conditions did not show an increase to full burst amplitude, similar to those data shown in [Figure 3.7B](#). Taken together, these results suggest that P_i product release after ATP hydrolysis was irreversible, thus disfavoring the hypothesis that P_i product re-binds the active site to promote ATP re-synthesis.

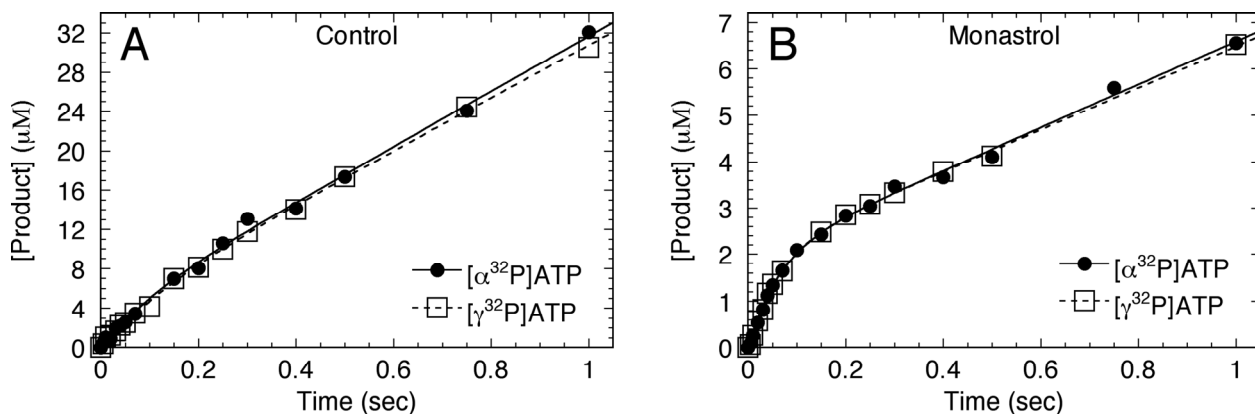


Figure 3.7 Acid-quench experiments for P_i product re-binding to Eg5 active site

Time course of radiolabeled product formation after rapidly mixing a Mt•Eg5 complex in the absence (A) or presence (B) of monastrol with either $[\alpha\text{-}^{32}\text{P}]\text{MgATP}$ (●) or $[\gamma\text{-}^{32}\text{P}]\text{MgATP}$ (□) plus excess non-radioactive KH_2PO_4 in a chemical quench-flow instrument. Final concentrations: 5 μM apoEg5, 6 μM tubulin, 20 μM Taxol, \pm 150 μM monastrol, 200 μM $[\alpha\text{-}^{32}\text{P}]$ or $[\gamma\text{-}^{32}\text{P}]\text{MgATP}$, 10 mM KH_2PO_4 , 90 mM KCl. Each data set was fit to [Equation 3.4](#). For control reactions, $[\alpha\text{-}^{32}\text{P}]\text{ATP}$: $k_b = 9.4 \pm 3.3 \text{ s}^{-1}$, $A_o = 0.76 \pm 0.14 \text{ ADP/site}$. $[\gamma\text{-}^{32}\text{P}]\text{ATP}$: $k_b = 7.2 \pm 1.6 \text{ s}^{-1}$, $A_o = 0.78 \pm 0.11 \text{ ADP/site}$. For monastrol reactions, $[\alpha\text{-}^{32}\text{P}]\text{ATP}$: $k_b = 15.8 \pm 1.4 \text{ s}^{-1}$, $A_o = 0.39 \pm 0.02 \text{ ADP/site}$. $[\gamma\text{-}^{32}\text{P}]\text{ATP}$: $k_b = 15.7 \pm 0.9 \text{ s}^{-1}$, $A_o = 0.40 \pm 0.01 \text{ ADP/site}$.

3.3.5 P_i Product Release Was Faster in the Presence of Monastrol

To directly measure the kinetics of P_i product release from the Mt•Eg5 complex in the absence and presence of monastrol, we performed stopped-flow experiments that detect the change in MDCC-PBP fluorescence upon binding P_i released into solution (163). In the absence of monastrol, the maximum observed rate of P_i product release was the slowest step measured in the pathway ($k_{obs,max} = 6.0 \text{ s}^{-1}$) ([Figure 2.13](#)). The maximum amplitude of the exponential burst of P_i product release during the first ATP turnover event was 0.75 P_i /site (100% of expected amplitude based on Eg5 site concentration), consistent with the ATP hydrolysis kinetics reported in [Figure 3.5F](#). Again, these kinetics are suggestive of the entire Mt•Eg5 population binding and

hydrolyzing ATP during the first ATP turnover in the absence of monastrol. Surprisingly, in the presence of monastrol, the observed rate of P_i product release increased from 6.0 s^{-1} to 15.8 s^{-1} . We also detected a decrease in burst amplitude in the presence of monastrol ($0.38 P_i/\text{site}$; 39% of expected amplitude; [Figure 3.8D](#)), which again was consistent with our ATP hydrolysis kinetics ([Figure 3.5F](#)). The increased rate of P_i product release was intermediate between the observed rate of the formation of the $\text{Mt}\cdot\text{Eg5}^*\cdot\text{ATP}$ intermediate (pulse-chase; [Figure 3.5C](#)) and the rate of ATP hydrolysis (acid-quench; [Figure 3.5D](#)), which was suggestive that observed rate of P_i release was limited by a slower preceding step. If the rate of P_i product release were relatively fast in the presence of monastrol, then the likelihood of ATP hydrolysis reversals would diminish, as the post-hydrolysis intermediate would be drawn forward in the pathway (disfavoring Hypothesis #5). Therefore, another explanation of the lowered burst amplitudes determined in the acid-quench and P_i release experiments must be raised.

The experimental design to measure P_i product release from the $\text{Mt}\cdot\text{Eg5}$ complex assumes that P_i released from Eg5 rapidly and tightly binds to MDCC-PBP, thus rendering the P_i release step irreversible. In [Figure 3.8 \(E and F\)](#), the presteady-state burst kinetics of P_i release were modeled to a two-step irreversible mechanism ([Equations 3.4–3.7](#)). The modeled rate of P_i product release (k_{+3} ; [Scheme 3.1](#)) was similar to the k_{cat} measured by steady-state ATPase assays: $k_{+3} = 5.2 \pm 0.1 \text{ s}^{-1}$ versus $k_{cat} = 5.5 \pm 0.3 \text{ s}^{-1}$ ([Figure 2.7](#)), thus supporting the hypothesis that in the absence of monastrol, the entire $\text{Mt}\cdot\text{Eg5}$ population binds and hydrolyzes ATP during subsequent ATP turnovers as well. Additionally, we detected a 4.1-fold decrease in the rate of steady-state ATP turnover in the presence of monastrol (from 0.78 s^{-1} to 0.19 s^{-1} ; [Figure 3.8F](#)), which was consistent with the results from [Figure 3.1B](#).

If the rate of P_i product release increases in the presence of monastrol, then another step in the mechanism must be dramatically slowed to lower the steady-state k_{cat} (e.g. inhibition of $\text{Eg5}^*\cdot\text{ADP}$ association with microtubules) and/or a significant population of the Eg5 sites remain “non-productive” (catalytically inert) during steady-state ATP turnover.

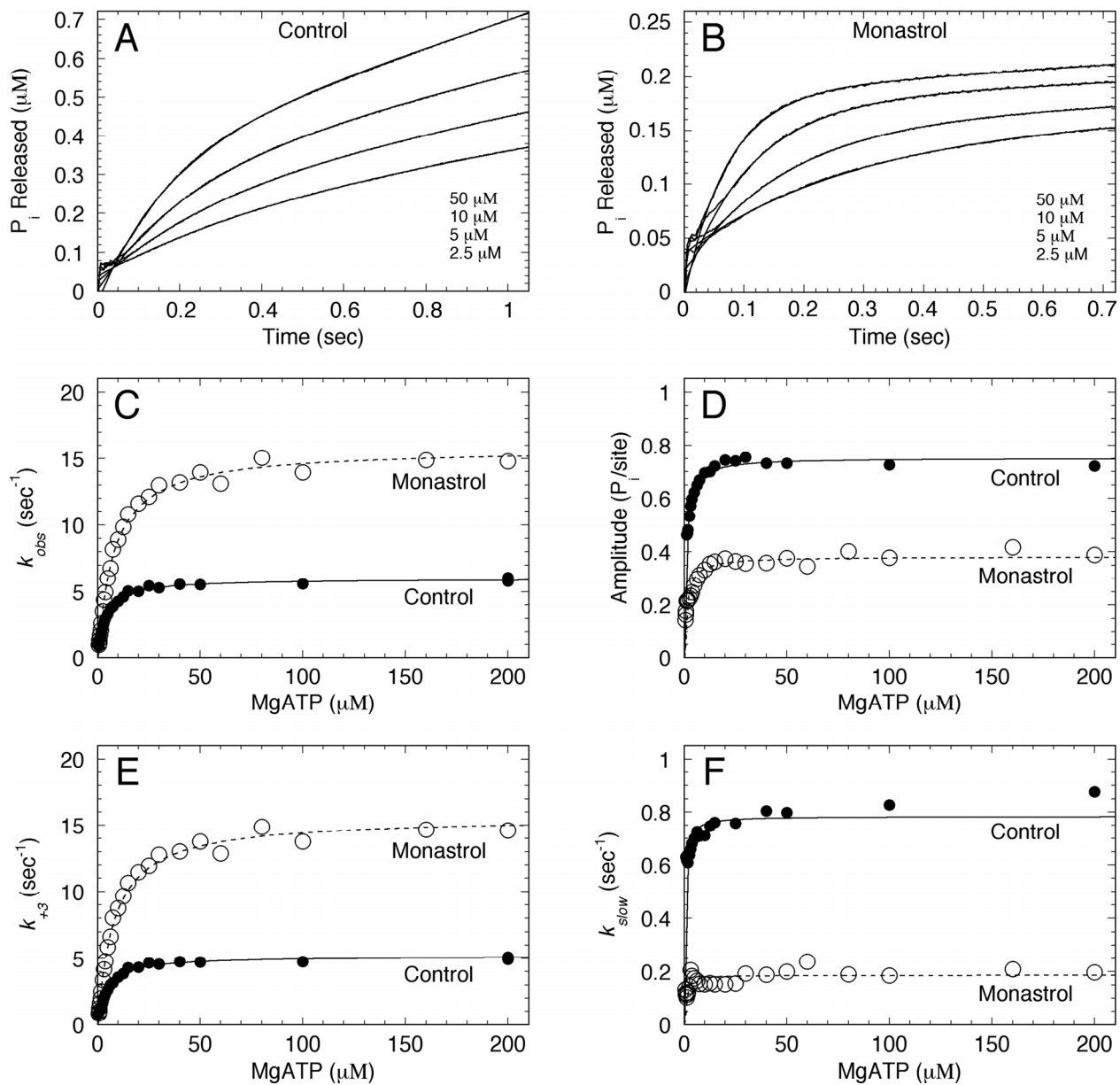


Figure 3.8 Presteady-state kinetics of P_i product release from $Mt \cdot Eg5$ complex \pm monastrol

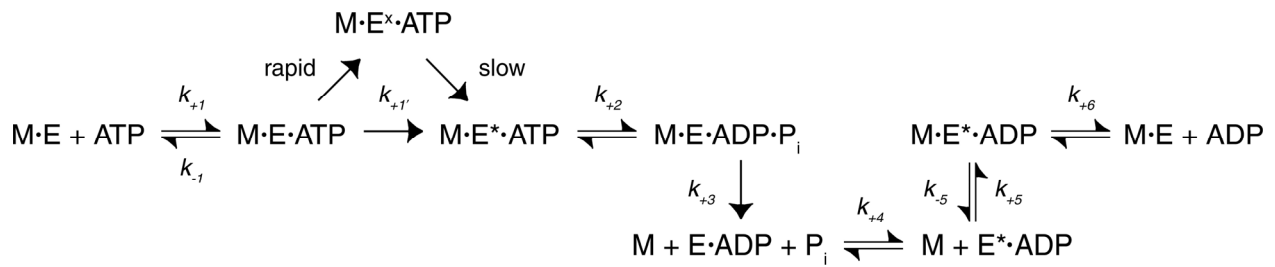
A preformed Mt•Eg5 complex and MDCC-PBP ± monastrol was rapidly mixed with increasing MgATP concentrations plus KCl, and the fluorescence enhancement of MDCC-PBP binding inorganic phosphate (P_i) was monitored in a stopped-flow instrument. Final concentrations: 0.5 μM apoEg5, 1 μM tubulin, 20 μM Taxol, ± 150 μM monastrol, 5 μM MDCC-PBP, 0.05 U/ml PNPase, 75 μM MEG, 0.3125–200 μM MgATP, 100 mM KCl. Representative stopped-flow transients of P_i product released from Mt•Eg5 in the absence **(A)** and presence **(B)** of monastrol are shown (MgATP concentrations are indicated). Each transient displayed burst kinetics and was fit to [Equation 3.4](#). **(C)** The exponential rate of P_i product release was plotted *versus* MgATP concentration, and each data set was fit to a hyperbola. Control: $k_{b,max} = 6.0 \pm 0.1 \text{ s}^{-1}$ and $K_{1/2,ATP} = 3.7 \pm 0.2 \text{ μM}$. Monastrol: $k_{b,max} = 15.8 \pm 0.2 \text{ s}^{-1}$ and $K_{1/2,ATP} = 7.9 \pm 0.4 \text{ μM}$. **(D)** The amplitude of the rapid exponential phase of each transient was plotted as a function of MgATP concentration, and each data set was fit to a hyperbola. Control: $A_{o,max} = 0.75 \pm 0.006 \text{ P}_i/\text{site}$ (100% of expected amplitude based on Eg5 site concentration) and $K_{1/2,ATP} = 0.94 \pm 0.05 \text{ μM}$. Monastrol: $A_{o,max} = 0.38 \pm 0.007 \text{ μM}$ (39% of expected amplitude) and $K_{1/2,ATP} = 1.3 \pm 0.1 \text{ μM}$. **(E)** The rate of P_i product release (k_{+3}) determined by fitting the P_i release transients to [Equations 3.4–3.7](#) was plotted as a function of MgATP concentration, and each data set was fit to a hyperbola. Control: $k_{+3} = 5.2 \pm 0.1 \text{ s}^{-1}$ and $K_{1/2,ATP} = 4.4 \pm 0.3 \text{ μM}$. Monastrol: $k_{+3} = 15.6 \pm 0.2 \text{ s}^{-1}$ and $K_{1/2,ATP} = 8.1 \pm 0.4 \text{ μM}$. **(F)** The rate of the slow step after P_i release (k_{slow}) was plotted as a function of MgATP concentration, and each data set was fit to a hyperbola. Control: $k_{slow} = 0.78 \pm 0.01 \text{ s}^{-1}$ and $K_{1/2,ATP} = 0.39 \pm 0.07 \text{ μM}$. Monastrol: $k_{slow} = 0.19 \pm 0.01 \text{ s}^{-1}$ and $K_{1/2,ATP} = 0.57 \pm 0.15 \text{ μM}$.

3.3.6 ATP Hydrolysis Reversals Do Not Explain the Reduction in Burst Amplitude

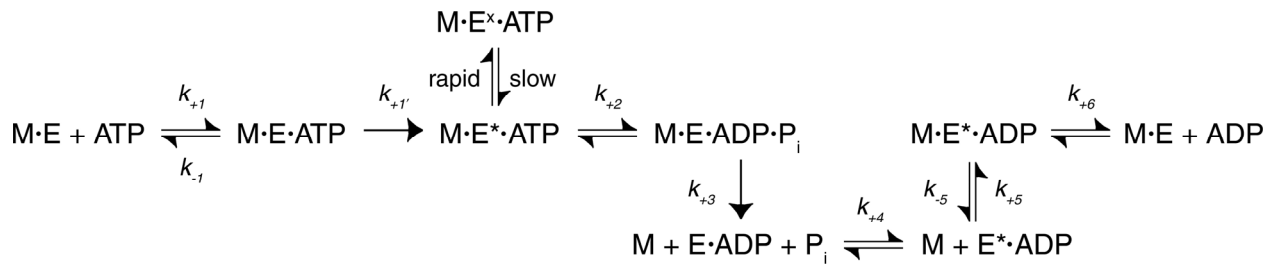
The [γ -³²P]ATP acid-quench experiments ([Figure 3.7](#)) and the P_i product release experiments in the presence of monastrol ([Figure 3.8](#)) suggest that reversals at the ATP hydrolysis step are not probable. We used DynaFit software to simulate the kinetics of product formation observed in acid-quench and P_i release experiments in the absence [[Figure 3.9 \(A and B\)](#)] and presence [[Figure 3.9 \(C–F\)](#)] of monastrol. When the intrinsic rate constant for ATP re-synthesis (k_{-2}) increases, the burst amplitude was reduced; however, the simulated curves did not follow the actual experimental data at any value of k_{-2} tested [[Figure 3.9 \(C and D\)](#)].

On the other hand, if we decreased the apoEg5 concentration to a value similar to the fraction of sites that reported during ATP hydrolysis and P_i release experiments (~40%), we were able to simulate transients for acid-quench and P_i release experiments [[Figure 3.9 \(E and F\)](#)]. There are several possible mechanisms to explain this decrease in “productive” sites. From our pulse-chase results, we know the the entire Mt•Eg5 population can bind MgATP tightly during the first ATP turnover in the absence and presence of monastrol ([Figure 3.5](#)). Therefore, we know that the alteration in the mechanism lies between the ATP collision step and the ATP hydrolysis step. We propose three mechanisms that are consistent with the observed acid-quench kinetics as well as the P_i release kinetics ([Schemes 3.2 and 3.3](#)). [Scheme 3.2](#) hypothesizes that the Mt•Eg5•ATP collision complex proceeds forward via two pathways to form distinct intermediates that both have ATP tightly bound. One intermediate (Mt•Eg5^x•ATP) cannot

proceed forward rapidly to form the ATP hydrolysis-competant state, the other intermediate ($Mt \cdot Eg5^* \cdot ATP$) proceeds forward rapidly to hydrolyze ATP and continue in the pathway. The $Mt \cdot Eg5^x \cdot ATP$ intermediate will slowly attain the ATP hydrolysis-competant state, and continue in the pathway. Scheme 3.2 hypothesizes that the $Mt \cdot Eg5^* \cdot ATP$ intermediate is in equilibrium with the $Mt \cdot Eg5^x \cdot ATP$ intermediate. The intrinsic rate constant that governs the conversion of $Mt \cdot Eg5^* \cdot ATP$ to $Mt \cdot Eg5^x \cdot ATP$ is rapid, while the reverse rate constant is slow. At the current time, we are not sure which model is correct for representing the stabilization of the subpopulation of “non-productive” $Mt \cdot Eg5$ complexes. If the rate of ATP hydrolysis could be somehow dramatically enhanced (10–100 fold), then the burst amplitude would be expected to increase if [Scheme 3.3](#) were correct due to the change in the partition coefficient for the $Mt \cdot Eg5^* \cdot ATP$ intermediate.



Scheme 3.2



Scheme 3.3

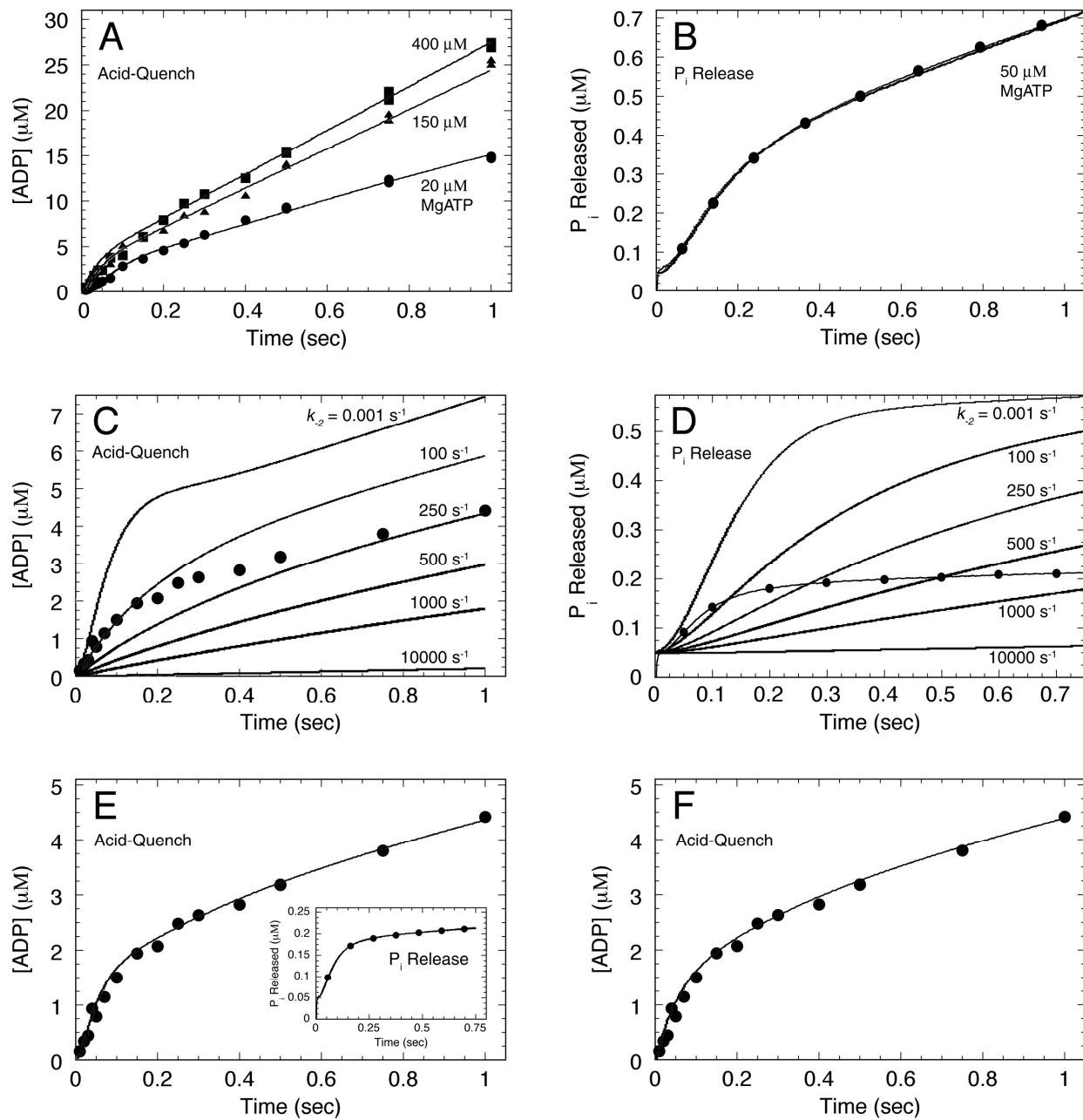


Figure 3.9 DynaFit simulations of Mt•Eg5 mechanism \pm monastrol

(A) Simulation of acid-quench data using transients for three ATP concentrations in the absence of monastrol. Experimental conditions: 5 μM Eg5-367, 6 μM tubulin, 20 μM Taxol, 20, 150, and 400 μM MgATP (as indicated), 100 mM KCl. Simulated constants: $k_{+1} = 100 \mu\text{M}^{-1}\text{s}^{-1}$; $k_{-1} = 909 \text{ s}^{-1}$; $k_{+1'} = 20 \text{ s}^{-1}$; $k_{+2} = 30 \text{ s}^{-1}$; $k_{-2} = 0.001 \text{ s}^{-1}$; $k_{+3} = 6 \text{ s}^{-1}$; $k_{+4} = 4 \text{ s}^{-1}$; $k_{+5} = 43 \text{ s}^{-1}$; $E_0 = \text{total Eg5 protein}$. (B) Simulation of P_i product release data in the absence of monastrol. Experimental conditions: 0.5 μM Eg5-367, 1 μM tubulin, 20 μM Taxol, 50 μM MgATP, 100 mM KCl. Simulated constants: $k_{+1} = 100 \mu\text{M}^{-1}\text{s}^{-1}$; $k_{-1} = 909 \text{ s}^{-1}$; $k_{+1'} = 20 \text{ s}^{-1}$; $k_{+2} = 30 \text{ s}^{-1}$; $k_{-2} = 0.001 \text{ s}^{-1}$; $k_{+3} = 6 \text{ s}^{-1}$; $k_{+4} = 4 \text{ s}^{-1}$; $k_{+5} = 43 \text{ s}^{-1}$; $E_0 = \text{total Eg5 protein}$. The acid-quench (C) and P_i release (D) transients in the presence of monastrol were simulated based on a mechanism where the intrinsic rate of ATP re-synthesis (k_{-2}) increased from 0.001 s^{-1} to $10,000 \text{ s}^{-1}$. Acid-quench experimental conditions: 5 μM Eg5-367, 6 μM tubulin, 20 μM Taxol, 150 μM monastrol, 150 μM MgATP, 100 mM KCl. P_i release experimental conditions: 0.5 μM Eg5-367, 1 μM tubulin, 20 μM Taxol, 150 μM monastrol, 50 μM MgATP, 100 mM KCl. Simulated constants: $k_{+1} = 100 \mu\text{M}^{-1}\text{s}^{-1}$; $k_{-1} = 909 \text{ s}^{-1}$; $k_{+1'} = 20 \text{ s}^{-1}$; $k_{+2} = 30 \text{ s}^{-1}$; $k_{-2} = 0.001$ to $10,000 \text{ s}^{-1}$ (as indicated); $k_{+3} = 15 \text{ s}^{-1}$; $k_{+4} = 1 \text{ s}^{-1}$; $k_{+5} = 15 \text{ s}^{-1}$; $E_0 = \text{total Eg5 protein}$. (E and F) simulations of acid-quench and P_i release kinetics (*inset*) based on a mechanisms depicted in [Scheme 3.2](#) and [Scheme 3.3](#), respectively.

3.3.7 Monastrol Increases the Observed Rate of ATP-Promoted Dissociation of the Mt•Eg5 Complex

The preformed Mt•Eg5 complex in the absence and presence of monastrol was rapidly mixed in a stopped-flow instrument with increasing concentrations of MgATP plus KCl, and the change in solution turbidity due to motor detachment from the microtubule was monitored ([Figure 3.10](#)). In this experimental design, the motor binds and hydrolyzes ATP followed by Eg5 detachment from the microtubule, but the additional salt weakens the interaction of Eg5 with the microtubule upon association, thus allowing the measurement of the ATP-promoted dissociation kinetics. In [Figure 3.10 \(A and B\)](#), representative stopped-flow transients are shown corresponding to different MgATP concentrations in the absence and presence of monastrol, respectively. The transients show an initial lag due to the time required for ATP binding and ATP hydrolysis prior to dissociation. In the absence of monastrol, the dissociation kinetics show an ATP-concentration dependence with the maximum observed rate of Mt•Eg5 dissociation at 7.7 s^{-1} , which was consistent with results from [Figure 2.14A](#).

However, in the presence of monastrol, the maximum observed rate was 15.6 s^{-1} , similar to the monastrol-promoted increase in the observed rate of P_i product release ([Figure 3.8C](#)). The exponential amplitude of the transients in the presence of monastrol also increased compared to control reactions ([Figure 3.10D](#)). This observation can be explained by the reduced rate of Eg5•ADP association with the microtubule subsequent to ATP-promoted dissociation of the Mt•Eg5 complex (see below). These results suggest that Eg5 detachment from the microtubule is tightly coupled to P_i product release, however, the temporal ordering of these two kinetic steps

cannot be determined in this study (Figure 3.16). Nevertheless, the experimental design for both P_i release and ATP-promoted dissociation experiments allows us to hypothesize a relatively slow step after ATP hydrolysis and a relatively fast step (>10 -fold faster) subsequent to the slow step. In the presence of monastrol, this slow step after ATP hydrolysis was dramatically accelerated.

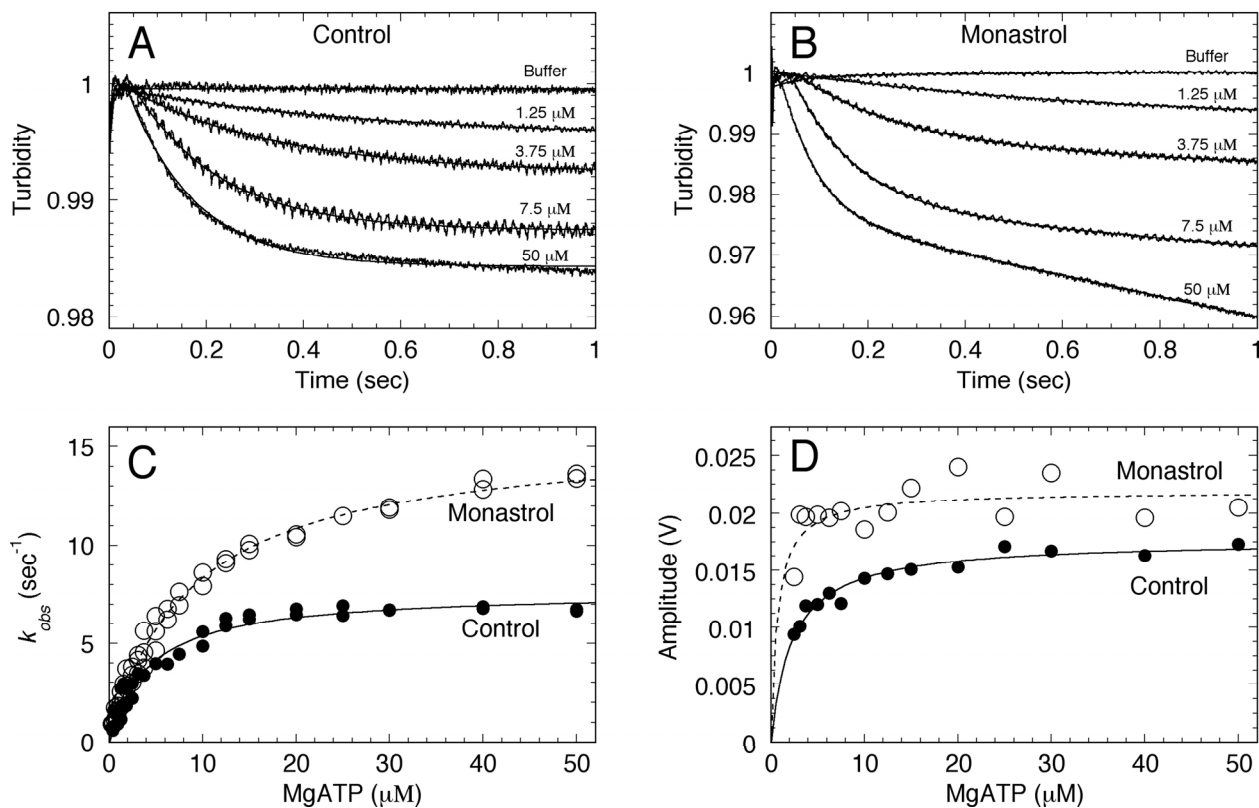


Figure 3.10 ATP-promoted dissociation of the Mt•Eg5 complex \pm monastrol

A preformed Mt•Eg5 complex in the absence (A) and presence (B) of monastrol was rapidly mixed in a stopped-flow instrument with varying concentrations of MgATP plus KCl, and solution turbidity was monitored as a function of time. Final concentrations: 2 μ M apoEg5, 1.95 μ M tubulin, 20 μ M Taxol, \pm 150 μ M monastrol, 0.3125–200 μ M MgATP, 100 mM KCl. The Mt•Eg5 complex was serially diluted to measure dissociation at low MgATP concentrations. (C) The rate of the rapid exponential phase of Mt•Eg5 dissociation in the absence (\bullet) and presence (\circ) was plotted as a function of MgATP concentration and each data set was fit to a hyperbola. For control reactions, $k_{obs,max} = 7.7 \pm 0.2 \text{ s}^{-1}$ and $K_{1/2,ATP} = 4.2 \pm 0.3 \text{ }\mu\text{M}$. For monastrol reactions, $k_{obs,max} = 15.6 \pm 0.2 \text{ s}^{-1}$ and $K_{1/2,ATP} = 8.7 \pm 0.3 \text{ }\mu\text{M}$. (D) The amplitude of the exponential phase in the absence (\bullet) and presence (\circ) was plotted against MgATP concentration and each data set was fit to a hyperbola. For control reactions, $A_{o,max} = 0.0176 \pm 0.0004 \text{ V}$ and $K_{1/2,ATP} = 2.3 \pm 0.2 \text{ }\mu\text{M}$. For monastrol reactions, $A_{o,max} = 0.0219 \pm 0.0008 \text{ V}$ and $K_{1/2,ATP} = 0.7 \pm 0.3 \text{ }\mu\text{M}$.

3.3.8 Monastrol Binding Occurs Prior to ATP Hydrolysis for Eg5-367, but not Eg5-437

To determine whether the sequential order of monastrol addition affected the outcome of the experimental results presented in Figures [3.5](#), [3.6](#), [3.7](#), and [3.8](#), we designed three independent acid-quench and P_i product release reactions ([Figure 3.11](#)). In Rxn. 1, monastrol was omitted; Rxn. 2, monastrol was included with the MgATP syringe, and in Rxn. 3, monastrol was included with the Mt•Eg5 syringe. The data from Rxn. 2 and Rxn. 3 superimposed for both methodologies for Eg5-367, which was contrary to results for Eg5-437. One contributing factor for this anomaly could be the observed rate of ATP hydrolysis being slightly slower for Eg5-367 than Eg5-437 ($k_{obs} = 11.1 \text{ s}^{-1}$ versus 14.9 s^{-1}). In addition, the monastrol binding behavior may be intrinsically different between the two proteins when they are bound to the microtubule, as suggested from the difference in $K_{d,S}$ (Eg5-367: $14 \mu\text{M}$ versus Eg5-437: $4 \mu\text{M}$) determined in our steady-state ATPase assays in the presence of microtubules ([Figure 3.1B](#)).

We demonstrated in [Figure 3.1B](#) that the $K_{d,S}$ was $13.8 \mu\text{M}$ for the Mt•Eg5-367 complex based on the inhibition of the maximum rate of ATP turnover under steady-state conditions. In the reactions presented in [Figure 3.11](#), the monastrol concentration was $150 \mu\text{M}$, thus >90% of the Mt•Eg5 complexes would have monastrol bound at equilibrium. Therefore, for Eg5-367, monastrol binding and inhibition occurs prior to ATP hydrolysis to result in a reduction of the burst amplitude for both acid-quench and P_i release transients, and also increasing the observed rate of P_i product release. If monastrol binds and elicits its effect prior to ATP hydrolysis, then perhaps either the Mt•Eg5_S complex, the Mt•Eg5•ATP collision complex, or the Mt•Eg5_S*•ATP isomerization intermediate is altered in some way to cause the reduction in burst amplitude for these transients.

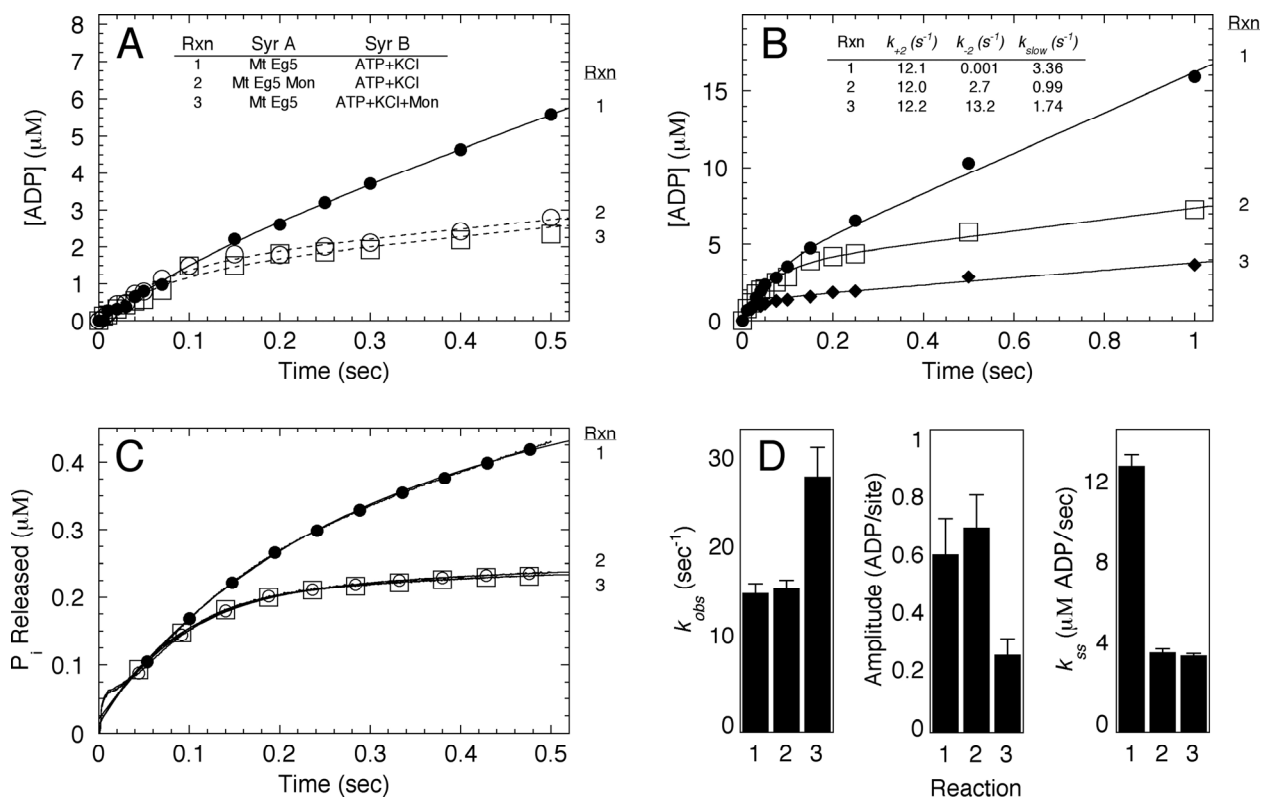


Figure 3.11 Experiments to evaluate sequential addition of monastrol

The time course of $[\alpha\text{-}^{32}\text{P}]\text{ADP}\cdot\text{P}_i$ product formation (A) and P_i product release (B) under three different reaction conditions was determined for Eg5-367. Rxn. 1: Mt•Eg5 complex (no monastrol) was reacted with MgATP (●). Rxn. 2: Mt•Eg5 complex was reacted with MgATP plus monastrol (○). Rxn. 3: Mt•Eg5 complex plus monastrol was reacted with MgATP (□). Final concentrations for acid-quench experiment: 5 μM Eg5-367, 6 μM tubulin, 20 μM Taxol, ± 150 μM monastrol, 200 μM MgATP, 100 mM KCl. Final concentrations for P_i release experiment: 0.5 μM Eg5-367, 1 μM tubulin, 20 μM Taxol, ± 150 μM monastrol, 5 μM MDCC-PBP, 0.05 U/ml PNPase, 75 μM MEG, 200 μM MgATP, 100 mM KCl. Each transient was fit to Equation 3.4. (C) The time course of product formation for Eg5-437 under the three experimental conditions from Panels A and B. (D) The exponential burst rate, burst amplitude, and the rate constant of the linear phase defining steady-state turnover were plotted for each experimental setup. Error bars represent the standard error in the fit of the data.

3.3.9 Monastrol Dissociates Neither the Mt•Eg5 Complex nor the Mt•Eg5*•AMPPNP Complex Prior to ATP Hydrolysis

There are two remaining hypotheses that would explain the reduction in burst amplitude observed in both acid-quench and P_i release experiments in the presence of monastrol: monastrol-promoted dissociation of either the Mt•Eg5 complex, or the Mt•Eg5*•ATP complex prior to ATP hydrolysis (Hypothesis #4), and/or “non-productive” Mt•Eg5 complexes where the motor domain cannot generate the ATP-promoted structural transitions required to proceed

forward to ATP hydrolysis (Hypothesis #6). To test Hypothesis #4, we investigated whether monastrol binding to Eg5 induced the dissociation of the Mt•Eg5 complex in the absence of nucleotide and in the presence of AMPPNP, a non-hydrolyzable ATP analog (Figure 3.12). In Figure 3.12A, the monastrol-promoted dissociation transients in the absence and presence of additional KCl are shown. These transients show that monastrol does not dissociate the Mt•Eg5 complex in the absence of ATP (compare Rxn. 4 with Rxn. 6). In Figure 3.12B, the transients show that monastrol does not dissociate the Mt•Eg5*•AMPPNP complex as well. Therefore, Hypothesis #4 seems unlikely due to these results. By a process of elimination, Hypothesis #6 remains as being the best explanation for the observed decrease in burst amplitude. However, a direct test of the “non-productive” Mt•Eg5_S complex is currently unavailable.

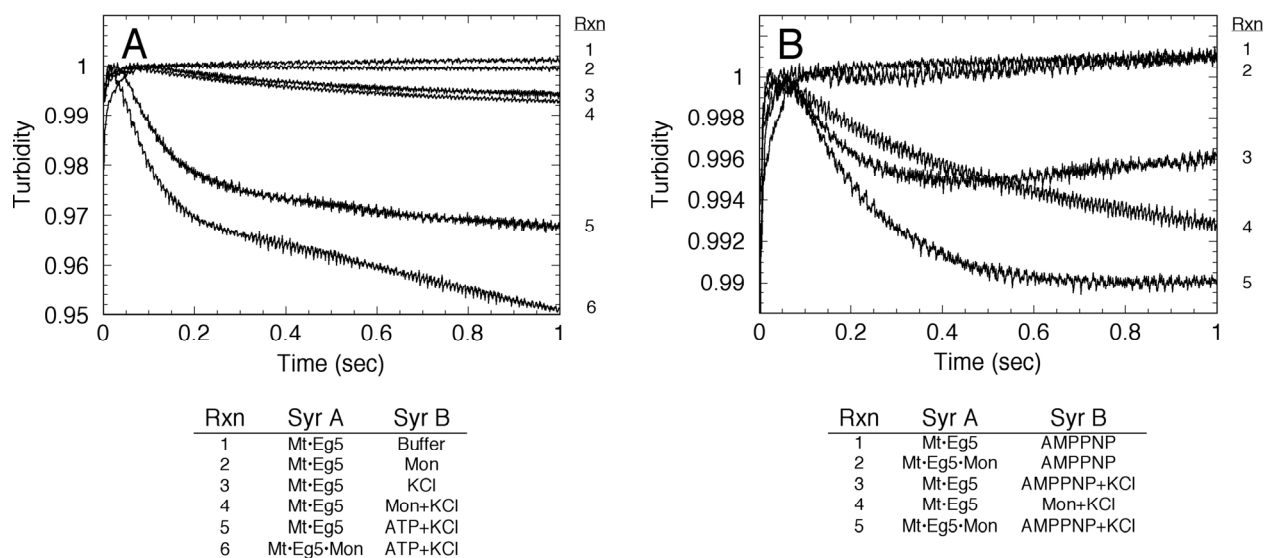


Figure 3.12 Monastrol-promoted dissociation of the Mt•Eg5 complex

A preformed Mt•Eg5 complex \pm monastrol was rapidly mixed in a stopped-flow instrument with various reactants (as indicated), and solution turbidity was monitored as a function of time. Final concentrations: 5 μ M apoEg5, 6 μ M tubulin, 20 μ M Taxol, \pm 150 μ M monastrol, \pm 200 μ M MgAXP, \pm 100 mM KCl. (A) Stopped-flow transients showing monastrol-promoted dissociation of the Mt•Eg5 complex (nucleotide-free conditions) compared ATP-promoted dissociation transients shown in Figure 3.9. (B) Stopped-flow transients showing AMPPNP-promoted dissociation of the Mt•Eg5 complex \pm monastrol. Note the difference in the y-axis scale between Panels A and B.

3.3.10 Monastrol Dramatically Slows Eg5_S Association with Microtubules

In order to determine the effectiveness of Mt•Eg5_S complex formation, we used the stopped-flow instrument to monitor changes in solution turbidity as the motor associates with the microtubule lattice ([Figure 3.13](#)). For Eg5-367 and Eg5-437, the observed rate of Eg5 association decreased as a function of monastrol concentration (Eg5-367: 57 s⁻¹ to 4 s⁻¹ and Eg5-437: 5.7 s⁻¹ to 1.2 s⁻¹). From the fit of each data set, the apparent $K_{d,S}$ was 5–6 μM, consistent with the $K_{d,S}$ determined from the microtubule-activated steady-state experiments for Eg5-437 ([Figure 3.1B](#); [Table 3.1](#)). Also, the amplitude of the rapid exponential phase decreased as a function of monastrol concentration, suggesting that a proportion of Eg5_S motors did not bind the microtubule lattice stably enough to elicit a turbidity change. A decrease in the observed rate of Eg5 association with the microtubule suggests that the isomerization of the Mt•Eg5_S•ADP collision complex must be slowed. Therefore, the conformational change in the motor domain that promotes tight microtubule binding is inhibited by monastrol. These data confirm the results from our steady-state experiments and cosedimentation assays, which show that monastrol weakens the interaction of Eg5 with the microtubule lattice. If ADP release from the Mt•Eg5•ADP intermediate were triggered by this isomerization event, we would expect the observed rate of mantADP release to be slowed as well (see [Figure 3.14](#) below).

We also determined the kinetics of Eg5_S association with microtubules under nucleotide-free conditions. The apoEg5 transients in [Figure 3.13B](#) were similar in the absence and presence of monastrol; however, Eg5•ADP transients showed a reduction in the observed rate (from 26.4 s⁻¹ to 11.8 s⁻¹) and the amplitude (from 0.0095 V to 0.0035 V) ([Figure 3.13B, inset](#)). Taken together, these experimental results suggest that Eg5 requires ADP to be bound at the active site in order for monastrol binding to weaken its affinity for microtubules, consistent with the results from cosedimentation experiments in the presence of excess MgATP or MgADP ([Figure 3.3](#)).

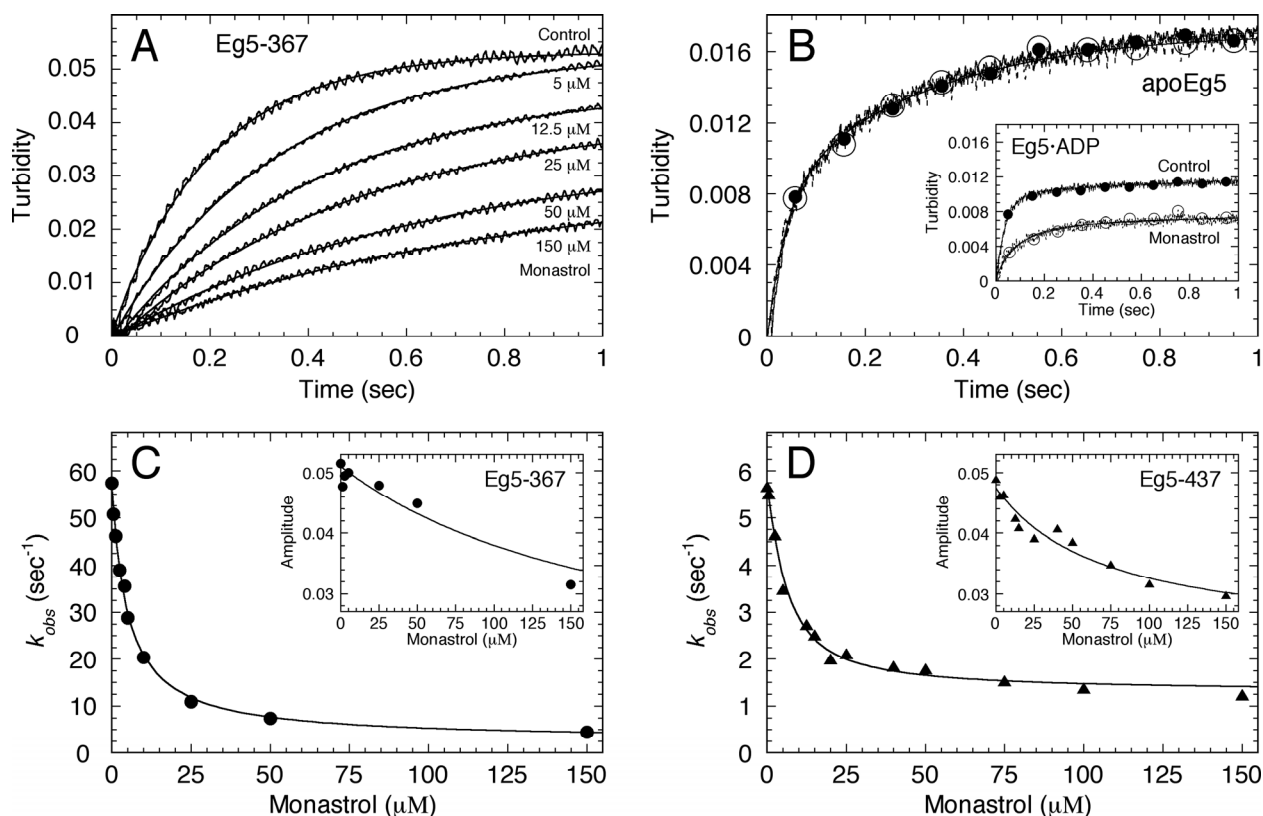


Figure 3.13 Eg5_s association with microtubules

Eg5 was treated with increasing monastrol concentrations, then rapidly mixed in the stopped-flow instrument with Taxol-stabilized microtubules. Final concentrations: 5 μM Eg5, 6 μM tubulin, 20 μM Taxol, 0–150 μM monastrol. **(A)** Representative stopped-flow transients are shown at various monastrol concentrations (as indicated). Each transient was fit to a single exponential function. **(B)** ApoEg5 and Eg5•ADP (1:1) were treated in the absence and presence of monastrol, then rapidly mixed in a stopped-flow instrument with microtubules. Final concentrations: 2.5 μM apoEg5, \pm 2.5 μM MgADP, 3 μM tubulin, 20 μM Taxol, \pm 150 μM monastrol. Stopped-flow transients for apoEg5 are shown in the absence (\bullet) and presence (\circ) of monastrol. *Inset*, stopped-flow transients for Eg5•ADP (1:1) are shown in the absence (\bullet) and presence (\circ) of monastrol. Each transient was fit to a single exponential function. For apoEg5, control: $k_{obs} = 30.7 \pm 0.9 \text{ s}^{-1}$ and Amp = $0.0098 \pm 0.0001 \text{ V}$; Monastrol: $k_{obs} = 25.2 \pm 1.2 \text{ s}^{-1}$ and Amp = $0.0078 \pm 0.0002 \text{ V}$. For Eg5•ADP, control: $k_{obs} = 26.4 \pm 0.7 \text{ s}^{-1}$ and Amp = $0.0095 \pm 0.0001 \text{ V}$; Monastrol: $k_{obs} = 11.8 \pm 0.3 \text{ s}^{-1}$ and Amp = $0.0035 \pm 0.0002 \text{ V}$. **(C)** For Eg5-367 (\bullet), the rate constant obtained from the rapid exponential phase of each transient was plotted as a function of monastrol concentration. The data were fit to [Equation 3.10](#), yielding $K_{d,S} = 5.1 \pm 0.4 \mu\text{M}$. **(D)** For Eg5-437 (\blacktriangle), the observed rate of microtubule association versus monastrol concentration; $K_{d,S} = 6.2 \pm 0.7 \mu\text{M}$. *Insets* for C and D, the amplitude of the exponential phase versus monastrol concentration for each Eg5 motor, respectively.

3.3.11 Monastrol Slows MantADP Release

Eg5 was incubated with mantADP to exchange ADP at the active site with mantADP, and the Eg5•mantADP complex was treated with increasing concentrations of monastrol. This complex

was then reacted in a stopped-flow instrument with microtubules plus MgATP to prevent the mantADP from rebinding the Mt•Eg5_S complex. [Figure 3.14](#) shows the exponential rate of mantADP release as a function of monastrol concentration. For each Eg5 motor, mantADP release was slowed as monastrol concentration increased. For Eg5-367, monastrol inhibited mantADP release from 36 s⁻¹ to 17 s⁻¹ with the apparent $K_{d,S}$ at 14 μM. For Eg5-437, monastrol decreased mantADP release from 18 s⁻¹ to 6 s⁻¹ with the apparent $K_{d,S}$ at 15 μM. In contrast, the apparent $K_{d,S}$ measured in our steady-state ATPase assays were 14 μM for Eg5-367 and 4 μM for Eg5-437. In order to measure microtubule-activated mantADP release from the Eg5 motor domain, the Eg5_S•mantADP complex must first associate with the microtubule, which has been shown to be dramatically affected by monastrol binding ([Figure 3.13](#)). The slowed rate of mantADP release in the presence of monastrol could be interpreted as either a strict effect on product release and/or a result of aberrant microtubule-motor complex formation.

The amplitude of the rapid exponential phase corresponding to mantADP release decreased as a function of monastrol as well, which could be interpreted as a stabilization of the Mt•Eg5_S•mantADP intermediate. Alternatively, we could interpret this decrease in amplitude as a secondary effect of poor microtubule association. In order to test if monastrol traps the Mt•Eg5_S•ADP intermediate, we designed a phosphocreatine kinase-coupled assay to monitor tightly bound [α -³²P]ADP under these conditions (see below).

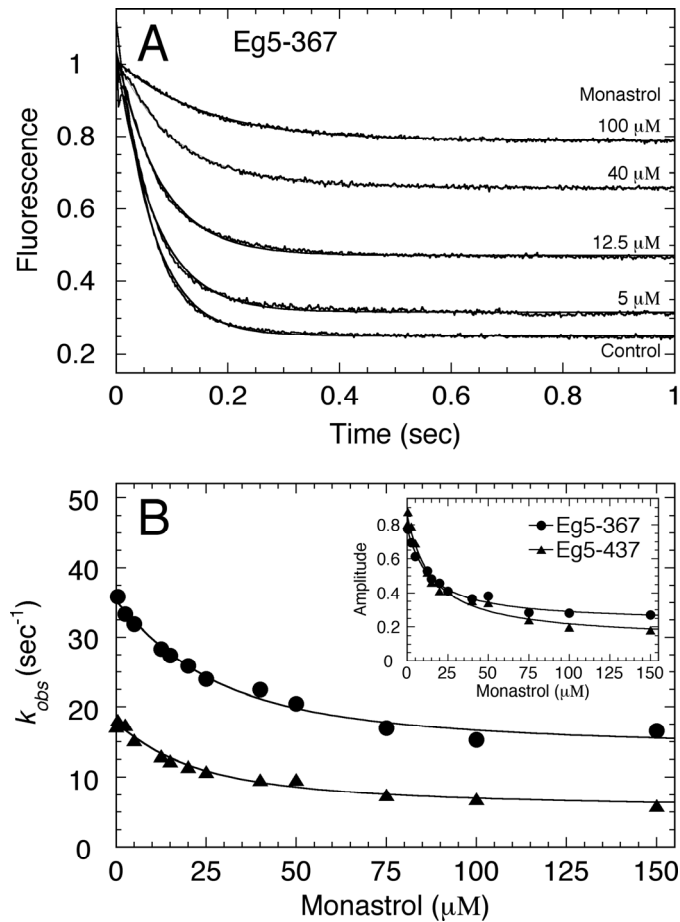


Figure 3.14 MantADP release from Mt•Eg5_S complex

A preformed Eg5•mantADP complex was treated with increasing monastrol concentrations, then the Eg5_S•mantADP complex was rapidly mixed in a stopped-flow instrument with microtubules and MgATP. Final concentrations: 2 μM Eg5, 4 μM mantADP, 25 μM tubulin, 20 μM Taxol, 0–150 μM monastrol, 1 mM MgATP. **(A)** Representative transients are shown for increasing monastrol concentrations (as indicated). **(B)** The rate obtained from the exponential decrease in fluorescence of each transient was plotted as a function of monastrol concentration, and the data were fit to [Equation 3.10](#). For Eg5-367 (●), $K_{d,S} = 14.4 \pm 3.4 \mu\text{M}$. For Eg5-437 (▲), $K_{d,S} = 15.2 \pm 3.2 \mu\text{M}$. **Insets**, the amplitude of the exponential decrease in fluorescence was plotted as a function of monastrol concentration. For Eg5-367 (●), $K_{d,S} = 13.5 \pm 2.0 \mu\text{M}$. For Eg5-437 (▲), $K_{d,S} = 15.2 \pm 2.7 \mu\text{M}$.

3.3.12 Monastrol Does Not Trap the Mt•Eg5_S•ADP Complex

We wanted to answer two questions by performing the phosphocreatine kinase-coupled assays: First, does monastrol slow ADP release in the absence of microtubules? Second, does monastrol trap the Mt•Eg5_S•ADP intermediate? In this experiment, the Eg5 motors were incubated with [α -³²P]ATP to exchange the ADP at the active site with [α -³²P]ADP (see [Figure 2.6](#)). The

motors ($\text{Eg5}\cdot[\alpha\text{-}^{32}\text{P}]\text{ADP}$ or $\text{Eg5}_S\cdot[\alpha\text{-}^{32}\text{P}]\text{ADP}$) were mixed with a creatine kinase/phosphocreatine ATP regeneration system plus 2.5 mM unlabeled MgATP \pm microtubules. The motor domain releases $[\alpha\text{-}^{32}\text{P}]\text{ADP}$ from the active site, and the ATP regeneration system converts the $[\alpha\text{-}^{32}\text{P}]\text{ADP}$ to $[\alpha\text{-}^{32}\text{P}]\text{ATP}$. Because the unlabeled MgATP was in excess, the active site of Eg5 was more likely to bind unlabeled MgATP than $[\alpha\text{-}^{32}\text{P}]\text{ATP}$; therefore, the data show a decrease in $[\alpha\text{-}^{32}\text{P}]\text{ADP}$ as a function of time. Only $[\alpha\text{-}^{32}\text{P}]\text{ADP}$ at the active site was protected from the enzymatic conversion to $[\alpha\text{-}^{32}\text{P}]\text{ATP}$ by creatine kinase. [Figure 3.15](#) shows that the concentration of tightly bound $[\alpha\text{-}^{32}\text{P}]\text{ADP}$ decreased as a function of time. For both Eg5 motors, monastrol treatment promoted slowed ADP release in the absence of microtubules (Eg5-367: 0.05 s^{-1} to 0.007 s^{-1} ; Eg5-437: 0.004 s^{-1} to 0.001 s^{-1}). In the presence of 100 μM monastrol and 3 μM microtubules, no tightly bound $[\alpha\text{-}^{32}\text{P}]\text{ADP}$ was detected for Eg5-367 by 5 sec and for Eg5-437 by 30 sec, which shows that monastrol does not trap a stable $\text{Mt}\cdot\text{Eg5}_S\cdot\text{ADP}$ intermediate. The microtubule-activated rate of $[\alpha\text{-}^{32}\text{P}]\text{ADP}$ release was too fast to measure by this coupled assay, although the data clearly show complete release of $[\alpha\text{-}^{32}\text{P}]\text{ADP}$ from Eg5 sites.

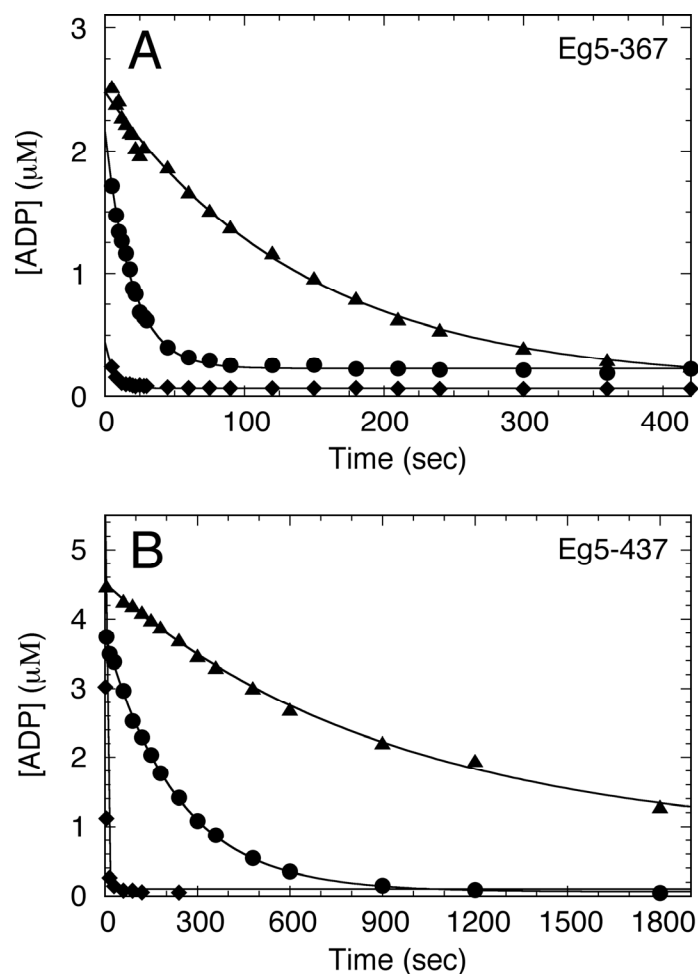


Figure 3.15 Equilibrium state of Eg5_S complexes

Eg5•[α -³²P]ADP was incubated in the presence (▲, □) or absence (●) of monastrol. The complexes were reacted with a creatine kinase/phosphocreatine ATP regeneration system plus MgATP in the presence (□) or absence (●, ▲) of microtubules. Final concentrations: 5 μ M Eg5, 10 μ M tubulin, 20 μ M Taxol, 100 μ M monastrol, 0.3 mg/ml creatine kinase, 4 mM phosphocreatine, and 2.5 mM MgATP. The concentration of tightly bound [α -³²P]ADP was plotted *versus* time, and each data set was fit to [Equation 3.11](#). **(A)** For Eg5-367, in the absence of monastrol (no microtubules), $k_{off,ADP} = 0.05 \pm 0.001 \text{ s}^{-1}$ (●). In the presence of monastrol (no microtubules), $k_{off,ADP} = 0.007 \pm 0.0002 \text{ s}^{-1}$ (▲). **(B)** For Eg5-437, in the absence of monastrol (no microtubules), $k_{off,ADP} = 0.004 \pm 0.0001 \text{ s}^{-1}$ (●). In the presence of 100 μ M monastrol (no microtubules), $k_{off,ADP} = 0.001 \pm 0.0001 \text{ s}^{-1}$ (▲). For both Eg5 motors, in the presence of monastrol and microtubules, a stable Mt•Eg5_S•ADP intermediate was not trapped (□); ADP was rapidly released, but the $k_{off,ADP}$ could not be accurately measured by this coupled assay.

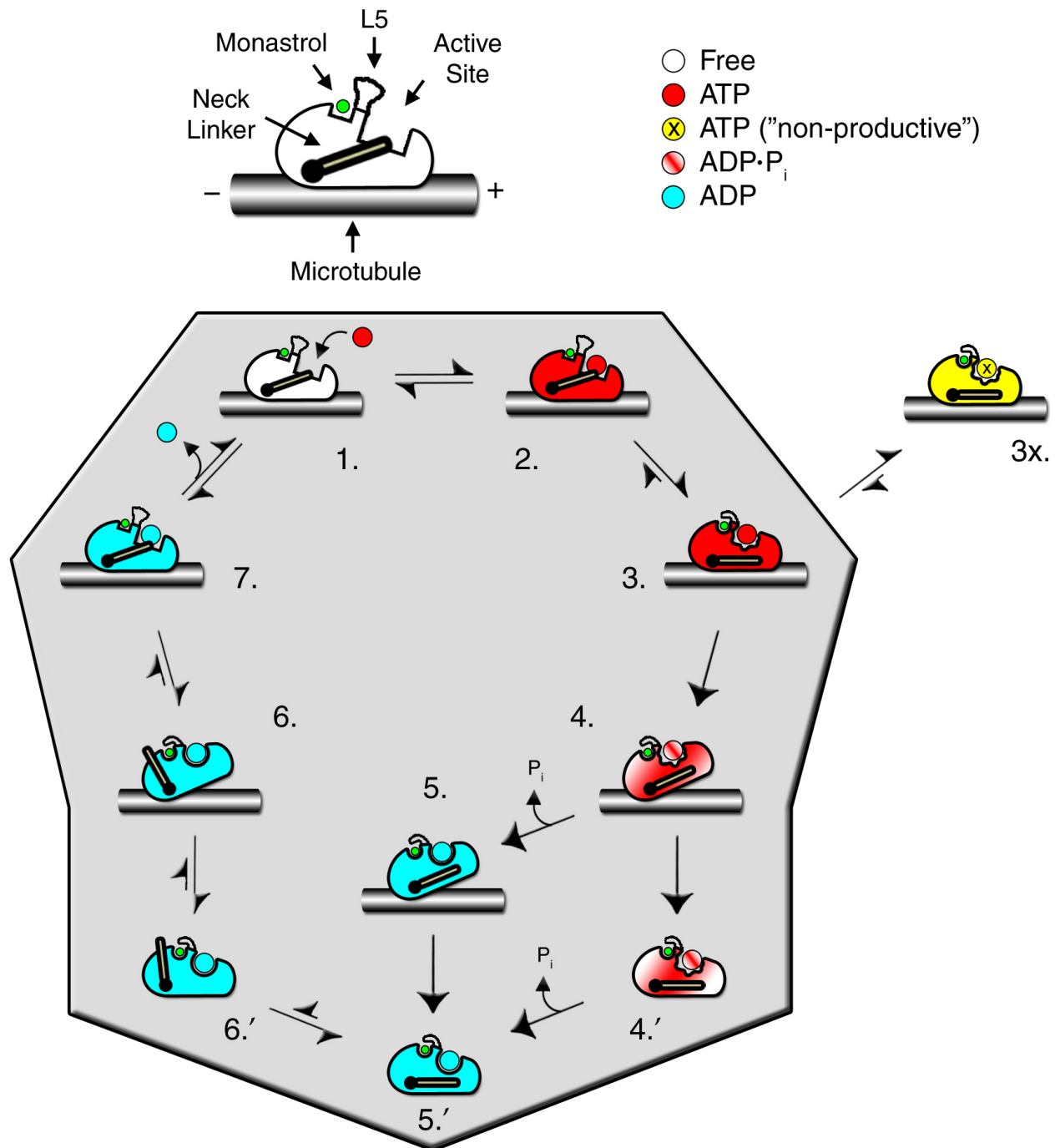


Figure 3.16 Model of Eg5 ATPase inhibition by monastrol

The Eg5 ATPase mechanism in the absence and presence of microtubules is depicted. The Mt•Eg5 mechanism is highlighted in gray. The P_i product release and Eg5 detachment steps are shown in two possible sequential orders. The neck-linker conformations along the ATPase pathway are inferred from previous studies (68, 69, 79, 100).

Table 3.1 Monastrol Inhibition of the Eg5 ATPase Mechanism

		Eg5-367		Eg5-437	
Constants		Control	Monastrol	Control	Monastrol
MantATP Binding	$K_{+1}k_{+1}'$	$2.2 \pm 0.3 \mu\text{M}^{-1}\text{s}^{-1}$	$2.1 \pm 0.3 \mu\text{M}^{-1}\text{s}^{-1}$		
	k_{+1}'	$30.5 \pm 1.3 \text{ s}^{-1}$	$30.0 \pm 1.1 \text{ s}^{-1}$	ND ^a	ND
	$K_{d,ATP}$	$7.9 \pm 1.6 \mu\text{M}$	$8.3 \pm 1.6 \mu\text{M}$		
	k_{-1}'	$16.5 \pm 1.0 \text{ s}^{-1}$	$17.8 \pm 0.8 \text{ s}^{-1}$		
ATP Binding	$k_{b,max}$	$22 \pm 3 \text{ s}^{-1}$	$18.2 \pm 1.3 \text{ s}^{-1}$	$21 \pm 1 \text{ s}^{-1}$	
(Pulse-chase)	$K_{d,ATP}$	$26 \pm 15 \mu\text{M}$	$5.0 \pm 2.5 \mu\text{M}$	$45 \pm 8 \mu\text{M}$	ND
	$A_{0,max}$	$0.75 \pm 0.02 \text{ ADP/site}$	$0.78 \pm 0.03 \text{ ADP/site}$	$0.78 \pm 0.05 \text{ ADP/site}$	
ATP Hydrolysis	$k_{b,max}$	$11.3 \pm 1.4 \text{ s}^{-1}$	$11.1 \pm 0.3 \text{ s}^{-1}$	$14.9 \pm 0.5 \text{ s}^{-1}$	$36.3 \pm 3.2 \text{ s}^{-1}$
(Acid-quench)	$K_{d,ATP}$	$31 \pm 15 \mu\text{M}$	$9.2 \pm 1.5 \mu\text{M}$	$46 \pm 6 \mu\text{M}$	$154 \pm 28 \mu\text{M}$
	$A_{0,max}$	$0.75 \pm 0.02 \text{ ADP/site}$	$0.40 \pm 0.01 \text{ ADP/site}$	$0.78 \pm 0.03 \text{ ADP/site}$	$0.29 \pm 0.01 \text{ ADP/site}$
P _i Release	$k_{b,max}$	$6.0 \pm 0.1 \text{ s}^{-1}$	$15.8 \pm 0.2 \text{ s}^{-1}$		
(MDCC-PBP)	$K_{1/2,ATP}$	$3.7 \pm 0.2 \mu\text{M}$	$7.9 \pm 0.4 \mu\text{M}$		
	$A_{0,max}$	$0.75 \pm 0.01 \text{ P}_i/\text{site}$	$0.38 \pm 0.01 \text{ P}_i/\text{site}$		
P _i Release	k_{+3}	$5.2 \pm 0.1 \text{ s}^{-1}$	$15.6 \pm 0.2 \text{ s}^{-1}$	ND	ND
(Modeling)	k_{slow}	$0.78 \pm 0.01 \text{ s}^{-1}$	$0.19 \pm 0.01 \text{ s}^{-1}$		
	E_o	$0.499 \text{ of } 0.5 \mu\text{M}$ (100%)	$0.193 \text{ of } 0.5 \mu\text{M}$ (39%)		
ATP-Promoted Dissociation ^b	$k_{b,max}$	$7.7 \pm 0.2 \text{ s}^{-1}$	$15.6 \pm 0.2 \text{ s}^{-1}$	$8.7 \pm 0.3 \text{ s}^{-1}$	ND
	$K_{1/2,ATP}$	$4.2 \pm 0.3 \mu\text{M}$	$8.7 \pm 0.3 \mu\text{M}$	$15.1 \pm 2.5 \mu\text{M}$	
Microtubule Association ^b	$K_{+5}k_{+6}$	$11.0 \pm 0.2 \mu\text{M}^{-1}\text{s}^{-1}$	$0.28 \pm 0.03 \mu\text{M}^{-1}\text{s}^{-1}$	$0.66 \pm 0.3 \mu\text{M}^{-1}\text{s}^{-1}$	
	K_{obs}	57.4 s^{-1}	4.4 s^{-1}	5.7 s^{-1}	1.2 s^{-1}
	k_{-5}	$2.8 \pm 1.1 \text{ s}^{-1}$	$2.7 \pm 0.2 \text{ s}^{-1}$	$2.7 \pm 0.1 \text{ s}^{-1}$	
	$K_{d,S}$		$5.1 \pm 0.4 \mu\text{M}$		$6.2 \pm 0.7 \mu\text{M}$
[α - ³² P]ADP Release (-Mts)	$k_{off,ADP}$	$0.05 \pm 0.001 \text{ s}^{-1}$	$0.007 \pm 0.0002 \text{ s}^{-1}$	$0.004 \pm 0.0001 \text{ s}^{-1}$	$0.001 \pm 0.0001 \text{ s}^{-1}$
MantADP Release ^c	K_{obs}	35.9 s^{-1}	16.6 s^{-1}	17.8 s^{-1}	5.9 s^{-1}
	$K_{d,S}$		$14.4 \pm 3.4 \mu\text{M}$		$15.2 \pm 3.2 \mu\text{M}$
Mt-Activated ATPase	k_{cat}	$5.5 \pm 0.3 \text{ s}^{-1}$	$1.2 \pm 0.03 \text{ s}^{-1}$	$2.9 \pm 0.1 \text{ s}^{-1}$	$0.6 \pm 0.03 \text{ s}^{-1}$
	$K_{d,S}$		$13.8 \pm 1.0 \mu\text{M}$		$4.0 \pm 0.4 \mu\text{M}$
	$K_{m,ATP}$	$9.5 \pm 0.4 \mu\text{M}$	$3.6 \pm 0.3 \mu\text{M}$	$20.7 \pm 3.2 \mu\text{M}$	$4.1 \pm 0.7 \mu\text{M}$
	$K_{1/2,Mt}$	$0.71 \pm 0.15 \mu\text{M}$	$6.7 \pm 0.4 \mu\text{M}$	$4.5 \pm 0.6 \mu\text{M}$	$33.3 \pm 3.3 \mu\text{M}$
Mt Equilibrium Binding	$K_{d,Mt}$	$0.046 \pm 0.019 \mu\text{M}$	ND	$0.07 \pm 0.03 \mu\text{M}$	$2.3 \pm 0.2 \mu\text{M}$
ADP Equilibrium Binding	$K_{d,ADP}$	$117 \pm 86 \mu\text{M}$	$99 \pm 20 \mu\text{M}$	$202 \pm 64 \mu\text{M}$	$1.7 \pm 0.6 \mu\text{M}$

^a ND, not determined. ^b Turbidity (*I*₂₂, *I*₂₇). ^c MantADP competed with excess unlabeled MgATP.

3.4 DISCUSSION

In this study, we sought to determine the mechanistic basis for monastrol inhibition of the Mt•Eg5 ATPase cycle ([Scheme 3.1](#)). The results presented here reveal an altered ATPase mechanism in which monastrol promotes a “non-productive” subpopulation of Mt•Eg5 complexes that cannot properly bind and hydrolyze ATP, the affinity of the Mt•Eg5_S complex was weakened, and ADP release was slowed.

In the absence or presence of monastrol, we found the entire Mt•Eg5 population was capable of binding MgATP tightly; however, only a fraction of the population hydrolyzed MgATP and released P_i product during the first ATP turnover event. We also discovered that monastrol binding and inhibition occurs on a time scale much faster than the first-order rate of ATP hydrolysis for Eg5-367 ([Figure 3.11](#)). The inhibition by monastrol to cause the lowered burst amplitude for ATP hydrolysis transients cannot be explained by “pre-mature” dissociation of the Mt•Eg5 complex or the Mt•Eg5*•AMPPNP complex prior to the hydrolysis step in the mechanism ([Figure 3.12](#)). I propose that a subpopulation of “non-productive” Mt•Eg5_S complexes fails to undergo the ATP-promoted conformational changes needed to rapidly advance forward in the pathway toward ATP hydrolysis ([Figure 3.16](#)). This phenomenon has been observed for Eg5 in the absence of both microtubules and monastrol (see [Chapter 4.0](#) below), suggesting that in the presence of microtubules, monastrol uncouples Eg5’s ATPase from force generation on the microtubule lattice. These “non-productive” Eg5 sites would contribute to the reduction in the measured steady-state rate of ATP turnover in the presence of monastrol.

3.4.1 “Non-Productive” Mt•Eg5^x•ATP Intermediate

A recent study has demonstrated that the neck-linker conformation plays a pivotal role in the Eg5 mechanochemical cycle (*100*). In addition, the conformation of loop L5 – part of monastrol

binding cleft (69) – was found to be correlated to structural changes that occur upon tight MgATP binding (see [Chapter 4.0](#) below). Our data are consistent with monastrol binding to Eg5 to somehow alter the conformation of the Mt•Eg5^{*}•ATP intermediate such that the ATP hydrolysis-competent state is not attained ([Figure 3.16](#)).

I propose that the subpopulation of “non-productive” Mt•Eg5^x•ATP complexes will slowly attain the conformation needed to hydrolyze ATP and continue forward in the pathway ([Figure 3.16](#)). During this time, ATP remains tightly bound to the active site, given the full burst amplitude observed in the pulse-chase experiments ([Figure 3.5E](#)). Thus, even though the “non-productive” subpopulation does not report on the time scale of the acid-quench experiments, these sites will slowly hydrolyze ATP, release P_i product, and detach from the microtubule. This hypothesis is supported by our ATP-promoted Mt•Eg5 dissociation transients in the presence of monastrol ([Figure 3.10](#)), which display kinetics that best fit a double exponential function. The second exponential phase occurs very slowly ($k_{obs} = 0.89 \pm 0.04 \text{ s}^{-1}$ at 50 μM MgATP) with a similar amplitude to the first rapid exponential phase ($A^1_o = 0.0287 \pm 0.0002 \text{ V}$; $A^2_o = 0.0334 \pm 0.0007 \text{ V}$ at 50 μM MgATP). The observed rate of the second exponential phase correlates with the steady-state k_{cat} ([Figure 3.1](#)). Nevertheless, we have not been able to directly measure the rate of turnover from the “non-productive” population.

3.4.2 Monastrol Promotes Rapid P_i Release Coupled to Mt•Eg5 Dissociation

We observed a similar monastrol-promoted increase in the rate of P_i product release and ATP-promoted dissociation of the Mt•Eg5 complex. Therefore, these steps are most likely coupled and the rate of the slow reaction will be observed in both experiments. Regardless of the order of these steps, monastrol promotes the accumulation of the Eg5_s•ADP intermediate after rapid detachment from the microtubule that cannot effectively bind the microtubule lattice in order to release the ADP product. In order for monastrol to inhibit Eg5•ADP association with the microtubule lattice, we found that ADP bound at the active site was required ([Figure 3.13B](#)). The lack of a monastrol “effect” could be explained by monastrol binding to apoEg5 that does not alter the structure of the motor domain, thereby yielding no apparent effect on Eg5 associating with the microtubule. It is more likely that monastrol either binds weakly to apoEg5 or does not bind at all. The affinity of apoEg5 for monastrol has not been determined; however,

we have demonstrated that monastrol binds weakly to the Eg5•ATP and Eg5•ADP collision complexes in the absence of microtubules (see [Chapter 4.0](#)). We hypothesize that monastrol would also bind weakly to the nucleotide-free state of the motor as well, thus not affecting apoEg5's binding to microtubules as observed in [Figure 3.13B](#). This experiment was performed using a single microtubule concentration; however, the kinetics of apoEg5_S association with microtubules not expected to differ at higher microtubule concentrations.

3.4.3 Weakening of the Microtubule Interactions by Monastrol

In addition to the aberrant ATP hydrolysis kinetics, monastrol also alters the microtubule-binding ability of the motor ([Table 3.1](#)). The weakened affinity was detected in the steady-state kinetics ([Figure 3.1](#)), the microtubule equilibrium binding studies (Figures [3.2](#) and [3.3](#)), and the presteady-state kinetics of microtubule association ([Figure 3.13](#)). Although the rate of ADP release was also slowed by monastrol treatment (Figures [3.14](#) and [3.15](#)), there was no evidence to support a model in which monastrol stabilizes the Mt•Eg5_S•ADP intermediate and traps ADP at the active site (Species 6 or 7, [Figure 3.16](#)). In fact, the results presented in [Figure 3.15](#) show that ADP was released from the active site of the Mt•Eg5_S complex. The data do support a model of monastrol inhibition whereby the ADP release rate from the Mt•Eg5_S•ADP intermediate is slowed (Species 7, [Figure 3.16](#)). The apparent $K_{d,S}$ obtained from the microtubule association kinetics at 5–6 μM is more similar to the apparent $K_{d,S}$ observed during steady-state ATP turnover ([Table 3.1](#)). In contrast, the $K_{d,S}$ obtained from the mantADP release kinetics is significantly higher at 15 μM , suggesting that these two experiments are measuring the affinity of Eg5 for monastrol either “off” the microtubule (inhibition of Eg5 association with microtubules) or “on” the microtubule (inhibition of mantADP release). Our steady-state ATPase kinetics suggested that monastrol binds more weakly to the Mt•Eg5 complex than the Eg5•ADP complex, which is consistent with the difference in the $K_{d,S}$ observed in these experiments.

3.4.4 Model of Mt•Eg5•Monastrol ATPase Mechanism

This study provides a kinetic and equilibrium characterization of the allosteric inhibition of Eg5 by monastrol ([Figure 3.16](#)). Our results clearly show monastrol-induced effects on the ATPase cycle. In summary, monastrol inhibition of the Eg5 ATPase occurs at important steps along the pathway in order to alter force-production. If Eg5 is not bound to the microtubule, then the motor can neither contribute to the assembly of the spindle, nor to the generation of tension to maintain the mitotic spindle. If Eg5 is bound to the microtubule, then preventing Eg5 from hydrolyzing ATP will stall the motor and hinder the production of force that is necessary for spindle function. If the motor hydrolyzes the nucleotide, monastrol promotes rapid detachment from the microtubule, thus disconnecting any force generation from the microtubule lattice. The inhibitory effect of monastrol tackles all three situations. The data presented in this chapter are consistent with a motor that can no longer produce and sustain the force required to establish and to maintain the bipolar spindle for chromosome segregation.

4.0 CHAPTER FOUR: ATPASE MECHANISM OF EG5 IN THE ABSENCE OF MICROTUBULES: INSIGHT INTO MICROTUBULE ACTIVATION AND ALLOSTERIC INHIBITION BY MONASTROL⁵

The ATPase mechanism of kinesin superfamily members in the absence of microtubules remains largely uncharacterized. We have adopted a strategy to purify monomeric human Eg5 (HsKSP/Kinesin-5) in the nucleotide-free state (apoEg5) in order to perform a detailed transient state kinetic analysis. We have used steady-state and presteady-state kinetics to define the minimal ATPase mechanism for apoEg5 in the absence and presence of the Eg5-specific inhibitor, monastrol. ATP and ADP binding both occur via a two-step mechanism with the isomerization of the collision complex limiting each forward reaction. ATP hydrolysis and phosphate product release are rapid steps in the mechanism, and the observed rate of these steps is limited by the relatively slow isomerization of the Eg5•ATP collision complex. A conformational change coupled to ADP release is the rate-limiting step in the pathway. We propose that the microtubule amplifies and accelerates the structural transitions needed to form the ATP hydrolysis competent state and for rapid ADP release, thus stimulating ATP turnover and increasing enzymatic efficiency. Monastrol appears to bind weakly to the Eg5•ATP collision complex, but after tight ATP binding, the affinity for monastrol increases, thus inhibiting the conformational change required for ADP product release. Taken together, we hypothesize that loop L5 of Eg5 undergoes an “open” to “closed” structural transition that correlates with the rearrangements of the switch-1 and switch-2 regions at the active site during the ATPase cycle.

⁵ Reproduced in part with permission from BIOCHEMISTRY, in press. Unpublished work copyright 2005 American Chemical Society.

4.1 BACKGROUND AND SIGNIFICANCE

Motor proteins from the myosin, kinesin, and dynein superfamilies are important molecular machines that utilize the energy of ATP turnover to generate force and perform various functions in eukaryotic cells. These enzymes coordinate movements of conserved structural elements located at the nucleotide-binding site (P-loop, switch-1, switch-2) with structural elements that interact with the filament surface (actin- or microtubule-binding interface) (77, 92, 113, 115, 116, 206-209). The ATPase activity and enzymatic efficiency of these molecular motors are activated in the presence of their filament partner, which is thought to be mediated through acceleration of the rate of product release [reviewed in (210)]. However, the structural basis for this phenomenon is not well understood.

The ATPase mechanisms of several different monomeric kinesins have been extensively studied in the presence of microtubules: conventional kinesin/Kinesin-1 (127, 128, 176, 177, 190, 204, 211), Eg5/Kinesin-5 ([Chapter 2.0](#)), and Ncd/Kar3/Kinesin-14 (141, 143, 145). On the other hand, very little is known about the ATPase mechanism of kinesins in the absence of microtubules (117, 176, 204). Historically, kinesins have been purified with ADP bound to the nucleotide-binding site (212), and attempts to isolate a homogeneous, nucleotide-free population have been difficult due to the instability of the catalytic domain in the absence of nucleotide (117, 141, 213).

The present studies were undertaken to define the minimal ATPase mechanism for monomeric human Eg5-367⁶ (KSP/Kinesin-5) in the absence of microtubules. We adopted a purification strategy that yielded pure, stable, and fully active protein in the nucleotide-free state. We have employed a combination of steady-state and presteady-state kinetic methodologies to characterize the steps of ATP binding, ATP hydrolysis, P_i and ADP product release, and ADP product binding. We also performed experiments in the presence of the specific Eg5 inhibitor, monastrol, in order to elucidate the mechanistic basis of Eg5 inhibition in the absence of

⁶ Eg5-367, human Eg5/KSP motor domain containing N-terminal 367 residues followed by a C-terminal His₆ tag; apoEg5, nucleotide-free Eg5-367; MDCC-PBP, 7-diethylamino-3-(((2-maleimidyl)ethyl)amino)carbonyl coumarin-labeled phosphate binding protein; PNPase, purine nucleotide phosphorylase; MEG, 7-methylguanosine; P_i, inorganic phosphate; Mt, microtubule; HPLC, high performance liquid chromatography; AXP, any adenosine nucleotide; mant, 2'-(3')-O-(N-methylanthraniloyl); AMPPNP, adenosine 5'-(β,γ-imino)triphosphate; FRET, fluorescence resonance energy transfer; BSA, bovine serum albumin; IgG, bovine gamma globulin; Oval, ovalbumin

microtubules. A six-step pathway is suggested that is similar to the mechanism of Kinesin-1 ATPase (117). However, the rate of the isomerization to form the ATP hydrolysis competent intermediate was much slower and was non-productive for a subpopulation of apoEg5 such that only a fraction of the Eg5 sites contributed to the formation of product during the first and subsequent ATP turnovers.

We propose that monastrol weakly binds the Eg5•ATP collision complex and alters the environment of the Eg5 nucleotide-binding site. However, we cannot experimentally detect monastrol binding to apoEg5 in the absence of microtubules and/or nucleotide. The isomerization of the Eg5•ATP collision complex that occurs during the Eg5 ATPase mechanism leads to an “open” to “closed” structural transition in loop L5 to tighten Eg5’s affinity for both ATP and monastrol. We propose that monastrol stabilizes the “closed” conformation of loop L5, and after rapid ATP hydrolysis and P_i product release, inhibits the very slow isomerization of the Eg5*•ADP complex, which corresponds to the observed rate of ADP release. Therefore, these studies have enabled us to hypothesize a structural communication pathway between loop L5 and the functional elements at the Eg5 nucleotide-binding site. By comparing the basal Eg5 ATPase mechanism to the microtubule-activated mechanism (Chapters [2.0](#) and [3.0](#)), we can also gain insight into how the microtubule activates the Eg5 ATPase cycle.

4.2 MATERIALS AND METHODS

4.2.1 Experimental Conditions

All experiments reported were performed at 22–25 °C in ATPase buffer (20 mM Hepes, pH 7.2 with KOH, 5 mM magnesium acetate, 0.1 mM EDTA, 0.1 mM EGTA, 50 mM potassium acetate, 1 mM dithiothreitol, 5% sucrose) with the concentrations reported as final after mixing. Experiments containing monastrol were performed using the more active *S*-enantiomer [[Figure 3.1B, inset](#); (69, 102, 147)].

4.2.2 Purification of ApoEg5

In this study, we have expressed and purified Eg5-367, as described in [Section 2.2.2](#), with the following modifications in order to isolate Eg5 in the absence of nucleotide at the active site (apoEg5) (117, 204). In all column chromatography buffers, magnesium chloride and ATP were excluded. After Eg5 was eluted from the nickel-nitrilotriacetic acid agarose column (Qiagen, Valencia, CA), the enriched fractions were pooled and incubated with 5 mM EGTA and 5 mM EDTA for 30 min at 4 °C. Following the incubation, the mixture was loaded onto a 100-ml Bio-Gel P-6 size exclusion column (Bio-Rad Laboratories Inc.; exclusion limit 6000 Daltons) to remove chelating reagents and any residual nucleotide. The elution volume containing the excluded apoEg5 was concentrated by ultrafiltration and dialyzed against ATPase buffer. We determined the apoEg5 protein concentration by the Bio-Rad Protein Assay with IgG as the standard. This purification strategy yielded >99% pure protein with >95% basal and microtubule-activated ATPase activity under the same experimental conditions when compared to prior Eg5 purifications [[Table 4.1](#), [Table 2.2](#)]. In addition, we performed pulse-chase, acid-quench, and P_i product release experiments with apoEg5 in the presence of microtubules and observed a burst stoichiometry near unity [[Figure 4.8 \(B–D\)](#)], suggesting the entire population of apoEg5 enzyme binds and hydrolyzes ATP during the first ATP turnover.

4.2.3 Nucleotide-Free Determination of ApoEg5 Preparation

Purified apoEg5 protein was resolved by using a Superose-6 HR 10/30 gel filtration column (Amersham Biosciences) that was equilibrated in ATPase buffer using the System Gold HPLC system (Beckman Coulter Inc.) ([Figure 4.1A](#)). The elution profiles were obtained by continuous monitoring of solution absorbance at 259 nm (λ_{\max} for ADP) and intrinsic protein fluorescence (Ex: 280 nm; Em: 340 nm) at a constant flow rate of 0.5 ml/min. The duration of the elution provides time for >100 ADP release events to occur at each Eg5 site ($k_{off,ADP} = 0.05\text{--}0.14\text{ s}^{-1}$), thus allowing any remaining ADP bound at the Eg5 nucleotide-binding site to be released and diffuse into the included volume of the column. The elution profile of ADP in the absence of Eg5 was compared to the elution profiles of apoEg5 and Eg5•ADP (1:1) to quantify the

nucleotide that remained in each apoEg5 preparation. ImageGauge (version 4.0) software (Fuji Photo Film USA) was used to analyze the data.

We designed another experiment to assess the nucleotide-free state of our apoEg5 preparation. By treating a sample of apoEg5 with apyrase (Sigma-Aldrich Co.; Type VII) for 60 min, any remaining ADP bound to Eg5 would be released into solution and cleaved to AMP+P_i. Using a coupled-assay system with coumarin-labeled phosphate binding protein (MDCC-PBP), as described (122, 163), we were able to directly measure P_i liberated from the apyrase cleavage reaction. Any P_i in solution would bind to the MDCC-PBP and induce a fluorescence enhancement. Apyrase-treated samples of apoEg5, Eg5•ADP (1:1), and ADP (no Eg5) were rapidly mixed in a KinTek SF-2003 stopped-flow instrument (KinTek Corp., Austin, TX) with MDCC-PBP (Ex: 425 nm; Em: 450-nm cutoff) (Figure 4.1B). Contaminating P_i was removed from the MDCC-PBP solution, stopped-flow syringes, and observation cell by incubation with a “P_i mop” consisting of 0.05 U/ml purine nucleotide phosphorylase (PNPase) and 75 μM 7-methylguanosine (MEG). However, the Eg5 and ADP samples were not incubated with the “P_i mop” prior to mixing with the MDCC-PBP.

4.2.4 Steady-State ATPase Kinetics

ApoEg5 steady-state ATPase activity (in the absence of microtubules) was determined by measuring [α -³²P]ADP•P_i product formation as described previously (178). In Figure 4.2, the rate of ATP turnover was plotted as a function of MgATP concentration, and the data were fit to the following quadratic equation:

Equation 4.1

$$Rate = 0.5 * k_{cat} * \{ (E_0 + K_{m,ATP} + [ATP]) - \{ (E_0 + K_{m,ATP} + [ATP])^2 - (4E_0[ATP]) \}^{1/2} \}$$

where *Rate* is the concentration of product formed per second per Eg5 site, *k_{cat}* is the maximum rate constant of product formation at saturating substrate, *E₀* is the total Eg5 site concentration, and *K_{m,ATP}* is the MgATP concentration needed to provide one-half the maximal velocity.

ApoEg5 stability was determined by monitoring the ATPase activity (no microtubules) at various time points after incubation at either 4 °C or 22 °C (Figure 4.2, inset). The observed

steady-state rates as a function of incubation time were fit to a single exponential decay. In [Figure 4.8A](#), apoEg5 steady-state ATPase was determined in the absence and presence of 0.25 mg/ml bovine serum albumin (BSA, BioRad), bovine gamma globulin (IgG, BioRad), or ovalbumin (Oval, Sigma). These reactions were performed to evaluate the potential loss of apoEg5 active sites by adsorption of apoEg5 to the reaction tubes.

4.2.5 Fluorescence Measurements

Steady-state fluorescence measurements of the single Eg5 tryptophan (W127) and 2'(3')-*O*-(*N*-methylanthraniloyl) (mant) nucleotides were obtained at 22 °C using an Aminco-Bowman Series 2 luminescence spectrometer (Thermo Spectronic, Madison, WI) equipped with a 150-Watt continuous wave xenon arc lamp source. ApoEg5 samples were excited at 295 nm (2-nm halfwidth) and tryptophan emission spectra were scanned from 300–400 nm (2-nm halfwidth) ([Figure 4.3A](#)). The appropriate buffer controls were subtracted from each spectrum to adjust for Raman scatter and background fluorescence. Mant-emission spectra were obtained by exciting the solution at 360 nm (4-nm halfwidth) and collecting emitted fluorescence from 400–600 nm (2-nm halfwidth) ([Figure 4.4G](#)). MantATP was used at 10 μM in order to avoid inner-filter effects associated with the mant probe.

4.2.6 Acrylamide Quenching Experiment

In order to determine the relative solvent accessibility of the W127 residue, acrylamide quenching experiments were performed in the absence and presence of ATP. The fluorescence values from 340 nm in the absence of quencher (F_0) were divided by the fluorescence in the presence of quencher (F). These values were plotted as a function of quencher concentration (Q), and each data set was fit to the Stern-Volmer equation ([Figure 4.3B](#)):

Equation 4.2

$$F_0 / F = 1 + K_{sv} * [Q]$$

where K_{SV} is the Stern-Volmer quenching constant, which equals the product of the bimolecular quenching constant (k_q) and the lifetime of the tryptophan fluorophore in the absence of quencher (τ_0).

4.2.7 Stopped-Flow Experiments

Presteady-state kinetic measurements of MgATP binding, mantATP binding, P_i product release, and mantADP binding were made in a stopped-flow instrument (KinTek Corp.). For tryptophan fluorescence experiments [Figure 4.3 (C and D)], fluorescence emission at 340 nm was measured using a 340-nm specific bandpass filter with excitation at 295 nm. MgATP and mantATP binding data shown in Figure 4.3D and Figure 4.4E, respectively, were fit to the following equation:

Equation 4.3

$$k_{obs} = k_{+1'} * [ATP] / (K_{d,ATP} + [ATP]) + k_{-1'}$$

where $k_{+1'}$ equals the rate constant for the ATP-dependent isomerization (Scheme 4.1), $k_{-1'}$ is the ATP off-rate, and $K_{d,ATP}$ is the dissociation constant for weak ATP binding. In Figure 4.4H and Figure 4.10D, the data were fit to the following quadratic equation,

Equation 4.4

$$Amp = -0.5 * \{ (A_{inh} + K_{d,S} + [Mon]) - \{ (A_{inh} + K_{d,S} + [Mon])^2 - (4A_{inh}[Mon]) \}^{1/2} \} + A_{max}$$

where Amp is the magnitude of the exponential change in fluorescence intensity upon mantATP binding, A_{inh} is the amplitude of monastrol inhibition defined by A_{max} (amplitude at no monastrol) minus A_{min} (amplitude at saturating monastrol), $K_{d,S}$ is the apparent dissociation constant for monastrol, and Mon is the monastrol concentration. MantADP binding data shown in Figure 4.10B were fit to the following equation:

Equation 4.5

$$k_{obs} = k_{-4} * [mADP] / (K_{1/2,mADP} + [mADP]) + k_{+4}$$

where k_{-4} equals the forward rate constant for the ADP-dependent isomerization ([Scheme 4.2](#)), k_{+4} equals the reverse rate constant correlated with the ADP off-rate, and $K_{1/2,mADP}$ is the mantADP concentration required to provide half the maximal rate.

The kinetics of P_i product release from apoEg5 were measured using the MDCC-PBP coupled-assay ([163](#)). ApoEg5 plus MDCC-PBP and “ P_i mop” were rapidly mixed with increasing MgATP concentrations plus “ P_i mop”. The concentrations of the “ P_i mop” reagents were experimentally determined to eliminate competition with the MDCC-PBP for P_i in solution ([138](#)). The experimental design assumes that after ATP hydrolysis, P_i product will be released from the Eg5 active site, followed immediately by P_i binding rapidly and tightly to MDCC-PBP, thus triggering the fluorescence enhancement of the MDCC-PBP• P_i complex ([163](#)). In order to convert the observed change in fluorescence into units of P_i concentration, a phosphate calibration curve was used ([Figure 4.7D, inset](#)). The data in [Figure 4.7 \(A and B\)](#) and [Figure 4.8D](#) show a burst of P_i product release at a rate faster than a subsequent rate-limiting step, thus the data were fit to the following equation to describe the time dependence of product release:

Equation 4.6

$$[\text{Product}]_{\text{obs}} = A_0 * [1 - \exp(-k_b t)] + k_{ss} t$$

where A_0 equals the amplitude of the exponential burst phase, k_b is the observed exponential rate of P_i product release from apoEg5, and k_{ss} is the slope of the linear phase corresponding to subsequent ATP turnovers.

4.2.8 Quench-Flow Experiments

The presteady-state kinetics of MgATP binding and ATP hydrolysis ([Figures 4.5, 4.6, 4.8](#)) were determined by utilizing pulse-chase and acid-quench methodologies, respectively, using a KinTek RQF-3 chemical quench-flow instrument (KinTek Corp.). When apoEg5 was rapidly mixed with MgATP, we observed a burst of product formation at a rate faster than the rate of a subsequent step in the pathway that limits steady-state ATP turnover. In acid-quench experiments, the presteady-state burst is correlated to product formation at the Eg5 active site during the first ATP turnover event. After the reaction is quenched with formic acid, Eg5

denatures and the products can be quantified. The observed quantity of products includes the sum of the Eg5-bound products and the products free in solution at the time of the quench. Radiolabeled product was separated from unreacted substrate by thin layer chromatography, and the concentration of product formed was plotted as a function of reaction time. We observed two phases in the kinetics of product formation: 1) a rapid exponential phase that corresponds to the product formed during the first turnover event, and 2) a slow linear phase that corresponds to subsequent ATP turnovers. From the exponential phase, we gain information about the observed presteady-state rate of ATP hydrolysis, and the amplitude of the exponential, which is correlated to the concentration of Eg5 sites that report during the first ATP turnover. From the linear phase, we obtain an estimate of the rate of the slow step (downstream in the pathway from ATP hydrolysis) that limits steady-state ATP turnover.

In the acid-quench experiments, apoEg5 was rapidly mixed with increasing concentrations of $[\alpha\text{-}^{32}\text{P}]\text{MgATP}$, and the reaction continued for various times (0.04–7 sec) followed by quenching with formic acid. The concentration of $[\alpha\text{-}^{32}\text{P}]\text{ADP}$ was plotted as function of time, and each transient was fit to [Equation 4.6](#) [[Figures 4.5 \(A and B\), 4.6 \(A and B\), 4.8 \(B and C\)](#)]. For [Equation 4.6](#), A_0 corresponds to the concentration of $[\alpha\text{-}^{32}\text{P}]\text{ADP}\cdot\text{P}_i$ formed at the active site during the first ATP turnover, and k_b is the rate constant of this exponential phase of product formation.

The presteady-state kinetics of MgATP binding was determined by pulse-chase methodologies using a KinTek RQF-3 chemical quench-flow instrument (KinTek Corp.). The quench-flow instrument consists of three syringes controlled by a computerized motor to force the mixing of apoEg5 with increasing $[\alpha\text{-}^{32}\text{P}]\text{MgATP}$ concentrations, followed a chase solution (excess unlabeled MgATP) to allow time for any tightly bound radiolabeled MgATP to continue forward in the pathway. Whereas, any weakly bound or unbound MgATP substrate will be diluted by the unlabeled chase. The reaction was quenched with formic acid after a chase time sufficient for 8-10 turnovers. Radiolabeled product was separated from substrate by thin layer chromatography, and the concentration of product formed was plotted as a function of reaction time. We observed two phases in the kinetics of product formation: 1) a rapid exponential phase that corresponds to the product formed during the first turnover event, and 2) a slow linear phase that corresponds to subsequent ATP turnovers. From the exponential phase, we gain information about the observed presteady-state rate of MgATP binding, and the amplitude of the exponential,

which is correlated to the concentration of apoEg5 sites that report during the first ATP turnover. From the linear phase, we obtain an estimate of the rate of the slow step (downstream in the pathway from MgATP binding) that limits steady-state ATP turnover.

In the pulse-chase experiments, apoEg5 was rapidly mixed with increasing concentrations of [α - 32 P]MgATP, and the reaction continued for various times (0.04–7 sec) followed by the non-radioactive MgATP chase (10 mM) for 8 min (>10 turnovers). The concentration of [α - 32 P]ADP was plotted as function of time, and each transient was fit to [Equation 4.6](#) [[Figure 4.5 \(A and B\)](#)]. For [Equation 4.6](#), A_0 corresponds to the fraction of tightly-bound Eg5*•ATP that proceeds in the forward direction toward ATP hydrolysis, and k_b is the rate constant of the exponential phase. For both pulse-chase and acid-quench experiments, the amplitude and observed rate of the exponential burst phase for each transient were plotted against MgATP concentration, and each data set was fit to a hyperbola.

4.2.9 Modeling Acid-Quench and P_i Product Release Kinetics

In [Figure 4.7 \(E and F\)](#), the P_i release kinetics were modeled in terms of a two-step irreversible mechanism, where the amplitude and rate constants were defined by:

Equation 4.7

$$A_0 = E_0 * \{ [k_{+1'} / (k_{+1'} + k_{slow})]^2 \}$$

Equation 4.8

$$k_b = k_{+1'} + k_{slow}$$

Equation 4.9

$$k_{ss} = E_0 * [k_{+1'} k_{slow} / (k_{+1'} + k_{slow})]$$

where E_0 is the apoEg5 site concentration that reports during the first ATP turnover, $k_{+1'}$ denotes the rate constant for the slow isomerization step prior to ATP hydrolysis and P_i product release that limits the observed rate of P_i product release ([Scheme 4.1](#)), and k_{slow} is the rate constant of the slow step that occurs after P_i product release for apoEg5 and limits steady-state ATP

turnover. We allowed E_o , k_{+1} , and k_{slow} to float in the analysis due to the unknown Eg5 site concentration that contributed to the first ATP turnover event.

We used DynaFit software (BioKin Ltd., Pullman, WA) to model the acid-quench and P_i product release kinetics at 10, 25, and 50 μ M MgATP to the mechanism proposed in [Scheme 4.1](#) (205). For our acid-quench transients, we modeled the formation of ADP product, which represents $Eg5 \cdot ADP \cdot P_i + Eg5 \cdot ADP + ADP$. Our P_i release transients were modeled by the P_i product that was released from the nucleotide-binding site of Eg5, which bound the MDCC-PBP to elicit the fluorescence enhancement. In [Figure 4.9A](#), acid-quench and P_i release transients at 50 μ M MgATP were simulated based on our proposed kinetic mechanism ([Scheme 4.1](#); [Figure 4.11](#)). In [Figure 4.9\(B–D\)](#), the apoEg5 site concentration was held constant based on the total apoEg5 protein used in the reaction, and the rate constants for all steps in the mechanism were held constant during the simulation, except for the rates of tight ATP binding (k_{+1}), ATP re-synthesis (k_{-2}), and P_i release (k_{+3}) as indicated.

4.3 RESULTS

4.3.1 ApoEg5 Was Active and Nucleotide-Free

We initiated this study by modifying the purification strategy of Eg5-367 in order to isolate Eg5 in a stable, nucleotide-free state (apoEg5). Our previous Eg5-367 purification strategy yielded a population of motors that retained MgADP bound at the active site ([Figure 2.6](#), [Figure 3.15](#)). The modifications (see [Materials & Methods 4.2.2](#) for details) were sufficient to isolate apoEg5 at >99% purity. The apoEg5 protein preparations were tested for activity by measuring the steady-state ATPase kinetics as a function of microtubule concentration at saturating MgATP, and as a function of MgATP concentration at saturating microtubule concentration ([Table 4.1](#)). These experiments demonstrated that under the same experimental conditions as previous studies ([Table 2.2](#)), apoEg5 retained 95–99% of its microtubule-activated ATPase activity. In addition, pulse-chase, acid-quench, and P_i release experiments were performed using the purified apoEg5

in the presence of microtubules, and we observed full burst amplitude from each transient, demonstrating that the entire population of apoEg5 sites was fully active ([Figure 4.8](#)).

In order to determine the nucleotide state of apoEg5, we designed two experiments to directly test the presence of ADP in each apoEg5 preparation. First, we utilized analytical gel filtration to monitor the presence of nucleotide in a sample of apoEg5. We observed a marked decrease in the relative absorbance (A_{259}) at the elution time for ADP when comparing apoEg5 with Eg5•ADP (1:1) or ADP profiles ([Figure 4.1A](#)). After analyzing the ADP peaks (peak apex at 42.7 min) for each condition, apoEg5 appeared to retain approximately 0.07 ADP/Eg5 site compared to Eg5•ADP. However, the sensitivity range of this assay precludes the ability to quantify the precise amount of ADP present in our apoEg5 sample at ≤ 0.07 ADP/site. By simultaneously monitoring intrinsic protein fluorescence (Ex: 280 nm; Em: 340 nm), we did not detect a peak at 16.2 min (void volume), suggesting that there was no detectable aggregation at these conditions ([Figure 4.1A, inset](#)).

Second, we used a MDCC-PBP coupled-assay to detect inorganic phosphate (P_i) product that resulted from the apyrase cleavage reaction. By treating a sample of apoEg5 with apyrase for 60 min, any ADP bound at the active site was released (>150 ADP release events at each site) and converted to AMP+ P_i ([Figure 4.1C](#)). When this reaction was mixed with MDCC-PBP, there was very little amplitude associated with the fluorescence enhancement (<0.05 P_i /Eg5 site) compared to the Eg5•ADP (1:1) reaction ([Figure 4.1B](#)). This slight increase in fluorescence may be due to contaminating P_i that resides in the apyrase stock solution because of the small amplitude associated with apyrase in the absence of apoEg5 (black arrows in [Figure 4.1B](#)). Taken together, these experiments suggest that the apoEg5 preparations were fully active and essentially nucleotide-free.

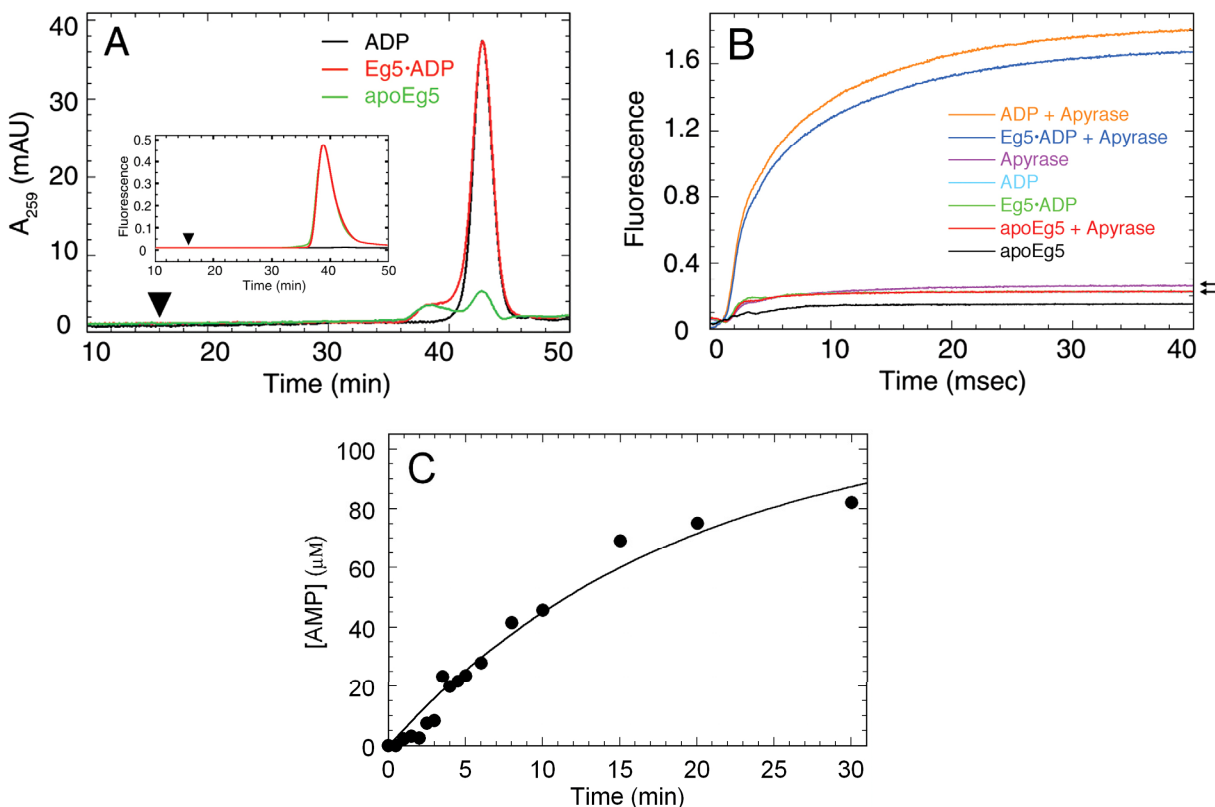


Figure 4.1 Determination of nucleotide-free state of apoEg5

(A) Analytical gel filtration was performed using a Superose-6 HR column with detection by continuous monitoring of solution absorbance at 259 nm (λ_{\max} for ADP) and intrinsic protein fluorescence (*inset*). Conditions: 10 μM apoEg5, 10 μM Eg5•ADP, 10 μM MgADP. Eg5 eluted from the column at 38.8 min and MgADP eluted at 42.7 min. Void volume indicated by arrowhead. (B) Inorganic phosphate liberated from apyrase cleavage of ADP to AMP+P_i was detected by monitoring the fluorescence enhancement of MDCC-PBP•P_i in a stopped-flow instrument. Final concentrations: 1 μM apoEg5, 1 μM Eg5•ADP, 1 μM MgADP, 0.05 U/ml apyrase, 5 μM MDCC-PBP, 0.05 U/ml PNPase, 75 μM MEG. ApoEg5 only, MgADP only, and Eg5•ADP (1:1) were incubated in the absence or presence of apyrase for 60 min at room temperature, followed by rapidly mixing with MDCC-PBP plus “P_i mop” reagents. Transients for MgADP only, Eg5•ADP, and apoEg5+apyrase overlay each other. Black arrows highlight difference between transients for apoEg5+apyrase and apyrase only. (C) Apyrase cleavage of [α -³²P]ADP to [α -³²P]AMP+P_i as a function of time. Final concentrations: 0.1 U/ml apyrase, 100 μM ADP.

4.3.2 Steady-State ATPase Reveals Tight ATP Binding, Yet Inefficient Catalysis

We characterized apoEg5 by following steady-state ATP turnover as a function of MgATP concentration in the absence of microtubules. [Figure 4.2](#) shows that the maximum observed rate of MgATP turnover by apoEg5 was 0.02 s⁻¹, similar to former Eg5 preparations ([Figure 2.7A](#)), with a very tight $K_{m,ATP}$ at 0.17 μM . The $K_{m,ATP}$ was greater than 40-fold tighter in the absence of microtubules compared to microtubule-activated steady-state ATPase: 0.17 μM (apoEg5)

versus $6.95 \mu\text{M}$ (Mt•Eg5) ([Table 4.1](#)). However, in the absence of microtubules, the efficiency of apoEg5 ($k_{cat}/K_{m,ATP}$) decreased approximately 5-fold: $0.12 \mu\text{M}^{-1}\text{s}^{-1}$ (apoEg5) versus $0.58 \mu\text{M}^{-1}\text{s}^{-1}$ (Mt•Eg5). These steady-state ATPase kinetics suggest that apoEg5 has a high affinity for substrate, however, the slow turnover rate leads to enzymatic inefficiency.

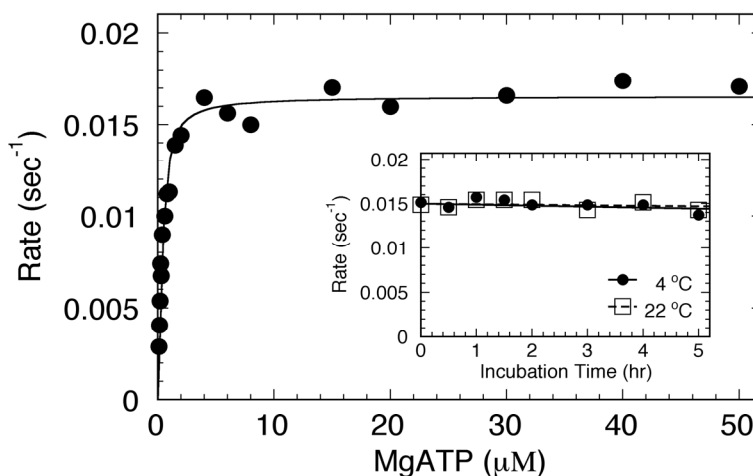


Figure 4.2 ApoEg5 steady-state ATPase

ApoEg5 was reacted with increasing MgATP concentrations in the absence of microtubules. Final concentrations: $0.1 \mu\text{M}$ apoEg5, 0.25 mg/ml BSA, $0.1\text{--}50 \mu\text{M}$ [$\alpha\text{-}^{32}\text{P}$] MgATP. The data were fit to [Equation 4.1](#): $k_{cat} = 0.017 \pm 0.0003 \text{ s}^{-1}$ and $K_{m,ATP} = 0.17 \pm 0.03 \mu\text{M}$. **Inset**, apoEg5 stability was determined by measuring ATPase activity at various time points after incubation. Final concentrations: $0.5 \mu\text{M}$ apoEg5, $10 \mu\text{M}$ [$\alpha\text{-}^{32}\text{P}$]MgATP, $4 \text{ }^\circ\text{C}$ or $22 \text{ }^\circ\text{C}$ incubation temperature. The ATPase reactions were performed at $22 \text{ }^\circ\text{C}$, and the rate of MgATP turnover was plotted as a function of incubation time. The fit of the data to a single exponential decay provided a rate constant at $0.004 \pm 0.003 \text{ hr}^{-1}$ at both incubation temperatures.



Scheme 4.1



Scheme 4.2

The stability of kinesin family members in the absence of nucleotide has historically been an issue of concern. For *Drosophila* Ncd (Kinesin-14), all attempts to isolate apoNcd under physiological conditions have failed (141, 213), and conventional kinesin (Kinesin-1) in the absence of nucleotide was less stable than Kinesin•ADP and aggregated at high protein concentrations (117). Incubation of apoEg5 at either 4 °C or 22 °C for a time domain that exceeds the duration of any kinetic experiment presented in this manuscript did not significantly affect the ATPase activity (Figure 4.2, inset). These data suggest that apoEg5 exists as a very stable monomeric kinesin under these experimental conditions, despite the lack of nucleotide at the active site.

4.3.3 Intrinsic ApoEg5 Fluorescence Enhancement on Nucleotide Binding

The motor domain of human Eg5 contains a single tryptophan residue (W127) that is located on the insertion loop L5 between α 2a and α 2b [(68), see Figure 4.3 (E and F)]. Loop L5 is eight amino acids longer than the homologous loop in Kinesin-1, exists in a relatively flexible conformation in the Eg5•ADP crystal structure (68), and resides in a rigid conformation in the Eg5•ADP•inhibitor crystal structures (69, 79). The primary structure of this loop has been shown to be critical for the binding of and inhibition by specific Eg5 inhibitors (105). The conformation of loop L5 in apoEg5 remains unknown. However, when MgATP or MgADP was bound to the nucleotide-binding site, a significant enhancement (10.6%) in the steady-state tryptophan fluorescence emission was observed (Figure 4.3A). In order to assess the relative accessibility of the tryptophan residue to the solvent, acrylamide quenching studies were performed (Figure 4.3B). In the absence or presence of nucleotide at the active site, the tryptophan fluorophore was found to have a similar degree of solvent accessibility ($K_{sv} = 4.5 \text{ M}^{-1}$), suggesting that the residue remains at the surface of the catalytic domain.

In order to measure the kinetics of the transient increase in tryptophan fluorescence upon nucleotide binding, apoEg5 was rapidly mixed with various nucleotides in a stopped-flow instrument (Figure 4.3C). MgATP and MgADP appeared to elicit an equivalent fluorescence enhancement at a similar rate and amplitude. The binding of MgAMPPNP, a nonhydrolyzable ATP analog, also produced a change in tryptophan fluorescence, suggesting the exponential increase in fluorescence upon MgATP binding corresponds to an event that occurs prior to ATP

hydrolysis. Control experiments showed that rapid mixing of apoEg5 with either MgAMP+P_i (1:1) ([Figure 4.3C](#)) or mantAMP+P_i ([Figure 4.4A](#)) did not elicit a change in fluorescence, providing evidence that apoEg5 does not bind MgAMP+P_i. Taken together, these data argue for a mechanistically relevant conformational change in loop L5 upon nucleotide binding that results in a change in the environment of the tryptophan residue [[Figure 4.3 \(E and F\)](#)].

4.3.4 ATP Binding Occurs Via a Two-Step Mechanism

The observed rate of MgATP binding by tryptophan fluorescence enhancement was investigated as a function of MgATP concentration. The exponential rate of MgATP binding displayed curvature in the concentration dependence ([Figure 4.3D](#)), indicative of (at least) a two-step mechanism where ATP binding was limited by a first-order isomerization event that follows the formation of a collision complex ([Scheme 4.1](#)) (179). The fit of these data provided a maximum rate of MgATP binding (k_{+1}) at 0.54 s⁻¹ and the dissociation constant for weak ATP binding ($K_{d,ATP}$) at 2.6 μM. These constants indicate a relatively slow isomerization event that tightens ATP binding to the apoEg5 active site.

The rate of mantATP binding was investigated by direct mant-fluorescence enhancement (Ex: 360 nm; Em: 400-nm cutoff) and by fluorescence resonance energy transfer (FRET) between the tryptophan and the mant-fluorophore (Ex: 295 nm; Em: 400-nm cutoff). Both methods provided similar rates and amplitudes for mantATP binding ([Figure 4.4B](#)), suggesting that both methods are monitoring the ATP-dependent isomerization step. By monitoring direct mant-fluorescence, we could assess the effect of monastrol on the ATP binding steps in the mechanism. [Figure 4.4E](#) shows that, in the absence or presence of monastrol, there was no significant difference in both the observed rate of mantATP binding (0.85 s⁻¹ versus 0.78 s⁻¹) and the $K_{d,mATP}$ (9.9 μM versus 11.4 μM). On the other hand, there was a dramatic decrease in the amplitude of each transient in the presence of monastrol ([Figure 4.4F](#)). We cannot correlate the loss of amplitude to weaker ATP binding due to the similar $K_{d,mATP}$, and the similar ATP binding data obtained from pulse-chase experiments ± monastrol, as discussed below ([Figure 4.5](#)).

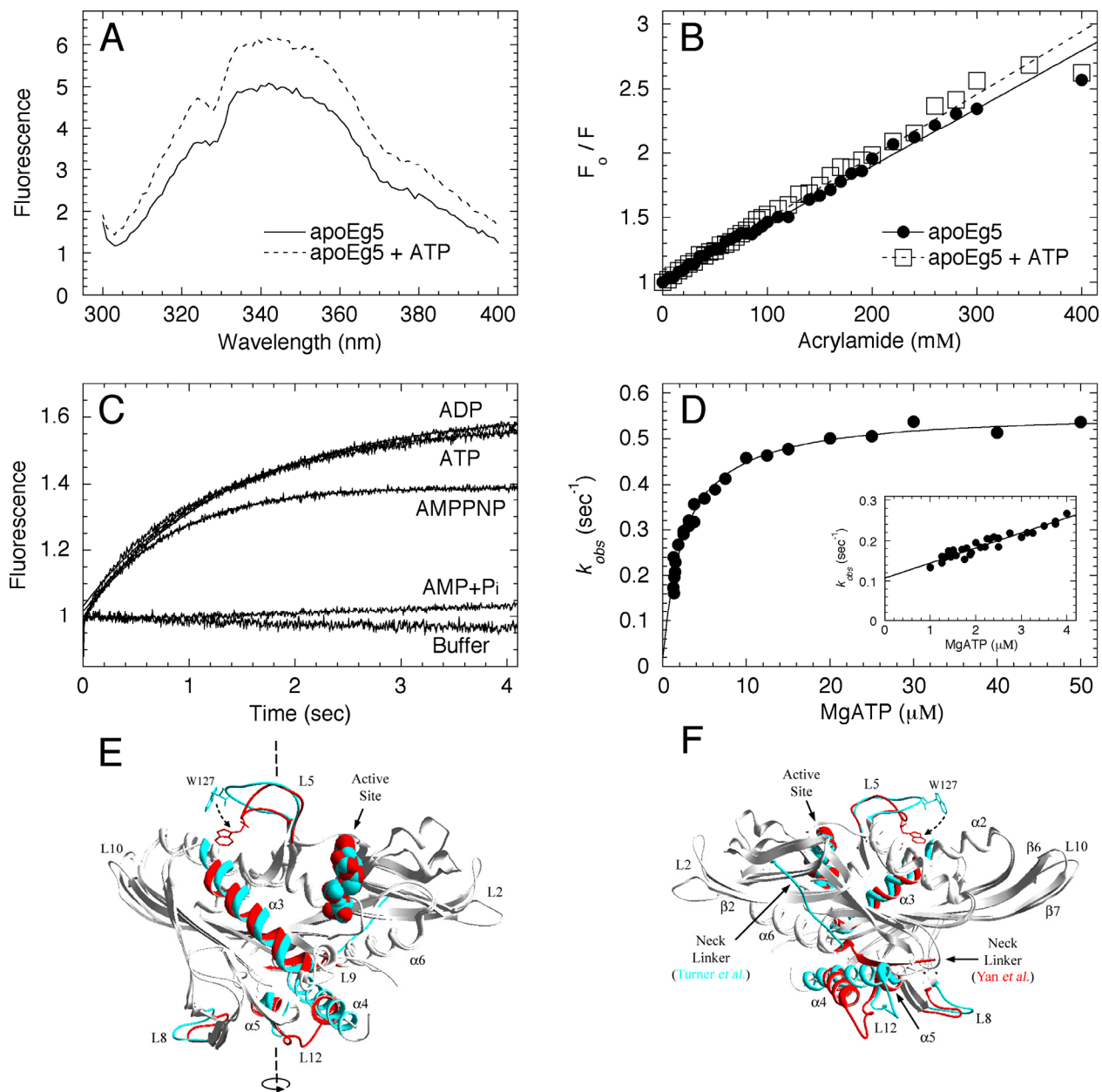


Figure 4.3 MgATP binding to apoEg5 by tryptophan fluorescence enhancement

(A) The steady-state fluorescence emission spectra of apoEg5 in the absence and presence of MgATP. Final concentrations: 2 μM apoEg5, \pm 200 μM MgATP. (B) Stern-Volmer plot for acrylamide quenching of apoEg5 tryptophan fluorescence in the absence or presence of MgATP. Final concentrations: 2 μM apoEg5, \pm 500 μM MgATP, 0–400 mM acrylamide. Relative fluorescence intensity changes from quenching (F_0/F) were plotted against acrylamide concentration, and each data set was fit to [Equation 4.2](#). ApoEg5: $K_{sv} = 4.5 \pm 0.5 \text{ M}^{-1}$ and apoEg5+ATP: $K_{sv} = 4.9 \pm 0.6 \text{ M}^{-1}$. (C) The transient increase in apoEg5 tryptophan fluorescence upon rapid mixing with various nucleotides in a stopped-flow instrument. Final concentrations: 2 μM apoEg5, 250 μM MgAXP (as indicated). MgAMP+P_i conditions were achieved by incubating 250 μM MgADP with 0.1 U/ml apyrase for 60 min, followed by mixing in a stopped-flow instrument. (D) The observed exponential rate of MgATP binding to apoEg5 was plotted as a function of MgATP concentration. Final concentrations: 1 μM apoEg5, 1.25–100 μM MgATP. The data were fit to [Equation 4.3](#): $k_{+1}' = 0.54 \pm 0.03 \text{ s}^{-1}$, $k_{-1}' = 0.014 \pm 0.03 \text{ s}^{-1}$, and $K_{d,ATP} = 2.6 \pm 0.5 \text{ }\mu\text{M}$. Note that the constant k_{-1}' has a significant error due to the loss of sensitivity below 1 μM apoEg5. *Inset*, the rates of MgATP binding to apoEg5 at low MgATP concentrations. The data were fit to a linear relationship to yield the apparent second order rate constant defined by the slope ($K_{+1}k_{+1}' = 0.037 \pm 0.002 \text{ }\mu\text{M}^{-1}\text{s}^{-1}$) and the apparent rate of Eg5•ATP dissociation defined by the y-intercept ($k_{-1}^{app} = 0.11 \pm 0.01 \text{ s}^{-1}$). (E and F) Structural representation of the proposed conformational change in loop L5 leading to the enhanced tryptophan fluorescence upon tight ATP binding. The model was generated using DeepView Swiss Pdb Viewer (version 3.7) to superposition the Eg5•ADP structure [PDB code: 1II6 (68); labeled blue] with the monastrol•Eg5•ADP structure [PDB code: 1Q0B (69); labeled red] based on the position of C α atoms of the P-loop region (F102–T112). The microtubule-binding region was oriented at the bottom and loop L5 was visible at the top in both panels. Panel (F) depicts a view of the model after rotating $\sim 180^\circ$ around the axis indicated in panel (E).

A wide variety of chemicals can quench the fluorescence intensity of a fluorophore due to collisional encounters between the two molecules. In order to test whether monastrol could dynamically quench mant-fluorescence in solution, we analyzed the emission spectrum of mantATP in the absence and presence of monastrol. The emission spectra superimposed ([Figure 4.4G](#)), suggesting that monastrol does not quench mant-fluorescence; therefore, the decreased amplitude in [Figure 4.4F](#) cannot be due to collisional fluorescence quenching by monastrol. Because the collision step for ATP binding comes to equilibrium on a time scale much faster than the rate of the isomerization, this experiment monitors the formation of the tightly-bound Eg5*•ATP intermediate. In order for the amplitude to decrease, we assume that monastrol must be bound to the Eg5•ATP collision complex before the first-order isomerization event occurs. One possible explanation for the decreased amplitude is a change in the local environment at the nucleotide-binding site when monastrol binds to Eg5, which results in a lower quantum yield from the mant fluorophore when mantAXP binds tightly to the active site. However, the nature of the structural change(s) at the nucleotide-binding site upon monastrol binding to the Eg5•ATP collision complex remains speculative, though, it does not appear to alter the intrinsic rate constants for the steps of ATP binding.

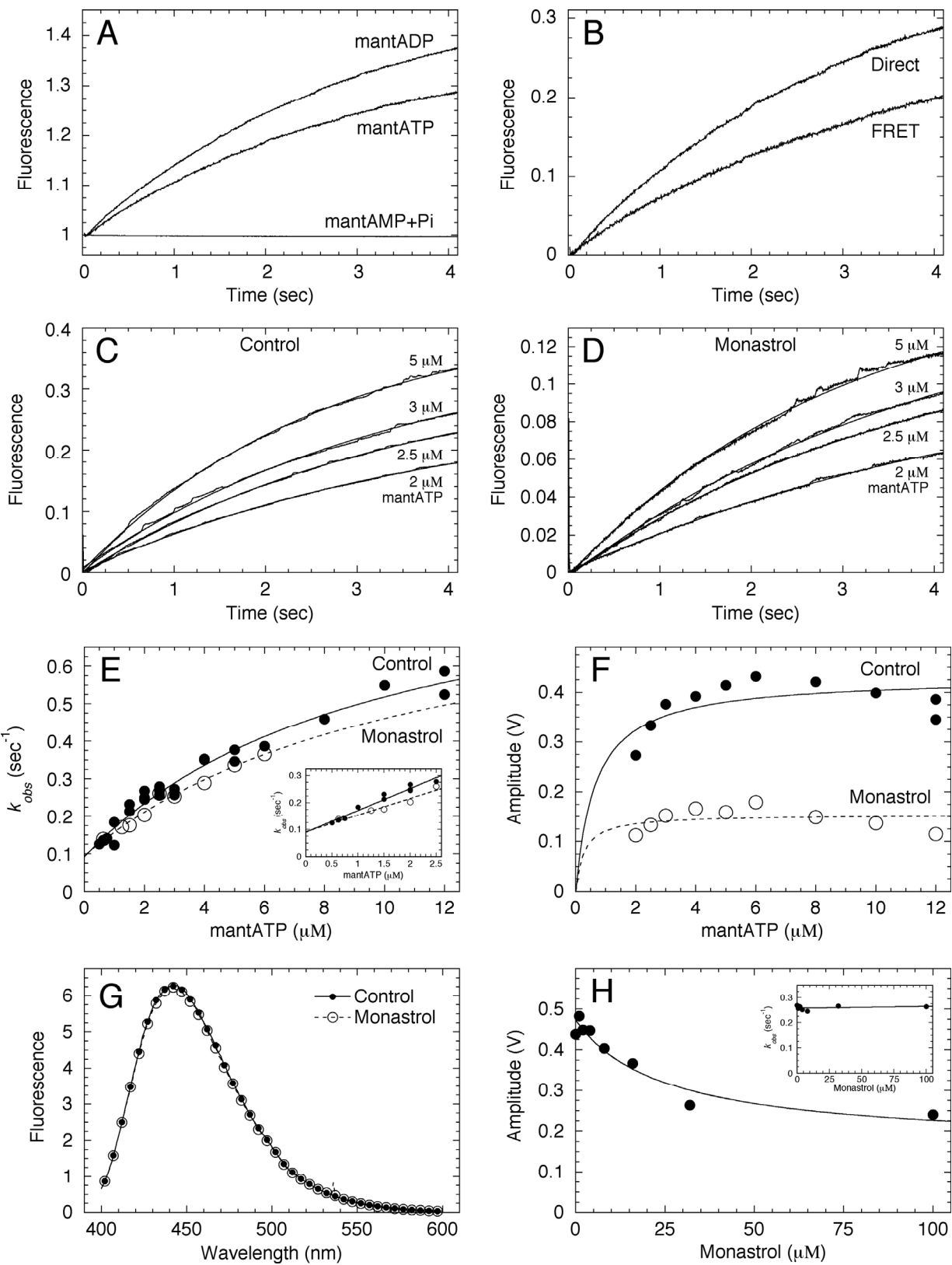


Figure 4.4 MantATP binding to apoEg5 \pm monastrol

(A) Stopped-flow transients showing the exponential increase in mantATP and mantADP fluorescence as a function of time. There was no increase in fluorescence when apoEg5 was rapidly mixed with mantAMP+P_i. Final concentrations: 2 μM apoEg5 for 5 μM mantAXP. (B) Stopped-flow transients showing the exponential increase in mant-fluorescence by either exciting the mant-fluorophore directly, or by monitoring fluorescence resonance energy transfer (FRET) from W127 to the mant-fluorophore. Direct: Ex. 360 nm; Em. 400 nm-cutoff filter. FRET: Ex. 295 nm; Em. 400 nm-cutoff filter. Final concentrations: 2 μM apoEg5 for 5 μM mantATP. Representative stopped-flow transients are shown for mantATP binding to apoEg5 in the absence (C) and presence (D) of monastrol. Final concentrations: 0.5 μM apoEg5 for 0.5–2 μM mantATP, 2 μM apoEg5 for 2–12 μM mantATP, ± 150 μM monastrol. (E) The observed exponential rate of mantATP binding to apoEg5 was plotted as a function of mantATP concentration. Each data set was fit to [Equation 4.3](#). Control: $k_{+1}' = 0.85 \pm 0.1 \text{ s}^{-1}$, $k_{-1}' = 0.09 \pm 0.02 \text{ s}^{-1}$, and $K_{d,mATP} = 9.9 \pm 2.6 \text{ μM}$. Monastrol: $k_{+1}' = 0.78 \pm 0.33 \text{ s}^{-1}$, $k_{-1}' = 0.09 \pm 0.02 \text{ s}^{-1}$, and $K_{d,mATP} = 11.4 \pm 7.9 \text{ μM}$. *Inset*, the rates of mantATP binding to apoEg5 at low mantATP concentrations. The data were fit to a linear relationship to yield the apparent second order rate constant defined by the slope ($K_{+1}k_{+1}' = 0.081 \pm 0.006 \text{ μM}^{-1}\text{s}^{-1}$ and $0.062 \pm 0.01 \text{ μM}^{-1}\text{s}^{-1}$ for control and monastrol, respectively) and the apparent rate of Eg5•mantATP dissociation defined by the y-intercept ($k_{-1}^{app} = 0.09 \pm 0.01 \text{ s}^{-1}$ for both). (F) The amplitude of each transient was plotted against mantATP concentration, and each data set was fit to a hyperbola. Maximum amplitude was $0.43 \pm 0.03 \text{ V}$ for control and $0.15 \pm 0.02 \text{ V}$ for monastrol. (G) The emission spectra of mantATP (no Eg5) in the absence and presence of monastrol. Final concentrations: 10 μM mantATP, ± 150 μM monastrol. (H) The amplitude of mantATP binding transients plotted as a function of monastrol concentration, and the data were fit to [Equation 4.4](#). Final concentrations: 1 μM apoEg5, 2.5 μM mantATP, 0–100 μM monastrol. From the fit of the data, $K_{d,S}$ was $25.3 \pm 13.5 \text{ μM}$. The *inset* shows the observed rate of mantATP binding plotted against monastrol concentration.

4.3.5 Pulse-Chase Experiments Reveal Transient Pre-Hydrolysis Intermediate

In order to measure the presteady-state kinetics of the formation of a tightly-bound Eg5*•ATP complex, we performed pulse-chase experiments in a chemical quench-flow instrument. The experimental design assumes any stably-bound substrate will proceed in the forward reaction, while any loosely-bound or unbound substrate will be diluted by the excess MgATP present in the chase (179). The comparison of the kinetics of product formation obtained by pulse-chase experiments with those obtained by acid-quench experiments can provide 1) direct evidence for the partitioning of the Eg5•ATP intermediate and 2) evidence for a long-lived, stable Eg5*•ATP intermediate prior to ATP hydrolysis. The transients in [Figure 4.5](#) reveal similar kinetics for ATP binding (pulse-chase) and ATP hydrolysis (acid-quench). However, we did observe a difference in the amplitude of the exponential burst phase for the acid quench data when the experiment was performed with monastrol ([Figures 4.5 and 4.6](#)). In the absence of monastrol, the acid quench $A_{0,max} = 0.10 \text{ ADP/site}$ and with monastrol, $A_{0,max} = 0.15 \text{ ADP/site}$ ([Figures 4.5 and 4.6](#)). The acid-quench data lack a significant initial lag phase preceding the exponential phase, suggesting that the Eg5*•ATP complex proceeds immediately and rapidly toward the chemistry step, and that the observed rate of ATP hydrolysis is limited by the slow

conformational change that leads to the tightly-bound $\text{Eg5}^*\cdot\text{ATP}$ hydrolysis competent intermediate.

If monastrol were to bind to apoEg5 and stabilize a conformation that results in an obstructed nucleotide-binding site where ATP cannot collide, then we would expect an additional reduction in burst amplitude in the presence of monastrol. However, by comparing pulse-chase transients in the absence and presence of monastrol, we found that the amplitudes were similar ($A_0 = 0.14$ ADP/site). These results suggest that monastrol is not reducing the apoEg5 population that has the potential to bind ATP.

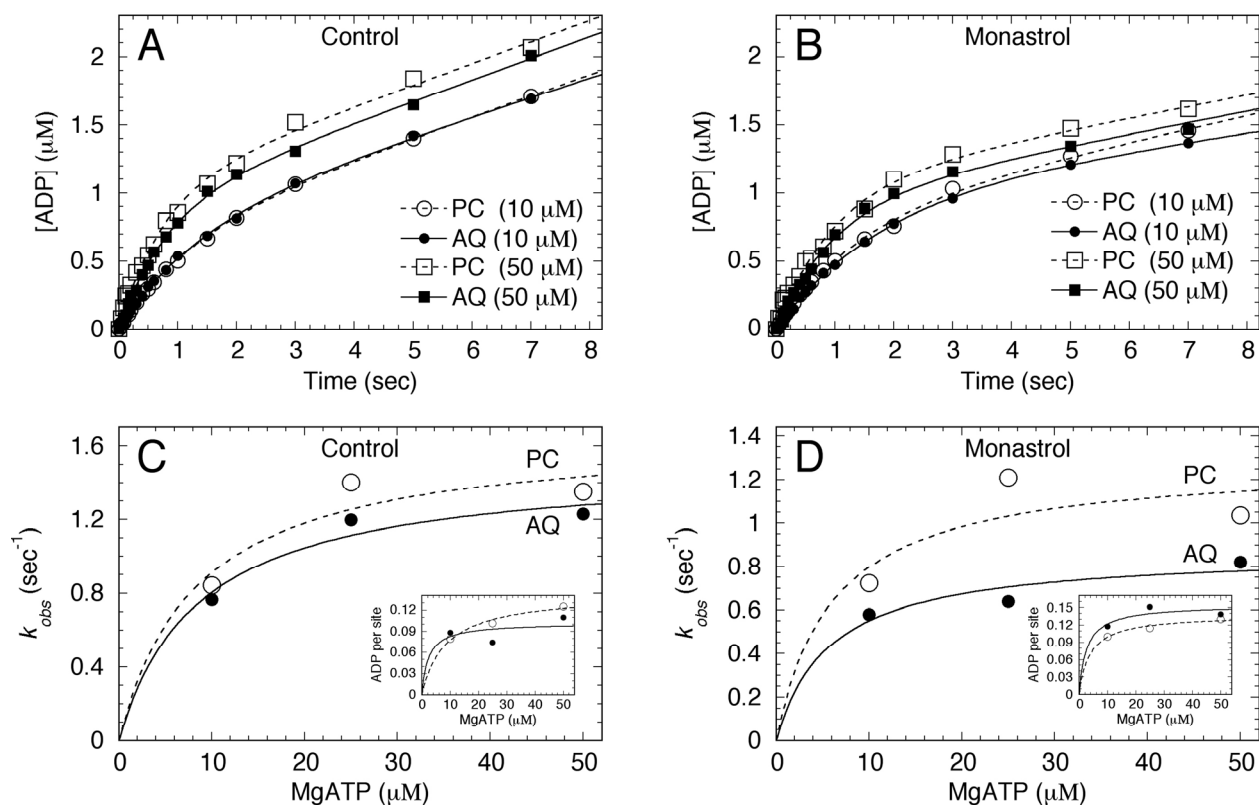


Figure 4.5 MgATP binding to apoEg5 by pulse-chase \pm monastrol

ApoEg5 was reacted with [α - 32 P]MgATP for 0–7 sec in a chemical quench-flow instrument, followed by the non-radioactive MgATP chase for 8 min (>10 turnovers). Final concentrations: 8 μ M apoEg5, \pm 150 μ M monastrol, 10–50 μ M [α - 32 P]MgATP, 10 mM unlabeled MgATP chase. Shown are time courses of [α - 32 P]MgADP product formation for pulse-chase (PC) and acid-quench (AQ) experiments (similar to [Figure 4.6](#); see below) in the absence (**A**) and presence (**B**) of monastrol (MgATP concentrations are indicated). Each transient displayed burst kinetics and was fit to [Equation 4.6](#) to provide the amplitude (A_0) and observed exponential rate (k_b) of the formation of a tight Eg5*•ATP complex (pulse-chase) or the formation of Eg5•ADP•P_i complex (acid-quench), followed by the linear steady-state ATP turnover (k_{ss}). Shown are the maximum observed rates from the pulse-chase and acid-quench experiments in the absence (**C**) and presence (**D**) of monastrol plotted against MgATP concentration. Each data set was fit to a hyperbola. Control: $k_{b,max} = 1.7 \pm 0.3 \text{ s}^{-1}$ for PC and $1.5 \pm 0.2 \text{ s}^{-1}$ for AQ. Monastrol: $k_{b,max} = 1.3 \pm 0.4 \text{ s}^{-1}$ for PC and $0.9 \pm 0.1 \text{ s}^{-1}$ for AQ. **Insets** show amplitude of exponential phase versus MgATP concentration, with each data set fit to a hyperbola. Control: pulse-chase $A_0 = 0.14 \pm 0.01 \text{ ADP/site}$ and acid-quench $A_0 = 0.10 \pm 0.03 \text{ ADP/site}$. Monastrol: pulse-chase $A_0 = 0.14 \pm 0.01 \text{ ADP/site}$ and acid-quench $A_0 = 0.15 \pm 0.02 \text{ ADP/site}$.

4.3.6 ATP Hydrolysis and P_i Product Release are Rapid Steps in Mechanism

We performed acid-quench experiments as a function of MgATP concentration to determine the maximum observed rate of the ATP hydrolysis step and the apparent $K_{d,ATP}$. [Figure 4.6](#) shows that in the absence or presence of monastrol, the maximum observed burst rate of ATP hydrolysis was 1.14 s^{-1} and 0.59 s^{-1} , respectively, while each transient lacked a significant lag phase even at low MgATP concentrations. We also observed a decrease in the expected amplitude for each transient: Control = 0.09 ADP/site (13% of expected amplitude) *versus* Monastrol = 0.15 ADP/site (18% of expected amplitude). These kinetics are quite similar to those obtained from our pulse-chase experiments ([Figure 4.5](#)). Based on these data, ATP hydrolysis appears to be limited by the ATP-dependent isomerization event, and after Eg5 binds ATP tightly, it hydrolyzes the nucleotide and presumably releases the P_i product very rapidly.

To directly measure the kinetics of P_i product release from the Eg5 active site after ATP hydrolysis, we performed stopped-flow experiments that detect the change in MDCC-PBP fluorescence upon binding P_i released into solution. Our P_i release kinetics for apoEg5 suggest a rapid P_i product release step after ATP hydrolysis ([Figure 4.7](#)), thereby rendering the ATP hydrolysis step as kinetically irreversible. We also observed a decrease in burst amplitude (0.10 and 0.14 P_i/site; 19% and 16% of expected amplitude; [Figure 4.7D](#)), which was consistent with our ATP hydrolysis kinetics ([Figure 4.6](#)). As shown in [Figure 4.7E](#), the maximum observed rate of P_i product release that was limited by the relatively slow isomerization of the Eg5•ATP collision complex (k_{+1}) was similar in the absence or presence of monastrol (Control: 0.42 s^{-1} ; Monastrol: 0.44 s^{-1}).

These results suggest that after apoEg5 undergoes the ATP-dependent isomerization, it rapidly hydrolyzes ATP and immediately releases P_i product. The rate of ATP hydrolysis by the Mt•Eg5 complex was at least 12-fold faster than the observed rate for apoEg5 (1.14 s⁻¹ *versus* 13.3 s⁻¹; [Figures 3.5 and 3.6](#)). A fast reaction that occurs in series with a slow reaction will proceed at the rate of the slow reaction (179), thus the rate of ATP hydrolysis will be limited by the relatively slow, ATP-promoted isomerization step. There was not a considerable lag phase in the ATP hydrolysis kinetics, thus implying that the two steps in the mechanism occur at significantly different rates (>10-fold) (179). Likewise, the release of P_i product was measured at the same observed rate as the isomerization step without a substantial initial lag phase corresponding to ATP binding and ATP hydrolysis. Taken together, these data indicate that the Eg5*•ATP and the Eg5•ADP•P_i intermediates are kinetically transient. Our pulse-chase data support this hypothesis given the similar rates and amplitudes of the pulse-chase transients compared to acid-quench transients ([Figure 4.5](#)).

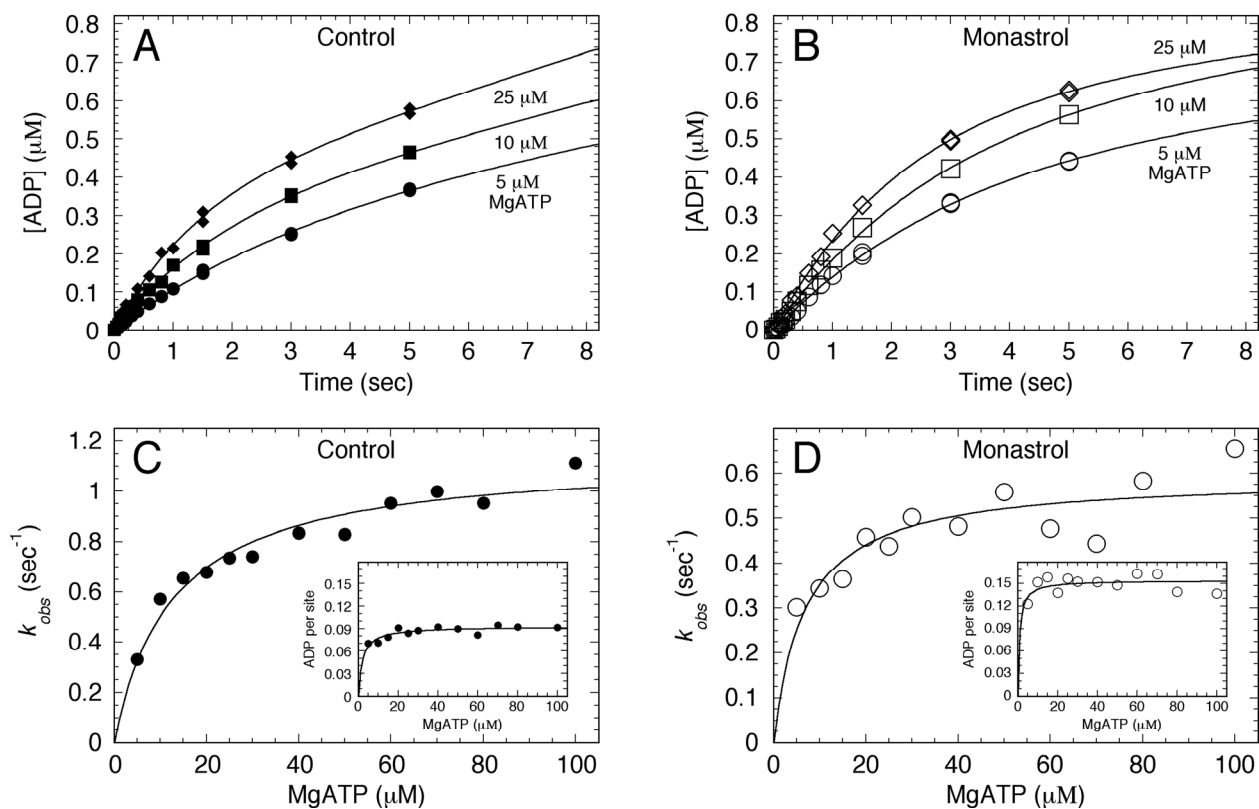


Figure 4.6 Presteady-state kinetics of ATP hydrolysis \pm monastrol

Time course of $[\alpha\text{-}^{32}\text{P}]\text{MgADP}\cdot\text{P}_i$ product formation after rapidly mixing apoEg5 in the absence (A) or presence (B) of monastrol with increasing MgATP concentrations in a chemical quench-flow instrument. Final concentrations: 4 μM apoEg5, 5–100 μM $[\alpha\text{-}^{32}\text{P}]\text{MgATP}$, \pm 150 μM monastrol. (C) The observed exponential rate of product formation in the absence of monastrol was plotted as a function of MgATP concentration. The data were fit to a hyperbola to define the maximum observed rate of ATP hydrolysis, $k_{b,max} = 1.14 \pm 0.05 \text{ s}^{-1}$ and $K_{d,ATP} = 12.7 \pm 2.0 \mu\text{M}$. *Inset*, the amplitude of the exponential burst phase was plotted versus MgATP and the data were fit to a hyperbola: $A_{0,max} = 0.093 \pm 0.002 \text{ ADP/site}$ (13% of expected amplitude based on Eg5 site concentration). (D) The exponential burst rate in the presence of monastrol was plotted as a function of MgATP concentration: $k_{b,max} = 0.59 \pm 0.04 \text{ s}^{-1}$ and $K_{d,ATP} = 6.8 \pm 2.1 \mu\text{M}$. *Inset*, the burst amplitude was plotted versus MgATP: $A_{0,max} = 0.15 \pm 0.005 \text{ ADP/site}$ (18% of expected amplitude).

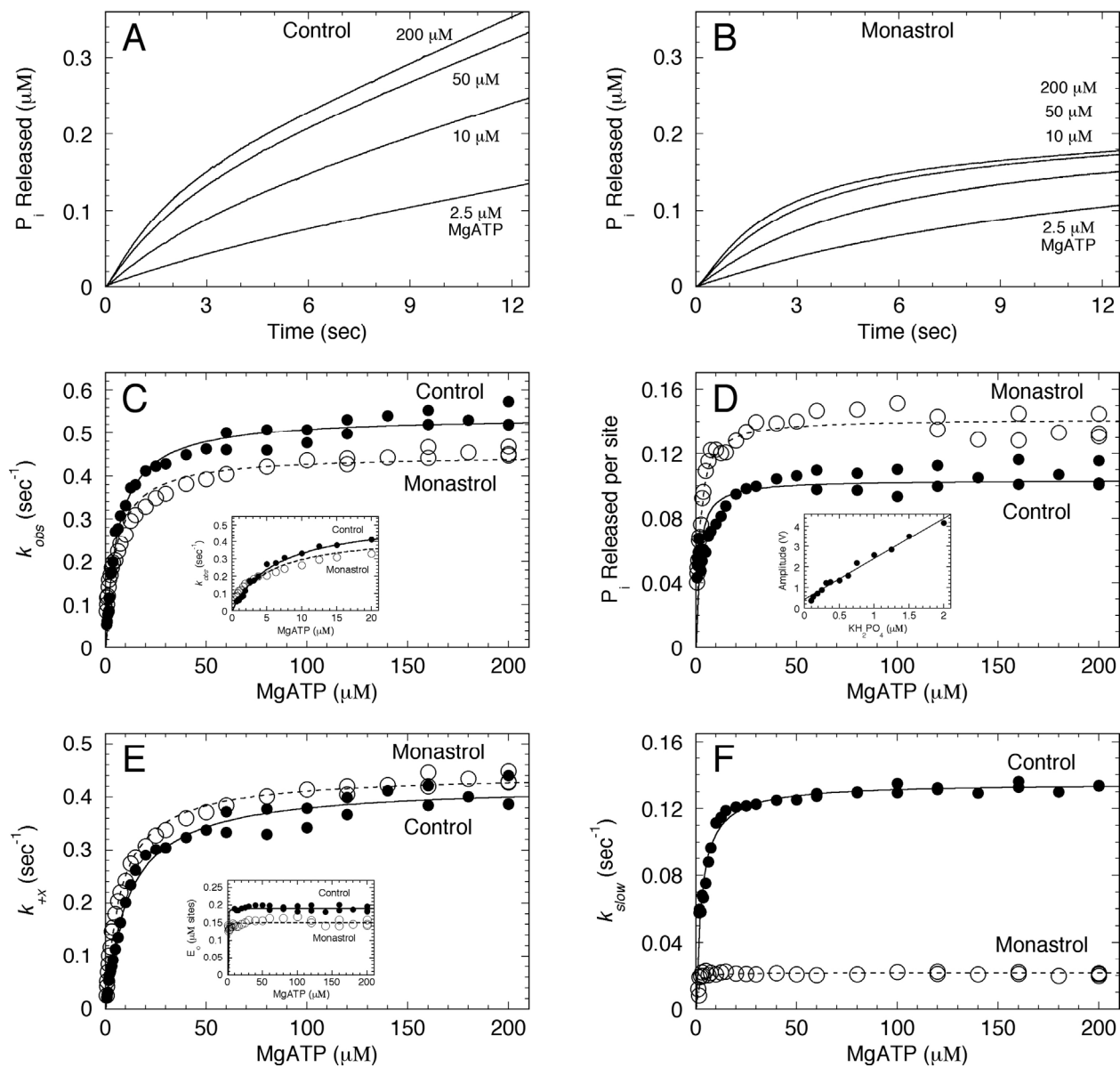


Figure 4.7 Presteady-state kinetics of P_i product release \pm monastrol

ApoEg5 plus MDCC-PBP was rapidly mixed with increasing MgATP concentrations, and the fluorescence enhancement of MDCC-PBP binding inorganic phosphate (P_i) was monitored in a stopped-flow instrument. Final concentrations: 1 μ M apoEg5, \pm 150 μ M monastrol, 5 μ M MDCC-PBP, 0.05 U/ml PNPase, 75 μ M MEG, 0.625–200 μ M MgATP. The concentration of P_i product released from apoEg5 (MgATP concentrations are indicated) in the absence (**A**) and presence (**B**) of monastrol was plotted as a function of time. Each transient displayed burst kinetics and was fit to [Equation 4.6](#). (**C**) The exponential rate of P_i release was plotted *versus* MgATP concentration. The data were fit to a hyperbola. Control: $k_{b,max} = 0.54 \pm 0.01 \text{ s}^{-1}$ and $K_{1/2,ATP} = 6.3 \pm 0.3 \text{ }\mu\text{M}$. Monastrol: $k_{b,max} = 0.45 \pm 0.01 \text{ s}^{-1}$ and $K_{1/2,ATP} = 5.1 \pm 0.4 \text{ }\mu\text{M}$. The *inset* shows the data from 0–20 μ M MgATP. (**D**) The amplitude of the fast exponential phase of each transient was plotted as a function of MgATP concentration. Each data set was fit to a hyperbola. Control: $A_{0,max} = 0.10 \pm 0.003 \text{ P}_i/\text{site}$ (19% of expected amplitude based on Eg5 site concentration) and $K_{1/2,ATP} = 1.6 \pm 0.3 \text{ }\mu\text{M}$. Monastrol: $A_{0,max} = 0.14 \pm 0.002 \text{ }\mu\text{M}$ (15% of expected amplitude) and $K_{1/2,ATP} = 1.8 \pm 0.1 \text{ }\mu\text{M}$. The *inset* shows the calibration curve used to convert monitored fluorescence voltage to known phosphate concentration. (**E**) The rate of P_i product release, which was limited by the slow isomerization of the Eg5•ATP collision complex, was determined by fitting the P_i release data to [Equations 4.6-4.9](#), then $k_{+1'}$ was plotted as a function of MgATP concentration. Each data set was fit to a hyperbola. Control: $k_{+1'} = 0.42 \pm 0.006 \text{ s}^{-1}$ and $K_{1/2,ATP} = 11.5 \pm 0.8 \text{ }\mu\text{M}$. Monastrol: $k_{+1'} = 0.44 \pm 0.003 \text{ s}^{-1}$ and $K_{1/2,ATP} = 7.6 \pm 0.3 \text{ }\mu\text{M}$. The *inset* shows the modeled Eg5 site concentration (E_0) that contributed to the first ATP turnover as a function of MgATP concentration. (**F**) The slow rate after P_i release (k_{slow}) was plotted as a function of MgATP concentration and each data set was fit to a hyperbola. Control: $k_{slow} = 0.14 \pm 0.001 \text{ s}^{-1}$ and $K_{1/2,ATP} = 2.9 \pm 0.2 \text{ }\mu\text{M}$. Monastrol: $k_{slow} = 0.022 \pm 0.001 \text{ s}^{-1}$ and $K_{1/2,ATP} = 0.6 \pm 0.2 \text{ }\mu\text{M}$.

4.3.7 Reduction of Product Burst Amplitude Rescued by Microtubules

Data sets from pulse-chase, acid-quench, and P_i product release experiments show a considerable decrease in amplitude of the fast exponential phase for each transient. Several factors could contribute to the reduced amplitude: 1) a slightly heterogeneous apoEg5 preparation where a subpopulation (< 5%) retains ADP at the nucleotide-binding site, 2) inactive apoEg5, 3) weak ATP binding, 4) reversals at the ATP hydrolysis step, and/or 5) “non-productive” apoEg5 enzyme that cannot generate the ATP-promoted structural transitions required to proceed forward to ATP hydrolysis. A slight heterogeneity in the apoEg5 population and inactive apoEg5 protein cannot fully explain the reduced burst amplitude based on the results presented in [Figure 4.1](#). In addition, there is no evidence for weak ATP binding. In fact, the $K_{m,ATP}$ was 0.17 μ M. As already mentioned, an increase in the intrinsic rate of ATP re-synthesis (k_{-2}) cannot explain the observed kinetics of ATP hydrolysis and P_i product release ([Figure 4.9](#); see further details in [Section 4.3.8](#)). In order to evaluate whether adsorption of apoEg5 to the walls of the reaction tubes was leading to a loss in enzymatic sites, we followed steady-state ATP turnover in the presence of BSA, IgG, or ovalbumin at 0.25 mg/ml. We did not observe a significant difference in the rate of ATP turnover by adding the additional protein ([Figure 4.8A](#)). Interestingly, the steady-state ATPase activity of apoEg5 in the presence of microtubules

provided a maximum rate of ATP turnover that was suggestive of fully active protein ([Table 4.1](#)).

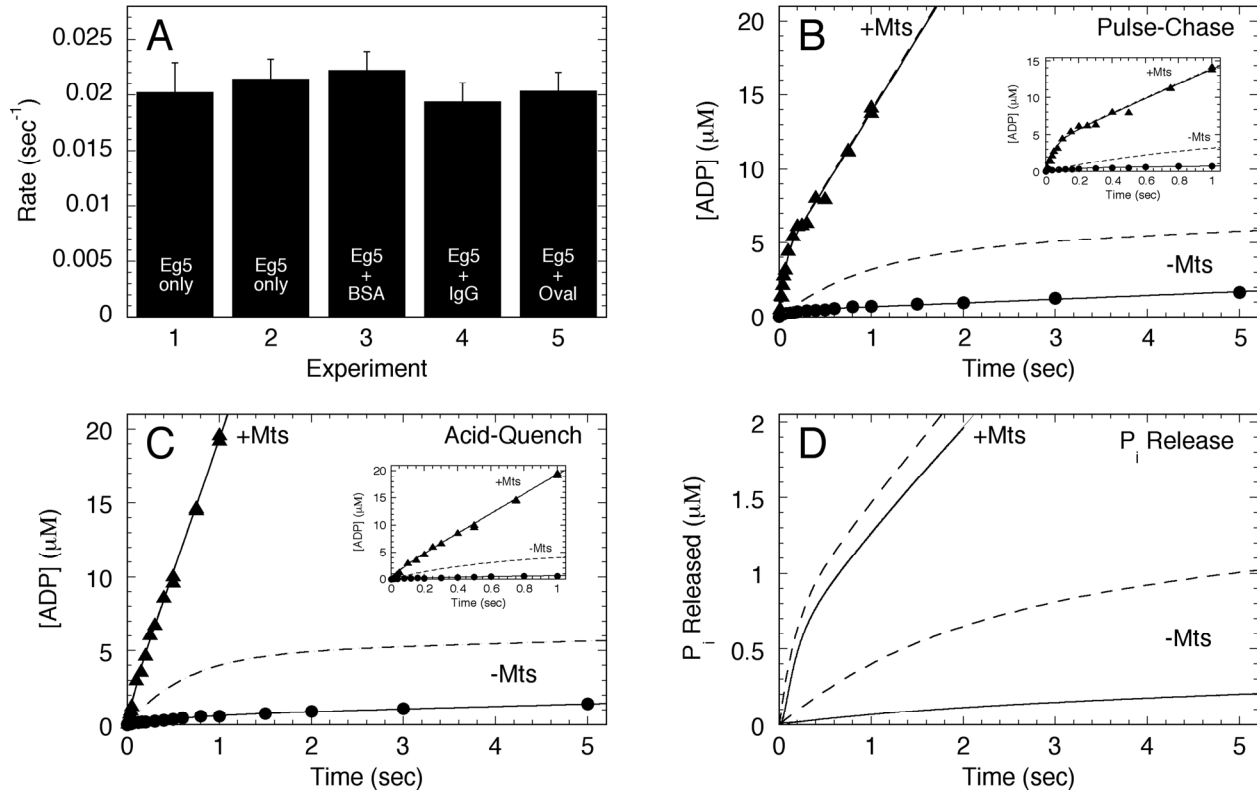


Figure 4.8 Microtubules rescue lowered burst amplitudes

(A) The maximum rate of ATP turnover by apoEg5 was determined under various reaction conditions (as indicated). Final concentrations: 2 μM apoEg5, \pm 0.25 mg/ml BSA, IgG, or Ovalbumin, 200 μM [α -³²P]MgATP. Error bars indicate the standard error in the fit of the velocity data for each experiment. **(B)** Time courses of [α -³²P]MgADP product formation for pulse-chase experiments in the absence and presence of microtubules (as indicated). Final concentrations: 5 μM apoEg5, \pm 6 μM tubulin, 20 μM Taxol, 100 μM [α -³²P]MgATP, \pm 100 mM KCl, 10 mM unlabeled MgATP chase. The dashed curves represent expected kinetics of product formation assuming that the entire Eg5 population contributed to the first turnover event. The *insets* show the data between 0–1 sec. In the absence of microtubules, the amplitude was 0.09 ADP/site (10% of expected), and in the presence of microtubules, the amplitude was 0.76 ADP/site (98% of expected). **(C)** Time courses of [α -³²P]MgADP product formation for acid-quench experiments in the absence and presence of microtubules (as indicated). Final concentrations: 5 μM apoEg5, \pm 6 μM tubulin, 20 μM Taxol, 100 μM [α -³²P]MgATP, \pm 100 mM KCl. In the absence of microtubules, the amplitude was 0.12 ADP/site (12% of expected), and in the presence of microtubules, the amplitude was 0.26 ADP/site (96% of expected). **(D)** The concentration of P_i product released from apoEg5 in the absence and presence of microtubules was plotted as a function of time. Final concentrations: 1 μM apoEg5, \pm 2 μM tubulin, 20 μM Taxol, 5 μM MDCC-PBP, 0.05 U/ml PNPase, 75 μM MEG, 100 μM MgATP, \pm 100 mM KCl. In the absence of microtubules, the amplitude was 0.11 P_i released/site (14% of expected), and in the presence of microtubules, the amplitude was 0.57 P_i released/site (80% of expected).

In order to directly measure the activity of the apoEg5 protein used in the presteady-state experiments, we repeated the experiments with the Mt•Eg5 complex. When pulse-chase, acid-quench, and P_i product release experiments were performed with the Mt•Eg5 complex, we observed >95% of the expected amplitude for the burst of product formation [Figure 4.8 (B–D)], suggesting that all apoEg5 protein has the potential for ATP binding and hydrolysis during the first turnover event. These data are consistent with the hypothesis that there is a subpopulation of apoEg5 that cannot drive the structural transitions for ATP hydrolysis; therefore, this population remains silent in the pulse-chase, acid quench, and phosphate release kinetics in the absence of microtubules leading to the observation of a reduction in burst amplitude.

4.3.8 ATP Hydrolysis Reversals and Weak ATP Binding Do Not Explain the Reduction in Burst Amplitude

Two possible explanations for the reduction in burst amplitude are an internal equilibrium that is established at the ATP hydrolysis step, where ATP hydrolysis is followed by ATP re-synthesis and weak ATP binding. Experiments to directly test the first hypothesis (intermediate O¹⁸ exchange) have not been employed in this study. However, we used DynaFit software to simulate the kinetics of product formation when the intrinsic rate constant for ATP re-synthesis (k_{-2}) increases, while the total apoEg5 site concentration remained constant based on the conditions of the experiment. As we increased the value for k_{-2} , the burst amplitude was reduced; however, the initial lag phase was substantially increased and the simulated curves did not follow the actual experimental data at any value of k_{-2} tested [Figure 4.9 (A and B)]. We also tried increasing the off-rate of ATP binding (k_{-1}) during these simulations, but again were unable to attain a good fit of the data [Figure 4.9 (C and D)]. We were unable to find a combination of rate constants for the entire apoEg5 population reporting for ATP binding, ATP hydrolysis, P_i release, and ADP release (Scheme 4.1) that provided a reasonable fit of the data.

On the other hand, if we decreased the apoEg5 concentration to a value similar to the fraction of sites that reported during ATP hydrolysis and P_i release experiments (~15%), the maximum rate of ATP binding at 1 s⁻¹, the forward rates of ATP hydrolysis and P_i release at 10 s⁻¹, and the rate of ADP release at 0.1 s⁻¹, we were able to simulate transients at 10, 25, and 50 μM MgATP within the error of the experiment [Figure 4.9 (E and F)]. For the 25 μM MgATP

transient, the mean square of the least-squares fit using DynaFit was 0.00023 and 0.0000033 for the acid-quench and the P_i release transients, respectively [Figure 4.9 (E and F)]. Whereas, by adjusting the rate constants and holding the apoEg5 concentration fixed (as described above), the “best” least-squares fit provided a mean square of 0.013 and 0.0031 for the acid-quench and P_i release transients, respectively [Figure 4.9 (A–D), insets]. These simulation results suggest that our proposed mechanism, in which a substantial fraction of “non-productive” apoEg5 is unable to properly bind and hydrolyze ATP, remains the best explanation for the observed kinetics in the presteady-state experiments.

4.3.9 MantADP Binding Occurs Via a Two-Step Process

We performed mantADP binding experiments in the absence and presence of monastrol to determine the kinetics of ADP binding and release from apoEg5 (Figure 4.10; Scheme 4.2). We observed hyperbolic mantADP binding kinetics, which is indicative of at least two-step binding of ADP as observed for ATP (Figures 4.3 and 4.4). The off-rate for mantADP binding, as determined from the extrapolation of the fit of the data back to the y -axis (Control: 0.13 s^{-1} ; Monastrol: 0.08 s^{-1}), was similar to the rate of the slow step after P_i product release that limits steady-state ATP turnover (Control: 0.14 s^{-1} ; Monastrol: 0.022 s^{-1}) (Figure 4.7F). The results in Figure 4.10 document two ADP intermediates (Scheme 4.2): the Eg5•ADP collision complex and the Eg5*•ADP intermediate detected by saturation of the observed rate for mantADP binding.

In the presence of monastrol, we observed a faster rate for the isomerization of the Eg5•mantADP collision complex (Control: 0.55 s^{-1} versus Monastrol: 1.3 s^{-1}) (Figure 4.10B). In addition, the amplitude of each transient was decreased to a similar extent as the mantATP binding transients (compare Figure 4.4F with Figure 4.10C), suggesting that an alteration of the nucleotide-binding site environment by monastrol lowers the quantum yield of mantADP as well.

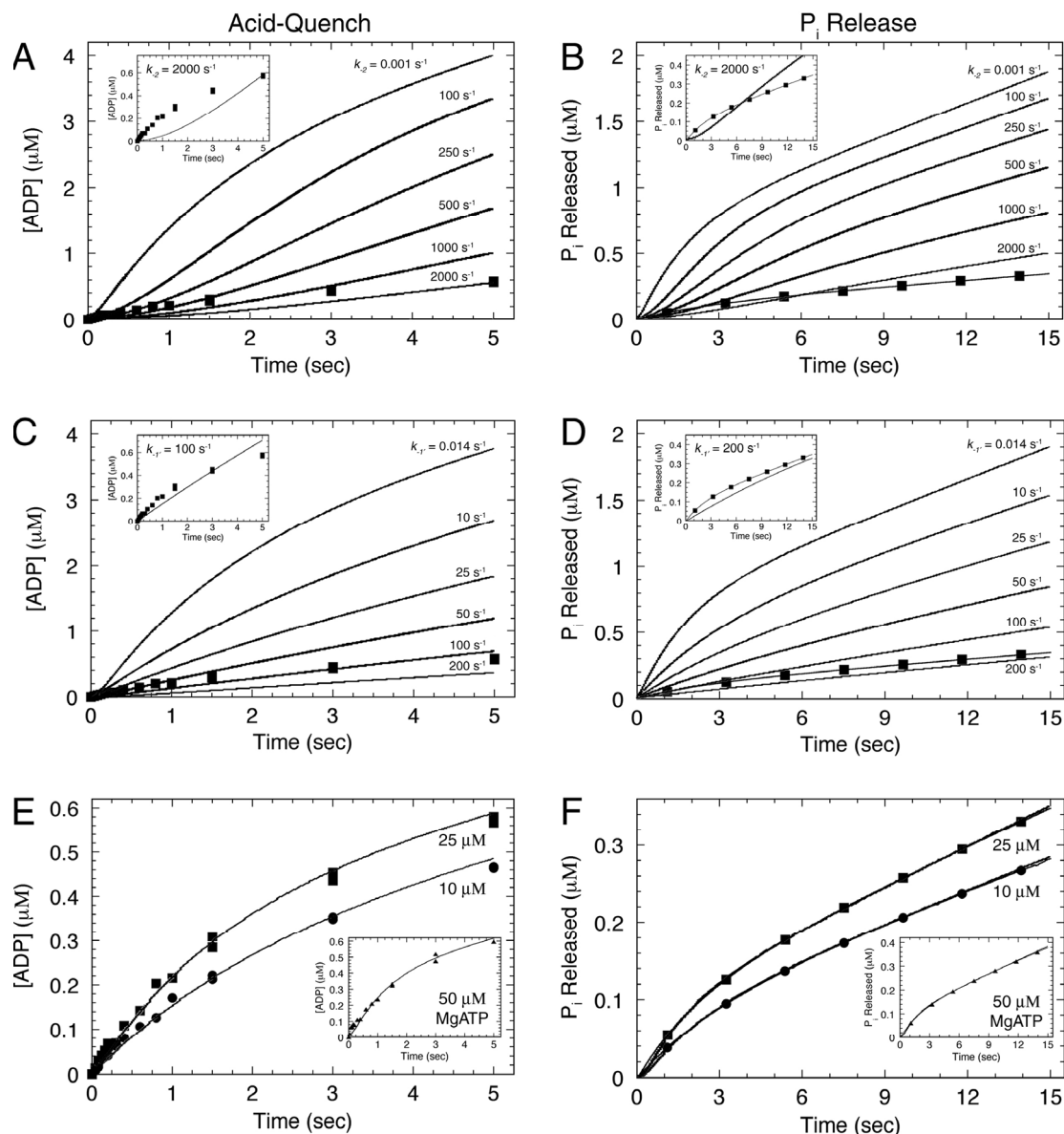


Figure 4.9 DynaFit simulations to understand burst amplitude reduction

The acid-quench (**A**) and P_i release (**B**) kinetics at $25 \mu\text{M}$ MgATP were simulated based on a mechanism where the intrinsic rate of ATP re-synthesis (k_{-2}) increased from 0.001 s^{-1} to 2000 s^{-1} . Experimental conditions: $4 \mu\text{M}$ apoEg5 (acid-quench) and $1 \mu\text{M}$ apoEg5 (P_i release), $25 \mu\text{M}$ MgATP. Simulated constants: $k_{+1} = 100 \mu\text{M}^{-1}\text{s}^{-1}$; $k_{-1} = 2700 \text{ s}^{-1}$; $k_{+1'} = 1 \text{ s}^{-1}$; $k_{-1'} = 0.014 \text{ s}^{-1}$; $k_{+2} = 10 \text{ s}^{-1}$; $k_{-2} = 0.001$ to 2000 s^{-1} (as indicated); $k_{+3} = 10 \text{ s}^{-1}$; $k_{+4} = 0.1 \text{ s}^{-1}$; E_0 = total apoEg5 protein. **Insets**, the “best” fit of the kinetics at $25 \mu\text{M}$ MgATP where $k_{-2} = 2000 \text{ s}^{-1}$. (**C and D**) Simulations of acid-quench and P_i release kinetics, respectively, based on a mechanism where the off-rate for ATP binding increases from 0.014 s^{-1} to 200 s^{-1} (as indicated). Simulated constants: $k_{+1} = 100 \mu\text{M}^{-1}\text{s}^{-1}$; $k_{-1} = 2700 \text{ s}^{-1}$; $k_{+1'} = 1 \text{ s}^{-1}$; $k_{-1'} = 0.014$ – 200 s^{-1} (as indicated); $k_{+2} = 10 \text{ s}^{-1}$; $k_{-2} = 0.001 \text{ s}^{-1}$; $k_{+3} = 10 \text{ s}^{-1}$; $k_{+4} = 0.1 \text{ s}^{-1}$; E_0 = total apoEg5 protein. **Insets**, the “best” fit of the kinetics at $25 \mu\text{M}$ MgATP where $k_{-1'} = 100 \text{ s}^{-1}$ (acid-quench) and 200 s^{-1} (P_i release). (**E and F**) The simulations at 10 , 25 , and $50 \mu\text{M}$ MgATP (**insets**) as proposed for the apoEg5 mechanism from [Scheme 4.1](#) and [Figure 4.11](#). Simulated constants: $k_{+1} = 100 \mu\text{M}^{-1}\text{s}^{-1}$; $k_{-1} = 2700 \text{ s}^{-1}$; $k_{+1'} = 1 \text{ s}^{-1}$; $k_{-1'} = 0.014 \text{ s}^{-1}$; $k_{+2} = 10 \text{ s}^{-1}$; $k_{-2} = 0.001 \text{ s}^{-1}$; $k_{+3} = 10 \text{ s}^{-1}$; $k_{+4} = 0.1 \text{ s}^{-1}$; $E_0 = 0.15$.

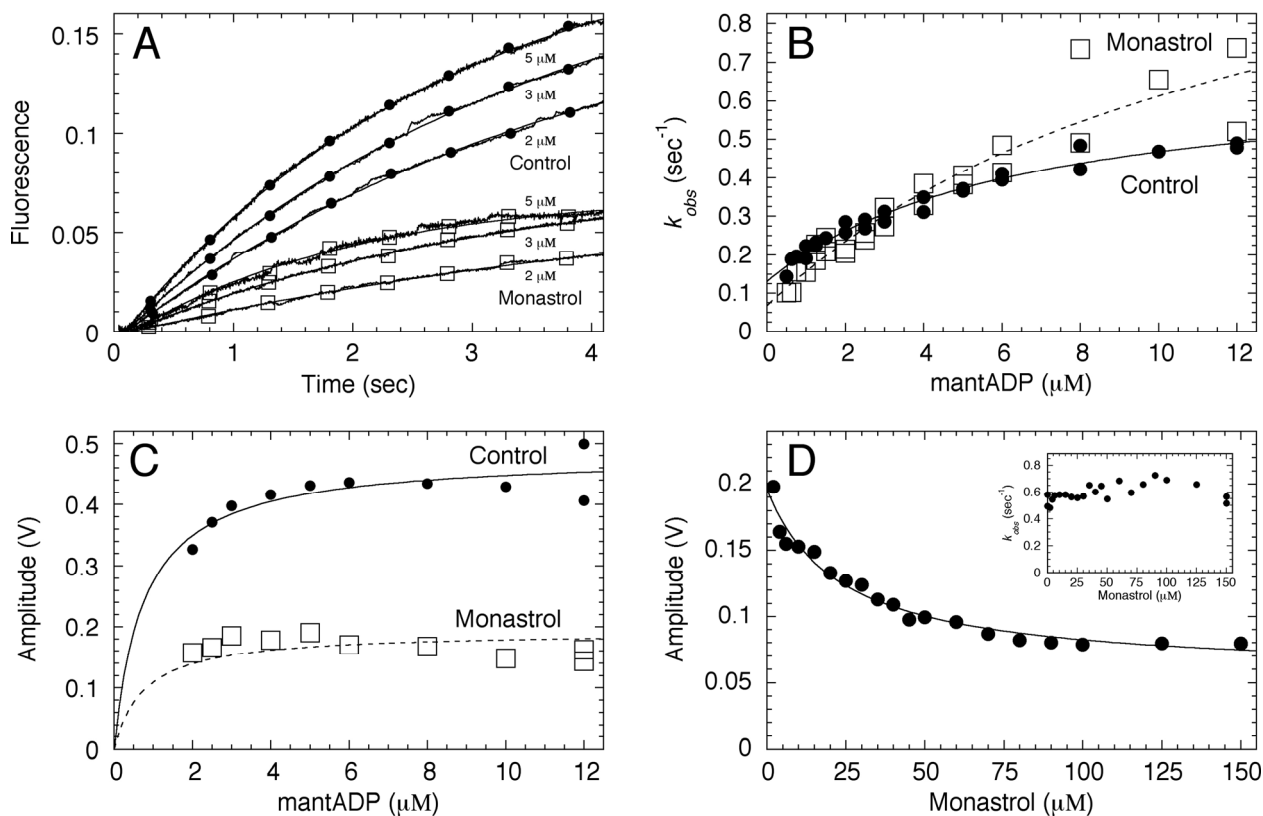


Figure 4.10 MantADP binding to apoEg5 \pm monastrol

(A) Representative stopped-flow transients are shown for mantADP binding to apoEg5 in the absence and presence of monastrol. Final concentrations: 0.5 μM apoEg5 for 0.5–2 μM mantADP, 2 μM apoEg5 for 2–12 μM mantADP, \pm 150 μM monastrol. (B) The observed exponential rate of mantADP binding to apoEg5 was plotted as a function of mantADP concentration. Each data set was fit to Equation 4.5. Control: $k_{-4} = 0.55 \pm 0.04 \text{ s}^{-1}$, $K_{1/2,mADP} = 6.5 \pm 1.4 \mu\text{M}$, and $k_{+4} = 0.13 \pm 0.01 \text{ s}^{-1}$. Monastrol: $k_{-4} = 1.3 \pm 0.4 \text{ s}^{-1}$, $K_{1/2,mADP} = 13.1 \pm 7.7 \mu\text{M}$, and $k_{+4} = 0.07 \text{ s}^{-1} \pm 0.04$. (C) The amplitude of each transient was plotted against mantADP concentration, and each data set was fit to a hyperbola. Maximum amplitude was $0.48 \pm 0.02 \text{ V}$ for control and $0.19 \pm 0.01 \text{ V}$ for monastrol. (D) The amplitude of mantADP binding transients plotted as a function of monastrol concentration, and the data were fit to Equation 4.4. Final concentrations: 1 μM apoEg5, 5 μM mantADP, 0–150 μM monastrol. From the fit of the data, $K_{d,S}$ was $23.4 \pm 4.8 \mu\text{M}$. The *inset* shows the observed rate of mantADP binding plotted against monastrol concentration.

4.3.10 Monastrol Slows ADP Product Release

$[\alpha\text{-}^{32}\text{P}]\text{ADP}$ release from Eg5 was a slow step in the absence of monastrol and was slowed further in the presence of monastrol (0.05 s^{-1} versus 0.007 s^{-1}). This is consistent with the observation of presteady-state burst kinetics in the pulse-chase, acid-quench, and P_i release experiments presented in this manuscript. The data for acid-quench and P_i release experiments were modeled to a two-step irreversible mechanism to obtain the rate constants of ATP

hydrolysis (k_{+2}) and P_i product release (k_{+3}), respectively, and the rate constant for the slow step after P_i release (ADP release) that limits steady-state ATP turnover (k_{slow}). For these experiments, k_{slow} was 0.14 s^{-1} in the absence of monastrol and 0.025 s^{-1} in the presence of monastrol, and the maximum observed rate of ATP turnover was inhibited by monastrol (0.019 s^{-1} to 0.003 s^{-1}). The inhibition of the rate of ADP release correlates well with the reduction in the rate of ATP turnover, however, there is a 7-fold difference between the rate of ADP release and the steady-state k_{cat} under both conditions. Our hypothesis for this difference is a subpopulation of apoEg5 that either cannot bind ATP or cannot promote the conformational change to generate the ATP hydrolysis-competent intermediate. Nevertheless, this “non-productive” subpopulation of apoEg5 is present in the absence of monastrol, suggesting that it is not the result of monastrol binding.

4.3.11 Monastrol Binds Weakly to the Eg5•ATP and Eg5•ADP Collision Complexes

In both mantATP and mantADP binding experiments, we observed a marked decrease in the amplitude of each transient in the presence of monastrol. To determine the monastrol concentration-dependence of this phenomenon, we performed mantAXP binding experiments as a function of monastrol concentration ([Figure 4.4H](#) and [Figure 4.10D](#)). In both experiments, we obtained an apparent $K_{d,S} = 25\text{ }\mu\text{M}$, which was an order of magnitude weaker than the apparent $K_{d,S}$ measured by steady-state ATPase inhibition: $K_{d,S} = 2.3\text{ }\mu\text{M}$; [see [Figure 3.1A](#)]. In addition, the results in [Figure 4.3C](#) show that MgADP and MgATP trigger the enhancement of tryptophan fluorescence at the same rate and amplitude, suggesting that this change in fluorescence is a readout of the same structural transition of loop L5 achieved by either ADP or ATP binding. There is not a detectable signal for direct binding of monastrol to apoEg5, yet these results indicate that monastrol binds by a two-step mechanism ([Figure 4.11](#)). In the first step, monastrol collides and binds weakly to apoEg5 in the absence of nucleotide, and its affinity for Eg5 is tightened by the ATP-dependent (or ADP-dependent) isomerization. We propose that this nucleotide-dependent isomerization is correlated with the “closing” of loop L5, which promotes both tight nucleotide and tight monastrol binding and was detected experimentally by the enhancement of the tryptophan fluorescence ([Figure 4.3](#)). The results suggest that the monastrol weak binding state is detected by the $K_{d,S}$ at $25\text{ }\mu\text{M}$ and that the isomerization to the second

intermediate is detected by the $K_{d,S}$ at 2.3 μM . This closed state achieved by tight nucleotide and monastrol binding would slow the rate of ADP release from the active site. We propose for ADP release that loop L5 adopts the “open” conformation, thus the affinity for ADP is weakened (Figure 4.11).

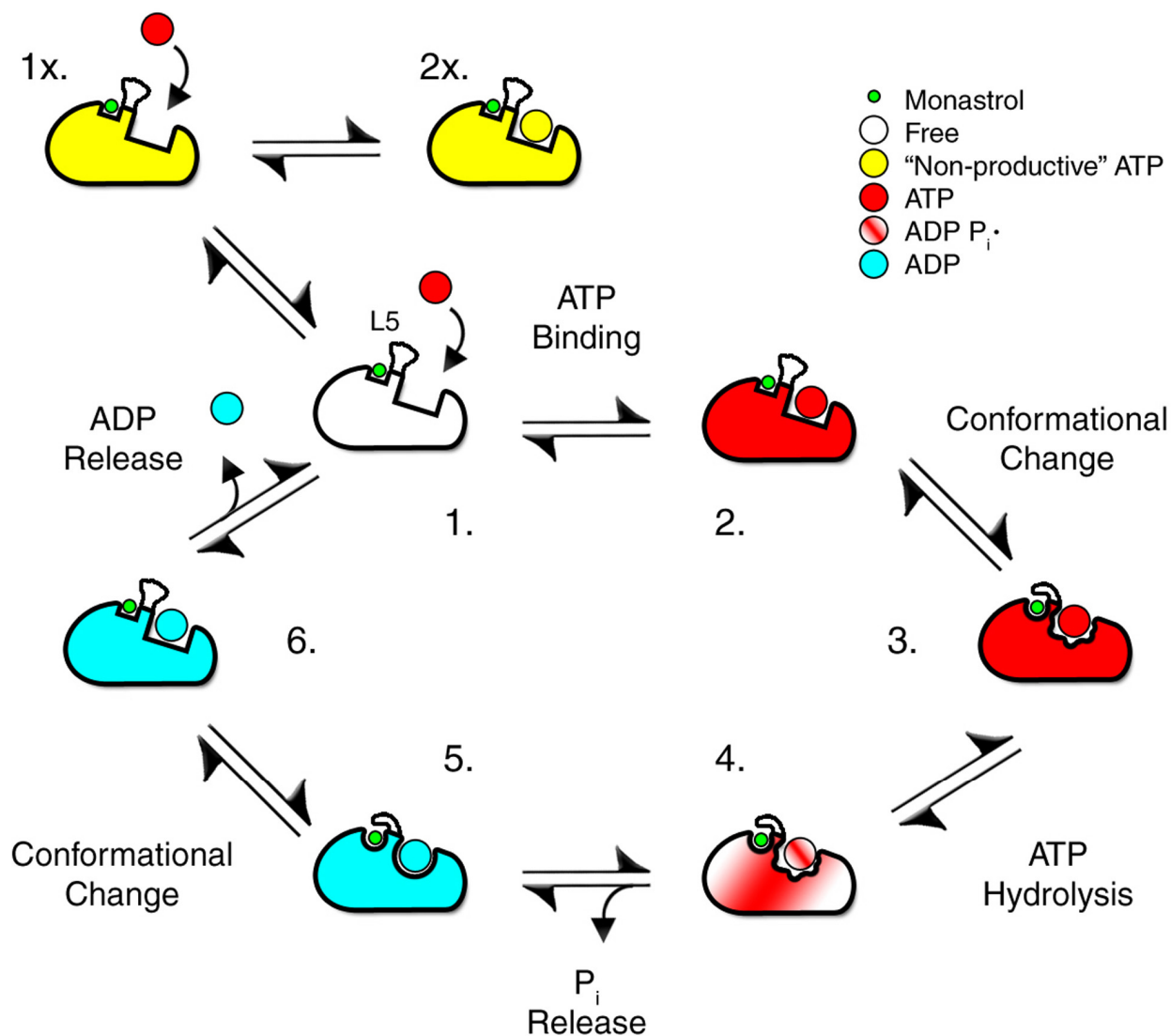


Figure 4.11 Model of apoEg5 ATPase mechanism

The Eg5 motor domain at each stage of the ATPase mechanism is shown with the monastrol binding pocket, the nucleotide-binding site, and loop L5 indicated. Species 1, 2, and 6 are shown as binding monastrol weakly, whereas Species 3, 4, and 5 are tight-binding states. Species 1x and 2x represent the “non-productive” apoEg5 state and the “non-productive” Eg5•ATP collision complex, respectively. The molecules of ATP, ADP, and monastrol are not drawn to scale relative to each other.

Table 4.1 Comparison of Kinetic Constants for ApoEg5 and Mt•Eg5 ATPase ± Monastrol

Constants		ApoEg5	ApoEg5 _s	Mt•Eg5 ^{a,b}	Mt•Eg5 _s ^b
MgATP Binding (Trp fluorescence)	$K_{+1}k_{+1}'$	$0.037 \pm 0.002 \mu\text{M}^{-1}\text{s}^{-1}$			
	k_{+1}'	$0.54 \pm 0.03 \text{ s}^{-1}$	ND ^c	ND	ND
	$K_{d,ATP}$	$2.6 \pm 0.5 \mu\text{M}$			
	k_{-1}'	$0.014 \pm 0.04 \text{ s}^{-1}$			
MantATP Binding	$K_{+1}k_{+1}'$	$0.08 \pm 0.01 \mu\text{M}^{-1}\text{s}^{-1}$	$0.06 \pm 0.01 \mu\text{M}^{-1}\text{s}^{-1}$	$2.2 \pm 0.3 \mu\text{M}^{-1}\text{s}^{-1}$	$2.1 \pm 0.3 \mu\text{M}^{-1}\text{s}^{-1}$
	k_{+1}'	$0.85 \pm 0.10 \text{ s}^{-1}$	$0.78 \pm 0.33 \text{ s}^{-1}$	$47.0 \pm 2.3 \text{ s}^{-1}$	$47.8 \pm 1.9 \text{ s}^{-1}$
	$K_{d,mATP}$	$9.9 \pm 2.6 \mu\text{M}$	$11.4 \pm 7.9 \mu\text{M}$	$7.9 \pm 1.6 \mu\text{M}$	$9.4 \pm 1.9 \mu\text{M}$
	k_{-1}'	$0.09 \pm 0.02 \text{ s}^{-1}$	$0.09 \pm 0.02 \text{ s}^{-1}$	$18 \pm 0.7 \text{ s}^{-1}$	$19.1 \pm 0.7 \text{ s}^{-1}$
	$K_{d,S}$		$25.3 \pm 13.5 \mu\text{M}$		
ATP Binding (Pulse-chase)	$k_{b,max}$	$1.7 \pm 0.3 \text{ s}^{-1}$	$1.3 \pm 0.4 \text{ s}^{-1}$	$22 \pm 3 \text{ s}^{-1}$	$18 \pm 1 \text{ s}^{-1}$
	$K_{d,ATP}$	$8.3 \pm 6.3 \mu\text{M}$	$6.1 \pm 7.6 \mu\text{M}$	$26 \pm 15 \mu\text{M}$	$5 \pm 2 \mu\text{M}$
	$A_{0,max}$	$0.14 \pm 0.01 \text{ ADP/site}$	$0.14 \pm 0.01 \text{ ADP/site}$	$0.75 \pm 0.02 \text{ ADP/site}$	$0.78 \pm 0.03 \text{ ADP/site}$
ATP Hydrolysis (Acid-quench)	$k_{b,max}$	$1.14 \pm 0.05 \text{ s}^{-1}$	$0.59 \pm 0.04 \text{ s}^{-1}$	$11.3 \pm 1.4 \text{ s}^{-1e}$	$11.1 \pm 0.3 \text{ s}^{-1e}$
	$K_{d,ATP}$	$12.7 \pm 2.0 \mu\text{M}$	$6.8 \pm 2.1 \mu\text{M}$	$31 \pm 15 \mu\text{M}$	$9 \pm 2 \mu\text{M}$
	$A_{0,max}$	$0.093 \pm 0.002 \text{ ADP/site}$	$0.15 \pm 0.005 \text{ ADP/site}$	$0.75 \pm 0.02 \text{ ADP/site}$	$0.40 \pm 0.01 \text{ ADP/site}$
	$K_{ss,max}/[\text{Eg5}]$	$0.017 \pm 0.001 \text{ s}^{-1}$	$0.008 \pm 0.001 \text{ s}^{-1}$		
ATP Hydrolysis (Modeling)	$k_{+1}'^e$	$1.03 \pm 0.05 \text{ s}^{-1}$	$0.57 \pm 0.04 \text{ s}^{-1}$	$11 \pm 1 \text{ s}^{-1f}$	$11 \pm 0.3 \text{ s}^{-1f}$
	k_{slow}	$0.14 \pm 0.003 \text{ s}^{-1}$	$0.025 \pm 0.002 \text{ s}^{-1}$	$2.3 \pm 0.2 \text{ s}^{-1}$	$0.1 \pm 0.03 \text{ s}^{-1}$
	E_o	0.5 of 4 μM (13%)	0.7 of 4 μM (18%)	4.9 of 5 μM (99%)	2.0 of 5 μM (40%)
P _i Release (MDCC-PBP)	$k_{b,max}$	$0.54 \pm 0.01 \text{ s}^{-1}$	$0.45 \pm 0.01 \text{ s}^{-1}$	$6.0 \pm 0.1 \text{ s}^{-1}$	$15.8 \pm 0.2 \text{ s}^{-1}$
	$K_{1/2,ATP}$	$6.3 \pm 0.3 \mu\text{M}$	$5.1 \pm 0.4 \mu\text{M}$	$3.7 \pm 0.2 \mu\text{M}$	$7.9 \pm 0.4 \mu\text{M}$
	$A_{0,max}$	$0.10 \pm 0.003 \text{ P}_i/\text{site}$	$0.14 \pm 0.002 \text{ P}_i/\text{site}$	$0.75 \pm 0.01 \text{ P}_i/\text{site}$	$0.38 \pm 0.01 \text{ P}_i/\text{site}$
	$K_{ss,max}/[\text{Eg5}]$	$0.019 \pm 0.0001 \text{ s}^{-1}$	$0.003 \pm 0.0001 \text{ s}^{-1}$		
P _i Release (Modeling)	k_{+1}'	$0.42 \pm 0.006 \text{ s}^{-1}$	$0.44 \pm 0.003 \text{ s}^{-1}$	$5.2 \pm 0.1 \text{ s}^{-1}$	$15.6 \pm 0.2 \text{ s}^{-1}$
	k_{slow}	$0.14 \pm 0.001 \text{ s}^{-1}$	$0.022 \pm 0.0005 \text{ s}^{-1}$	$0.78 \pm 0.01 \text{ s}^{-1}$	$0.19 \pm 0.01 \text{ s}^{-1}$
	E_o	0.19 of 1 μM (19%)	0.15 of 1 μM (15%)	0.5 of 0.5 μM (100%)	0.2 of 0.5 μM (39%)
[α - ³² P]ADP Release ^b	$k_{off,ADP}$	$0.05 \pm 0.001 \text{ s}^{-1}$	$0.007 \pm 0.001 \text{ s}^{-1}$		
MantADP Release		ND	ND	$35.2 \pm 0.6 \text{ s}^{-1}$	$13 \pm 1 \text{ s}^{-1}$
MantADP Binding	$K_{-5}k_{-4}$	$0.07 \pm 0.01 \mu\text{M}^{-1}\text{s}^{-1}$	$0.08 \pm 0.02 \mu\text{M}^{-1}\text{s}^{-1}$		
	k_{-4}	$0.55 \pm 0.04 \text{ s}^{-1}$	$1.3 \pm 0.4 \text{ s}^{-1}$		
	$K_{1/2,mADP}$	$6.5 \pm 1.4 \mu\text{M}$	$13.1 \pm 7.7 \mu\text{M}$	ND	ND
	k_{+4}	$0.13 \pm 0.01 \text{ s}^{-1}$	$0.08 \pm 0.03 \text{ s}^{-1}$		
	$K_{d,S}$		$23.4 \pm 4.8 \mu\text{M}$		
Basal ATPase	k_{cat}	$0.02 \pm 0.003 \text{ s}^{-1}$	$0.003 \pm 0.0001 \text{ s}^{-1h}$		
	$K_{m,ATP}$	$0.17 \pm 0.03 \mu\text{M}$	$0.19 \pm 0.05 \mu\text{M}^h$		
	$k_{cat}/K_{m,ATP}$	$0.12 \pm 0.01 \mu\text{M}^{-1}\text{s}^{-1}$	$0.016 \pm 1.4 \mu\text{M}^{-1}\text{s}^{-1h}$		
	$K_{d,S}$		$2.3 \pm 0.4 \mu\text{M}^b$		
Mt-Activated ATPase	k_{cat}	$5.47 \pm 0.07 \text{ s}^{-1}$		$5.5 \pm 0.3 \text{ s}^{-1}$	$1.2 \pm 0.03 \text{ s}^{-1}$
	$K_{m,ATP}$	$6.95 \pm 0.43 \mu\text{M}$		$9.5 \pm 0.4 \mu\text{M}$	$3.6 \pm 0.3 \mu\text{M}$
	$k_{cat}/K_{m,ATP}$	$0.79 \pm 0.16 \mu\text{M}^{-1}\text{s}^{-1}$	ND	$0.58 \pm 0.03 \mu\text{M}^{-1}\text{s}^{-1}$	$0.33 \pm 0.03 \mu\text{M}^{-1}\text{s}^{-1}$
	$K_{1/2,Mt}$	$0.29 \pm 0.02 \mu\text{M}$		$0.71 \pm 0.6 \mu\text{M}$	$6.7 \pm 0.4 \mu\text{M}$
	$K_{d,S}$				$13.8 \pm 1.0 \mu\text{M}$

^a Mechanistic analysis of the mitotic kinesin Eg5 ([Chapter 2.0](#)). ^b Monastrol inhibition of the mitotic kinesin Eg5 ([Chapter 3.0](#)). ^c ND, not determined. ^d Experiments performed with monomeric HsEg5-437. ^e $k_{+1'}$ = the rate of the slow isomerization of the Eg5•ATP collision complex. ^f Burst kinetics based on 300 μ M MgATP. ^g Fit of data from transient shown in [Figure 4.8D](#). ^h Determined from the linear steady-state phase of the P_i product release transients.

4.4 DISCUSSION

In this study, we have combined steady-state and presteady-state methodologies to define a minimal mechanism of the mitotic Eg5 ATPase in the absence of microtubules ([Figure 4.11](#), [Table 4.1](#)). By comparing the basal Eg5 ATPase to the microtubule-activated ATPase ([Chapter 2.0](#)), we were able to gain insight into the amplification and acceleration of the structural transitions that dictate the microtubule-dependent activation. In addition, we have investigated the mechanistic basis for the allosteric inhibition of the basal Eg5 ATPase by monastrol.

4.4.1 ApoEg5 Was Active, Stable, and Nucleotide-Free

A critical factor for this study was the characterization of the apoEg5 protein obtained from our adopted purification strategy. Steady-state ATPase assays were performed in the absence and presence of microtubules, and the activity under the same experimental conditions was found to be comparable to former Eg5 preparations [[Table 4.1](#); [Table 2.2](#)]. Remarkably, the apoEg5 protein was very stable ([Figure 4.2, inset](#)), despite the lack of ADP at the active site ([Figure 4.1](#)). Therefore, our apoEg5 site concentration can be reasonably estimated to >95% of total protein concentration determined by Bradford assays.

4.4.2 “Non-Productive” versus “Productive” ApoEg5 States

We observed a dramatic difference between the steady-state k_{cat} and the rate of ADP release (rate-limiting step). We also observed a reduction in the expected amplitude for our pulse-chase, acid-quench, and P_i product release experiments. When we divide the maximum velocity of steady-state ATP turnover (0.0017 μ M ADP•s⁻¹) by the concentration of apoEg5 sites that reported during the presteady-state experiments (0.013–0.019 μ M), we obtain a steady-state k_{cat}

at 0.09–0.13 s⁻¹, which is consistent with the rate of ADP release. Control experiments in the presence of microtubules demonstrated that >95% of the Eg5 population can contribute to the first ATP turnover event (Figure 4.8). These data seem to suggest that in the absence of microtubules, there is a subpopulation of apoEg5 that is unable to drive the ATP-dependent structural transitions that are required for ATP hydrolysis during both the first turnover and subsequent ATP turnover events. The experimental results presented in this manuscript support the hypothesis in which a “non-productive” subpopulation of apoEg5 is in equilibrium with a “productive” population, whereby the proportion of the two apoEg5 states is maintained throughout steady-state ATP turnover (Figure 4.11). In contrast, when apoEg5 was bound to microtubules, we observed the entire Eg5 population in the “productive” state, and thus was able to properly bind and hydrolyze ATP (Figure 4.8). These results provide evidence for the role of microtubules in amplifying and accelerating the structural transitions that account for Eg5’s ATPase efficiency.

4.4.3 Substrate Binding Was Dramatically Slower

The kinetics of ATP binding were determined by measuring the intrinsic tryptophan fluorescence enhancement upon MgATP binding (Figure 4.3), as well as monitoring the fluorescence change upon mantATP binding at the apoEg5 active site (Figure 4.4). Both experiments demonstrated that substrate binding to apoEg5 seemed to occur in at least two distinct kinetic steps: formation of the initial weak-binding collision complex (Eg5•ATP) followed by an isomerization of the collision complex that leads to tightened ATP binding (Eg5*•ATP). In comparison to the substrate binding kinetics for the Mt•Eg5 complex, we found that Eg5 has a similar affinity for ATP: $K_{d,mATP} = 9.9 \mu\text{M}$ (apoEg5) *versus* $7.9 \mu\text{M}$ (Mt•Eg5) (Figure 2.10). However, the rate of the isomerization step was approximately 25-fold slower for apoEg5: 0.85 s^{-1} (apoEg5) *versus* 21.0 s^{-1} (Mt•Eg5) (Figure 2.10). We propose that the microtubule amplifies and accelerates the structural transitions in the Eg5 motor domain that lead to tight ATP binding. A recent study suggests that a conformational change in the nucleotide-binding site via the switch-1 region occurs when kinesin-family motors bind to microtubules (194). The microtubule seems to lower the energy barrier for conformational changes in Eg5’s switch regions, thus rendering the kinetic steps of ATP binding much faster.

4.4.4 Structural Transition in Loop L5 Correlates with Movement of the Switch Regions

The insertion loop L5 that interrupts helix $\alpha 2$ varies considerably in sequence among different subfamilies of kinesins, and, for Eg5, seems to be a “hotspot” for specific inhibitors (69, 79, 105). Certainly this loop was not designed to facilitate the binding of these inhibitors, but likely undergoes structural transitions during the ATPase cycle that correlates with the movements of the functional components of the Eg5 catalytic domain, such as switch-1 and switch-2 regions. Loop L5 is located in close proximity to the N-terminal end of helix $\alpha 3$, which in turn is connected to loop L9 that contains the γ -phosphate sensing residue (S233) [Figure 4.3 (E and F)]. Loop L5 contains the lone tryptophan residue in the human Eg5 motor domain. In this study, we have demonstrated a nucleotide-dependent enhancement of tryptophan fluorescence, which marks the conformational changes that occur upon tight ATP or ADP binding to the Eg5 active site. This conformation change in loop L5 appears to occur before ATP hydrolysis, due to the fluorescence enhancement upon AMPPNP binding, and also seems to persist after ATP hydrolysis and P_i product release, due to the sustained fluorescence intensity over the time course for the first turnover event. Thus, we hypothesize that the movement of loop L5 is tightly correlated to Eg5’s mechanochemical cycle. A recent study demonstrated that if loop L5 from Eg5 were replaced with a homologous loop from Kinesin-1, the basal ATPase decreased ~ 2 -fold, thus supporting our hypothesis (105).

All Eg5 crystal structures solved to date contain ADP at the active site (69, 79, 105). Interestingly, the Eg5•ADP•inhibitor crystal structures display an altered conformation of loop L5 compared to the Eg5•ADP structure. The interpretation of this structure was a conformational change in loop L5 that was “induced” by the inhibitor binding. However, our data argue that this “open” to “closed” conformational change in loop L5 occurs normally during the Eg5 ATPase mechanochemical cycle. In addition, when the inhibitor is present in its allosteric site, it stabilizes this Eg5_S•ADP conformation of loop L5, and thus slows ADP product release dramatically. Our mantADP binding data suggest that ADP binds to apoEg5 in a two-step fashion, with a rapid-equilibrium collision step followed by an isomerization of the Eg5•ADP collision complex to tighten the binding of ADP. We also observed an enhancement of tryptophan fluorescence upon ADP binding that was quite similar in rate and amplitude when compared with ATP binding. Therefore, we propose that the structural transition coupled to

ADP product release is rate-limiting in the apoEg5 mechanism, and the conformation of loop L5 correlates with this structural transition to the “open” state ([Figure 4.11](#); Species 6).

4.4.5 Monastrol Binding Occurs Via a Two-Step Mechanism

As previously reported, the substrate binding steps of the Mt•Eg5 ATPase mechanism were not affected by monastrol ([Chapter 3.0](#)). As demonstrated in this study, monastrol also does not significantly affect the kinetics of substrate binding, ATP hydrolysis, and P_i release in the absence of microtubules. However, monastrol does appear to bind the Eg5•ATP and Eg5•ADP collision complexes, and surprisingly alters the nucleotide-binding site environment in a manner that leads to a reduction in the quantum yield from mantAXP fluorescence. Monastrol does not quench the fluorescence of the mant-fluorophore in solution, and ATP binding does not seem to be weakened in the presence of monastrol. A slight decrease in amplitude was also observed in similar experiments performed with the Mt•Eg5 complex ([Figure 3.4](#)), which suggests that a similar nucleotide-binding site environment may be attained when monastrol binds the Mt•Eg5•ATP collision complex.

In this study, we found that monastrol binds to the Eg5•ATP or Eg5•ADP collision complex more weakly than detected by steady-state turnover [25 μM *versus* 2.3 μM; [Figure 3.1A](#)]. We propose that monastrol binds weakly to the nucleotide-free state and Eg5•AXP collision complexes due to the “open” conformation of loop L5; and concomitant with tight nucleotide binding, a conformational change in loop L5 occurs to “close” the inhibitor pocket, thus dramatically increasing Eg5’s affinity for monastrol. A communication pathway from the nucleotide-binding site to loop L5 is possibly mediated through a conformational change in the switch-1 region and is relayed through helix α3 to the insertion loop L5, which is located in close proximity to the N-terminal end of helix α3 ([Figure 4.3E](#)).

In summary, the minimal apoEg5 ATPase mechanism shares similarities in the kinetic steps required for ATP turnover compared to the Mt•Eg5 mechanism, however, the rate constants that define these steps show dramatic differences. ATP binding occurs via a two-step process for both pathways, yet the isomerization of the Eg5•ATP collision complex is dramatically slower for apoEg5. The microtubule appears to amplify and accelerate the conformational changes that tighten ATP binding. ATP hydrolysis and P_i product release are

rapid steps in the mechanism, yet the observed rate constants are significantly slower in the absence of microtubules. In addition, there is no kinetic evidence for ATP hydrolysis reversals for apoEg5 as observed for myosin (214). The structural transition(s) of the Eg5•ADP intermediate coupled to ADP release is the rate-limiting step in the pathway, and this step is dramatically accelerated upon binding to the microtubule (0.05 s^{-1} to 35 s^{-1}) such that ADP release no longer limits steady-state ATP turnover for the Mt•Eg5 complex. Monastrol appears to bind weakly to apoEg5; but after ATP binding and the ATP-dependent isomerization, apoEg5 binds monastrol tightly. This monastrol-stabilized state inhibits the conformational change needed for rapid ADP product release. Therefore, monastrol has stabilized a mechanistically relevant structural state of the Eg5 to elicit its inhibitory effect upon the ATPase cycle.

5.0 CHAPTER FIVE: CONCLUSIONS

Molecular motor proteins that power various activities in eukaryotic cells are as diverse as the engines that power the different vehicles seen on the streets of a city. There are motor proteins that use different fuels (e.g. GTP, ATP, or a chemical potential across a membrane), similar to engines that run on diesel fuel, gasoline, or electricity. Among the molecular motors that utilize ATP as a fuel source, certain superfamilies can be organized (e.g. myosin, dynein, and kinesin), just as vehicles that run on gasoline can be categorized into cars, trucks, and buses. Each superfamily of motor proteins has further sub-divisions based on the similarity of structure and function (e.g. Kinesin-1 through Kinesin-14 families), analogous to various forms of trucks such as pick-ups, SUVs, and tow trucks. The structural similarities and differences that exist within a specific family of motors are vital for how the proteins function in the cell.

The amino acid sequence of a protein primarily dictates the three dimensional structure and function of the molecule (215). Proteins of the kinesin superfamily share a ~350 amino acid motor domain that contains the ATP binding site and the microtubule-binding region. These proteins share >35% sequence similarity to the conventional kinesin motor domain. The three dimensional structure of different kinesin motors show an overall similar fold between the structures; however, the motor domains alone do not behave the same when assayed for function. The work presented in this dissertation reveals that even though the motor domain of Eg5 shares ~50 % sequence similarity to the well-studied conventional kinesin/Kinesin-1, Ncd/Kinesin-14, and Kar3/Kinesin-14 motor domains, it is unique in its functional capacity. An analogy for this observation is the comparison of the engines found in different trucks (e.g. tow truck, racing truck, and simple pickup truck). The engines that power these vehicles are very similar in structure (i.e. cylinders, pistons, drive shafts, etc.), but the performance of these engines have been engineered for a specific purpose. So it is with various members of the kinesin

superfamily. The differences in the motor core give rise to functional diversity, which is utilized to accomplish specific tasks inside the cell.

Motor proteins have the ability to utilize the energy from nucleotide turnover to generate molecular motion, which ultimately is converted to mechanical work along their associated filament tracks. The investigation presented in this dissertation aimed at characterizing how the structure and function of Eg5 distinguishes this protein as a mitotic motor protein. Prior to this work, Eg5 was identified as a slow, plus-end-directed microtubule-based molecular motor of the Kinesin-5/BimC family that is essential for bipolar spindle formation during eukaryotic cell division. This protein *in vivo* is thought to exist as a homotetramer, whereby four heavy chains interact to form a “dumbbell”-shaped molecule with two motor domains positioned at the end of a coiled-coil stalk (see [Figure 1.4](#)). My initial aim for this dissertation was a reductionist approach to characterize two truncated Eg5 proteins, Eg5-367 and Eg5-437, in hopes to define the ATPase mechanism of a single motor domain in comparison to the mechanism of a dimer, respectively. However, as shown in [Chapter 2.0](#), both Eg5 proteins were monomeric under the experimental conditions employed. Therefore, my work centers on the detailed transient kinetic analysis of two monomeric Eg5 motors.

I have performed a more thorough analysis of the Eg5-367 protein due to the complicating element of having an extended α -helical C-terminal region of Eg5-437 that does not participate in dimerization of the molecule. These Eg5 proteins are similar in their overall ATPase mechanism; however, there are differences in the steady-state ATPase kinetics, Eg5 binding to the microtubule, and subtle differences at the ATP hydrolysis step. At this point, I do not understand the structural and/or mechanistic reason for this difference. I am still not confident that Eg5-437 is monomeric in the presence of microtubules, due to the lower steady-state k_{cat} . Certain kinesins have been shown to undergo a monomer to dimer transition when bound to the microtubule (216, 217). Attaining a stable dimeric construct of Eg5 was a major goal in the lab; however, my thesis work did not include these endeavors.

5.1 STRUCTURAL MODEL OF NORMAL EG5 FUNCTION

I have used steady-state and presteady-state kinetics, as well as equilibrium binding approaches to characterize a single motor domain of Eg5. This domain of Eg5 is necessary and sufficient for ATP turnover and force generation; therefore, by studying the function of a single motor unit, we can begin to understand how the homotetramer functions to establish and maintain the bipolar spindle. The experiments presented in this dissertation collectively define the functional capacity of the Eg5 motor domain (e.g. ATP binding rates, ATP hydrolysis rates, equilibrium dissociation constants, etc.). However, at the heart of these measurements lies a structural explanation for these rate and equilibrium constants. This structural model must be inferred from the mechanistic results. As structural studies of motor-filament interactions are completed, this model will likely contain elements that correlate well with the structure, elements that do not correlate at all with the structure, and those elements that are yet to be supported by experimental results. However, at the current time, this structural model is consistent with the data I have collected for how Eg5 converts the energy from nucleotide turnover to force generation ([Figure 5.1](#)).

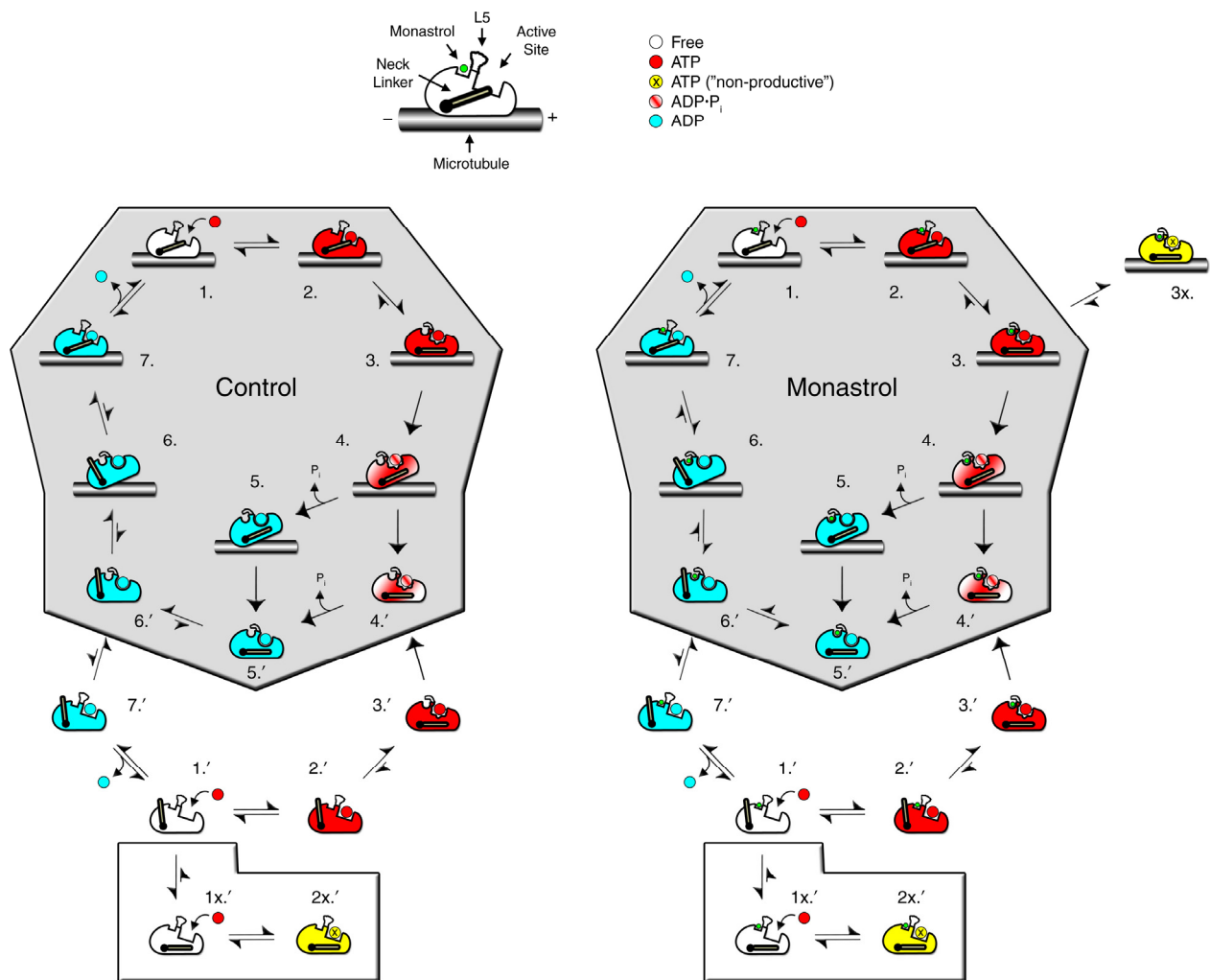


Figure 5.1 Models of Eg5 ATPase in the absence and presence of monastrol

5.1.1 Monomeric Eg5

At the onset of my thesis work, we were expressing each Eg5 protein in the *E. coli* cell line BL21 (DE3) pLysS and were obtaining marginal yields during each preparation. We surveyed the human Eg5 gene and found several codons that were under represented in *E. coli* due to codon usage bias. Therefore, we were able to find the *E. coli* cell line BL21-CodonPlus(DE3)-RIL (Stratagene), which supplemented the tRNAs and enhanced expression by greater than 10-fold. This approach may be useful to other investigators who wish to overexpress their protein of interest, though careful analysis of the DNA sequence is necessary before the investment of time into this expression system.

The Eg5 motor domain is a very stable protein, in both the presence and the absence of nucleotide at the active site ([Figure 4.2](#)). Other kinesin motors (in the absence of microtubules) have been unstable when nucleotide was not present at the active site (*117, 141, 213*), though the structural meaning for this phenomenon remains speculative. In a cell, Eg5 likely spends little time in the nucleotide-free state; however, this state of the motor is very important for the mechanism, because ADP and P_i products must vacate the active site for the ATPase cycle to continue. Nevertheless, we have purified Eg5-367 in the presence and absence of nucleotide and found the overall activity and ATPase mechanism in the presence of microtubules to be similar.

5.1.2 Microtubule Binding

If we begin our structural model at the microtubule association step (K_5 , [Scheme 2.1](#)), we observe the motor interaction with the microtubule occurring in at least two-steps: 1) formation of the Mt•Eg5•(ADP) collision complex, and 2) isomerization of the collision complex to form the tightly bound Mt•Eg5*•(ADP) intermediate. We observe similar transients for apoEg5 and Eg5•ADP binding to microtubules ([Figure 3.13B](#)), suggesting that the motor does not require nucleotide at the active site to properly bind to the microtubule lattice. The post-isomerization intermediate is very stable and tightly bound under equilibrium conditions ([Figure 2.8](#)). When the motor isomerizes to the tight microtubule-bound intermediate, we propose that the motor domain adopts a conformation that does not bind ADP nucleotide tightly ([Figure 2.9](#)). A recent study suggests that a conformational change in the nucleotide-binding site via the switch-1 region occurs when kinesin-family motors bind to microtubules (*194*). This conformational change in the switch-1 region could disrupt the coordination of the Mg²⁺ ion at the active site, thus promoting ADP to rapidly exit the active site (*92*). This switch-1 structural transition is very slow and rate-limiting for steady-state ATP turnover in the absence of microtubules; therefore, the microtubule actually accelerates this structural transition in the switch-1 region.

In addition to conformational changes in switch-1, the microtubule-binding interface contains multiple secondary structure elements (the “switch-2 cluster”) that are connected to the switch-2 region via loop L11, which is disordered in most kinesin crystal structures. This loop is proposed to become ordered when kinesin is bound to the microtubule, thus re-establishing the pathway of communication from the active site to the microtubule-binding interface. The

ordering of loop L11 likely occurs during the isomerization step of microtubule binding in order to achieve the tight microtubule-bound state. For Eg5, the “switch-2 cluster” likely re-organizes to facilitate the “rigor” conformation of the neck-linker (100). The vectorial ordering of the neck-linker would bias the rearward motor domain of a dimeric Eg5 protein to be positioned at the next microtubule binding site. The positioning of the neck-linker is believed to be critical to the force generation ability of Eg5 and other kinesins. Further tests on the structural dynamics of the neck-linker will better enhance our knowledge for how the neck-linker moves in response to binding the microtubule. Taken together, the structural transitions that accompany the tight microtubule-binding isomerization step in the mechanism are important for Eg5 force-generation.

5.1.3 ATP Binding

ATP binding to Eg5 occurs in at least two steps, analogous to how Eg5 binds to the microtubule. First, ATP collides with the Eg5 active site at a diffusion-limited rate ($k_{+1} \gg 100 \mu\text{M}^{-1}\text{s}^{-1}$), forming the Mt•Eg5•ATP collision complex, where ATP is only weakly bound (very large k_{-1}). Second, an isomerization of the Mt•Eg5•ATP collision complex promotes the increase in affinity for MgATP. This isomerization event likely involves a structural rearrangement in the switch-1 region, given the mechanism for ADP release upon tight microtubule binding. In addition, the “switch-2 cluster” ($\alpha 4$ -L12- $\alpha 5$) must undergo a structural transition due to the enhanced FRET efficiency between probes positioned on the neck-linker and Taxol, which is bound to the β -subunit of the tubulin heterodimer (100). This rearrangement of the “switch-2 cluster” allows the neck-linker to fully “dock” onto the motor core (75, 99). In our mantATP binding experiments and pulse-chase assays, we observed the maximum observed rate of ATP binding similar to the rate of the neck-linker “docking” event [$\sim 40 \text{ s}^{-1}$ in our mantATP binding experiments *versus* $\sim 60 \text{ s}^{-1}$ for FRET experiments (100)]. We propose that the structural transitions that accompany the nucleotide binding steps are actively driven by the nucleotide environment at the active site, rather than nucleotide binding being a passive process. In other words, when ATP occupies the active site, the new physiological environment disrupts the energetics of the system, and the motor reacts to attain a free energy minimum. The microtubule

also accelerates these structural transitions in the Eg5 motor domain, and acts as a “chaperone” to prevent “non-productive” complexes from becoming “trapped”.

5.1.4 ATP Hydrolysis

After nucleotide is bound tightly to the active site, a second conformational change must occur to align the water molecule for nucleophilic attack of the γ -phosphate bond. The intrinsic rate constant for the ATP hydrolysis step is similar to the rate of the ATP-promoted isomerization step ($\sim 30 \text{ s}^{-1}$). “When two reactions in series occur at exactly the same rate, the kinetics are difficult to distinguish from a single exponential, and the observed rate of reaction is approximately half of the rate of either reaction” (179). We observe single exponential kinetics for the first ATP turnover event, with a rate approximately 11-15 s^{-1} (Figure 2.12). This structural transition likely corresponds to the “closing” of the switch-2 region. This “closing” event would result in the rearrangement of loop L11, such that the interaction with the motor domain becomes weakened. Rosenfeld *et al.* proposed that the motor domain “rolls” on the microtubule at a rate similar to the rate of ATP hydrolysis that we measured (100). This weakening of the Eg5 motor domain for the microtubule would prepare the motor for detachment, and the tubulin C-terminal tails likely participate in the modulation of this binding state (191).

The actual chemical step of ATP cleavage is probably not accompanied by major structural rearrangements of the active site. However, this step appears to be irreversible in the mechanism due to the full burst amplitude obtained in acid-quench experiments in the absence of nucleotide. The data are consistent with a slight conformational change in the active site concomitant with bond cleavage in order for the P_i product to move into a position where ATP re-synthesis cannot occur. This re-positioning of the P_i within the active site of kinesins is supported by x-ray crystallographic data of Kif1a•ADP•Vanadate *versus* Kif1a•ADP•AlF₄, where they see the phosphate analog in two distinct locations within the active site (78). Due to the structural transitions that prepare the motor for ATP hydrolysis, the motor resides in a state that can actively detach from the microtubule. However, in order to maintain tension in the mitotic spindle, the Eg5 motor needs to remain tightly bound to the microtubule for a majority of its ATPase cycle. Therefore, Eg5’s mechanism is fine tuned for its function in the cell.

5.1.5 Phosphate Product Release and Eg5 Detachment from the Microtubule

After ATP hydrolysis, the Mt•Eg5•ADP•P_i intermediate populates during steady-state ATP turnover. This intermediate remains the most poorly understood intermediate along the pathway both kinetically and structurally. The steps of P_i product release and Mt•Eg5 dissociation are coupled in the Eg5 ATPase mechanism, whereby one step occurs at a slow rate and the other step occurs at a fast rate. For conventional kinesin, a mutant kinesin motor that did not detach from the microtubule showed the ability to release P_i product from the active site (138), thus suggesting that P_i release occurs before detachment. If the structural transition that leads to the ATP-hydrolysis competent state results in a weakening of Eg5 binding to the microtubule, then after ATP hydrolysis, this weak state would persist in the Mt•Eg5•ADP•P_i intermediate. If P_i release happens before detachment from the microtubule, and this P_i release event reverses the structural transition in the switch-2 region, then perhaps the motor would attain a tight binding conformation due to loop L11 ordering onto the microtubule. However, if the Mt•Eg5•ADP•P_i intermediate detaches from the microtubule, then in the dissociated state, Eg5 would release the P_i product rapidly and attain a conformation that can effectively re-bind the microtubule. At this time, we cannot distinguish between these two mechanisms. A mutant in Eg5, similar to the conventional kinesin mutant, would potentially uncover the hierarchical ordering of these steps.

Regardless of which step comes first – P_i product release or Mt•Eg5 dissociation – the step following ATP hydrolysis is the slow, rate-limiting step in the Eg5 ATPase mechanism, and the subsequent step is much faster (>10-fold faster). Again, this mechanism is fine tuned for the motor remaining associated with the microtubule so that Eg5 can contribute to the assembly and maintenance of the mitotic spindle.

5.2 STRUCTURAL MODEL OF EG5 INHIBITION BY MONASTROL

Monastrol is a small, cell-permeable molecule that arrests cells in mitosis by specifically inhibiting Eg5. I have used steady-state and presteady-state kinetics as well as equilibrium binding approaches to define the mechanistic basis for monastrol inhibition of monomeric Eg5. By investigating this small molecule inhibitor, we can gain further insight into the ATPase

mechanism of Eg5 as well as understanding how this inhibitor can be refined to make inhibition more efficient, not only for Eg5, but also for other motor proteins.

The Eg5 binding site for monastrol and other Eg5-specific inhibitors has been determined by X-ray crystallography as other structural studies (69, 79, 105). This binding site is ~12 Å from the active site and is quite distant from the microtubule-binding interface. However, it is still unclear how this small molecule inhibits the Eg5 ATPase mechanism. I present here my structural model for how monastrol inhibits the ATPase mechanism and the implications for Eg5-specific drug design ([Figure 5.1](#)).

5.2.1 Inhibition of Microtubule Binding

In [Chapter 3.0](#) and [Chapter 4.0](#), I have described the results from experiments that have provided insight into the allosteric mechanism of Eg5 inhibition by monastrol. In [Chapter 3.0](#), the data argue for a mechanism whereby monastrol binding to the Eg5•ADP intermediate leads to a decreased affinity for the microtubule during the presteady-state step of Eg5 association with the microtubule lattice, as well as under equilibrium conditions and steady-state ATP turnover. The monastrol “effect” on Eg5 association with the microtubule requires that the motor has ADP tightly bound to the active site. In [Chapter 4.0](#), the data presented suggest that the isomerization of the Eg5•ATP or Eg5•ADP collision complex leads to tightening of both nucleotide and monastrol due to a conformational change in loop L5 at the monastrol binding site. Therefore, I propose that monastrol binds weakly to the Eg5•AXP collision complexes and presumably to the nucleotide-free state as well.

How does tight monastrol binding inhibit effective microtubule binding? This question remains unanswered. The data in [Figure 3.13](#) show that the isomerization to the tight microtubule-binding state was dramatically slowed, suggesting the movement of the switch-1 region is inhibited by monastrol. This effect promotes in the slowing of ADP product release from the Mt•Eg5•ADP intermediate. The movement of switch-1 seems to correlate with the “closing” of loop L5 during the ATP hydrolysis cycle. Data suggests that when Eg5 tightly binds to the microtubule and releases ADP, then monastrol’s affinity weakens ([Figure 3.1](#)). If you were able to design a small molecule that bound to the inhibitor binding site more tightly and was better able to stabilize loop L5 from the natural conformational change it must undergo,

then the Eg5 inhibitor should show little (if any) association with the microtubule, and ADP strongly bound to the active site. There is no published data with the nanomolar inhibitors of Eg5 that demonstrates that Eg5 colocalizes with the microtubules in the monoastral spindle, as seen with monastrol ([Figure 1.12](#)).

However, when monoastral spindles induced by monastrol treatment are stained for Eg5, there is still localization of Eg5 with the microtubule array (see [Figure 1.12](#)). This is likely due to the “leaky” nature of the monastrol binding site. Monastrol does not have a nanomolar affinity for Eg5; therefore, monastrol will eventually dissociate from the motor and the motor can bind tightly to the microtubule. In order for monastrol to promote the dramatic reduction in the overall rate of ATP turnover, inhibition must occur elsewhere in the pathway.

5.2.2 “Non-Productive” Mt•Eg5*•ATP Complexes Promoted by Monastrol

Eventually, Eg5 will bind to the microtubule tightly and release its ADP, even in the presence of monastrol. However, we have observed a kinetic defect at the ATP hydrolysis step that is best explained by a “non-productive” subpopulation of Mt•Eg5*•ATP complexes that cannot properly hydrolyze ATP. By “non-productive” we mean enzymatic sites that remain catalytically inert during the first ATP turnover and also during subsequent ATP turnovers. The structure of this “non-productive” intermediate remains speculative, but in the absence of microtubules, a similar phenomenon is observed in the absence and presence of monastrol. In the absence of monastrol, the microtubule can act as a “chaperone” to prevent the formation of this “non-productive” species; however, in the presence of monastrol, this “chaperone-like” ability of the microtubule is diminished, but not eliminated. It is intriguing to speculate whether the C-terminal tails of tubulin mediate this “chaperone” ability of the microtubule, and monastrol binding to Eg5 somehow disrupts this interaction. This mechanism for Eg5 inhibition provides a “second line of defense”, but still does not provide an adequate means to disrupt the force production by the Eg5 population in the mitotic spindle. A “third line of defense” is needed to ensure the maximal inhibition of the enzyme.

5.2.3 Monastrol Accelerates the Rate of P_i Product Release and Mt•Eg5 Dissociation

It is interesting how a monastrol can inhibit the overall steady-state rate of ATP turnover, yet accelerate Eg5's rate-limiting step in the mechanism in the absence of monastrol. However, these are the results from P_i release and ATP-promoted Mt•Eg5 dissociation experiments in the presence of monastrol. This paradox can be resolved by realizing the observed rate of Eg5 association with the microtubule becomes the “new” rate-limiting step in the ATPase mechanism, with the “non-productive” intermediate contributing to a further decrease in the maximal rate of ATP turnover. This acceleration of detachment from the microtubule makes sense in terms of inhibiting the force generation of the motor. If the motor is not associated with its filament partner, it cannot transduce its force, thereby rendering the motor useless.

Monastrol and other inhibitors of Eg5 likely utilize a similar mechanism for inhibiting the ATPase cycle. It is unclear if this approach to cancer treatment will be long-standing due to the nature of the inhibitor binding site. Loop L5 “closes” during the ATPase mechanism and is responsible for tightening the binding of monastrol. However, if you replace loop L5 with a synonymous loop from conventional kinesin, the motor works “just fine” and the inhibitor is no longer able to bind and inhibit the motor (105). It would be interesting to know if you only remove the tryptophan from loop L5, will monastrol inhibit Eg5's ATPase? The answer to this question could raise serious issues for cancer-resistance to arise against monastrol-like chemotherapies, similar to the tumor lines that are resistant to Taxol. A cancerous cell could attain a point mutant in the Eg5 gene that leads to a substitution of the tryptophan residue, and the resulting Eg5 protein would become resistant to the drug. The task for the future in Eg5 inhibitors would be to screen for inhibitors that tightly bind to Eg5 mutants or other Kinesin-5's such as Klp61F, to eliminate this possibility.

5.3 FUTURE STUDIES

In order to better understand how motor proteins convert the energy of nucleotide turnover to force production, more detailed structural studies will be needed to physically characterize the dominant intermediates along the ATPase pathway. For kinesins, myosins, and dyneins, the co-crystal structure of the motor with the filament would open the “black box” that scientists have

been waiting to see for quite some time. For kinesins, the microtubule-kinesin co-crystal structure under different nucleotide conditions would greatly enhance our knowledge of the intimacy of the protein-protein interface, and how the non-covalent interactions between the motor and its filament promote varying conformations in the complex. So far, crystal structures of kinesins provide insight into conformations that are attained off the microtubule, but we know that force generation is tightly coupled to interactions with the microtubule.

Structural studies with higher-order oligomers of Eg5 (dimer, homotetramer) will provide mechanistic information for how the motor domains communicate and coordinate to achieve tension in the spindle. By directly comparing the ATPase mechanism of the dimer with the ATPase mechanism proposed for the monomer, we would be able to tease apart the physical attributes that are different, which arise due to tethering two motor domains together via a coiled-coil.

It would be interesting to attain a high-resolution crystal structure of the apoEg5 protein. To date, only one kinesin family member has been crystallized in the nucleotide-free state (81); however, the physiological relevance of this structure is questionable due to the crystal conditions used and the presence of a sulfate ion positioned at the active site where the β -phosphate of ADP would be positioned. Solving the structure of apoEg5 may also provide insight into the promotion of the “non-productive” subpopulation proposed in this dissertation.

Further work to investigate the neck-linker conformation of Eg5 in the presence of microtubules will provide insight into the movement of this critical component of the core domain. By introducing a clonable density marker (SH3 domain) inserted at the end of the neck-linker, we could localize the neck-linker using cryo-electron microscopy studies. Under various nucleotide conditions, the orientation of the neck-linker can be probed, and the location of the neck-linker can be correlated to the force generating steps in the mechanism.

Finally, the flexible tubulin C-terminal tails (CTTs) have recently been implicated in the walking mechanism of dynein and kinesin and were shown to modulate the binding of conventional kinesin to the microtubule (191, 218, 219). The CTTs of tubulin can be removed from microtubules using subtilisin, which cleaves ~10 amino acids from the C-terminus of α -subunit and ~20 amino acids from the β -subunit. The ATPase mechanism of monomeric Eg5 can be investigated in the absence of the tubulin CTTs and in the absence and presence of monastrol to characterize the physiological role for this protein-protein interaction.

APPENDIX.1 DYNAFIT SCRIPTS

A.1.1 Mt•Eg5 Mechanism: Fitting Acid-Quench Data

```
[task]

task      = fit
data      = progress
mechanism = Mt-Eg5 mechanism

[mechanism]

MEa + T <==> MEaT      :   k1  k2      ; ATP Collision Complex
MEaT    ---> MEbT      :   k3          ; ATP Isomerization
MEbT    <==> MEbDP     :   k5  k6      ; ATP Hydrolysis
MEbDP   ---> M + EaD + P :   k7          ; Pi Release/Dissoc
M + EaD -*> MEaD       :   k9          ; Mt Association (SLOW)
MEaD    ---> MEa + D   :   k11         ; ADP Release

[constants]

k1  = 100,          k2  = 909,
k3  = 20,
k5  = 30 ?,        k6  = 0.001,
k7  = 6,
k9  = 4 ?,
k11 = 43

[response]

MEbDP = 1
EaD   = 1
MEaD  = 1
D     = 1

[concentration]

MEa = 5 ?      ; used microMolar concentrations
T   = 400
M   = 6

[progress]
file      ./examples/Eg5/Control/Hydrolysis/AQ400control.txt

[output]
directory ./examples/Eg5/Control/Hydrolysis/E367/Model_2005_10_31/output

[end]
```

A.1.2 Mt•Eg5 Mechanism: Fitting P_i Release Data

```
[task]

task      = fit
data      = progress
mechanism = Mt-Eg5 mechanism

[mechanism]

MEa + T <==> MEaT      : k1    k2    ; ATP Collision Complex
MEaT    ---> MEbT      : k3          ; ATP Isomerization
MEbT    <==> MEbDP     : k5    k6    ; ATP Hydrolysis
MEbDP   ---> M + EaD + P : k7          ; Pi Release/Dissoc
M + EaD -*-> MEaD      : k9          ; Mt Association (slow)
MEaD    ---> MEa + D   : k11         ; ADP Release

[constants]

k1  = 100,          k2  = 909,
k3  = 20,           k5  = 30 ?,        k6  = 0.001,
k7  = 6 ?,         k9  = 0.8 ?,
k11 = 43

[response]

P = 1

[concentration]

MEa = 0.5 ? ; used microMolar concentrations
T   = 50
M   = 1

[progress]

offset 0.05
file    ./examples/Eg5/Control/Pi_Release/PR50control.txt

[output]

directory
./examples/Eg5/Control/Pi_Release/E367/Model_2005_10_31/output

[end]
```

A.1.3 Mt•Eg5 Mechanism: Simulation of Acid-Quench Kinetics

```
[task]

task      = simulate
data      = progress
mechanism = Mt-Eg5-Mon mechanism

[mechanism]

MEa + T <==> MEaT      : k1   k2      ; ATP Collision Complex
MEaT   ---> MEbT      : k3                ; ATP Isomerization
MEbT   <==> MEbDP     : k5   k6      ; ATP Hydrolysis
MEbDP  ---> M + EaD + P : k7                ; Pi Release/Dissoc
M + EaD -*-> MEaD      : k9                ; Mt Association (SLOW)
MEaD   ---> MEa + D   : k11             ; ADP Release

[constants]

k1  = 100,          k2  = 909,
k3  = 20,
k5  = 30 ?,        k6  = 0.001,
k7  = 6,
k9  = 4?,
k11 = 43

[sweep]

k6 = 0.001, 100, 250, 500, 1000, 10000

[response]

MEbDP = 1
EaD   = 1
MEaD  = 1
D     = 1

[concentration]

MEa = 5 ?      ; used microMolar concentrations
T   = 400
M   = 6

[progress]

mesh      from 0 to 1 step 0.001
file      ./examples/Eg5/Monastrol/Hydrolysis/AQ400mon.txt

[output]

directory
./examples/Eg5/Monastrol/Hydrolysis/E367/Model_2005_10_31/outputgood

[end]
```

A.1.4 Mt•Eg5 Mechanism: Simulation of P_i Release Kinetics

```
[task]

task      = simulate
data      = progress
mechanism = Mt-Eg5-Mon mechanism

[mechanism]

MEa + T <==> MEaT      : k1      k2      ; ATP Collision Complex
MEaT    ---> MEbT      : k3              ; ATP Isomerization
MEbT    <==> MEbDP     : k5      k6      ; ATP Hydrolysis
MEbDP   ---> M + EaD + P : k7              ; Pi Release/Dissoc
M + EaD -*-> MEaD      : k9              ; Mt Association (slow)
MEaD    ---> MEa + D   : k11             ; ADP Release

[constants]

k1 = 100,          k2 = 909,
k3 = 20,           k6 = 0.001 ?,
k5 = 30,           k7 = 6,
k9 = 0.8 ?,       k11 = 43

[response]

P = 1

[sweep]

k6 = 0.001, 100, 250, 500, 1000, 10000

[concentration]

MEa = 0.5 ? ; used microMolar concentrations
T   = 50
M   = 1

[progress]

mesh      from 0 to 0.75 step 0.001
offset 0.05
file      ./examples/Eg5/Monastrol/Pi_Release/PR50mon.txt

[output]

directory
./examples/Eg5/Monastrol/Pi_Release/E367/Model_2005_10_31/outputgood

[end]
```

A.1.5 ApoEg5 Mechanism: Fitting Acid-Quench Data

```
[task]

task      = fit
data      = progress
mechanism = apoEg5-367 mechanism

[mechanism]

Ea + T    <==>   EaT           :   k1    k2    ; ATP collision
EaT       <==>   EbT           :   k3    k4    ; ATP isomerization
EbT       <==>   EbDP          :   k5    k6    ; ATP Hydrolysis
EbDP      --->   EbD + P       :   k7          ; Pi Release
EbD       -*->   Ea + D        :   k9          ; ADP Release

[constants]

k1  = 100,           k2  = 2703,
k3  = 1 ?,          k4  = 0.014,
k5  = 10,           k6  = 0.001,
k7  = 10,
k9  = 0.1,

[response]

EbDP = 1
EbD  = 1
D    = 1

[concentration]

Ea  = 0.6 ?, ; used microMolar concentrations
T   = 50

[progress]

file      ./examples/Eg5/apoEg5/Hydrolysis/AQ50good.txt

[output]

directory
./examples/Eg5/apoEg5/Hydrolysis/ModelExpt20051020/output

[end]
```

A.1.6 ApoEg5 Mechanism: Fitting P_i Release Data

```
[task]

task      = fit
data      = progress
mechanism = apoEg5-367 mechanism

[mechanism]

Ea + T    <==>    EaT          :   k1    k2    ; ATP Collision Complex
EaT       <==>    EbT          :   k3    k4    ; ATP Isomerization
EbT       <==>    EbDP         :   k5    k6    ; ATP Hydrolysis
EbDP      --->    EbD + P      :   k7          ; Pi Release
EbD       -*->    Ea + D       :   k9          ; ADP Release

[constants]

k1  = 100,                k2  = 2700,
k3  = 0.5 ?,              k4  = 0.014,
k5  = 10,                  k6  = 0.001,
k7  = 10,
k9  = 0.13 ?,

[response]

P    = 1

[concentration]

Ea   = 1 ?, ; used microMolar concentrations
T    = 50

[progress]

file      ./examples/Eg5/apoEg5/Pi_Release/PR50good.txt

[output]

directory
./examples/Eg5/apoEg5/Pi_Release/ModelExpt20051018/output

[end]
```

A.1.7 ApoEg5 Mechanism: Simulation of Acid-Quench Kinetics

```
[task]

task      = simulate
data      = progress
mechanism = apoEg5-367 mechanism

[mechanism]

Ea + T    <==>   EaT          :   k1    k2    ; ATP collision
EaT       <==>   EbT          :   k3    k4    ; ATP isomerization
EbT       <==>   EbDP         :   k5    k6    ; ATP Hydrolysis
EbDP      --->   EbD + P      :   k7          ; Pi Release
EbD       -*->   Ea + D       :   k9          ; ADP Release

[constants]

k1    = 100,          k2    = 2703,
k3    = 1,           k4    = 0.014,
k5    = 10,          k6    = 0.001,
k7    = 10,
k9    = 0.10,

[sweep]

k6 = 0.001, 100, 250, 500, 1000, 2000

[response]

EbDP = 1
EbD  = 1
D    = 1

[concentration]

Ea    = 4, ; used microMolar concentrations
T     = 50

[progress]

mesh      from 0 to 7 step 0.005
file      ./examples/Eg5/apoEg5/Hydrolysis/AQ50good.txt
offset = 0

[output]

directory
./examples/Eg5/apoEg5/Hydrolysis/ModelExpt20051020/output

[end]
```

A.1.8 ApoEg5 Mechanism: Simulation of P_i Release Kinetics

```
[task]

task      = simulate
data      = progress
mechanism = apoEg5-367 mechanism

[mechanism]

Ea + T    <==>    EaT          :   k1    k2    ; ATP collision
EaT       <==>    EbT          :   k3    k4    ; ATP isomerization
EbT       <==>    EbDP         :   k5    k6    ; ATP Hydrolysis
EbDP      --->    EbD + P      :   k7          ; Pi Release
EbD       -*->    Ea + D       :   k9          ; ADP Release

[constants]

k1    = 100,          k2    = 2703,
k3    = 1,           k4    = 0.014,
k5    = 10,          k6    = 0.001,
k7    = 10,
k9    = 0.10,

[sweep]

k4 = 0.014, 10, 25, 50, 100, 200

[response]

P = 1

[concentration]

Ea    = 1, ; used microMolar concentrations
T     = 50

[progress]

mesh      from 0 to 15 step 0.005
file      ./examples/Eg5/apoEg5/Pi_Release/Pi50good.txt

[output]

directory
./examples/Eg5/apoEg5/Pi_Release/ModelExpt20051020/output

[end]
```

BIBLIOGRAPHY

1. Sauer, G., Korner, R., Hanisch, A., Ries, A., Nigg, E. A., and Sillje, H. H. (2005) Proteome analysis of the human mitotic spindle, *Mol Cell Proteomics* 4, 35-43.
2. Scholey, J. M., Brust-Mascher, I., and Mogilner, A. (2003) Cell division, *Nature* 422, 746-52.
3. Mermall, V., Post, P. L., and Mooseker, M. S. (1998) Unconventional myosins in cell movement, membrane traffic, and signal transduction, *Science* 279, 527-33.
4. Sellers, J. R. (2000) Myosins: a diverse superfamily, *Biochim Biophys Acta* 1496, 3-22.
5. Berg, J. S., Powell, B. C., and Cheney, R. E. (2001) A millennial myosin census, *Mol Biol Cell* 12, 780-94.
6. De La Cruz, E. M., and Ostap, E. M. (2004) Relating biochemistry and function in the myosin superfamily, *Curr Opin Cell Biol* 16, 61-7.
7. Vallee, R. B., and Gee, M. A. (1998) Make room for dynein, *Trends Cell Biol* 8, 490-4.
8. Vallee, R. B., Williams, J. C., Varma, D., and Barnhart, L. E. (2004) Dynein: An ancient motor protein involved in multiple modes of transport, *J Neurobiol* 58, 189-200.
9. Hirokawa, N., Noda, Y., and Okada, Y. (1998) Kinesin and dynein superfamily proteins in organelle transport and cell division, *Curr Opin Cell Biol* 10, 60-73.
10. Goldstein, L. S., and Philp, A. V. (1999) The road less traveled: emerging principles of kinesin motor utilization, *Annu Rev Cell Dev Biol* 15, 141-83.
11. Goldstein, L. S. (2001) Molecular motors: from one motor many tails to one motor many tales, *Trends Cell Biol* 11, 477-82.
12. Goshima, G., and Vale, R. D. (2003) The roles of microtubule-based motor proteins in mitosis: comprehensive RNAi analysis in the Drosophila S2 cell line, *J Cell Biol* 162, 1003-16.
13. Hirokawa, N., and Takemura, R. (2004) Kinesin superfamily proteins and their various functions and dynamics, *Exp Cell Res* 301, 50-9.
14. Wordeman, L. (2005) Microtubule-depolymerizing kinesins, *Curr Opin Cell Biol* 17, 82-8.

15. Severson, A. F., and Bowerman, B. (2002) Cytokinesis: closing in on the central spindle, *Dev Cell* 2, 4-6.
16. Nogales, E., Wolf, S. G., and Downing, K. H. (1998) Structure of the alpha beta tubulin dimer by electron crystallography, *Nature* 391, 199-203.
17. Desai, A., and Mitchison, T. J. (1997) Microtubule polymerization dynamics, *Annu Rev Cell Dev Biol* 13, 83-117.
18. Mountain, V., and Compton, D. A. (2000) Dissecting the role of molecular motors in the mitotic spindle, *Anat Rec* 261, 14-24.
19. Lodish, H., Berk, A., Zipursky, S. L., Matsudaira, P., Baltimore, D., and Darnell, J. (2000) *Molecular Cell Biology*, Fourth ed., W.H. Freeman and Company, New York, NY.
20. Brady, S. T. (1985) A novel brain ATPase with properties expected for the fast axonal transport motor, *Nature* 317, 73-5.
21. Vale, R. D., Reese, T. S., and Sheetz, M. P. (1985) Identification of a novel force-generating protein, kinesin, involved in microtubule-based motility, *Cell* 42, 39-50.
22. Vale, R. D., and Goldstein, L. S. (1990) One motor, many tails: an expanding repertoire of force-generating enzymes, *Cell* 60, 883-5.
23. Bloom, G. S., and Endow, S. A. (1994) Motor proteins. 1: kinesins, *Protein Profile* 1, 1059-116.
24. Scholey, J. M., Heuser, J., Yang, J. T., and Goldstein, L. S. (1989) Identification of globular mechanochemical heads of kinesin, *Nature* 338, 355-7.
25. Yang, J. T., Saxton, W. M., Stewart, R. J., Raff, E. C., and Goldstein, L. S. (1990) Evidence that the head of kinesin is sufficient for force generation and motility in vitro, *Science* 249, 42-7.
26. Brady, S. T., and Pfister, K. K. (1991) Kinesin interactions with membrane bounded organelles in vivo and in vitro, *J Cell Sci Suppl* 14, 103-8.
27. Skoufias, D. A., Cole, D. G., Wedaman, K. P., and Scholey, J. M. (1994) The carboxyl-terminal domain of kinesin heavy chain is important for membrane binding, *J Biol Chem* 269, 1477-85.
28. Goldstein, L. S. (1995) Structural features involved in force generation in the kinesin superfamily, *Biophys J* 68, 260S-265S; discussion 265S-266S.
29. Johnson, C. S., Buster, D., and Scholey, J. M. (1990) Light chains of sea urchin kinesin identified by immunoadsorption, *Cell Motil Cytoskeleton* 16, 204-13.

30. Cyr, J. L., Pfister, K. K., Bloom, G. S., Slaughter, C. A., and Brady, S. T. (1991) Molecular genetics of kinesin light chains: generation of isoforms by alternative splicing, *Proc Natl Acad Sci U S A* 88, 10114-8.
31. Gauger, A. K., and Goldstein, L. S. (1993) The *Drosophila* kinesin light chain. Primary structure and interaction with kinesin heavy chain, *J Biol Chem* 268, 13657-66.
32. Matthies, H. J., Miller, R. J., and Palfrey, H. C. (1993) Calmodulin binding to and cAMP-dependent phosphorylation of kinesin light chains modulate kinesin ATPase activity, *J Biol Chem* 268, 11176-87.
33. Lindesmith, L., McIlvain, J. M., Jr., Argon, Y., and Sheetz, M. P. (1997) Phosphotransferases associated with the regulation of kinesin motor activity, *J Biol Chem* 272, 22929-33.
34. Manning, B. D., and Snyder, M. (2000) Drivers and passengers wanted! the role of kinesin-associated proteins, *Trends Cell Biol* 10, 281-9.
35. Sproul, L. R., Anderson, D. J., Mackey, A. T., Saunders, W. S., and Gilbert, S. P. (2005) Cik1 targets the minus-end Kinesin depolymerase kar3 to microtubule plus ends, *Curr Biol* 15, 1420-7.
36. Lawrence, C. J., Dawe, R. K., Christie, K. R., Cleveland, D. W., Dawson, S. C., Endow, S. A., Goldstein, L. S., Goodson, H. V., Hirokawa, N., Howard, J., Malmberg, R. L., McIntosh, J. R., Miki, H., Mitchison, T. J., Okada, Y., Reddy, A. S., Saxton, W. M., Schliwa, M., Scholey, J. M., Vale, R. D., Walczak, C. E., and Wordeman, L. (2004) A standardized kinesin nomenclature, *J Cell Biol* 167, 19-22.
37. Endow, S. A. (1995) Determinants of motor polarity in the kinesin proteins, *Biophys J* 68, 271S-274S.
38. Henningsen, U., and Schliwa, M. (1997) Reversal in the direction of movement of a molecular motor, *Nature* 389, 93-6.
39. Case, R. B., Pierce, D. W., Hom-Booher, N., Hart, C. L., and Vale, R. D. (1997) The directional preference of kinesin motors is specified by an element outside of the motor catalytic domain, *Cell* 90, 959-66.
40. Sablin, E. P., Case, R. B., Dai, S. C., Hart, C. L., Ruby, A., Vale, R. D., and Fletterick, R. J. (1998) Direction determination in the minus-end-directed kinesin motor ncd, *Nature* 395, 813-6.
41. Endow, S. A., and Waligora, K. W. (1998) Determinants of kinesin motor polarity, *Science* 281, 1200-2.
42. Hirose, K., Henningsen, U., Schliwa, M., Toyoshima, C., Shimizu, T., Alonso, M., Cross, R. A., and Amos, L. A. (2000) Structural comparison of dimeric Eg5, *Neurospora* kinesin (Nkin) and Ncd head-Nkin neck chimera with conventional kinesin, *Embo J* 19, 5308-14.

43. Walczak, C. E., Mitchison, T. J., and Desai, A. (1996) XKCM1: a *Xenopus* kinesin-related protein that regulates microtubule dynamics during mitotic spindle assembly, *Cell* 84, 37-47.
44. Hunter, A. W., Caplow, M., Coy, D. L., Hancock, W. O., Diez, S., Wordeman, L., and Howard, J. (2003) The kinesin-related protein MCAK is a microtubule depolymerase that forms an ATP-hydrolyzing complex at microtubule ends, *Mol Cell* 11, 445-57.
45. Dagenbach, E. M., and Endow, S. A. (2004) A new kinesin tree, *J Cell Sci* 117, 3-7.
46. Kashina, A. S., Rogers, G. C., and Scholey, J. M. (1997) The bimC family of kinesins: essential bipolar mitotic motors driving centrosome separation, *Biochim Biophys Acta* 1357, 257-71.
47. Enos, A. P., and Morris, N. R. (1990) Mutation of a gene that encodes a kinesin-like protein blocks nuclear division in *A. nidulans*, *Cell* 60, 1019-27.
48. Hagan, I., and Yanagida, M. (1990) Novel potential mitotic motor protein encoded by the fission yeast *cut7+* gene, *Nature* 347, 563-6.
49. Hagan, I., and Yanagida, M. (1992) Kinesin-related *cut7* protein associates with mitotic and meiotic spindles in fission yeast, *Nature* 356, 74-6.
50. Roof, D. M., Meluh, P. B., and Rose, M. D. (1992) Kinesin-related proteins required for assembly of the mitotic spindle, *J Cell Biol* 118, 95-108.
51. Saunders, W. S., and Hoyt, M. A. (1992) Kinesin-related proteins required for structural integrity of the mitotic spindle, *Cell* 70, 451-8.
52. Hoyt, M. A., He, L., Loo, K. K., and Saunders, W. S. (1992) Two *Saccharomyces cerevisiae* kinesin-related gene products required for mitotic spindle assembly, *J Cell Biol* 118, 109-20.
53. Heck, M. M., Pereira, A., Pesavento, P., Yannoni, Y., Spradling, A. C., and Goldstein, L. S. (1993) The kinesin-like protein KLP61F is essential for mitosis in *Drosophila*, *J Cell Biol* 123, 665-79.
54. Barton, N. R., Pereira, A. J., and Goldstein, L. S. (1995) Motor activity and mitotic spindle localization of the *Drosophila* kinesin-like protein KLP61F, *Mol Biol Cell* 6, 1563-74.
55. Le Guellec, R., Paris, J., Couturier, A., Roghi, C., and Philippe, M. (1991) Cloning by differential screening of a *Xenopus* cDNA that encodes a kinesin-related protein, *Mol Cell Biol* 11, 3395-8.
56. Sawin, K. E., LeGuellec, K., Philippe, M., and Mitchison, T. J. (1992) Mitotic spindle organization by a plus-end-directed microtubule motor, *Nature* 359, 540-3.

57. Vernos, I., Heasman, J., and Wylie, C. (1993) Multiple kinesin-like transcripts in *Xenopus* oocytes, *Dev Biol* 157, 232-9.
58. Miki, H., Setou, M., and Hirokawa, N. (2003) Kinesin superfamily proteins (KIFs) in the mouse transcriptome, *Genome Res* 13, 1455-65.
59. Blangy, A., Lane, H. A., d'Herin, P., Harper, M., Kress, M., and Nigg, E. A. (1995) Phosphorylation by p34cdc2 regulates spindle association of human Eg5, a kinesin-related motor essential for bipolar spindle formation in vivo, *Cell* 83, 1159-69.
60. Sawin, K. E., and Mitchison, T. J. (1995) Mutations in the kinesin-like protein Eg5 disrupting localization to the mitotic spindle, *Proc Natl Acad Sci U S A* 92, 4289-93.
61. Kwok, B. H., Yang, J. G., and Kapoor, T. M. (2004) The rate of bipolar spindle assembly depends on the microtubule-gliding velocity of the mitotic kinesin Eg5, *Curr Biol* 14, 1783-8.
62. Kapoor, T. M., Mayer, T. U., Coughlin, M. L., and Mitchison, T. J. (2000) Probing spindle assembly mechanisms with monastrol, a small molecule inhibitor of the mitotic kinesin, Eg5, *J Cell Biol* 150, 975-88.
63. Cole, D. G., Saxton, W. M., Sheehan, K. B., and Scholey, J. M. (1994) A "slow" homotetrameric kinesin-related motor protein purified from *Drosophila* embryos, *J Biol Chem* 269, 22913-6.
64. Kashina, A. S., Baskin, R. J., Cole, D. G., Wedaman, K. P., Saxton, W. M., and Scholey, J. M. (1996) A bipolar kinesin, *Nature* 379, 270-2.
65. Sharp, D. J., McDonald, K. L., Brown, H. M., Matthies, H. J., Walczak, C., Vale, R. D., Mitchison, T. J., and Scholey, J. M. (1999) The bipolar kinesin, KLP61F, cross-links microtubules within interpolar microtubule bundles of *Drosophila* embryonic mitotic spindles, *J Cell Biol* 144, 125-38.
66. Sharp, D. J., Yu, K. R., Sisson, J. C., Sullivan, W., and Scholey, J. M. (1999) Antagonistic microtubule-sliding motors position mitotic centrosomes in *Drosophila* early embryos, *Nat Cell Biol* 1, 51-4.
67. Kapitein, L. C., Peterman, E. J., Kwok, B. H., Kim, J. H., Kapoor, T. M., and Schmidt, C. F. (2005) The bipolar mitotic kinesin Eg5 moves on both microtubules that it crosslinks, *Nature* 435, 114-8.
68. Turner, J., Anderson, R., Guo, J., Beraud, C., Fletterick, R., and Sakowicz, R. (2001) Crystal structure of the mitotic spindle kinesin Eg5 reveals a novel conformation of the neck-linker, *J Biol Chem* 276, 25496-502.
69. Yan, Y., Sardana, V., Xu, B., Homnick, C., Halczenko, W., Buser, C. A., Schaber, M., Hartman, G. D., Huber, H. E., and Kuo, L. C. (2004) Inhibition of a mitotic motor protein: where, how, and conformational consequences, *J Mol Biol* 335, 547-54.

70. Whitby, F. G., and Phillips, G. N., Jr. (2000) Crystal structure of tropomyosin at 7 Angstroms resolution, *Proteins* 38, 49-59.
71. Luisi, D. L., Kuhlman, B., Sideras, K., Evans, P. A., and Raleigh, D. P. (1999) Effects of varying the local propensity to form secondary structure on the stability and folding kinetics of a rapid folding mixed alpha/beta protein: characterization of a truncation mutant of the N-terminal domain of the ribosomal protein L9, *J Mol Biol* 289, 167-74.
72. Kull, F. J., Sablin, E. P., Lau, R., Fletterick, R. J., and Vale, R. D. (1996) Crystal structure of the kinesin motor domain reveals a structural similarity to myosin, *Nature* 380, 550-5.
73. Sack, S., Muller, J., Marx, A., Thormahlen, M., Mandelkow, E. M., Brady, S. T., and Mandelkow, E. (1997) X-ray structure of motor and neck domains from rat brain kinesin, *Biochemistry* 36, 16155-65.
74. Song, Y. H., Marx, A., Muller, J., Woehlke, G., Schliwa, M., Krebs, A., Hoenger, A., and Mandelkow, E. (2001) Structure of a fast kinesin: implications for ATPase mechanism and interactions with microtubules, *Embo J* 20, 6213-25.
75. Sindelar, C. V., Budny, M. J., Rice, S., Naber, N., Fletterick, R., and Cooke, R. (2002) Two conformations in the human kinesin power stroke defined by X-ray crystallography and EPR spectroscopy, *Nat Struct Biol* 9, 844-8.
76. Kozielski, F., Sack, S., Marx, A., Thormahlen, M., Schonbrunn, E., Biou, V., Thompson, A., Mandelkow, E. M., and Mandelkow, E. (1997) The crystal structure of dimeric kinesin and implications for microtubule-dependent motility, *Cell* 91, 985-94.
77. Kikkawa, M., Sablin, E. P., Okada, Y., Yajima, H., Fletterick, R. J., and Hirokawa, N. (2001) Switch-based mechanism of kinesin motors, *Nature* 411, 439-45.
78. Nitta, R., Kikkawa, M., Okada, Y., and Hirokawa, N. (2004) KIF1A alternately uses two loops to bind microtubules, *Science* 305, 678-83.
79. Cox, C. D., Breslin, M. J., Mariano, B. J., Coleman, P. J., Buser, C. A., Walsh, E. S., Hamilton, K., Huber, H. E., Kohl, N. E., Torrent, M., Yan, Y., Kuo, L. C., and Hartman, G. D. (2005) Kinesin spindle protein (KSP) inhibitors. Part 1: The discovery of 3,5-diaryl-4,5-dihydropyrazoles as potent and selective inhibitors of the mitotic kinesin KSP, *Bioorg Med Chem Lett* 15, 2041-5.
80. Garcia-Saez, I., Yen, T., Wade, R. H., and Kozielski, F. (2004) Crystal structure of the motor domain of the human kinetochore protein CENP-E, *J Mol Biol* 340, 1107-16.
81. Shipley, K., Hekmat-Nejad, M., Turner, J., Moores, C., Anderson, R., Milligan, R., Sakowicz, R., and Fletterick, R. (2004) Structure of a kinesin microtubule depolymerization machine, *Embo J* 23, 1422-32.

82. Ogawa, T., Nitta, R., Okada, Y., and Hirokawa, N. (2004) A common mechanism for microtubule destabilizers-M type kinesins stabilize curling of the protofilament using the class-specific neck and loops, *Cell* 116, 591-602.
83. Sablin, E. P., Kull, F. J., Cooke, R., Vale, R. D., and Fletterick, R. J. (1996) Crystal structure of the motor domain of the kinesin-related motor ncd, *Nature* 380, 555-9.
84. Kozielski, F., De Bonis, S., Burmeister, W. P., Cohen-Addad, C., and Wade, R. H. (1999) The crystal structure of the minus-end-directed microtubule motor protein ncd reveals variable dimer conformations, *Structure Fold Des* 7, 1407-16.
85. Gulick, A. M., Song, H., Endow, S. A., and Rayment, I. (1998) X-ray crystal structure of the yeast Kar3 motor domain complexed with Mg.ADP to 2.3 Å resolution, *Biochemistry* 37, 1769-76.
86. Yun, M., Zhang, X., Park, C. G., Park, H. W., and Endow, S. A. (2001) A structural pathway for activation of the kinesin motor ATPase, *EMBO J* 20, 2611-8.
87. Yun, M., Bronner, C. E., Park, C. G., Cha, S. S., Park, H. W., and Endow, S. A. (2003) Rotation of the stalk/neck and one head in a new crystal structure of the kinesin motor protein, Ncd, *EMBO J* 22, 5382-9.
88. Vinogradova, M. V., Reddy, V. S., Reddy, A. S., Sablin, E. P., and Fletterick, R. J. (2004) Crystal structure of kinesin regulated by Ca²⁺/calmodulin, *J Biol Chem*.
89. Vale, R. D., and Fletterick, R. J. (1997) The design plan of kinesin motors, *Annu Rev Cell Dev Biol* 13, 745-77.
90. Marx, A., Muller, J., and Mandelkow, E. (2005) The structure of microtubule motor proteins, *Adv Protein Chem* 71, 299-344.
91. Vale, R. D. (1996) Switches, latches, and amplifiers: common themes of G proteins and molecular motors, *J Cell Biol* 135, 291-302.
92. Kull, F. J., and Endow, S. A. (2002) Kinesin: switch I & II and the motor mechanism, *J Cell Sci* 115, 15-23.
93. Sack, S., Kull, F. J., and Mandelkow, E. (1999) Motor proteins of the kinesin family. Structures, variations, and nucleotide binding sites, *Eur J Biochem* 262, 1-11.
94. Woehlke, G., Ruby, A. K., Hart, C. L., Ly, B., Hom-Booher, N., and Vale, R. D. (1997) Microtubule interaction site of the kinesin motor, *Cell* 90, 207-16.
95. Hoenger, A., Sack, S., Thormahlen, M., Marx, A., Muller, J., Gross, H., and Mandelkow, E. (1998) Image reconstructions of microtubules decorated with monomeric and dimeric kinesins: comparison with x-ray structure and implications for motility, *J Cell Biol* 141, 419-30.

96. Hoenger, A., Thormahlen, M., Diaz-Avalos, R., Doerhoefer, M., Goldie, K. N., Muller, J., and Mandelkow, E. (2000) A new look at the microtubule binding patterns of dimeric kinesins, *J Mol Biol* 297, 1087-103.
97. Kikkawa, M., Okada, Y., and Hirokawa, N. (2000) 15 A resolution model of the monomeric kinesin motor, KIF1A, *Cell* 100, 241-52.
98. Skiniotis, G., Surrey, T., Altmann, S., Gross, H., Song, Y. H., Mandelkow, E., and Hoenger, A. (2003) Nucleotide-induced conformations in the neck region of dimeric kinesin, *Embo J* 22, 1518-28.
99. Rice, S., Lin, A. W., Safer, D., Hart, C. L., Naber, N., Carragher, B. O., Cain, S. M., Pechatnikova, E., Wilson-Kubalek, E. M., Whittaker, M., Pate, E., Cooke, R., Taylor, E. W., Milligan, R. A., and Vale, R. D. (1999) A structural change in the kinesin motor protein that drives motility, *Nature* 402, 778-84.
100. Rosenfeld, S. S., Xing, J., Jefferson, G. M., and King, P. H. (2005) Docking and rolling, a model of how the mitotic motor eg5 works, *J Biol Chem* 280, 35684-95.
101. Mayer, T. U., Kapoor, T. M., Haggarty, S. J., King, R. W., Schreiber, S. L., and Mitchison, T. J. (1999) Small molecule inhibitor of mitotic spindle bipolarity identified in a phenotypic-based screen, *Science* 286, 971-4.
102. DeBonis, S., Simorre, J. P., Crevel, I., Lebeau, L., Skoufias, D. A., Blangy, A., Ebel, C., Gans, P., Cross, R., Hackney, D. D., Wade, R. H., and Kozielski, F. (2003) Interaction of the mitotic inhibitor monastrol with human kinesin Eg5, *Biochemistry* 42, 338-49.
103. Nakazawa, J., Yajima, J., Usui, T., Ueki, M., Takatsuki, A., Imoto, M., Toyoshima, Y. Y., and Osada, H. (2003) A novel action of terpendole e on the motor activity of mitotic Kinesin eg5, *Chem Biol* 10, 131-7.
104. DeBonis, S., Skoufias, D. A., Lebeau, L., Lopez, R., Robin, G., Margolis, R. L., Wade, R. H., and Kozielski, F. (2004) In vitro screening for inhibitors of the human mitotic kinesin Eg5 with antimitotic and antitumor activities, *Mol Cancer Ther* 3, 1079-90.
105. Brier, S., Lemaire, D., Debonis, S., Forest, E., and Kozielski, F. (2004) Identification of the Protein Binding Region of S-Triptyl-L-cysteine, a New Potent Inhibitor of the Mitotic Kinesin Eg5, *Biochemistry* 43, 13072-82.
106. Hotha, S., Yarrow, J. C., Yang, J. G., Garrett, S., Renduchintala, K. V., Mayer, T. U., and Kapoor, T. M. (2003) HR22C16: a potent small-molecule probe for the dynamics of cell division, *Angew Chem Int Ed Engl* 42, 2379-82.
107. Sakowicz, R., Finer, J. T., Beraud, C., Crompton, A., Lewis, E., Fritsch, A., Lee, Y., Mak, J., Moody, R., Turincio, R., Chabala, J. C., Gonzales, P., Roth, S., Weitman, S., and Wood, K. W. (2004) Antitumor activity of a kinesin inhibitor, *Cancer Res* 64, 3276-80.

108. Garber, K. (2005) Divide and conquer: new generation of drugs targets mitosis, *J Natl Cancer Inst* 97, 874-6.
109. Haque, S. A., Hasaka, T. P., Brooks, A. D., Lobanov, P. V., and Baas, P. W. (2004) Monastrol, a prototype anti-cancer drug that inhibits a mitotic kinesin, induces rapid bursts of axonal outgrowth from cultured postmitotic neurons, *Cell Motil Cytoskeleton* 58, 10-6.
110. Marcus, A. I., Peters, U., Thomas, S. L., Garrett, S., Zelnak, A., Kapoor, T. M., and Giannakakou, P. (2005) Mitotic kinesin inhibitors induce mitotic arrest and cell death in Taxol-resistant and -sensitive cancer cells, *J Biol Chem* 280, 11569-77.
111. Geney, R., Ungureanu, M., Li, D., and Ojima, I. (2002) Overcoming multidrug resistance in taxane chemotherapy, *Clin Chem Lab Med* 40, 918-25.
112. Lockhart, A., and Cross, R. A. (1996) Kinetics and motility of the Eg5 microtubule motor, *Biochemistry* 35, 2365-73.
113. Vale, R. D., and Milligan, R. A. (2000) The way things move: looking under the hood of molecular motor proteins, *Science* 288, 88-95.
114. Miki, H., Setou, M., Kaneshiro, K., and Hirokawa, N. (2001) All kinesin superfamily protein, KIF, genes in mouse and human, *Proc Natl Acad Sci U S A* 98, 7004-11.
115. Vale, R. D. (2003) The molecular motor toolbox for intracellular transport, *Cell* 112, 467-80.
116. Schliwa, M., and Woehlke, G. (2003) Molecular motors, *Nature* 422, 759-65.
117. Sadhu, A., and Taylor, E. W. (1992) A kinetic study of the kinesin ATPase, *J Biol Chem* 267, 11352-9.
118. Ma, Y. Z., and Taylor, E. W. (1995) Mechanism of microtubule kinesin ATPase, *Biochemistry* 34, 13242-51.
119. Ma, Y. Z., and Taylor, E. W. (1995) Kinetic mechanism of kinesin motor domain, *Biochemistry* 34, 13233-41.
120. Hackney, D. D. (1994) The rate-limiting step in microtubule-stimulated ATP hydrolysis by dimeric kinesin head domains occurs while bound to the microtubule, *J Biol Chem* 269, 16508-11.
121. Gilbert, S. P., and Johnson, K. A. (1994) Pre-steady-state kinetics of the microtubule-kinesin ATPase, *Biochemistry* 33, 1951-60.
122. Gilbert, S. P., Webb, M. R., Brune, M., and Johnson, K. A. (1995) Pathway of processive ATP hydrolysis by kinesin, *Nature* 373, 671-6.

123. Schnitzer, M. J., and Block, S. M. (1997) Kinesin hydrolyses one ATP per 8-nm step, *Nature* 388, 386-90.
124. Hua, W., Young, E. C., Fleming, M. L., and Gelles, J. (1997) Coupling of kinesin steps to ATP hydrolysis, *Nature* 388, 390-3.
125. Ma, Y. Z., and Taylor, E. W. (1997) Interacting head mechanism of microtubule-kinesin ATPase, *J Biol Chem* 272, 724-30.
126. Gilbert, S. P., Moyer, M. L., and Johnson, K. A. (1998) Alternating site mechanism of the kinesin ATPase, *Biochemistry* 37, 792-9.
127. Moyer, M. L., Gilbert, S. P., and Johnson, K. A. (1998) Pathway of ATP hydrolysis by monomeric and dimeric kinesin, *Biochemistry* 37, 800-13.
128. Crevel, I., Carter, N., Schliwa, M., and Cross, R. (1999) Coupled chemical and mechanical reaction steps in a processive *Neurospora* kinesin, *EMBO J* 18, 5863-72.
129. Farrell, C. M., Mackey, A. T., Klumpp, L. M., and Gilbert, S. P. (2002) The role of ATP hydrolysis for Kinesin processivity, *J Biol Chem* 277, 17079-87.
130. Hackney, D. D. (2002) Pathway of ADP-stimulated ADP release and dissociation of tethered kinesin from microtubules. Implications for the extent of processivity, *Biochemistry* 41, 4437-46.
131. Rosenfeld, S. S., Xing, J., Jefferson, G. M., Cheung, H. C., and King, P. H. (2002) Measuring kinesin's first step, *J Biol Chem* 277, 36731-9.
132. Rosenfeld, S. S., Fordyce, P. M., Jefferson, G. M., King, P. H., and Block, S. M. (2003) Stepping and stretching. How kinesin uses internal strain to walk processively, *J Biol Chem* 278, 18550-6.
133. Uemura, S., and Ishiwata, S. (2003) Loading direction regulates the affinity of ADP for kinesin, *Nat Struct Biol* 10, 308-11.
134. Kaseda, K., Higuchi, H., and Hirose, K. (2003) Alternate fast and slow stepping of a heterodimeric kinesin molecule, *Nat Cell Biol* 5, 1079-82.
135. Asbury, C. L., Fehr, A. N., and Block, S. M. (2003) Kinesin Moves by an Asymmetric Hand-Over-Hand Mechanism, *Science*.
136. Schief, W. R., Clark, R. H., Crevenna, A. H., and Howard, J. (2004) Inhibition of kinesin motility by ADP and phosphate supports a hand-over-hand mechanism, *Proc Natl Acad Sci U S A*.
137. Yildiz, A., Tomishige, M., Vale, R. D., and Selvin, P. R. (2004) Kinesin walks hand-over-hand, *Science* 303, 676-8.

138. Klumpp, L. M., Hoenger, A., and Gilbert, S. P. (2004) Kinesin's second step, *Proc Natl Acad Sci U S A* 101, 3444-9.
139. Crevel, I. M., Nyitrai, M., Alonso, M. C., Weiss, S., Geeves, M. A., and Cross, R. A. (2004) What kinesin does at roadblocks: the coordination mechanism for molecular walking, *EMBO J* 23, 23-32.
140. Foster, K. A., Correia, J. J., and Gilbert, S. P. (1998) Equilibrium binding studies of non-claret disjunctional protein (Ncd) reveal cooperative interactions between the motor domains, *J Biol Chem* 273, 35307-18.
141. Pechatnikova, E., and Taylor, E. W. (1997) Kinetic mechanism of monomeric non-claret disjunctional protein (Ncd) ATPase, *J Biol Chem* 272, 30735-40.
142. Pechatnikova, E., and Taylor, E. W. (1999) Kinetics processivity and the direction of motion of Ncd, *Biophys J* 77, 1003-16.
143. Mackey, A. T., and Gilbert, S. P. (2000) Moving a microtubule may require two heads: a kinetic investigation of monomeric Ncd, *Biochemistry* 39, 1346-55.
144. Foster, K. A., Mackey, A. T., and Gilbert, S. P. (2001) A mechanistic model for Ncd directionality, *J Biol Chem* 276, 19259-66.
145. Mackey, A. T., and Gilbert, S. P. (2003) The ATPase cross-bridge cycle of the Kar3 motor domain. Implications for single head motility, *J Biol Chem* 278, 3527-35.
146. Crevel, I. M., Lockhart, A., and Cross, R. A. (1997) Kinetic evidence for low chemical processivity in ncd and Eg5, *J Mol Biol* 273, 160-70.
147. Maliga, Z., Kapoor, T. M., and Mitchison, T. J. (2002) Evidence that monastrol is an allosteric inhibitor of the mitotic kinesin Eg5, *Chem Biol* 9, 989-96.
148. Cochran, J. C., Sontag, C. A., Maliga, Z., Kapoor, T. M., Correia, J. J., and Gilbert, S. P. (2004) Mechanistic analysis of the mitotic kinesin Eg5, *J Biol Chem* 279, 38861-70.
149. Inoue, S. (1997) The role of microtubule assembly dynamics in mitotic force generation and functional organization of living cells, *J Struct Biol* 118, 87-93.
150. Compton, D. A. (2000) Spindle assembly in animal cells, *Annu Rev Biochem* 69, 95-114.
151. Mitchison, T. J., and Salmon, E. D. (2001) Mitosis: a history of division, *Nat Cell Biol* 3, E17-21.
152. Wittmann, T., Hyman, A., and Desai, A. (2001) The spindle: a dynamic assembly of microtubules and motors, *Nat Cell Biol* 3, E28-34.
153. Karsenti, E., and Vernos, I. (2001) The mitotic spindle: a self-made machine, *Science* 294, 543-7.

154. Nedelec, F., Surrey, T., and Karsenti, E. (2003) Self-organisation and forces in the microtubule cytoskeleton, *Curr Opin Cell Biol* 15, 118-24.
155. Gaglio, T., Saredi, A., Bingham, J. B., Hasbani, M. J., Gill, S. R., Schroer, T. A., and Compton, D. A. (1996) Opposing motor activities are required for the organization of the mammalian mitotic spindle pole, *J Cell Biol* 135, 399-414.
156. Saunders, W., Lengyel, V., and Hoyt, M. A. (1997) Mitotic spindle function in *Saccharomyces cerevisiae* requires a balance between different types of kinesin-related motors, *Mol Biol Cell* 8, 1025-33.
157. Mountain, V., Simerly, C., Howard, L., Ando, A., Schatten, G., and Compton, D. A. (1999) The kinesin-related protein, HSET, opposes the activity of Eg5 and cross-links microtubules in the mammalian mitotic spindle, *J Cell Biol* 147, 351-66.
158. Cytrynbaum, E. N., Scholey, J. M., and Mogilner, A. (2003) A force balance model of early spindle pole separation in *Drosophila* embryos, *Biophys J* 84, 757-69.
159. Chakravarty, A., Howard, L., and Compton, D. A. (2004) A Mechanistic Model for the Organization of Microtubule Asters by Motor and Non-Motor Proteins in a Mammalian Mitotic Extract, *Mol Biol Cell* 15, 2116-2132.
160. Kwon, M., and Scholey, J. M. (2004) Spindle mechanics and dynamics during mitosis in *Drosophila*, *Trends Cell Biol* 14, 194-205.
161. Blangy, A., Arnaud, L., and Nigg, E. A. (1997) Phosphorylation by p34cdc2 protein kinase regulates binding of the kinesin-related motor HsEg5 to the dynactin subunit p150, *J Biol Chem* 272, 19418-24.
162. Kapoor, T. M., and Mitchison, T. J. (2001) Eg5 is static in bipolar spindles relative to tubulin: evidence for a static spindle matrix, *J Cell Biol* 154, 1125-33.
163. Brune, M., Hunter, J. L., Corrie, J. E., and Webb, M. R. (1994) Direct, real-time measurement of rapid inorganic phosphate release using a novel fluorescent probe and its application to actomyosin subfragment 1 ATPase, *Biochemistry* 33, 8262-71.
164. Haldimann, A., Daniels, L. L., and Wanner, B. L. (1998) Use of new methods for construction of tightly regulated arabinose and rhamnose promoter fusions in studies of the *Escherichia coli* phosphate regulon, *J Bacteriol* 180, 1277-86.
165. Brune, M., Hunter, J. L., Howell, S. A., Martin, S. R., Hazlett, T. L., Corrie, J. E., and Webb, M. R. (1998) Mechanism of inorganic phosphate interaction with phosphate binding protein from *Escherichia coli*, *Biochemistry* 37, 10370-80.
166. Shelanski, M. L., Gaskin, F., and Cantor, C. R. (1973) Microtubule assembly in the absence of added nucleotides, *Proc Natl Acad Sci U S A* 70, 765-8.

167. Sloboda, R. D., Dentler, W. L., and Rosenbaum, J. L. (1976) Microtubule-associated proteins and the stimulation of tubulin assembly in vitro, *Biochemistry* 15, 4497-505.
168. Borisy, G. G., Olmsted, J. B., Marcum, J. M., and Allen, C. (1974) Microtubule assembly in vitro, *Fed Proc* 33, 167-74.
169. Omoto, C. K., and Johnson, K. A. (1986) Activation of the dynein adenosinetriphosphatase by microtubules, *Biochemistry* 25, 419-27.
170. Lowry, O. H., Rosebrough, N. J., Farr, A. L., and Randall, R. J. (1951) Protein Measurement with the Folin Phenol Reagent, *J Biol Chem* 193, 265-275.
171. Schacterle, G. R., and Pollack, R. L. (1973) A simplified method for the quantitative assay of small amounts of protein in biologic material, *Anal Biochem* 51, 654-5.
172. Philo, J. S. (2000) A method for directly fitting the time derivative of sedimentation velocity data and an alternative algorithm for calculating sedimentation coefficient distribution functions, *Anal Biochem* 279, 151-63.
173. Correia, J. J., Gilbert, S. P., Moyer, M. L., and Johnson, K. A. (1995) Sedimentation studies on the kinesin motor domain constructs K401, K366, and K341, *Biochemistry* 34, 4898-907.
174. Philo, J. S. (1997) An improved function for fitting sedimentation velocity data for low-molecular-weight solutes, *Biophys J* 72, 435-44.
175. Porath, J. (1960) Gel filtration of proteins, peptides and amino acids, *Biochim Biophys Acta* 39, 193-207.
176. Hackney, D. D. (1988) Kinesin ATPase: rate-limiting ADP release, *Proc Natl Acad Sci U S A* 85, 6314-8.
177. Moyer, M. L., Gilbert, S. P., and Johnson, K. A. (1996) Purification and characterization of two monomeric kinesin constructs, *Biochemistry* 35, 6321-9.
178. Gilbert, S. P., and Mackey, A. T. (2000) Kinetics: a tool to study molecular motors, *Methods* 22, 337-54.
179. Johnson, K. A. (1992) Transient-state kinetic analysis of enzyme reaction pathways, in *The Enzymes* pp 1-61, Academic Press, New York.
180. Crevel, I. M., Lockhart, A., and Cross, R. A. (1996) Weak and strong states of kinesin and ncd, *J Mol Biol* 257, 66-76.
181. Song, H., and Endow, S. A. (1998) Decoupling of nucleotide- and microtubule-binding sites in a kinesin mutant, *Nature* 396, 587-90.

182. Foster, K. A., and Gilbert, S. P. (2000) Kinetic studies of dimeric Ncd: evidence that Ncd is not processive, *Biochemistry* 39, 1784-91.
183. Woodward, S. K., Eccleston, J. F., and Geeves, M. A. (1991) Kinetics of the interaction of 2'(3')-O-(N-methylanthraniloyl)-ATP with myosin subfragment 1 and actomyosin subfragment 1: characterization of two acto-S1-ADP complexes, *Biochemistry* 30, 422-30.
184. Jontes, J. D., Milligan, R. A., Pollard, T. D., and Ostap, E. M. (1997) Kinetic characterization of brush border myosin-I ATPase, *Proc Natl Acad Sci U S A* 94, 14332-7.
185. Friedman, A. L., Geeves, M. A., Manstein, D. J., and Spudich, J. A. (1998) Kinetic characterization of myosin head fragments with long-lived myosin.ATP states, *Biochemistry* 37, 9679-87.
186. De La Cruz, E. M., Wells, A. L., Rosenfeld, S. S., Ostap, E. M., and Sweeney, H. L. (1999) The kinetic mechanism of myosin V, *Proc Natl Acad Sci U S A* 96, 13726-31.
187. Trybus, K. M., Krementsova, E., and Freyzon, Y. (1999) Kinetic characterization of a monomeric unconventional myosin V construct, *J Biol Chem* 274, 27448-56.
188. Lymn, R. W., and Taylor, E. W. (1971) Mechanism of adenosine triphosphate hydrolysis by actomyosin, *Biochemistry* 10, 4617-24.
189. Shimizu, T., Sablin, E., Vale, R. D., Fletterick, R., Pechatnikova, E., and Taylor, E. W. (1995) Expression, purification, ATPase properties, and microtubule-binding properties of the ncd motor domain, *Biochemistry* 34, 13259-66.
190. Ma, Y. Z., and Taylor, E. W. (1997) Kinetic mechanism of a monomeric kinesin construct, *J Biol Chem* 272, 717-23.
191. Skiniotis, G., Cochran, J. C., Muller, J., Mandelkow, E., Gilbert, S. P., and Hoenger, A. (2004) Modulation of kinesin binding by the C-termini of tubulin, *EMBO J* 23, 989-99.
192. Hackney, D. D. (1994) Evidence for alternating head catalysis by kinesin during microtubule-stimulated ATP hydrolysis, *Proc Natl Acad Sci U S A* 91, 6865-9.
193. Johnson, K. A. (1983) The pathway of ATP hydrolysis by dynein. Kinetics of a presteady state phosphate burst, *J Biol Chem* 258, 13825-32.
194. Naber, N., Rice, S., Matuska, M., Vale, R. D., Cooke, R., and Pate, E. (2003) EPR Spectroscopy Shows a Microtubule-Dependent Conformational Change in the Kinesin Switch 1 Domain, *Biophys J* 84, 3190-6.
195. Siegel, L. M., and Monty, K. J. (1966) Determination of molecular weights and frictional ratios of proteins in impure systems by use of gel filtration and density gradient

- centrifugation. Application to crude preparations of sulfite and hydroxylamine reductases, *Biochim Biophys Acta* 112, 346-62.
196. Moyer, M. L. (1998) Mechanism of the Microtubule Kinesin Motor ATPase, *Biochemistry, Microbiology, and Molecular Biology* pp 1-170, Pennsylvania State University, University Park, PA.
 197. Cochran, J. C., Gatial, J. E., 3rd, Kapoor, T. M., and Gilbert, S. P. (2005) Monastrol inhibition of the mitotic kinesin Eg5, *J Biol Chem* 280, 12658-67.
 198. Sharp, D. J., Rogers, G. C., and Scholey, J. M. (2000) Microtubule motors in mitosis, *Nature* 407, 41-7.
 199. Peterson, J. R., and Mitchison, T. J. (2002) Small molecules, big impact: a history of chemical inhibitors and the cytoskeleton, *Chem Biol* 9, 1275-85.
 200. Miyamoto, D. T., Perlman, Z. E., Mitchison, T. J., and Shirasu-Hiza, M. (2003) Dynamics of the mitotic spindle--potential therapeutic targets, *Prog Cell Cycle Res* 5, 349-60.
 201. Funk, C. J., Davis, A. S., Hopkins, J. A., and Middleton, K. M. (2004) Development of high-throughput screens for discovery of kinesin adenosine triphosphatase modulators, *Anal Biochem* 329, 68-76.
 202. Mailhes, J. B., Mastromatteo, C., and Fuseler, J. W. (2004) Transient exposure to the Eg5 kinesin inhibitor monastrol leads to syntelic orientation of chromosomes and aneuploidy in mouse oocytes, *Mutat Res* 559, 153-67.
 203. Crevel, I. M., Alonso, M. C., and Cross, R. A. (2004) Monastrol stabilises an attached low-friction mode of Eg5, *Curr Biol* 14, R411-2.
 204. Hackney, D. D., Malik, A. S., and Wright, K. W. (1989) Nucleotide-free kinesin hydrolyzes ATP with burst kinetics, *J Biol Chem* 264, 15943-8.
 205. Kuzmic, P. (1996) Program DYNAFIT for the analysis of enzyme kinetic data: application to HIV proteinase, *Anal Biochem* 237, 260-73.
 206. Holmes, K. C., and Geeves, M. A. (2000) The structural basis of muscle contraction, *Philos Trans R Soc Lond B Biol Sci* 355, 419-31.
 207. Sablin, E. P., and Fletterick, R. J. (2001) Nucleotide switches in molecular motors: structural analysis of kinesins and myosins, *Curr Opin Struct Biol* 11, 716-24.
 208. Endow, S. A. (2003) Kinesin motors as molecular machines, *Bioessays* 25, 1212-9.
 209. Cooke, R. (2004) The sliding filament model: 1972-2004, *J Gen Physiol* 123, 643-56.

210. Hackney, D. D. (1996) The kinetic cycles of myosin, kinesin, and dynein, *Annu Rev Physiol* 58, 731-50.
211. Steinberg, G., and Schliwa, M. (1996) Characterization of the biophysical and motility properties of kinesin from the fungus *Neurospora crassa*, *J Biol Chem* 271, 7516-21.
212. Muller, J., Marx, A., Sack, S., Song, Y. H., and Mandelkow, E. (1999) The structure of the nucleotide-binding site of kinesin, *Biol Chem* 380, 981-92.
213. Morii, H., Shimizu, T., Mizuno, N., Edamatsu, M., Ogawa, K., Shimizu, Y., and Toyoshima, Y. Y. (2005) Removal of tightly bound ADP induces distinct structural changes of the two tryptophan-containing regions of the ncd motor domain, *J Biochem (Tokyo)* 138, 95-104.
214. Bagshaw, C. R., Trentham, D. R., Wolcott, R. G., and Boyer, P. D. (1975) Oxygen exchange in the gamma-phosphoryl group of protein-bound ATP during Mg²⁺-dependent adenosine triphosphatase activity of myosin, *Proc Natl Acad Sci U S A* 72, 2592-6.
215. Anfinsen, C. B. (1973) Principles that govern the folding of protein chains, *Science* 181, 223-30.
216. Tomishige, M., Klopfenstein, D. R., and Vale, R. D. (2002) Conversion of Unc104/KIF1A kinesin into a processive motor after dimerization, *Science* 297, 2263-7.
217. Al-Bassam, J., Cui, Y., Klopfenstein, D., Carragher, B. O., Vale, R. D., and Milligan, R. A. (2003) Distinct conformations of the kinesin Unc104 neck regulate a monomer to dimer motor transition, *J Cell Biol* 163, 743-53.
218. Thorn, K. S., Ubersax, J. A., and Vale, R. D. (2000) Engineering the processive run length of the kinesin motor, *J Cell Biol* 151, 1093-100.
219. Wang, Z., and Sheetz, M. P. (2000) The C-terminus of tubulin increases cytoplasmic dynein and kinesin processivity, *Biophys J* 78, 1955-64.